Hybrid modeling techniques embracing permanent-magnet-biased salient machines

Citation for published version (APA):
Ilhan, E. (2014). *Hybrid modeling techniques embracing permanent-magnet-biased salient machines*. [Phd Thesis 1 (Research TU/e / Graduation TU/e), Electrical Engineering]. Technische Universiteit Eindhoven. https://doi.org/10.6100/IR782713

DOI:
10.6100/IR782713

Document status and date:
Published: 17/11/2014

Document Version:
Publisher’s PDF, also known as Version of Record (includes final page, issue and volume numbers)

Please check the document version of this publication:

• A submitted manuscript is the version of the article upon submission and before peer-review. There can be important differences between the submitted version and the official published version of record. People interested in the research are advised to contact the author for the final version of the publication, or visit the DOI to the publisher's website.
• The final author version and the galley proof are versions of the publication after peer review.
• The final published version features the final layout of the paper including the volume, issue and page numbers.

Link to publication

General rights
Copyright and moral rights for the publications made accessible in the public portal are retained by the authors and/or other copyright owners and it is a condition of accessing publications that users recognise and abide by the legal requirements associated with these rights.

- Users may download and print one copy of any publication from the public portal for the purpose of private study or research.
- You may not further distribute the material or use it for any profit-making activity or commercial gain
- You may freely distribute the URL identifying the publication in the public portal.

If the publication is distributed under the terms of Article 25fa of the Dutch Copyright Act, indicated by the “Taverne” license above, please follow below link for the End User Agreement:

www.tue.nl/taverne

Take down policy
If you believe that this document breaches copyright please contact us at:

openaccess@tue.nl

providing details and we will investigate your claim.

Download date: 05. Oct. 2023

Hybrid modeling techniques embracing permanent-magnet-biased salient machines

PROEFSCHRIFT

ter verkrijging van de graad van doctor
aan de Technische Universiteit Eindhoven,
op gezag van de rector magnificus, prof.dr.ir. C.J. van Duijn,
voor een commissie aangewezen door het College voor Promoties
in het openbaar te verdedigen
op maandag 17 november 2014 om 16.00 uur

door

Esin Ilhan

geboren te Istanbul, Turkije

Dit proefschrift is goedgekeurd door de promotoren en de samenstelling van de promotiecommissie is als volgt:

voorzitter:	prof.dr.ir. J.H. Blom
promotor:	prof.dr. E.A. Lomonova MSc
copromotor:	dr. J.J.H. Paulides, MPhil
leden:	prof.dr. P.H. Mellor (Bristol University)
	prof.dr. P.T. Krein (University of Illinois)
	prof.dr. H. Nijmeijer
adviseurs:	dr.ir. F.J.M. Thoolen (Centre for Concepts in Mechatronics)
	dr. B.L.J. Gysen MSc

Hybrid modeling techniques embracing permanent-magnet-biased salient machines

Doktora tezİ

Akı çevirmeli ve sabit mıknatıs etkileşimli motorların hibrit modellenmesi

adlı doktora tezinin savunması 17 Kasım 2014 tarihinde Eindhoven Teknik Üniversitesi'nde, önceki sayfada adı belirtilen komite üyelerinin karşısında ve halka açık bir oturumda gerçekleşmiştir. Bu çalışma Elektrik Mühendisliği bölümünün Elektrik Makinaları ve Güç Elektroniği programında hazırlanmıştır.

Esin İlhan

doğum yeri İstanbul, Türkiye

This research is part of the IOP-EMVT program (*I*nnovatiegerichte *O*nderzoeks*P*rogramma's - *E*lektromagnetische *V*ermogens*T*echniek) under IOP-EMVT 08205. This program is funded by AgentschapNL, an agency of the Dutch Ministry of Economical Affairs, Agriculture and Innovation.

Hybrid modeling techniques embracing permanent-magnet-biased salient machines / /
by E. Ilhan.
Eindhoven: Technische Universiteit Eindhoven, 2014

A catalogue record is available from the Eindhoven University of Technology Library.
ISBN: 978-94-6259-334-3

To my parents
Aileme, Atiye ve Yuriye...

Summary

Hybrid modeling techniques embracing permanent-magnet-biased salient machines

Dynamic applications mandate a high torque density and benefit from a robust rotor with low inertia. To date, these applications are dominated by brushless permanent magnet ac (PMAC) machines in the low-voltage region. However, PM-biased salient machines with an enhanced performance are emerging with both PMs and coils consigned to the stator. Consequently, torque is produced by exciting the stator coils which *see* a high level of PM-biased airgap flux density when the rotor poles are in alignment, providing a force between the stator tooth and rotor pole. Similar torque densities, albeit at reduced electrical loading, can be achieved with these machines compared to brushless PMAC motors. This is realized by utilizing a salient pole rotor with straight teeth, similar to rotor of a switched reluctance machine. This specific structure stipulates a switching high flux density pattern within the double salient airgap, hence numerical techniques are applied for their analysis. However, these techniques are generally computationally least efficient for such new machine topologies. Therefore, alternative modeling solutions are required, which are easier to manage in the preliminary design stage, when the influence of several design variables must be considered.

This thesis seeks cascaded forms of (semi-)analytical, spatially discretized and mapping techniques for the analysis of PM-biased salient machines, most commonly named flux switching PM machine (FSPM). In addition to the necessity for new electromagnetic modeling approaches for FSPMs, significant attention is also paid to design aspects specific to high-acceleration applications. These topics are evaluated in Part I and Part II of the thesis, respectively.

Modeling of structures with double saliency can be accomplished through numerous stand-alone techniques, i.e. for FSPMs a spatially discretized finite element method, magnetic equivalent circuit method and (semi-)analytical Fourier analysis. In Part I, alternative approaches are researched, that exploit individual method's advantages and allow for more design flexibility. These approaches solve either the first-order partial differential Maxwell equations or the second-order partial differential Poisson and Laplace equations by pairing mathematical approaches with different levels of abstraction resulting in three hybrid models (HM):

HM1 Fourier analysis and magnetic equivalent circuit,

HM2 Tooth contour method and electrostatic finite element method, and

HM3 Tooth contour method and Schwarz-Christoffel mapping.

Each hybrid model is first introduced on a reduced-order case study, a double salient structure with an airgap, followed by its implementation on an FSPM in an ascending overall accuracy. For both structures, the pairing of hybrid models is based on the magnetic calculations in the double salient airgap. For HM1, this is realized by means of changing the geometric parameters, for HM2 by a fine discretization within the electrostatic fields, and for HM3 by simplification via mapping functions. With their increased functionality, these hybrid models, unlike the finite element method, can deal with problems of random domains occurring as a result of uncertainties in the design process, such as discontinuity, lowered accuracy near boundaries, material properties or manufacturing tolerances. A comparison of these models is presented to point out individual advantages in accuracy, simulation time, inclusion of magnetic nonlinearity, end effects, and design flexibility, under certain limitations of applicability.

Design problems are often solved by optimizing a certain structure and making relative judgments if the final product is an adequate solution, which is not necessarily a global optimum. In Part II, focused on the design process of FSPMs for high-acceleration applications, these ambiguities are eliminated by eliciting the key design parameters in a generalized approach comprising magnetic, thermal and mechanical design steps. To predict its operational limits, a thermal model is created based on the equivalent circuit representation. Rotor optimization, aimed at minimizing inertia and obtaining a smooth torque profile, fall under the scope of mechanical design to satisfy the dynamic application requirements. To validate the dynamic capability of FSPMs, a new prototype was developed based on the generalized design methodology with specific criteria of high acceleration, torque profile and overloading capability. Physical constraints are established based on an industrial state-of-the-art brushless PMAC motor, as a benchmark with good acceleration capability. Under identical thermal limits, the newly developed FSPM prototype achieves a higher acceleration compared to the benchmark motor.

Contents

Chapter 1

Introduction

”A sharp knife is nothing without a sharp eye.” – Klingon Proverb

* * *

This chapter introduces the background of the thesis ”Necessity for electromagnetic modeling approaches with specific interest on the modeling of permanent-magnet-biased (PM-biased) salient machines”.

Hybrid modeling approaches are introduced that allow for the design and analysis of salient PM-biased structures with due consideration of the governing energy conversion and torque production mechanisms in electrical machines. In this respect, the fast modeling of PM-biased salient machines, while maintaining sufficient accuracy, challenges existing stand-alone techniques due to flux paths being less constrained to the soft magnetic material. The modeling of these complex, i.e. less constrained, flux paths necessitates the introduction of *hybrid models* to unite existing stand-alone analytical and numerical techniques, especially when material boundaries are in close proximity to the airgap. These *hybrid models* are applied to a flux switching permanent magnet machine, i.e. a particular example of a PM-biased salient machine, to verify their applicability for machine design. Their distinctive properties are compared to other machine classes in terms of torque production. Further, their structural advantage are illustrated on a machine developed for high-acceleration applications. Finally, the research goals are identified and the outline of the thesis is presented.

* * *

1.1 Journey to electrical machines

Throughout the ages, electromagnetism triggered the curiosity of mankind towards its environment. Ancient Egyptians were fascinated by a fish species using electrical charges to neutralize its prey [1]. Among other discoveries, a piece of a magnetite, an oxide of iron, was found with a very special property; it could attract a piece of iron but had no effect on other metals such as gold, silver, and copper. However, it was not until the 16^{th} century that experimental studies on classical electromagnetism began [2]. Among the notable scientists, the French physicist André Marie Ampère began developing theories for various experiments, including Ørsted's famous needle experiment [3]. His formulation presented that electrical energy could be transformed into magnetic energy. Later, a British scientist Michael Faraday showed in his experiment that another physical property of materials, *magnetism*, could interact with electrical fields [4, 5]. His findings showed that magnetic energy could be transformed (back) to electrical energy. Simultaneously, an American scientist Joseph Henry was busy building practical electromagnets, such as primitive electrical doorbells and relays [6]. His experiments led to the discovery of inductance, the link between magnetic and electrical energy. As the interaction between different energy forms became more evident, mathematicians like Carl Friedrich Gauss started to collaborate with physicists like Wilhelm Eduard Weber [7]. Their experiments on magnetic fields led to general equations of energy conservation [3]. The final milestone was set by a Dutch scientist Hendrik Lorentz, who presented the equation for the force due to the interaction of the electrical and magnetic fields [8]. With the Lorentz equation, that electromagnetic energy could be transformed to mechanical energy, hence the first designed, rather than empirically discovered, electrical machines emerged. Today, new electrical machine configurations continue to be developed at an increasing rate to answer the challenging industrial requirements, i.e. high torque, fast acceleration, and high efficiency. Albeit that the governing rules for the operation principle of electrical machines are still mostly based on classical theories of electromagnetism unified by the Scottish scientist James Clerk Maxwell [9]. These equations, summarized in Appendix A, present the relationships between electrical and magnetic energies, which provide a fundamental platform to acquaint novel machine topologies.

1.2 Energy conversion in PM-biased structures

Historically, electrical machines have been constructed from soft magnetic materials (usually in a laminated form), electrical conductors (copper, aluminium), insulation (for the conductors, slots) and mechanical parts (steel shaft, bearings) [2]. Although soft magnetic materials can be used alone, they can also be biased by hard magnetic materials, such as permanent magnets (PMs), to maximize the energy conversion of electrical machines. An example of a primitive PM-biased electrical machine is schematically illustrated in Fig. 1.1. In this example, both magnetomotive force (mmf) sources, a dc-exited coil and a PM, are located in the stationary part of the machine and act as $\mathcal{F}$, according to Ampère's law given in Appendix A. These structures are PM-biased and if moving the iron with Δ_x, the mmf variation that is a result of the PM dominates. To analyze this lossless and magnetically linearized system, a soft magnetic material with a constant relative permeability (no saturation), the resulting magnetic flux, Φ, is assumed to be free from fringing and leakage.

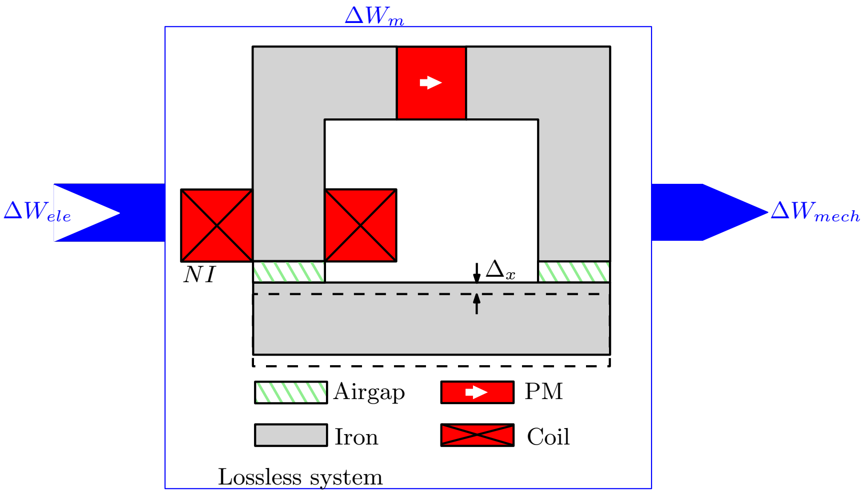

Figure 1.1: A primitive PM-biased electrical machine represented in a lossless electromechanical energy conversion system.

In essence, most electrical machines are energy converters between electrical and mechanical energies coupled via a stored magnetic field [11, 12]. These interrelations can be visualized by means of energy conversion diagrams, which take the form of flux linkage-current, $(\lambda - i)$, loops [13]. Alternatively, albeit less frequently, these energy conversion diagrams can also be represented by flux-mmf, $(\Phi - \mathcal{F})$, loops [14]. Such an example, given in [10], shows the stored magnetic energy associated with various sections of the PM-biased structure. The change in the stored energy is illustrated in Fig. 1.2 for a mechanical airgap increase of Δ_x, assuming a constant relative permeability (dotted line). It should be noted that the visual representations in these figures have been exaggerated for illustrative purposes. For example, the smallest energy storage and change are realized in the iron (Fig. 1.2a), which is considerably smaller compared to the changes realized in the PM (Fig. 1.2b), airgap (Fig. 1.2c), and coil (Fig. 1.2d), i.e. $(\Delta B, \Delta C, \Delta D) >> \Delta A$, respectively. Thus, in the analysis of PM-biased structures, accurate modeling of elements with a relative permeability close to that of air, such as a salient airgap, PMs and coils, is very important.

Neglecting the minimal influence of iron, ΔA, the resulting net change in stored magnetic energy can be illustrated by the difference between the tiled areas in

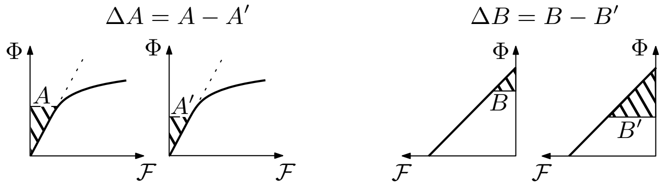

a) Iron b) PM

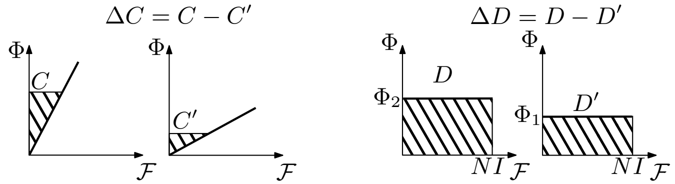

c) Airgap d) Coil

Figure 1.2: Flux-mmf, $(\Phi - \mathcal{F})$, diagrams for the calculation of energy changes in the structure (Fig.1.1) for an increase in airgap by Δ_x [10].

Fig. 1.2, i.e. $\Delta W_m = \Delta B + \Delta C$. As a result of the movement, the coil flux linked by N-turns is reduced from Φ_2 to Φ_1 in time interval $(t_2 - t_1)$, and a net change in electrical energy, ΔW_{ele}, is obtained:

$$\Delta W_{ele} = \int_{\Phi_1}^{\Phi_2} NId\Phi, \tag{1.1}$$

where I represents the constant current in the coil. In fact, this variation is shown by ΔD on the coil $\Phi - \mathcal{F}$ diagram in Fig. 1.2d. Considering energy conservation in a lossless system, the change in mechanical energy, $\Delta W_{mech} = F\Delta_x$, must satisfy the following relation:

$$\Delta W_{mech} = \Delta W_{ele} - \Delta W_m, \tag{1.2}$$

hence the average force for the displacement of Δ_x is given by constant I:

$$F = \frac{\Delta D - (\Delta B + \Delta C)}{\Delta_x}. \tag{1.3}$$

An alternative force expression can be developed from the same considerations in terms of the change in coenergy, $W'_m = \int_V \int_0^H (BdH)dV$, where B is the magnetic flux density, and H the magnetic field strength over a volume, V [15]. Since energy conversion is realized in the airgap, the values of W'_m depends physically on B and H as calculated in this region. Thus, based on the definition of coenergy, force can be calculated as the following:

$$F = \frac{\Delta W'_m}{\Delta_x}, \tag{1.4}$$

and can be extended to the torque expression for a rotational displacement of Δ_θ:

$$T = \frac{\Delta W'_m}{\Delta_\theta}, \tag{1.5}$$

where total coenergy is equal to the sum of components with a relative permeability close to that of air. Both expressions in (1.4) and (1.5) are referred to in literature as the energy or virtual work method (VWM) [15, 16]. The expression in (1.4) may vary depending on the choice of the independent variables current, position and flux. In this thesis, current and position are used as the two independent variables for the conversion between electrical and magnetic energies, which defines the force and torque production mechanisms.

1.2.1 Torque production mechanisms

The torque production mechanism can be defined using an approach strongly connected to a machine's operation principle. There are two specific types of mechanism [17]:

- *Mutual alignment torque* is produced due to the interaction between a rotor and stator's magnetic and/or electric fields, produced either by magnets, currents or a combination thereof. Variations of mutual alignment torque, i.e. Lorentz force, include the main component of synchronous, asynchronous, brushless ac/dc PM (PMAC) and dc machines.
- *Reluctance torque* occurs due to variations in the magnetic resistance of soft and hard magnetic materials or due to these variations *seen* by coil windings. This resistance can be represented in terms of reluctance, $\mathcal{R}$, or in terms of its inverse permeance, $\mathcal{P}$ [18]. An important structural characteristic of machines with reluctance torque is that they exhibit a salient airgap due to the slots present in stator and/or rotor. This torque can also be observed in nonsalient machines as a result of saturation or as an unwanted outcome of the production process. Both variable reluctance and switched reluctance machines (SRM) are examples of machines with reluctance torque as the main component. A special case of reluctance torque, *cogging*, occurs due to permeance variations in a magnetic circuit with PMs and a relative movement. Cogging torque cannot create a positive average torque. Examples include salient machines with PMs as illustrated in Fig. 1.3a.

The torque or force production in PM-biased structures depends mainly on the overall change in energy of components with a relative permeability close to that of air, as illustrated in Fig. 1.2 for the example of a primitive PM-biased machine. In this example, the force in x-direction occurs due to the reluctance change by increasing the mechanical airgap length. In structures with PM-bias, the reluctance change can be also attained by providing saliency in the airgap, i.e. a toothed structure between slots as shown in Fig. 1.3b. This structure, however, does not necessarily exhibit a reluctance torque component if it is periodically extended by alternating the magnetization direction of each consecutive PM, resulting in a PM-biased structure with saliency. In this case, the dc offset along Φ (Fig. 1.2b) is provided by PMs that dominate the magnetic flux path linked by the coils. This topic is addressed further in Chapter 1.4.

Although the working principle of PM-biased salient machines needs not to be based on reluctance torque, they still require saliency to operate. There are various terms and characteristics in use in the literature. Some authors in [13, 19] tend to quantify it by defining a *saliency ratio* between two inductances based on the well-known *dq* theory. Some authors go further and describe it as *negative*, *positive* or *normal* depending on the definition of this ratio [20, 21]. Another commonly used concept is *double saliency*, when the slotting effect, causing the saliency, comes from both the stator and rotor sides, as in the case of PM-biased salient machines [22]. In this thesis, saliency refers to all components inside the machine with a relative permeability close to that of air, since utilization of this area forms the basis for the design of PM-biased salient machines. Next section focuses on the modeling aspects of these machines.

1.3 Modeling of salient machines

Due to the dominant energy transformations taking place in the airgap region between the stator and rotor, accurate electromagnetic calculations are required for this region. Salient machines exhibit a nonuniform airgap due to slotting, therefore the magnetic flux does not always follow its intended path in this area, and creates leakage and fringing. These resulting complex flux paths pose a challenge for the development of adequate models of salient machines.

1.3.1 Modeling of complex flux paths

To simplify the salient electromagnetic geometry for modeling, several approaches are available, among which the most famous has been introduced by F. W. Carter. His work focused on the calculation of airgap permeance for a slot with infinite depth and a tooth with infinite width. Consequently, a factor known as the *Carter coefficient* was derived using the Schwarz-Christoffel (SC) conformal mapping function for a global representation of complex flux paths present in the salient airgap [23]. Introduction of this coefficient enables the airgap of salient machines to be modeled as nonsalient, by increasing the mechanical airgap length, g, with the Carter coefficient to an equivalent airgap length, g_e, as illustrated in Fig. 1.4 [15, 24]. In the modeling of double salient machines, such as with PM-bias as shown in Fig. 1.3b, when both rotor and stator surfaces are provided with

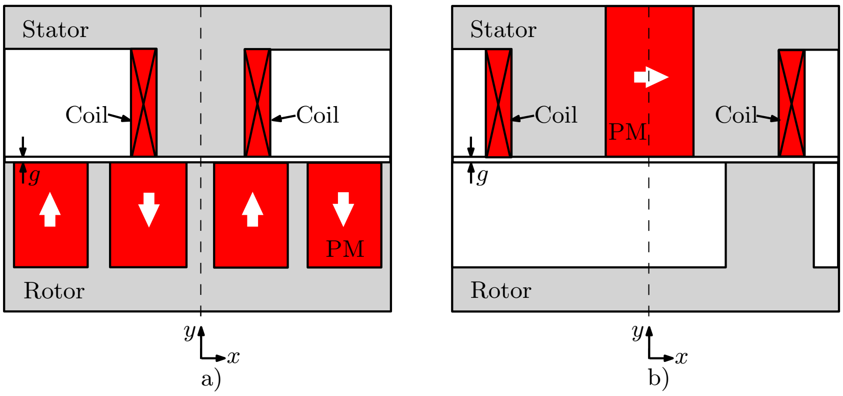

Figure 1.3: Salient machines represented in simplified rectangular shapes: a) brushless ac PM (PMAC) motor, and b) PM-biased motor.

slots, the calculations must be repeated by assuming both surfaces to be smooth in a sequence [15]. In the design phase, this updating procedure can become an iterative process with each new relative distance between two slotting effects, leading to longer calculation times until an adequate approximation is achieved. Such iterations could be avoided with alternative techniques, as discussed in this thesis.

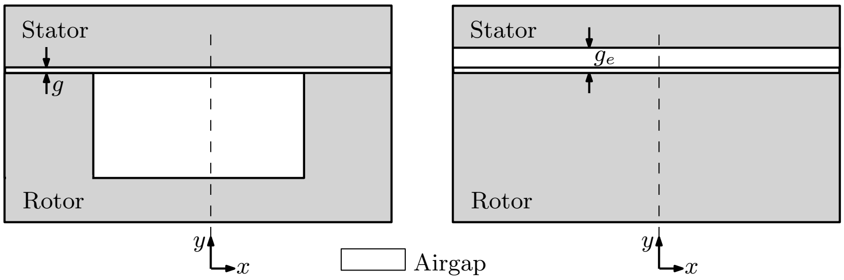

Figure 1.4: The Carter approximation for salient machines.

1.3.2 Stand-alone techniques

In modeling of salient machines, the Carter coefficient gives an approximation for the magnetic calculations in the airgap based on conformal mapping functions [23]. Similar approaches to this problem can be found in literature. Historically, first *stand-alone* models were design-oriented, based on electromagnetic field theory. As the systems grew more complicated, machine modeling had to be refined into graphical methods, e.g. phasor and circuit diagrams for control purposes [25].

With advances in material science, analogue circuit representations introduced by Hopkinson were applied to electrical machines [26, 27]. For detailed representations of the machines including material properties, numerical calculations techniques came to the scene. Overall methods can be summarized as follows [13]:

- *Reluctance network models:*
  Magnetic equivalent circuits (MEC), tooth contour method (TCM).
- *Semi-/Analytical solution of the Laplace/Poisson equations:*
  Fourier analysis (FA), boundary element method (BEM), method of moments (MoM).
- *Numerical models:*
  Finite element method (FEM), finite difference method (FDM).
- *Conformal mapping functions:*
  Schwarz-Christoffel (SC) mapping.

In general, all these stand-alone techniques are mathematical approaches with different levels of abstraction to solve the equations as given in Appendix A. Solutions provided by stand-alone methods, such as MEC and TCM, are based on the coarse discretization of machine geometry by means of reluctance, $\mathcal{R}$, or permeance, $\mathcal{P}$, elements. These are fast to build, can account for a large parameter space with an adequate accuracy, and furthermore permit integration of magnetic material properties (nonlinear BH-characteristic); although they are usually limited to predefined flux paths (tubes). Compared to the spatial discretization of reluctance networks, stand-alone methods, such as FA, are nondiscrete and provide solutions by means of analytical expressions or as series expansions. These solutions are fast to obtain and very accurate in the airgap; however, as this salient region comes in close proximity with soft magnetic material boundaries, their advantage in accuracy is lost due to the, if not only, required high number of harmonics and numerical convergence problems with the series. Another deficiency of these models is the representation of soft magnetic materials; for which case, numerical methods, such as FEM, could be useful. These realize spatial discretization of the global machine geometry by means of mesh elements, where the differential equations are linearized and the solution to the differential equations is approximated by different numerical approaches. Despite their accuracy, numerical methods tend to be less flexible to include the influence of multiple design variables and require pre-processing for a well-posed mesh (by user) to ensure the accuracy of the solution. Similar to techniques like FA, numerical approaches are also appertained to certain boundary conditions for the solving process. Due to the possible adverse effects on accuracy, this dependency can be reduced by transforming the salient airgap using a mapping function, such as SC, to simplify boundaries by uniting them. The accuracy of the solution is then dependent on the choice of mapped region, which defines the location, if present, of the boundaries in the mapped structure.

Consequently, the solutions provided by these stand-alone techniques are not always efficient. Therefore, they cannot account for modeling uncertainties, such as decreased accuracy near boundaries, nonperiodical geometries or nonlinear behavior, all of which are regularly observed in the design phase of double salient machines. To include such uncertainties, an alternative approach is proposed in the next section.

1.3.3 Hybrid modeling techniques

An alternative approach to solving either the first-order partial differential Maxwell equations or the second-order partial differential Poisson and Laplace equations, can be accomplished by pairing the mathematical approaches (stand-alone techniques) discussed above into *hybrid models* [28–35]. The particular advantages of hybrid modeling can be diminishing near boundary problems, avoiding large computational time and gaining more physical insight to the structure. Examples of this approach are presented in [36, 37], where a (semi-)analytical model of an airgap region is coupled with a numerical modeling of the remaining machine parts to overcome modeling limitations. In another example by [38], a space-mapping technique is combined with an analytical model to create fast and accurate design tools.

The specific structure of a PM-biased salient machine in Fig. 1.3b stipulates a high flux density within the double salient airgap, leading numerous researchers to apply numerical techniques in their design and analysis [39–44]. However, these techniques generally lack flexibility and provide little to no physical insight during the design stage, when the influence of several variables must be considered [45]. To overcome these modeling challenges, specific hybrid models (HM) are proposed in this thesis comprising the stand-alone (semi-)analytical, spatially discretized and mapping techniques. Namely, these three hybrid models are:

- *HM1*: MEC and FA,
- *HM2*: TCM and electrostatic FEM, and
- *HM3*: TCM and SC mapping.

These stand-alone models are paired over flux calculations performed in a double salient airgap, as explained in Chapters 2-4. Each model is evaluated based on overall accuracy, and their performance is considered in a comparative analysis in Chapter 5. With their increased functionality, the proposed hybrid models are capable of dealing with problems of random domains of new structures, such as PM-biased salient machines. These motors still require much additional research to exploit their advantages; therefore, this thesis focuses on a particular representative of this class, i.e. flux switching PM machines.

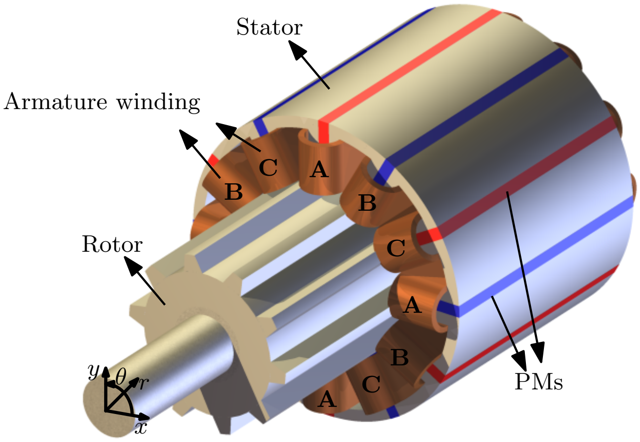

Figure 1.5: A 3D CAD representation of a 3-phase 12/10 flux switching permanent magnet machine.

1.4 Flux switching permanent magnet machines

A flux switching permanent magnet (FSPM) machine is a forthcoming example of PM-biased salient electrical machines. Concept designs were first proposed by [47, 48], and were later extended to polyphase machines by [49] as shown in Fig. 1.5. Its name, *flux switching*, comes due to the alignment of the rotor tooth to stator tooth. The armature flux linked to one phase switches direction in the next alignment. The resulting bidirectional flux between stator and rotor is linked by concentrated windings surrounding each PM. The excitation field can be also produced with a dc-winding instead of PMs, as illustrated in Fig. 1.6 [39, 46, 50]. In this construction, high hard magnetic material costs and resulting attraction forces can be avoided and a more effective flux weakening operation can be achieved by an interaction of field weakening with field control [51]. However, extra costs arise due to increased copper use, more complex power electronics in the control, and additional thermal issues. With torque densities of $10 - 50[kNm/m^3]$, FSPM can provide an up to 50% reduction in copper volume and 20% decrease in soft magnetic material, which, in return, requires an approximately 15% increase in hard magnetic material [52, 53]. High-acceleration applications can favor from these merits, since they require a high torque density and benefit from a robust rotor with low inertia for a fast response. Therefore, the next sections highlight the torque production mechanism and structural advantages of FSPM.

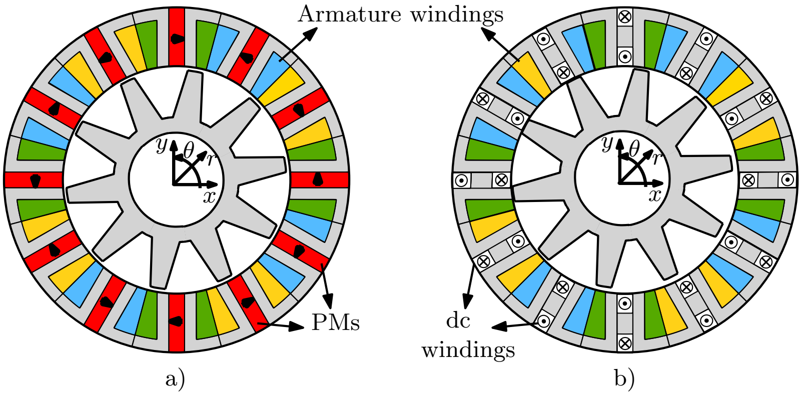

Figure 1.6: Flux switching machines a) with permanent magnets, and b) with dc excitation [46].

1.4.1 Torque production

Torque production within an FSPM is realized by exciting the stator armature windings which *see* a high level of PM-biased B in the airgap when the rotor poles are in alignment, as observed in Fig. 1.7, hence providing mutual alignment torque between the stator tooth and rotor pole. In traditional PMAC machines with PMs on the rotor, polarity of phase flux linkage, λ_{ph}, changes as the rotor moves from magnetic north to south or vice versa; whereas in FSPM, the rotor tooth acts like a magnetic mirror corresponding one north and one south pole. When the rotor tooth is aligned with PM at $\Delta_\theta = 0°$, zero armature flux is created, as illustrated in Fig. 1.7, where the blue and red colored flux lines represent opposing flux directions. As the rotor continues to rotate, the rotor mid-slot is aligned with PM at $\Delta_\theta = 18°$ as shown in Fig. 1.7. At this position, λ_{ph} switches its polarity again leading to a bidirectional sinewave λ_{ph}. This phenomenon causes a double operational frequency in the electromagnetic field. Consequently, rotor tooth number of FSPM corresponds to the rotor pole pair number in a PMAC, i.e. 10 pole pairs for FSPM in Fig. 1.5. A version of the 12/10 combination with less coils is the 6/5, which does not have periodicity albeit with near sinusoidal back-emfs; however, its rotor suffers from radial stress due to unbalanced forces [54–57].

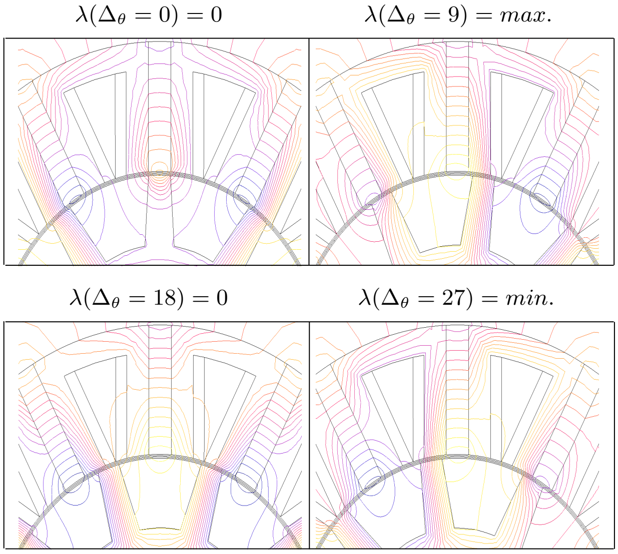

$\lambda(\Delta_\theta = 0) = 0$ $\lambda(\Delta_\theta = 9) = max.$

$\lambda(\Delta_\theta = 18) = 0$ $\lambda(\Delta_\theta = 27) = min.$

Figure 1.7: Open-circuit flux distribution of a flux switching permanent magnet machine at different rotor positions.

1.4.2 Structural advantages

A PM-biased structure based on the magnetic coupling of armature coils and PMs results in potentially a high torque density. Further, within this magnetic arrangement, it is almost impossible to even partially demagnetize PMs, since the magnetic operating point of the machine is continuously biased around the knee point of its energy conversion loop in the first quadrant [58,59]. Hence, a very high $\Delta W'_m$ and consequently T can be obtained according to (1.5) even with reduced electrical loading compared to PMAC machines. These attributes, together with a salient iron rotor, but without PMs, is very advantageous for dynamic applications with a high-acceleration requirement, as discussed in Chapter 6 [60, 61]. An overview of motor design parameters for this application are investigated in Chapter 7 leading to a final design and its verification in Chapter 8.

1.5 Research goals

Applying a numerical stand-alone technique to solve the Maxwell equations leads, in general, to accurate predictions. To deal with random domains, these tools require input from the user to adequately define the interconnected mesh elements. While ensuring the accuracy of calculations, such methods can lead to a long calculation time in the design of PM biased salient machines, especially when boundaries come close in proximity. Other stand-alone techniques, such as fast analytical methods, could even fail to account for physical interactions, discontinuities, material characteristics or manufacturing tolerances. Furthermore, the lack of accurate electromagnetic modeling approaches also limits the exploitation of the advantages of PM-biased salient machines, such as their applicability in high-acceleration applications. In this respect, the research in this thesis consists of two complementary parts with respective goals: The main goal of Part I is to research fast, yet sufficiently accurate, modeling of PM-biased salient machines by pairing stand-alone techniques. The main goal of Part II is to research the applicability of these paired (hybrid) techniques to a PM-biased machine, FSPM, for high-acceleration applications.

Part I: Hybrid modeling techniques

- **Research of design tools including the effects of double saliency with a PM-bias**
  Discussed in Chapters 2-4
  Double salient machines with a PM-bias have more leakage, because of less constrained, i.e. complex, flux paths due to their nonuniform airgap, which can be modeled using various stand-alone techniques. These models, such as MEC, are fast to build and can account for a large parameter space with adequate accuracy. For increased accuracy, semi-analytical techniques, such as FA, can be opted for; however, their accuracy drops significantly in close proximity to the boundaries. Therefore, a high level of accuracy, for calculations performed in a double salient airgap, can also be obtained using a more detailed reluctance network model, such as TCM, which provides an infinite number of airgap permeances (flux tubes). Compared to analytical approaches, numerical techniques, such as FEM, have the highest accuracy but also generally require the largest simulation time. An alternative approach in the modeling of such problems is reducing the saliency effect with conformal mapping functions, such as SC mapping. This method offers high accuracy throughout the airgap including regions near or on the boundaries; however, approximation problems may occur while determining the mapping function for structures with large ratios of slot depth-to-airgap length [62–64].

- **Combination of methods for modeling double salient structures**
  Discussed in Chapters 2-5
  By themselves, stand-alone techniques are not always functional to avoid the drawbacks, in modeling problems near boundaries, to avoid large computational time or to achieve adequate accuracy. Their functionality can be increased by pairing them into hybrid models, to solve the differential form of Maxwell or Poisson and Laplace equations. Therefore, three such hybrid models are proposed in this thesis, consisting of (semi-)analytical, spatially discretized and mapping techniques. These hybrid models are explained on a reduced-order case study, a simplified structure with double salient airgap, and implemented on a PM-biased salient machine, FSPM. Further-

more, the performance of the proposed models is discussed in a comparative analysis in terms of accuracy, simulation time, inclusion of a nonlinear BH-characteristic, end effects and design flexibility [62–65].

Part II: Flux switching permanent magnet machines

- **Extension of classical machine design approaches to suit PM-biased salient machines**
  Discussed in Chapter 6
  In many FSPM designs researched today, design rules are augmented on existing machine structures with a practically nonexistent relationship to basic sizing equations, as generally observed in classical machine designs. Therefore, electromagnetic design considerations should be laid out as the first step for the flux switching machine design. In this process, constraints, arising from application, should also be incorporated into the design procedure. Specifically to this study, a FSPM is evaluated for high-acceleration applications. Therefore, an analysis is selected in the form of a *paralleled* comparison to an industrial state-of-the-art benchmark motor. Thus, most geometrical constraints are derived from the benchmark, i.e. outer dimensions, shaft, bearings, cooling type, etc. Since this application benefits from a low mass, inertia equations should also be included in the design process. Furthermore, it is important to estimate the operational limits of FSPM with a significantly detailed thermal model.

- **Identification of the effect of slotting, cogging and end effects in dynamic applications**
  Discussed in Chapter 7
  Dynamic applications, such as those with high acceleration, require a smooth torque profile. This is a challenge for FSPM, since, due to its slotted PM-biased structure, it has an inherent torque ripple. Therefore, in the design phase, the effects of the machine parameters on torque ripple are also evaluated. In addition, a model is created to identify the influence of the end effects [66].

- **Analysis of the performance under thermal limits compared to an industrial motor solution**
  Discussed in Chapter 8
  Comparing different machine topologies is a cumbersome task since many variables have to be considered and it is difficult to decide which variables should be kept as constants. Most generally, the basis for comparison is founded on constant electromagnetic airgap shear stress, being the product of electric loading and magnetic loading, and indeed the constancy of both of those factors. The metric used for these comparisons is usually that of the masses of the active materials, i.e. steel, copper, and magnet material. However, in order to establish a reliable comparison, a sufficient amount of

different machine designs has to be considered. In this thesis, a comparison of FSPM's performance is made on its high-acceleration capability. The industrial benchmark motor is used in this comparison, which is performed under identical thermal limits [67–70].

1.6 Thesis outline

The outline of the thesis is divided into three parts concerning the hybrid modeling techniques, flux switching permanent magnet machines, and closing:

In Part I, three differently configured hybrid modeling techniques are introduced first on a reduced-order case study, a structure with double salient airgap. Further, each hybrid model is implemented to enable the design of PM-biased salient machines, including a noteworthy 3-phase 12/10 FSPM. The hybrid modeling concept is presented as a combination of mathematical approaches with different levels of abstraction (stand-alone techniques) to solve either first-order partial differential Maxwell equations or second-order partial differential Poisson and Laplace equations. In Chapter 2, the first hybrid model (HM1) is introduced, pairing the (semi-)analytical modeling technique, FA, with a reluctance network method, MEC. In this method, the structure under investigation is brought virtually to a different magnetic operation point by changing a geometric parameter. In Chapter 3, the second hybrid model (HM2) is introduced, pairing TCM with electrostatic FEM, eFEM. The parameter-dependent airgap permeance, an element of TCM network, is calculated by eFEM. The equivalent machine network of TCM is constructed based on MEC from HM1, except for the airgap region. In Chapter 4, the third hybrid model (HM3) is introduced, pairing TCM with SC mapping. The structure and integration technique of HM3 follows the same principles as HM2. With mapping, the complex flux paths in the airgap are transformed to geometries with reduced complexity for magnetic calculations based on orthogonal field diagrams. In Chapter 5, the proposed hybrid models are evaluated in a comparative analysis that includes consideration of accuracy, simulation time, inclusion of a BH-characteristic, end effects and design flexibility.

In Part II, a design routine is researched for a specific PM-biased salient machine structure, i.e. a 3-phase 12/10 FSPM meant for high-acceleration applications. The applicability of PM-biased salient machines in high-acceleration applications is assessed in a parallel analysis between a newly-designed FSPM (prototype) and a state-of-the-art industrial brushless PMAC (benchmark) motor. In Chapter 6, the design space of FSPM is restricted by this paralleled performance evaluation based on the physical specifications of the benchmark. These constraints are incorporated into electromagnetic design considerations including inertia equations. Additionally, a thermal model is derived for FSPM based on the equivalent circuit approach to estimate operational limits. In Chapter 7, a generalized design framework is provided to investigate the key design parameters. The resulting motor structures are investigated for a high torque output, low inertia, high overloading capability and minimum torque ripple. Based on this study, one motor structure is selected as the FSPM prototype, and constructed to demonstrate its performance compared to the benchmark motor, as discussed in Chapter 8.

In Part III, the conclusions of the presented work are summarized along with scientific contributions. For further research, recommendations are given.

Part I

Hybrid modeling (HM) techniques

Chapter 2

HM1: Fourier analysis and magnetic equivalent circuit

"Insufficient facts always invite danger." – Spock (Space Seed)

* * *

Part I of this thesis focuses on three hybrid techniques used to model PM-biased salient structures. Each of these hybrid models is attained by pairing widely used stand-alone techniques.

This chapter introduces the first hybrid model, HM1, which pairs the Fourier analysis (FA) and magnetic equivalent circuit (MEC) modeling techniques. Models based on FA have been praised for their accuracy and short simulation time. However, if model saliency is extreme, e.g. in terms of slot depth-to-airgap length ratio, solution accuracy is compromised due to the close proximity to the boundaries in salient structures. Consequently, a reluctance network model, i.e. MEC, is paired to reduce these inaccuracies in double salient structures. Both models are illustrated on a reduced-order case study, i.e. a double salient airgap consisting of a dc-excited stator and rotor tooth. HM1 pairs FA-MEC in an optimization routine in which the airgap, as is the case for the Carter coefficient, is enlarged to increase the accuracy. Subsequently, HM1 is implemented to explore its suitability for the analysis of flux switching permanent magnet machines. Finally, the calculations performed using HM1 are verified with finite element analyses.

* * *

The contributions of this chapter are published in the following articles:

- Ilhan, E., Paulides, J. J. H. and Lomonova, E. A. [2014]. Hybrid modeling techniques for complex magnetic flux paths in airgap. *Proceedings of Intermag Conference*, Dresden, Germany.
- Ilhan, E., Gysen, B. L. J., Paulides, J. J. H. and Lomonova, E. A. [2010]. Analytical hybrid model for flux switching permanent magnet machines. *Magnetics, IEEE Transactions on*, 46(6):1762-1765.
- Gysen, B. L. J., Ilhan, E., Meessen, K. J., Paulides, J. J. H. and Lomonova, E. A. [2010]. Modeling of flux switching permanent magnet machines with Fourier analysis. *Magnetics, IEEE Transactions on*, 46(6), 1499-1502.
- Ilhan, E., Gysen, B. L. J., Paulides, J. J. H. and Lomonova, E. A. [2010]. Analytical hybrid model for flux switching permanent magnet machines. *Proceedings IEEE, Young Researchers Symposium*, Leuven.

2.1 Introduction to hybrid modeling

Design methods or modeling techniques demand specific detailing related to the electromagnetic structure under investigation. The overall performance of an electromechanical device is often significantly affected by the interactions between electrical and magnetic fields governing inside, which are represented either by Maxwell or by Poisson and Laplace equations. To solve these equations, summarized in Appendix A, stand-alone techniques with different levels of abstraction, introduced in Chapter 1.3.2, can be used with different advantages and disadvantages. For accurate predictions of these equations, the designer has to adopt numerical stand-alone techniques [45]. Following the advances in computers, different mesh-based solutions have been proposed to model challenging electromagnetic structures. This optimized, hence efficient use, of computer power for numerical methods, such as finite element method (FEM). As a result, FEM has been increasingly implemented as an active design and analysis tool [43,44]. These improvements have opened doors for more detailed design analysis of electrical machines, such as PM-biased salient machines introduced in Chapter 1. Albeit the aforementioned, for such new electrical machine structures with double saliency (Chapter 1.2.1), numerical methods provide little flexibility to include the effect of several design variables, e.g. when boundaries come close in proximity. Additionally, such stand-alone techniques require a well defined mesh (by user) in the pre-processing operation, and can lead to long calculation time [71]. Thus, one should examine other stand-alone techniques as introduced in Chapter 1.3.2.

For fast and high accurate field calculations, (semi-)analytical methods, e.g. Fourier analysis (FA), are suitable; however, it is challenging to incorporate odd-shaped soft magnetic materials [72–74]. Furthermore, their high level of accuracy is affected negatively near to the soft magnetic boundaries. This drawback can be reduced by an alternative approach, hybrid modeling, as introduced in Chapter 1.3.3. The resulting hybrid model 1 (HM1), discussed in this chapter, pairs FA with another stand-alone technique, i.e. a reluctance network model based on magnetic equivalent circuits (MEC) [75, 76] for the modeling of PM-biased salient structures.

2.2 Fourier analysis

In the composition of HM1, the first analyzed stand-alone technique is Fourier analysis (FA), which is based on a harmonic notation of the electromagnetic fields. Among several studies, [76] provides a general framework. The solution of differential form of Maxwell equations, or more precisely Poisson equation (A.11), forms the basis of field calculations, which can be written for any region depending on normal, p, and tangential, q, directions in general form:

$$\mathbf{B} = B_p(p, q)\mathbf{e}_r + B_q(p, q)\mathbf{e}_q, \tag{2.1}$$

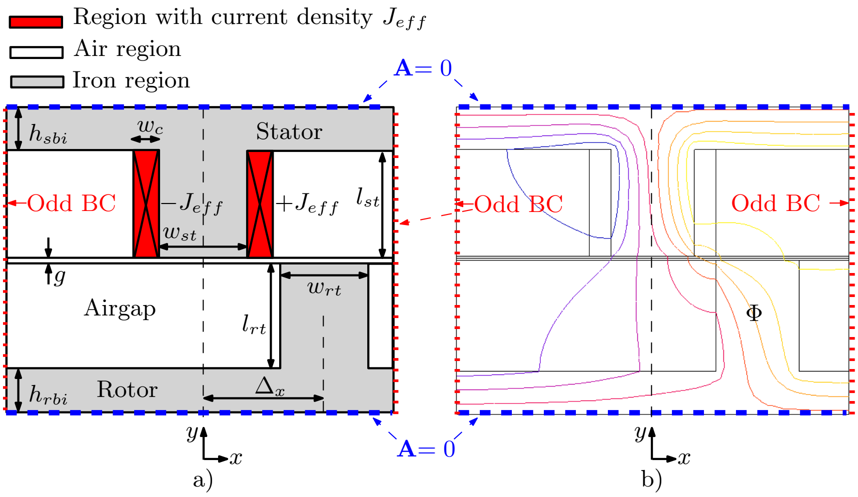

Figure 2.1: Case study: A double salient airgap with dc-excited stator and rotor tooth with a) geometric dimensions including the boundary conditions (BC), and b) magnetic vector potential $\mathbf{A}$ distribution at $\Delta_x = 10[mm]$.

where $\mathbf{e}$ is the unit vector in the respective coordinate system directions. The normal, $B_p(p,q)$, and tangential, $B_q(p,q)$, components can be written as a Fourier series:

$$B_p(p,q) = \sum_{n=1}^{\infty} \Big(B_{p_s}(p) \sin(w\,q) + B_{p_c}(p) \cos(w\,q) \Big), \tag{2.2}$$

$$B_q(p,q) = \sum_{n=1}^{\infty} \Big(B_{q_s}(p) \sin(w\,q) + B_{q_c}(p) \cos(w\,q) \Big) + B_{q_0}(p), \tag{2.3}$$

where w is the spatial frequency, B_{*_s} the sine term and B_{*_c} the cosine term of the concerned series. This stand-alone technique is mentioned in this thesis only to emphasize the necessity for the hybrid model concept; therefore, it is not in the scope of this thesis to make a detailed analysis of it as done in [72, 76].

2.2.1 Application to the case study

The PM-biased salient machines have an airgap comprising air, PM and coil regions with a relative permeability close to that of air, as discussed in Chapter 1.2.1 and Chapter 1.3. Therefore, this salient airgap, simply referred to as airgap in this thesis, is more complex than the mere mechanical airgap. Prior to the complete machine model, FA is first implemented on a reduced-order case study, i.e. a double salient airgap structure as shown in Fig. 2.1a. This case study consists of a

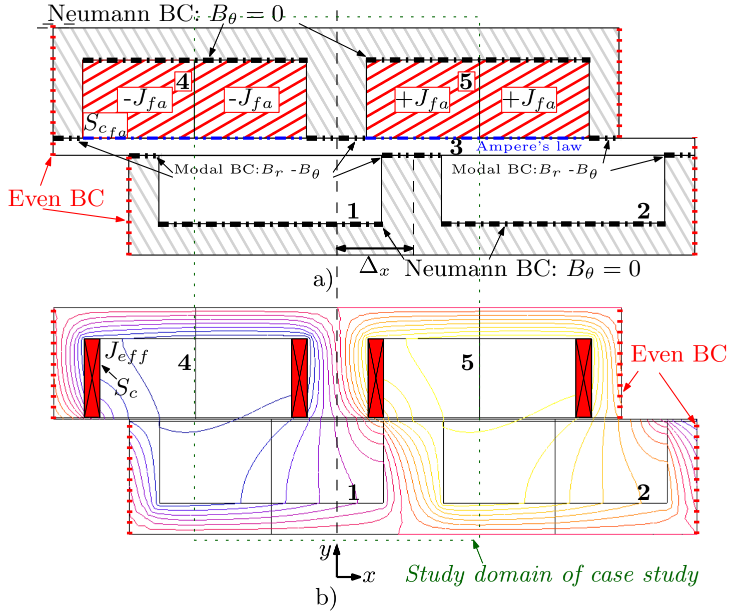

Figure 2.2: Modified model of Fig. 2.1 for Fourier analysis with a) boundary conditions (BC), 5 regions, and b) magnetic vector potential $\mathbf{A}$ distribution at $\Delta_x = 10[mm]$.

dc-excited stator tooth and a rotor tooth with dimensions in as summarized in Table 2.1 [77]. The magnetic boundaries of the structure are shown in Fig. 2.1b. On the sides of this structure, odd periodicity (anti-cyclic) boundary conditions (BC) are implemented, where on the top and bottom the magnetic vector potential is $\mathbf{A} = 0$.

In FA, the soft magnetic material is assumed to have a relative permeability of infinity ($\mu_r = \infty$), and the stator and rotor back-irons are represented by BCs. Due to the required periodical (even or cyclic) boundary conditions, the case study with odd periodicity is transformed to Fig. 2.2a with even periodicity. It needs noting that this modified structure is not an identical representation of the original case study due to the extra iron boundaries appearing outside of the study domain indicated as a dotted box. However, the difference is not significant as long as the movement of the rotor tooth is confined in the study domain. Furthermore, since the stator and rotor back-iron parts are represented by Neumann BCs, the magnetic field inside those regions is zero, hence they are not considered.

The airgap, including coil area, is divided into 5 regions according to their BCs in Fig. 2.2a. The original coil area, S_c, is expanded to $S_{c_{fa}}$ with a re-definition of the current density:

$$J_{fa} = \frac{J_{eff} S_c}{S_{c_{fa}}}. \tag{2.4}$$

Table 2.1: Parameters of the case study topology

Symbol	Description	Value	Unit
Δ_x	Rotor position	-	$[mm]$
g	Airgap length	0.5	$[mm]$
w_{st}	Stator tooth width	10.9	$[mm]$
l_{st}	Stator tooth length	36	$[mm]$
h_{sbi}	Stator back-iron height	4	$[mm]$
w_c	Coil slot width	1.8	$[mm]$
w_{rt}	Rotor tooth width	10.9	$[mm]$
l_{rt}	Rotor tooth length	39	$[mm]$
h_{rbi}	Rotor back-iron height	4	$[mm]$
L_a	Axial length	25	$[mm]$
J_{eff}	Current density (rms)	8	$[A/mm^2]$
S_c	Coil area	65.4	$[mm^2]$

Verification

To verify the constructed FA model of the case study at $\Delta_x = 0[mm]$, the normal component of the airgap flux density, B_{fa}, is evaluated and compared to FEM in Fig. 2.3. For the nonzero values, FA estimates the field distribution in region 3 accurately. Over the region of stator-rotor tooth alignment, the peak value reaches $1.23[T]$, with a discrepancy of 2.3% compared to FEM. Additionally, FA values oscillate around the mean value smoothly, which are dominantly observed in the neighborhood of zero. Among other causes, this could be due to the Gibbs phenomenon or the correlation functions used in mode-matching [76, 78]. Since this topic falls outside the scope of this thesis, only a common solution is provided in terms of increasing the harmonic number, in this case to 50. This solution costs a longer calculation time, and it should be noted that it is not effective in case the calculation comes in close proximity of boundaries or any spatial harmonic is located at points of discontinuity.

2.2.2 Sensitivity to parameter variations

According to the results obtained in Fig. 2.3, FA has proven to be accurate for field calculations in airgap of the case study within a discrepancy of 2.3% compared to FEM. This result is obtained for the initial parameters given in Table 2.1. To investigate whether FA is adequate for the design of PM-biased salient machines, specifically for parameter variations leading to extreme saliency, the initial parameters are varied to $J_{eff} = 2[A/mm^2]$ and $g = 0.1[mm]$ at $\Delta_x = 0[mm]$. The airgap field distribution is illustrated in Fig. 2.4. Results show that the accuracy of FA can be compromised with discrepancies $< 16\%$ compared to FEM due to the close proximity to the boundaries. This drawback can be avoided by introducing another stand-alone technique, MEC, into FA.

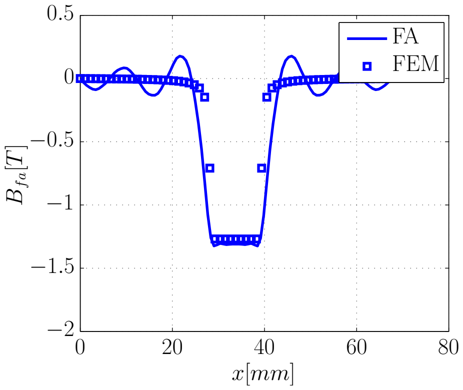

Figure 2.3: Normal component of airgap flux density calculated by Fourier analysis, B_{fa}, and by finite element method in case study at $\Delta_x = 0[mm]$.

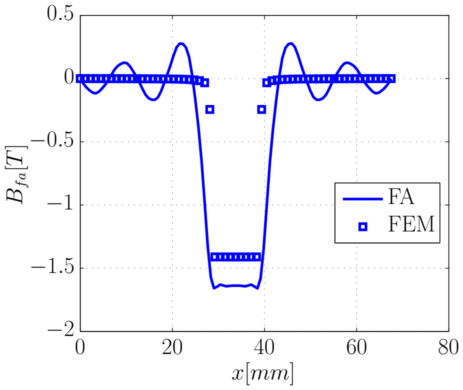

Figure 2.4: Normal component of airgap flux density calculated by Fourier analysis, B_{fa}, and by finite element method for parameter variations in case study at $\Delta_x = 0[mm]$.

2.3 Magnetic equivalent circuit

In the composition of HM1, the second analyzed stand-alone technique magnetic equivalent circuit (MEC) is based on the analogy between electrical and magnetic circuits to solve the Maxwell equations. This analogy relates to electrical and magnetic material properties that are subject to alterations, or even mutations, in the presence of electromagnetic fields. An example of this phenomenon was discovered by the Irish scientist William Thomson (The Lord Kelvin), who witnessed the dependency of electrical resistance on an external magnetic field [79]. Experiments in this field not only revealed the inter-relationships between electrical and magnetic circuits but also commonalities. A historically important analogy between electrical and magnetic circuits was drawn by the British scientist Hopkinson as [18]:

$$\mathcal{F} = \Phi \mathcal{R}, \tag{2.5}$$

where as a result of mmf, $\mathcal{F}$, magnetic flux Φ is created due to the reluctance, $\mathcal{R}$, of the medium. The inverse of $\mathcal{R}$, permeance, $\mathcal{P}$, is also a regularly used terminology. This analogy permits Maxwell equations to be approximated by certain techniques developed for electrical networks. The approach instigated reluctance network models such as MEC to be applied with contemplation of various implementations ranging from multiscale design approximations to performance analysis for electromagnetic problems [80–82].

In MEC, each $\mathcal{P}$ or $\mathcal{R}$ discretizes the investigated structure spatially in regions with identical magnetic properties, therefore the connectivity of each element depends on the flux distribution. The represented spatial flux in each region can be visualized as a flux tube in Fig. 2.5. For PM-biased salient machines, this procedure is not straightforward and can create the appeal of extra modeling approaches such as FEM to estimate the complex flux paths. To model these flux paths, (A.1) and (A.2) are simplified by assuming a constant field intensity, H, along the path, C, as well as the current density, J, through surface, S. Consequently, flux in each region is integrated over a flux tube and represented by a permeance as illustrated in Fig. 2.5. The permeance is calculated as [83]:

$$\mathcal{P} = \frac{1}{\mathcal{R}} = \int\limits_{l} \frac{\mu_0 \mu_r(l) S(l)}{dl}, \tag{2.6}$$

where μ_0 is the permeability of free space, μ_r the relative permeability of the concerned medium, S the cross section of the considered flux tube and l the length of the flux tube as seen in Fig. 2.5. Based on these relationships, MEC is created, like FA, for the case study.

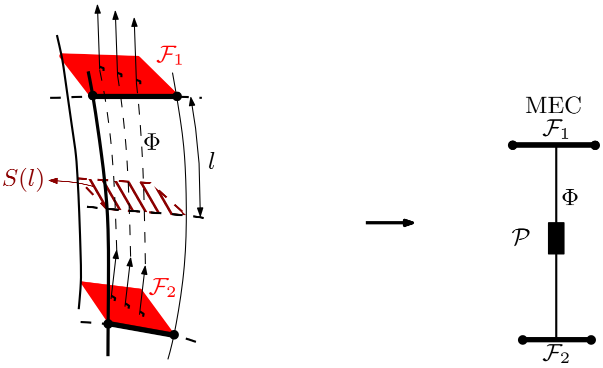

Figure 2.5: Visualization of magnetic equivalent circuit by a flux tube of Φ in a field between two magnetic potential planes $\mathcal{F}_1$ and $\mathcal{F}_2$.

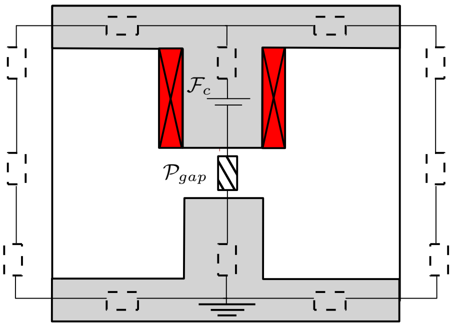

Figure 2.6: Magnetic equivalent circuit of the case study, double salient airgap structure, at $\Delta_x = 0[mm]$ with a soft magnetic material of $\mu_r = 1000$. The dotted permeances represent the denser circuit.

2.3.1 Application to the case study

For modeling of structures with complex flux paths, MEC can require a-priori knowledge of the flux distribution as illustrated in Fig. 2.1b, e.g. obtained from numerical methods such as FEM. If the structure is changed to the rotor position with $\Delta_x = 0[mm]$, FEM is unnecessary since the expected magnetic flux paths can be predicted accurately. MEC for this case is shown in Fig. 2.6 including soft magnetic materials with a linear $B(H)$ relationship ($\mu_r = 10000$) for an operation only in the first quadrant of the BH-curve. The equivalent circuit elements are calculated by:

$$\mathcal{F}_c = J_{eff} S_c, \tag{2.7}$$

$$\mathcal{P}_{gap} = \frac{\mu_0 w_{rt} L_a}{g}, \tag{2.8}$$

and the flux density in airgap between the rotor and stator tooth by:

$$B_{mec} = \frac{\mathcal{F}_c \mathcal{P}_{gap}}{w_{rt} L_a}. \tag{2.9}$$

Verification

To verify the constructed MEC model of the case study at $\Delta_x = 0[mm]$, the normal component of the airgap flux density, B_{mec} is evaluated. The result from MEC is $B_{mec} = 1.31[T]$, whereas FEM result is $1.26[T]$, a 3.9% difference, respectively. This result can be improved with a denser circuit by including additional permeances, such as the dotted ones shown in Fig. 2.6. In case of geometric parameter variation or rotor tooth displacement, additional MECs are required to represent the new structure. However, this action is not necessary due to the integration to FA.

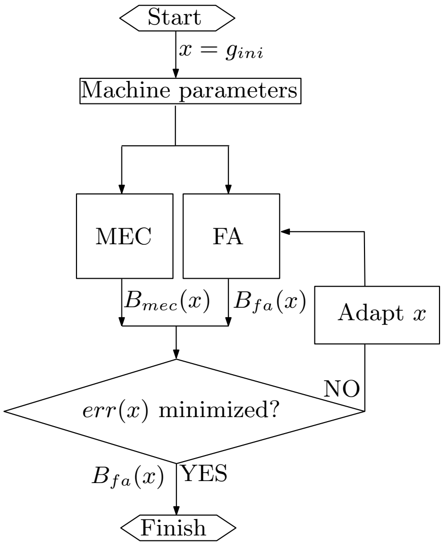

Figure 2.7: Flowchart of HM1 for the case study.

2.4 Integration of Fourier analysis and magnetic equivalent circuit

Stand-alone techniques based on FA provide a high level of accuracy, such as shown for the case study; however, if model saliency is extreme, e.g. in terms of a high slot depth-to-airgap length ratio, its accuracy has been compromised due to the close proximity to the boundaries. To overcome this problem, MEC is paired with FA into HM1 for reduction of these inaccuracies in double salient structures. The main idea of HM1, like the approach of Carter discussed in Chapter 1.3.1, is capturing the MEC behavior by virtually changing one geometric parameter, as illustrated in Fig.2.7. This parameter, x, can be the airgap length, g, or the coil slot width, w_c. To do so, firstly the machine parameters are initialized. Next, the reference flux density values in the airgap are obtained from MEC, B_{mec}, while FA calculates the initial normal component, B_{fa}. These values are calculated for the initial x, i.e. the initial airgap length, g_{ini}. Afterwards, the iteration to obtain the most appropriate g for the best FA-MEC agreement starts and continues until the predefined error function is minimized numerically by the golden section method (GSM) [84].

Golden section method (GSM)

The GSM is a numerical technique for one or multidimensional optimization problems, here one dimensional optimization of x is considered. By applying GSM, it is aimed to estimate x while the predefined error function, $err(x)$, is minimized. The iteration intervals are derived from the golden section ratio [84], which is independent of $err(x)$. The number of iterations, to find the minimum error point, is established by a set tolerance value before the iteration loop. A sample code used for HM1 is given in Appendix C.

Error function

The iteration loop with $err(x)$ in Fig. 2.7 is a crucial part of the integration technique in HM1. For an adequately fast and accurate result, a point-wise comparison is used between the airgap field solutions of FA and MEC, and consequently the error function is defined as:

$$err(x) = \frac{1}{n}\sum_{i=1}^{n}\left|\frac{B_{mec_i}(x) - B_{fa_i}(x)}{B_{mec_i}(x)}\right| \times 100\%, \tag{2.10}$$

where B_{fa} and B_{mec} are calculated on a total number of n points, which are indicated with i to represent each airgap permeance ($\mathcal{P}_{gap}$) in MEC. Each single iteration sweeps i points and calculates the mean error with reference to (2.10) until the maximum number of iterations is reached.

Verification

To verify the constructed HM1 in terms of extreme saliency, the sensitivity study conducted on FA in Chapter 2.2.2 is repeated for HM1. Previous results in Fig. 2.4 have shown that the accuracy of FA is compromised in airgap with discrepancies up to 16% due to the close proximity to the boundaries. Results in Fig. 2.8 show that HM1, i.e. FA-MEC, achieves an improvement with a discrepancy of 8.5%. This process took a total simulation time of 8[s], which is four times faster than FEM. In the next step, HM1 is applied to a PM-biased salient machine.

2.5 Application of HM1 to a flux switching permanent magnet machine

Most researchers use numerical techniques in the design and evaluation of flux switching permanent magnet machines (FSPM) due to its double salient airgap

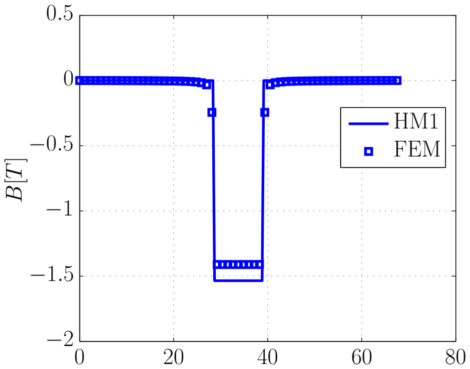

Figure 2.8: Flux density in airgap calculated by HM1 and finite element method for the parameter variations in the case study at $\Delta_x = 0[mm]$.

with PM-bias, as introduced in Chapter 1, whereas the use of stand-alone techniques is very rare [40, 72, 77, 85–88]. Its airgap comprises magnet, coil and air, i.e. regions with a relative permeability close to that of air. The location of these regions creates an increased modeling challenge, i.e. the unbound magnet region, compared to the case study, for which HM1 has been introduced in the previous section. Subsequently, HM1 is implemented in this section to explore its appropriateness to analyze a 3-phase 12/10 FSPM with a moderate saliency. For generalization, the comparison to FEM is normalized to the values in open-circuit analysis. Similar to the case study, the stand-alone techniques, Fourier analysis and magnetic equivalent circuit, are implemented separately on the machine.

2.5.1 Fourier analysis for the machine

In the composition of HM1, the first analyzed stand-alone technique is FA, which is implemented in [72, 76] for FSPM. For this structure, additional assumptions are required than the ones indicated in Chapter 2.2.1. A linear 2^{nd} quadrant demagnetization characteristic is considered for PMs with a remanent flux density, B_r, and a magnet relative permeability, μ_{pm}. Furthermore, regions are created according to their tangential boundary conditions in Fig. 2.9a, i.e. rotor teeth slots, uniform airgap, magnets, coils, and surrounding air. The surrounding air region is required due to the unbound PM region. Additionally, FA is performed in polar coordinates (r,θ) for half periodicity of the 12/10 FSPM. Consequently, geometric modifications are performed because each region is defined solely by their angular width and radial height as shown in Fig. 2.9b.

Geometric modifications

The geometry, where FA is applied, can be different than the original machine as illustrated in Fig. 2.9b. This is especially observed in the shape of PM, coil slot and rotor slots, e.g. PMs could be as in Fig. 2.9a or in block shapes as in in Fig. 2.9b. In such cases, a certain set of geometric modifications are introduced to FA with negligible effect on the airgap field calculations. By keeping the stator and rotor tooth width unchanged, these modifications are instead implemented on the source side. As such, to account for the change in the electrical loading, the original slot area, S_c, is modified to $S_{c_{fa}}$:

$$\theta_{c_{total}} = \frac{\theta_s}{2} - \frac{R_{st}}{R_s - h_{sbi}}(\frac{\theta_s}{2} - \theta_c), \tag{2.11}$$

$$S_c = ((R_{st} + h_c)^2 - R_{st}^2)\frac{\theta_{c_{total}}}{2} - \frac{(\theta_{c_{total}} - \theta_c)R_{st}h_c}{2}, \tag{2.12}$$

$$S_{c_{fa}} = \theta_c(R_{st}h_c + \frac{h_c}{2}), \tag{2.13}$$

as shown in Fig. 2.9b. This results in a current density of J_{fa} as:

$$J_{fa} = J_{eff}\frac{S_c}{S_{c_{fa}}}. \tag{2.14}$$

To account for the change in the magnetic loading, the original magnet area, $S_m = \theta_m R_{st} l_m$, can be modified to $S_{m_{fa}}$ and the original magnet remanence, B_r, to $B_{r_{fa}}$ as:

$$S_{m_{fa}} = (R_s^2 - R_{st}^2)\frac{\theta_m}{2}, \text{ and} \tag{2.15}$$

$$B_{r_{fa}} = B_r\frac{S_m}{S_{m_{fa}}}. \tag{2.16}$$

2.5.2 Magnetic equivalent circuit for the machine

In the composition of HM1, the second analyzed stand-alone technique is MEC. Compared to the case study, MEC of FSPM requires a-priori knowledge of the flux distribution. The corresponding finite element model of the 3-phase 12/10 FSPM is only periodical through half of the machine [53,77,89]. Therefore, for the open-circuit analysis, FSPM's minimum and maximum phase flux linkage, λ_{ph}, rotor positions (q, d-axis) are shown in Figs. 2.10a-b respectively for the indicated phase A. In these particular positions, a symmetrical behavior is observed, therefore, in the open-circuit case, the machine can be modeled as a quarter model as illustrated in Fig. 2.11. While, the type of symmetry to be employed in $\Delta_\theta = 9°$ is odd, even symmetry is appropriate for $\Delta_\theta = 0°$. For the open-circuit MEC, $\Delta_\theta = 9°$ rotor position is considered with the symmetry axis shown in Fig. 2.10b.

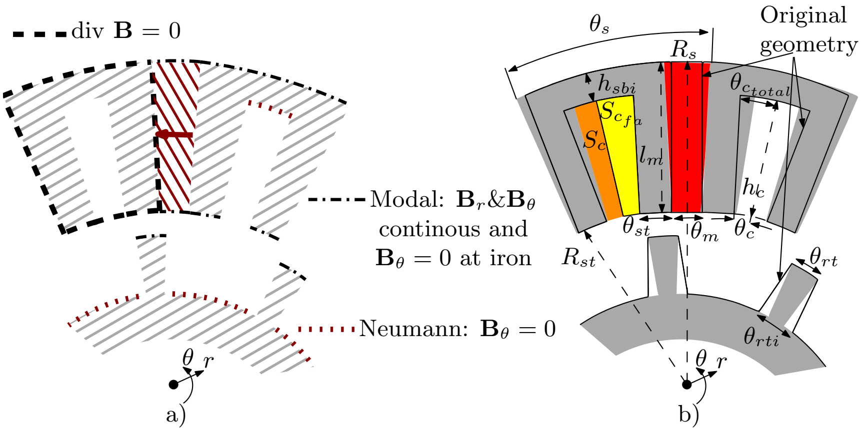

Figure 2.9: a) Boundary conditions of the Fourier analysis, and b) original and modified geometries of the flux switching permanent magnet machine.

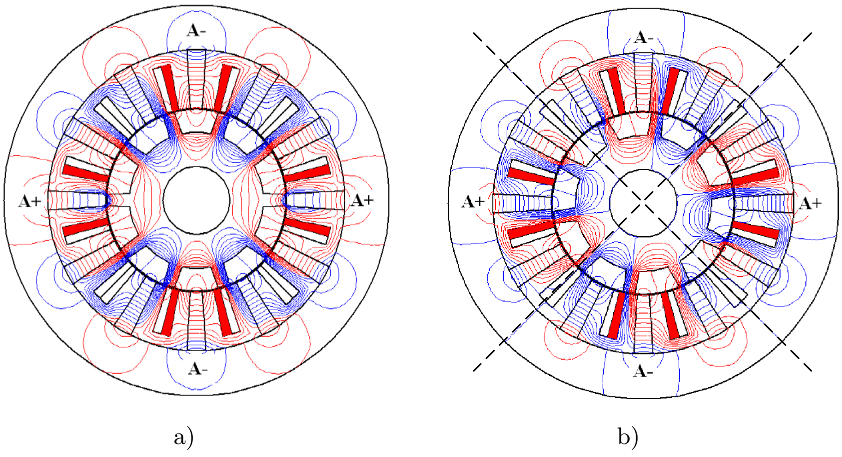

Figure 2.10: Open-circuit flux distribution of the flux switching permanent magnet machine at a) $\Delta_\theta = 0°$, and b) $\Delta_\theta = 9°$.

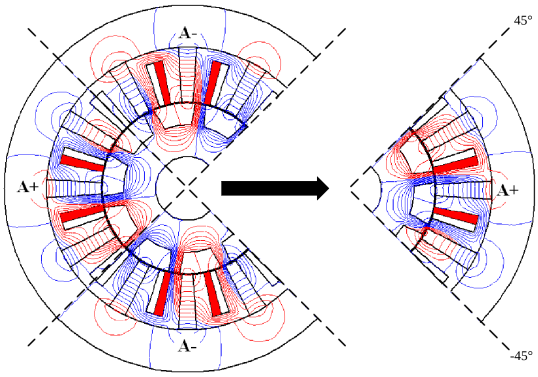

Figure 2.11: Quarter machine model at $\Delta_\theta = 9°$.

In addition to MEC assumptions indicated in Chapter 2.3.1, a linear second quadrant demagnetization characteristic is considered for PMs at open-circuit.

Based on these assumptions, the equivalent circuit elements in Fig. 2.12 are calculated using (2.5) and (2.6) by:

$$\begin{aligned}
&\mathcal{F}_m = \frac{B_r w_m}{\mu_0 \mu_r},\ \mathcal{P}_m = \frac{\mu_0 \mu_{pm} l_m L_a}{w_m},\\
&\mathcal{P}_{Sbi} = \mu_0 \mu_{Fe} \frac{h_{sbi} L_a}{3 w_{st}},\ \mathcal{P}_S = \mu_0 \mu_{Fe} \frac{w_{st} L_a}{(l_m - h_{sbi})},\\
&\mathcal{P}_{Rbi} = \mu_0 \mu_{Fe} \frac{h_{rbi} L_a}{w_r}, \mathcal{P}_R = \mu_0 \mu_{Fe} \frac{w_{rt} L_a}{l_{rt}},\ \text{or}\\
&\mathcal{P}_R = 0.26 \mu_0 \mu_{Fe} L_a,\ \text{if rotor tooth is aligned with PM.}
\end{aligned} \tag{2.17}$$

The most challenging part of MEC is to determine $\mathcal{P}_{gap}$. Due to the double salient airgap, a high number of different flux paths has to be approximated here. To increase the discretization level, airgap permeances are written explicitly as parallel permeances encircled in Fig. 2.12, for which six fundamental paths in Fig. 2.13 are approximated with the relationships given in Table 2.2. Using (2.6),

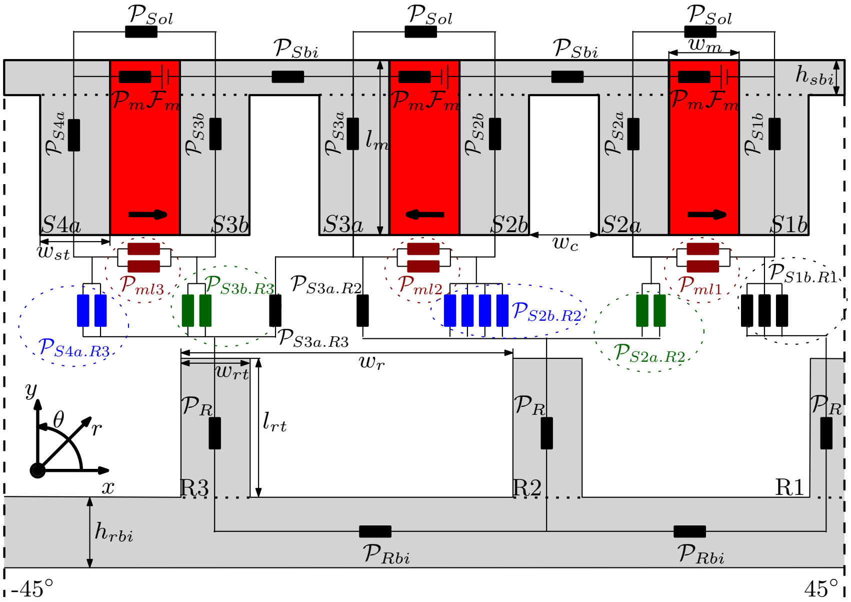

Figure 2.12: Magnetic equivalent circuit of the quarter machine for the open-circuit analysis.

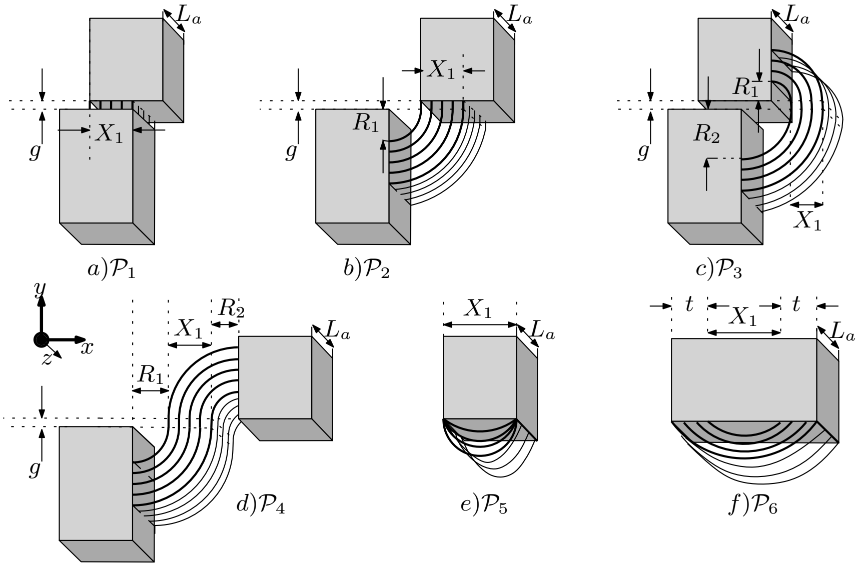

Figure 2.13: Fundamental airgap permeances, $\mathcal{P}_{gap}$, used in the magnetic equivalent circuit.

the parallel permeances are approximated [90]:

$$
\begin{aligned}
\mathcal{P}_1 &= \frac{\mu_0 X_1 L_a}{g}, \\
\mathcal{P}_2 &= \int_{R_1}^{R_1+X_1} \frac{\mu_0 L_a}{g+\frac{2\pi x}{4}}\,dx = \frac{2\mu_0 L_a}{\pi} ln(1+\frac{\pi X_1}{\pi R_1 + 2g}), \\
\mathcal{P}_3 &= \int_{0}^{X_1} \frac{\mu_0 L_a}{\frac{2\pi(x+R_1)}{4}+g+\frac{2\pi(x+R_2)}{4}}\,dx = \frac{\mu_0 L_a}{\pi} ln(1+\frac{2\pi X_1}{\pi(R_1+R_2)+2g}), \\
\mathcal{P}_4 &= \frac{2\mu_0 L_a X_1}{\pi(R_1+R_2+X_1)+2g}, \\
\mathcal{P}_5 &= 0.26\mu_0 L_a, \\
\mathcal{P}_6 &= \frac{2\mu_0 t L_a}{\pi(X_1+t)}[(\text{if } X_1 < 3t) \Rightarrow \mathcal{P}_6 = \frac{\mu_0 L_a}{\pi} ln(1+\frac{2t}{X_1})]. \qquad (2.18)
\end{aligned}
$$

In this model, the slot leakage permeances are neglected. Once all parameters in Fig. 2.12 are determined, MEC is solved as detailed in Appendix C.

Table 2.2: Calculation of airgap permeances from −45° to 45°

Airgap Permeances	**Approximated Paths**
$\mathcal{P}_{S4a.R3}$	$\mathcal{P}_3 \parallel \mathcal{P}_2$
$\mathcal{P}_{ml3}$	$\mathcal{P}_7 \parallel \mathcal{P}_5 \parallel \mathcal{P}_6$
$\mathcal{P}_{S3b.R3}$	$\mathcal{P}_1 \parallel \mathcal{P}_2$
$\mathcal{P}_{S3a.R3}$	$\mathcal{P}_4$
$\mathcal{P}_{S3a.R2}$	$\mathcal{P}_2$
$\mathcal{P}_{ml2}$	$\mathcal{P}_6 \parallel \mathcal{P}_5 \parallel \mathcal{P}_6$
$\mathcal{P}_{S2b.R2}$	$\mathcal{P}_2 \parallel \mathcal{P}_1 \parallel \mathcal{P}_2 \parallel \mathcal{P}_3$
$\mathcal{P}_{S2a.R2}$	$\mathcal{P}_4 \parallel \mathcal{P}_2$
$\mathcal{P}_{ml1}$	$\mathcal{P}_6 \parallel \mathcal{P}_5 \parallel \mathcal{P}_6$
$\mathcal{P}_{S1b.R1}$	$\mathcal{P}_2 \parallel \mathcal{P}_1 \parallel \mathcal{P}_2$

2.5.3 Integration of HM1 for the machine

The integration technique of HM1, i.e. Fourier analysis and magnetic equivalent circuit, introduced in Fig. 2.7 is extended for modeling of the flux switching machine as shown in Fig. 2.14 to include torque calculations. After initializing the machine parameters, the reference airgap flux density, $B_{mec}(\theta)$, values are obtained from the magnetic equivalent circuit. For the initial machine parameters, the Fourier model calculates as $B_{g_r}(\theta) = B_{fa}(\theta)$. With $x = g_{ini}$, the rated torque, T_{em}, can be calculated as well. The iteration of the airgap length continues until $err(x)$ is minimized by GSM. As the airgap varies in length, rotor radius is adapted accordingly. Since the rotor solely consists of iron, it is preferred to adjust its radius rather than the stator radius. Once the *updated* airgap field distribution is known, the rated torque can conveniently be calculated with the

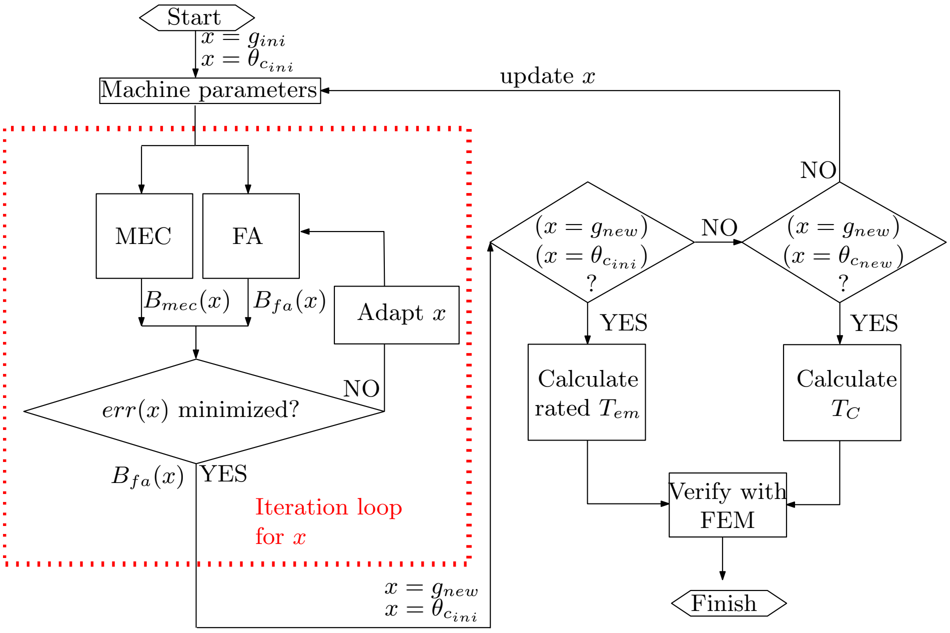

Figure 2.14: Flowchart of HM1 for the flux switching permanent magnet machine.

Fourier analysis for the virtually adapted geometry. If cogging torque, T_C, is considered, after updating g by g_{new} for the rated torque calculation, the iteration loop in Fig. 2.14 reruns, in the same order, as previous until the optimum x is achieved. For the calculation of T_C, x could be θ_m, θ_c, θ_{st} or θ_{rt}, among these, θ_c is chosen due to its facile optimization in the mathematical model.

Verification

To verify the constructed HM1, T_{em} and T_C calculations are performed. These torque calculations in electrical machines are important due to their strong coupling with the operation principle as discussed in Chapter 1.2. The VWM, based on (1.5), is commonly used by reluctance network models like MEC due to its dependency on quantities such as permeance and flux linkage. For MEC, torque can be calculated for polar coordinates (r,θ) by:

$$T(\Delta_\theta) = \frac{0.5\sum_{i=1}^{n} \mathcal{F}_i \mathcal{P}_{i,gap}(\Delta_\theta)}{d\Delta_\theta}\Bigg|_{J=constant}, \qquad (2.19)$$

where n is the total number of $\mathcal{P}_{gap}$. For methods like FA, Maxwell stress tensor (MST) is suitable due to its dependency on accurate local quantities such as airgap

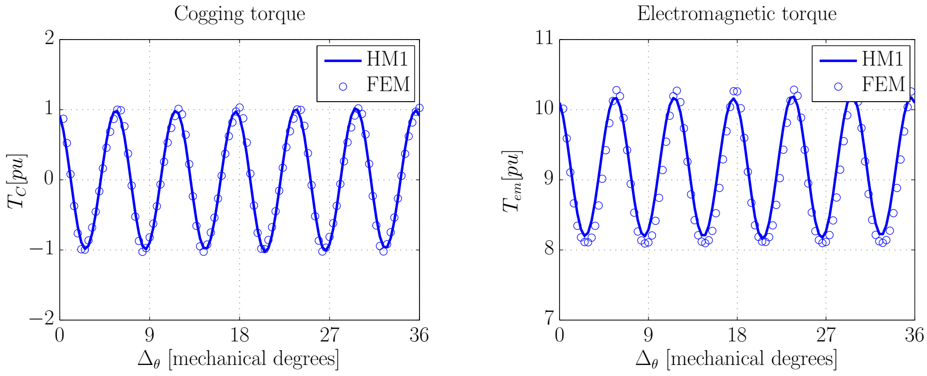

a) b)

Figure 2.15: a) Cogging, and b) electromagnetic torque calculations using HM1 verified with finite element method.

flux density. Torque based on MST can be calculated for polar coordinates (r,θ) by:

$$T(\Delta_\theta) = \frac{R_{ag}}{\mu_0} \oint_S B_\theta B_r dS, \tag{2.20}$$

where B_θ and B_r are determined according to the general formulation in (2.1). The torque calculations are presented in Figs. 2.15a-b, and verified using FEM. The discrepancies between the rms-values of respective comparison are 0.62% for T_C and 1.3% for T_{em} calculations. The solving process with FEM lasts 900[s], whereas it takes only 198[s] with HM1.

2.6 Summary and conclusions

In this chapter, a hybrid model, denoted HM1, has been introduced, which integrates the (semi-) analytical harmonic modeling technique, Fourier analysis (FA), in a cascaded form with a reluctance network model, magnetic equivalent circuit (MEC), in the modeling of structures with a double salient airgap. As such, a double salient airgap structure has been created as a case study for both models. Subsequently, HM1 has been applied to a 3-phase 12/10 flux switching permanent magnet machine.

In general, the Fourier analysis has proven to be accurate compared to the finite element method for field calculations in airgap with a discrepancy of 2.3%, whereas the results obtained with magnetic equivalent circuit, due to its coarse spatial discretization, have been within a discrepancy of 5%. These results have been obtained in the case study for a ratio of slot depth-to-airgap length equal to 72.

If model saliency is extreme, e.g. if slot depth-to-airgap length ratio increases by five times, the accuracy of the Fourier analysis is compromised, with discrepancies in the airgap up to 16%, due to the close proximity to the boundaries. Therefore, a magnetic equivalent circuit has been used to eliminate the modeling problems occurring near boundaries, observed by the Fourier model, due to the extremely small double salient structures. Results have shown that HM1, i.e. the Fourier analysis and the magnetic equivalent circuit, achieved an improvement with a discrepancy of 8.5%.

The integration of FA-MEC has been performed by equating the airgap field calculations between the magnetic equivalent circuit and varying the Fourier analysis. As such, the structure under investigation has been virtually brought to the correct magnetic operation point by enlarging the airgap. For each adjusted geometry, the results of the Fourier analysis have been updated in an iterative manner until they are in agreement with the results of the magnetic equivalent circuit. Using the same principle, the HM1 can also be extended to capture the nonlinear operating point of soft magnetic materials as discussed in Appendix B. The total calculation time of the solving process, including iterations in the Fourier analysis, has been proven four times shorter with HM1 compared to the finite element method.

The performance results achieved with HM1 are striking; however, pre-requisites of the Fourier analysis for certain geometries and coarse spatial discretization of the magnetic equivalent circuit limit the general applicability of HM1. However, by replacing the magnetic equivalent circuit with an advanced form of reluctance network and substituting a similarly accurate technique in place of the Fourier analysis, these issues are addressed, as proposed in the next chapter.

Chapter 3

HM2: Tooth contour and electrostatic finite element methods

"I know engineers, they love to change things." – Dr. McCoy (The Motion Picture)

* * *

This chapter introduces a second hybrid model, HM2, which pairs the tooth contour method (TCM) and electrostatic finite element method (eFEM). To allow more accurate modeling near the boundaries, TCM advances MEC to a finer permeance discretization and therefore provides a more detailed estimation of leakage and fringing fluxes near the boundaries. This allows the inclusion of a larger number of permeances between the double salient structure boundaries, i.e. in the complex airgap. To model these permeances, located between the boundaries (tooth contours), equivalent magnetic scalar potentials have been defined using eFEM. Therefore, HM2 pairs TCM-eFEM without the need for an extra optimization routine, as was the case when using HM1, directly over the calculation of these airgap permeances. Similar to HM1, HM2 is illustrated first on a case study with a double salient airgap, and subsequently implemented to explore its suitability for the analysis of flux switching permanent magnet machines. Finally, the calculations performed using HM2 are verified with finite element analyses.

* * *

The contributions of this chapter are published in the following articles:

- Ilhan, E., Paulides, J. J. H. and Lomonova, E. A. [2014]. Hybrid modeling techniques for complex magnetic flux paths in airgap. *Proceedings of Intermag Conference*, Dresden, Germany.
- Ilhan, E., Kremers, M. F. J., Motoasca, T. E., Paulides, J. J. H. and Lomonova, E. A. [2012]. Spatial discretization methods for air gap permeance calculations in double salient traction motors. *Industry Applications, IEEE Transactions on*, 48(6):2165-2172.
- Ilhan, E., Paulides, J. J. H., Encica, L. and Lomonova, E. A. [2010]. Tooth contour method implementation for the flux-switching PM Machines. *Proceedings of the International Conference on Electric Machines*, Rome, Italy.

In hybrid model 1 (HM1), introduced in the previous chapter, the stand-alone technique magnetic equivalent circuit (MEC) has an accuracy depending on the number of permeance elements, particularly in the airgap region. To allow more accurate modeling of PM-biased salient machines in case of extreme saliency, MEC can be advanced by another stand-alone technique based on reluctance networks, i.e. the tooth contour method (TCM), which provides a finer permeance discretization in the airgap compared to MEC. In TCM, the permeance is not calculated by simplified flux tube shapes, but accurately determined by electromagnetic field distribution in the airgap by means of permeance function, which can account for leakage and fringing fluxes near boundaries [91]. Therefore, a higher number of permeances are evaluated in TCM compared to MEC. This also simplifies the incorporation of motion to MEC, which normally needs to be updated for every new position [92]. Another forthcoming feature of TCM is its suitability for hybrid modeling approaches. To model these permenaces located between boundaries of airgap, any stand-alone technique with adequate accuracy discussed in Chapter 1.3.2 can be opted for. Due to the lowered accuracy of FA near boundaries, this stand-alone technique has not been favored in the construction of HM2, but instead a numerical model based on finite element method (FEM) is selected. Thus, the resulting hybrid model 2 (HM2), discussed in this chapter, pairs TCM with a numerical stand-alone technique based on electrostatic FEM (eFEM).

3.1 Tooth contour method

In the composition of HM2, the first analyzed stand-alone technique is the tooth contour method (TCM), based on a fine discretization of the airgap region [93]. This region with a relative permeability, μ_r, close to that of air, i.e. coil, PM, and air, is divided on the soft magnetic boundaries by the so called tooth contours (TCs). In principle, every TC is connected to each other via a permeance, which causes a finer spatial discretization in the airgap compared to the MEC as visualized in Fig. 3.1. The sum of the local fields, represented over these permeances, gives the total magnetic field in the airgap [94]. The remaining permeances representing the soft-magnetic material are estimated similar to MEC as discussed in Chapter 2.3. Although TCM is generally applied in the Cartesian coordinate system on polygons, it can also be implemented on odd shaped structure such as arc shaped magnets [95]. Similar to HM1, TCM is first implemented on the case study.

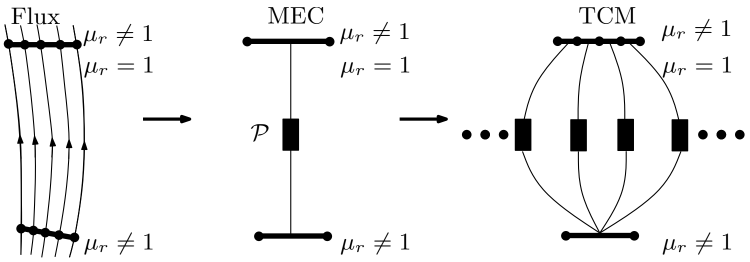

Figure 3.1: Visualization of tooth contour method.

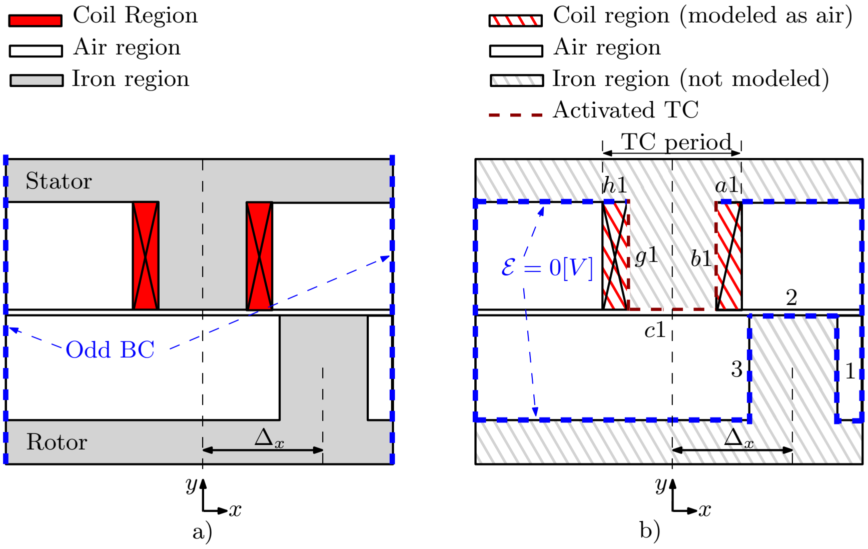

Figure 3.2: a) Magnetostatic model, and b) electrostatic model with tooth contours for the case study in Fig. 2.1.

3.1.1 Application to the case study

Prior the modeling of a PM-biased salient machine, TCM is first implemented, similar to HM1, on the reduced-order case study in Fig. 3.2a. For TCM, the reluctance network in Fig. 2.6 is used partially, i.e. for modeling of soft magnetic material, according to the assumptions discussed in Chapter 2.3.1. The stator and rotor iron boundaries are divided into line regions, i.e. TCs, which are referred to by letters for the stator and by numbers for the rotor section. For the stator TCs, additional numbering is used together with the letters indicating the TC period. The period indicators may not be important for the case study topology, but they are necessary for more complex structures, such as for PM-biased salient machines as discussed in Chapter 3.4.

For the calculation of the airgap permeance, the potential difference or mmf, $\mathcal{F}$, drop between relevant TCs needs to be calculated. This is realized by considering two TCs simultaneously, from which two, one is assigned to a known potential, i.e. *activated*, whereas the remaining TCs are to zero potential. This procedure is discussed in the following part.

Activation of tooth contour

In TCM, the permeance between relevant TCs is calculated by *activating* or exciting one TC at each rotor tooth position, Δ_x, where a known potential is assigned to the active TC [83]. Because all energy sources are located in the stator, only stator TCs need to be activated at each Δ_x. One example is given for the case study in Fig. 3.3, where the stator tooth is activated by three TCs, i.e. $TC_{g1,c1,b1}$. Activation can be done by imposing a magnetic or an electrical scalar potential. Because these TCs are activated on a small area, it should be ensured that all other TCs and boundaries have zero potential. Therefore, it is generally recommended to consider three rotor pole pitches and three TC periods for structures with complex flux paths [96]; however, for the case study, this is not necessary. Based on the resulting potential and flux distribution, the airgap permeance, $\mathcal{P}_{gap}$, can be written according to the Hopkinson's law in (2.5):

$$\mathcal{P}_{gap} = \frac{\Phi}{\mathcal{F}} = \frac{\oint_S \mathbf{B} \cdot d\mathbf{S}}{\mathcal{F}} = L_a\left(\int_{x_1}^{x_2} B_r dx\right)\Bigg|_{\mathcal{F}=1}, \tag{3.1}$$

where, for convenience, a unity scalar potential drop over the active TC is assigned. To calculate $\mathcal{P}_{gap}$ in (3.1), the normal component of the magnetic flux density, B_r, along the length $(x_1 - x_2)$ in the xy-plane of the nonactive TC needs to be calculated. These calculations give only one value of the airgap permeance at a certain rotor position Δ_x. To model these permeances located between TCs, equivalent magnetic scalar potentials are defined using eFEM.

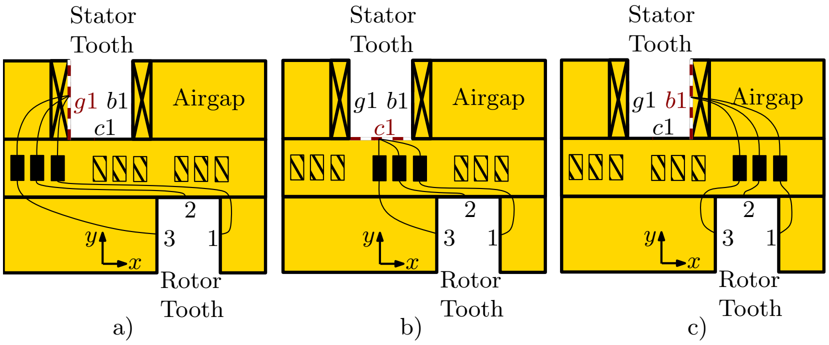

Figure 3.3: Relevant airgap permeances between stator tooth and rotor tooth when a) TC_{g1} is activated, b) TC_{c1} is activated, and c) TC_{b1} is activated.

3.2 Electrostatic finite element method

In the composition of HM2, the second stand-alone technique is the electrostatic finite element method (eFEM), based on a high spatial discretization of the studied domain by means of mesh elements. In these finite elements, the differential form of Maxwell equations, summarized in Appendix A, are linearized and the solution is approximated numerically. For modeling of the salient airgap, such methods are preferred due to the high accuracy of the solutions. In a likely approach [91] gives a successful integration between boundary element method (BEM) and TCM based on (3.1). A numerical method such as magnetostatic FEM can also be integrated into TCM to determine $\mathcal{P}_{gap}$; however, the magnetostatic 2D FEM software does not allow magnetic scalar potentials to be assigned on TCs [97]. This problem can be overcome either by placing representative coil regions in the magnetostatic FEM or by using eFEM, which is based on scalar potential calculations. The calculations in electrostatic domain would provide an equivalent solution of the magnetostatic problem for the analyzed region. Consequently, eFEM is first applied to the case study similar to TCM.

3.2.1 Application to the case study

The airgap of the case study, given in Fig. 3.2, comprises coil and air regions with similar μ_r as discussed in Chapter 2.2.1, therefore both regions are included in eFEM. Since only $\mathcal{P}_{gap}$ between relevant stator and rotor tooth are of interest, the iron, denoted as the grey tiled region in Fig. 3.2b, is not modeled in eFEM. If the magnetostatic model is based on:

$$\Phi = \mathcal{F}\mathcal{P}_{mag}, \tag{3.2}$$

where $\mathcal{P}_{mag}$ is the magnetic permeance, a similar relationship can be derived for the electrostatic case as follows for the electrical flux, Ψ:

$$\Psi = \mathcal{E}\mathcal{P}_{ele}, \tag{3.3}$$

where $\mathcal{E}$ represents the electrical potential and $\mathcal{P}_{ele}$ electrical equivalent of $\mathcal{P}_{mag}$. In this case, an active TC, as explained in Chapter 3.1.1, is realized by imposing $\mathcal{E} = 1[V]$ on the relevant TC. The results obtained from eFEM in Figs. 3.4a-b show the potential distribution when the stator tooth is activated at $\Delta_x = 0[mm]$ and $\Delta_x = 12[mm]$.

According to (3.3), $\mathcal{P}_{ele} = \Psi$ when $\mathcal{E} = 1[V]$ at the tooth, which can be calculated directly from the flux entering the nonactive TC. Similar to magnetostatic case (3.1), in eFEM the normal electrical flux density, D_r, is calculated along the path x, which is the length of the nonactive TC in xy-plane. This procedure is repeated for multiple rotor positions Δ_x, as illustrated in the example of Fig. 3.5.

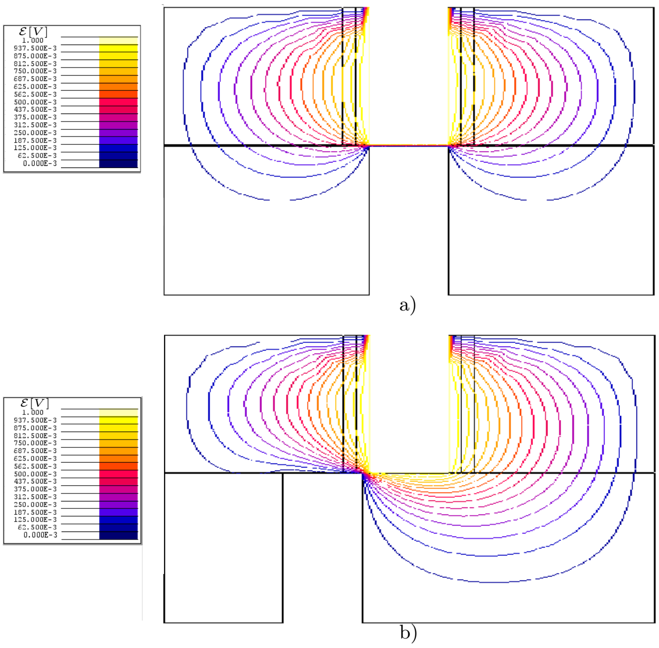

a)

b)

Figure 3.4: Electrical scalar potential, $\mathcal{E}$, distribution in the salient airgap of case study when the stator tooth (TC_{b1}, TC_{c1}, TC_{g1}) is activated a) $\Delta_x = 0[mm]$ and b) $\Delta_x = 12[mm]$.

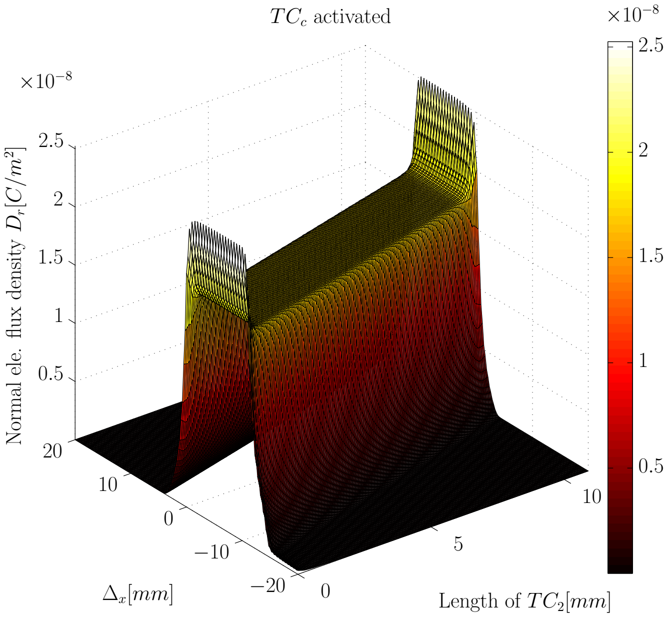

Figure 3.5: Normal component of electrical flux entering TC_2 on the rotor tooth in Fig. 3.2 when TC_{c1} on the stator tooth is activated.

Consequently, (3.1) can be rewritten for the electrostatic analysis:

$$\mathcal{P}_{ele} = L_a \left(\int_{x_1}^{x_2} D_r \; dx \right) \Bigg|_{\mathcal{E}=1}, \tag{3.4}$$

$$\mathcal{P}_{mag} = \mathcal{P}_{ele} \frac{\mu_0}{\epsilon_0}, \tag{3.5}$$

where ϵ_0 is the permittivity of free space. Here, $\mathcal{P}_{ele}$ is converted to $\mathcal{P}_{mag}$, i.e. to $\mathcal{P}_{gap}$. The estimation of $\mathcal{P}_{gap}$ forms the basis of the integration of HM2, which pairs TCM and eFEM.

3.3 Integration of tooth contour method and electrostatic finite element method

To allow more accurate modeling near boundaries, HM2 advances HM1, introduced in Chapter 2, by replacing MEC with TCM. The structure of TCM provides a more suitable integration of another stand-alone technique, i.e. eFEM, without the need for an extra optimization routine, as it was in HM1. The integration of both techniques is realized over the calculation of $\mathcal{P}_{gap}$, which is first calculated by eFEM, transformed to a magnetic quantity and finally implemented in TCM network. Peculiarities of the integration technique are discussed in the following parts.

3.3.1 Mitigation of tooth contours

The number of tooth contours depend on the accuracy demands of the model. A high number can increase accuracy, however, also the calculation time of eFEM. This drawback can be avoided by the mitigation of tooth contours around the source, i.e. by treating multiple adjacent stator TCs as one. To evaluate the effect of the mitigation on the accuracy, stator tooth in Fig. 3.3 is excited first separately as three $TC_{g1,c1,b1}$ and then simultaneously as one TC. Results in Fig. 3.6 show the mitigation of stator tooth contours do not affect the end result in terms of accuracy, but improve the simulation time.

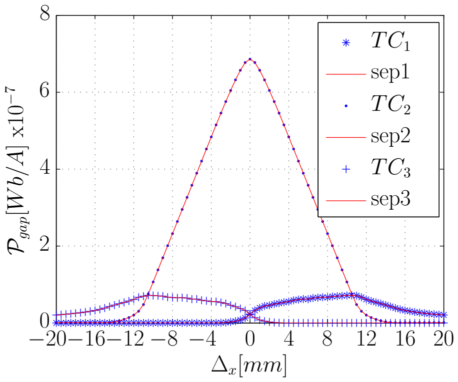

Figure 3.6: Simple comparison between separately and simultaneously activated stator tooth contours.

3.3.2 Airgap permeance function

The study conducted in Fig. 3.6 indicates that the most dominant permeance is located between the stator tooth TC ($TC_{g,c,b}$) and TC_2. Thus, this permeance determines the shape of $\mathcal{P}_{gap}(\Delta_x)$ predominantly, which follows a normal (Gaussian) distribution used in the probability theory and statistics [98]:

$$\mathcal{P}_{gap}(\Delta_x) = \frac{1}{\sigma\sqrt{2\pi}} e^{-(\Delta_x - mean)^2/(2\sigma^2)}, \tag{3.6}$$

where σ stands for standard deviation and *mean* for the mean value of $\mathcal{P}_{gap}(\Delta_x)$. The maximum permeance is reached when the considered rotor and stator TCs come at minimum distance, i.e. if they are aligned. Depending on the position of the TCs, the shape of permeance function changes as shown in Fig. 3.6.

Verification

To verify the constructed HM2 in terms of extreme saliency, the sensitivity study conducted in Chapter 2.4 for HM1 is repeated for HM2. Previous results in Fig. 2.8 have shown that HM1, i.e. FA-MEC, achieves an improvement with a discrepancy of 8.5% compared to 16% of FA. Under the same conditions, results in Fig. 3.7 show that HM2, i.e. TCM-eFEM, achieves an improvement with a discrepancy of 1.4%. The total simulation time is 32[s] for HM2 compared to the 36[s] of FEM. Compared to HM1, the simulation time has increased due to the partial involvement of eFEM; however, HM2 still improves simulation time by 11% compared to FEM.

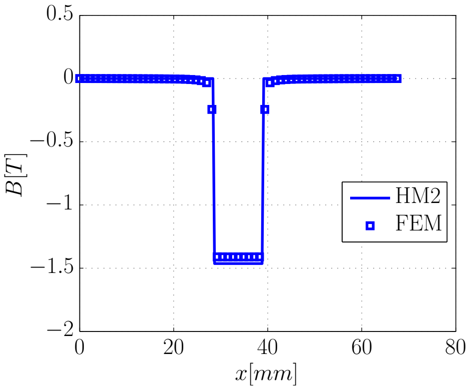

Figure 3.7: Flux density in airgap calculated by HM2 and finite element method for the parameter variations in the case study at $\Delta_x = 0[mm]$.

3.4 Application of HM2 to the flux switching permanent magnet machine

This section explores the appropriateness of HM2 to analyze PM-biased salient machines on an example flux switching permanent magnet (FSPM) machine as discussed in Chapter 2.5. Similar to the case study, the stand-alone techniques, TCM and eFEM, are implemented separately on the FSPM.

3.4.1 Tooth contour method for the machine

In the composition of HM2, the first analyzed stand-alone technique is TCM, which is mainly based on MEC of FSPM in Fig. 2.12 except for the airgap region. The new structure shown in Fig. 3.8 is position dependent, i.e. the permeance values change depending on the relative position of rotor to stator, Δ_θ. The tiled permeances interconnect all TCs around the airgap, which are $\mathcal{P}_{S*R*}(\Delta_\theta)$, $\mathcal{P}_c(\Delta_\theta)$ and $\mathcal{P}_{ml}(\Delta_\theta)$. Of the three airgap permeances ($\mathcal{P}_{gap}(\Delta_\theta)$), $\mathcal{P}_{S*R*}(\Delta_\theta)$ has considerably higher values compared to the other two similar to the analysis conducted in Fig. 3.6. Additionally, due to the half periodicity of FSPM, MEC in Fig. 2.12 is expanded from a quarter to a half machine model, i.e. 6 stator and 5 rotor TC periods.

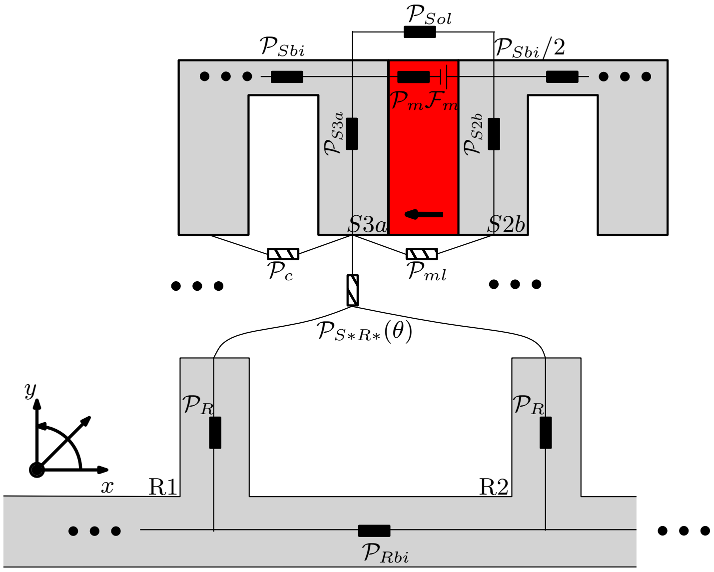

Figure 3.8: The tooth contour method of the flux switching permanent magnet machine.

3.4.2 Electrostatic finite element method for the machine

In the composition of HM2, the second analyzed stand-alone technique is eFEM. Compared to the case study, eFEM of FSPM requires a minimum of three TC periods and three rotor pole pitches, as mentioned in Chapter 3.1.1. To keep similar notations as in the case study, the preceding TC period is denoted with 0 and the following one with 2, resulting in eFEM shown in Fig. 3.9. Because the PM relative permeability is very similar to that of air, PMs are included in eFEM as well. Since energy sources of FSPM are located in the stator, hence it is sufficient to set the stator TCs at $\mathcal{E} = 1[V]$ potential for the permeance calculations based on the relationships given in (3.4)-(3.5). The activated stator TCs, eight TCs labeled $a - h$, are located on stator tooth faces, and rotor TCs, labeled $1 - 3$, are located on rotor tooth faces, as shown in Fig. 3.8. Due to the considered three pole pitches in the model, all three rotor teeth in Fig. 3.8 are numbered in the same order. Consequently, TCs with the same numbering contribute to the same permeance, just with a shift in the relative position of Δ_θ. Based on the potential distribution, such as given in Figs. 3.10a-b at $\Delta_\theta = 0°$ and $\Delta_\theta = 12°$, D_r along the nonactive TC is calculated for every position in one stator cycle as shown in Fig. 3.11.

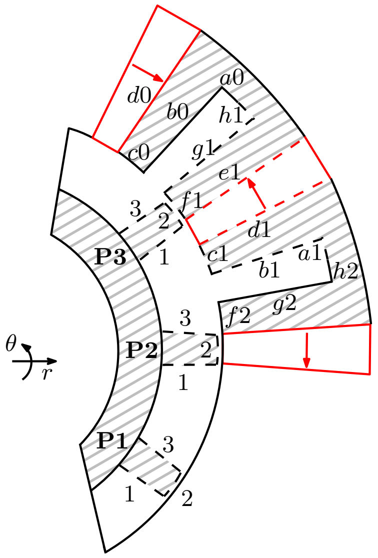

Figure 3.9: The electrostatic finite element method of the flux switching permanent magnet machine with the tooth contours located in rotor and stator.

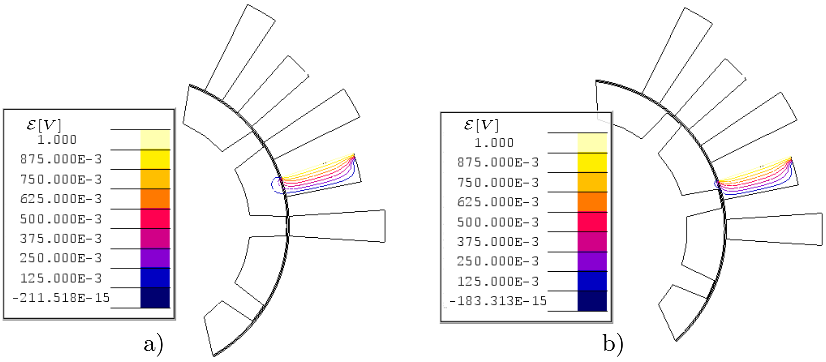

a)

b)

Figure 3.10: Electrical scalar potential, $\mathcal{E}$, distribution of the flux switching permanent magnet machine when TC_b is activated (by applying $1[V]$ potential) at a) $\Delta_\theta = 0^\circ$, and b) $\Delta_\theta = 12^\circ$.

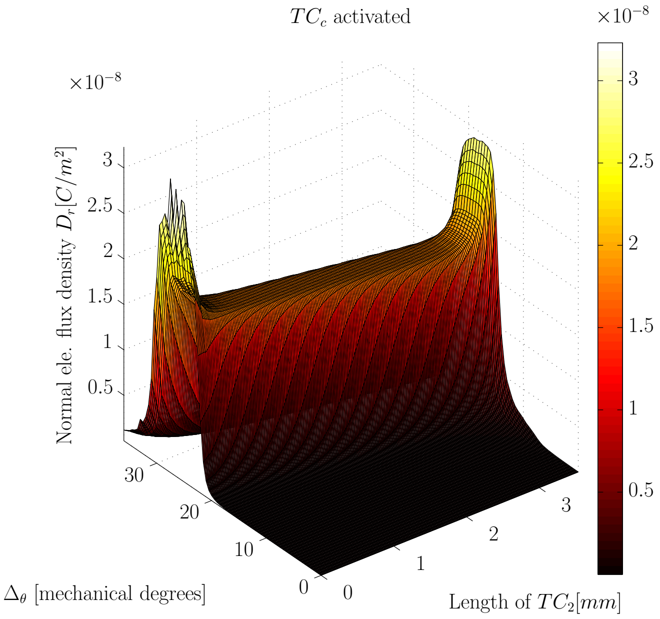

Figure 3.11: Normal component of electrical flux entering TC_2 (on the rotor) in Fig. 3.9 when stator TC_{c1} is activated.

3.4.3 Integration of HM2 for the machine

As mentioned earlier in Chapter 3.3, HM2 combines TCM and eFEM over the calculation of airgap permeance. In salient machines, the dominant airgap permeances are located on the outer tooth sides, i.e. TC_2 for rotor tooth side, TC_c and TC_f for stator tooth side. Results in Fig. 3.12 show that permeances located between $TC_2 - TC_c$ or $TC_2 - TC_f$ determine the general shape of $\mathcal{P}_{gap}(\Delta_\theta)$. The dominant permeance shape has a standard deviation of approximately $\sigma = 0.5$. If more permeances are required in addition to $\mathcal{P}_{gap}$, such as $\mathcal{P}_c$ or $\mathcal{P}_{ml}$, these can be also calculated by the same TCM. For a detailed analysis, partial TCMs illustrated in Figs. 3.13a show examples of the airgap permeances $\mathcal{P}_{gap}$ calculated by eFEM; these permeances denoted as $\mathcal{P}_{S1b}$, $\mathcal{P}_{S2a}$, and $\mathcal{P}_{S2b}$ are located between the five rotor teeth $P1 - P5$ and stator teeth $c1, f1, c2$ respectively. Results in Figs. 3.13b show how differently located airgap permeances are changing with the same rotor position, where permeance values are distributed over one electrical cycle. The $\mathcal{P}_{gap}$ values calculated by HM2 are identical to the results obtained through FEM.

Due to the higher number of procedures required for HM2 of FSPM, a MATLAB script has been prepared for the evaluation of these permeances, as illustrated in Fig. 3.14. In principle, the script selects a certain permeance located at a certain place for a certain rotor position. The script comprises three stages, where in the

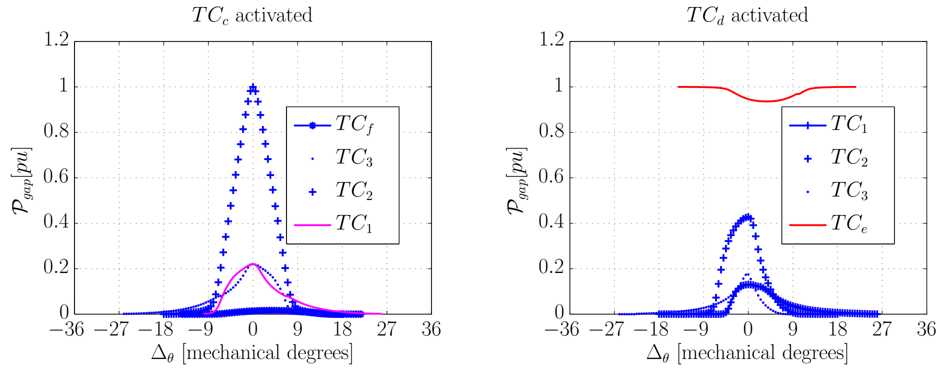

a) b)

Figure 3.12: Airgap permeance functions, $\mathcal{P}_{gap}$, between a) TC_c, b) TC_d and the rotor TCs in Fig. 3.9.

1^{st} stage calculation of TCM permeances are realized by eFEM. The 2^{nd} part sorts these permeances in the right order into 3D permeance matrices for PM, coil and leakage permeances. In the 3^{rd} and last stage, the reluctance network of TCM is solved using the pre-calculated permeances for each step denoted as m. Furthermore, for improving the simulation time, some modifications are performed based on the symmetries present between certain TCs. For example, the activated TC_b-TC_g give symmetrical results due their relative location to rotor. To accelerate the MATLAB code, only one of the symmetrical TCs is calculated, i.e. TC_b, TC_d and TC_c. Their symmetrical counterparts, TC_g, TC_e and TC_f, are calculated by means of only one extra line code. Consequently, the main increase in speed is obtained using this symmetry in the 1^{st} stage of HM2.

Verification

To verify the constructed HM2 of FSPM, phase flux linkage, λ_{ph}, and torque, T_C, calculations are performed based on (2.19). The discrepancies observed in Figs. 3.15a-b between the rms-values of respective comparisons are 1.1% for λ_{ph} and 1.12% for T_C calculations. The maximum discrepancies in the overall values are 9.7% for λ_{ph} and 5.10% for T_C. The required simulation time of HM2 is 792[s] compared to FEM with 900[s] due to the decreased simulation space in eFEM.

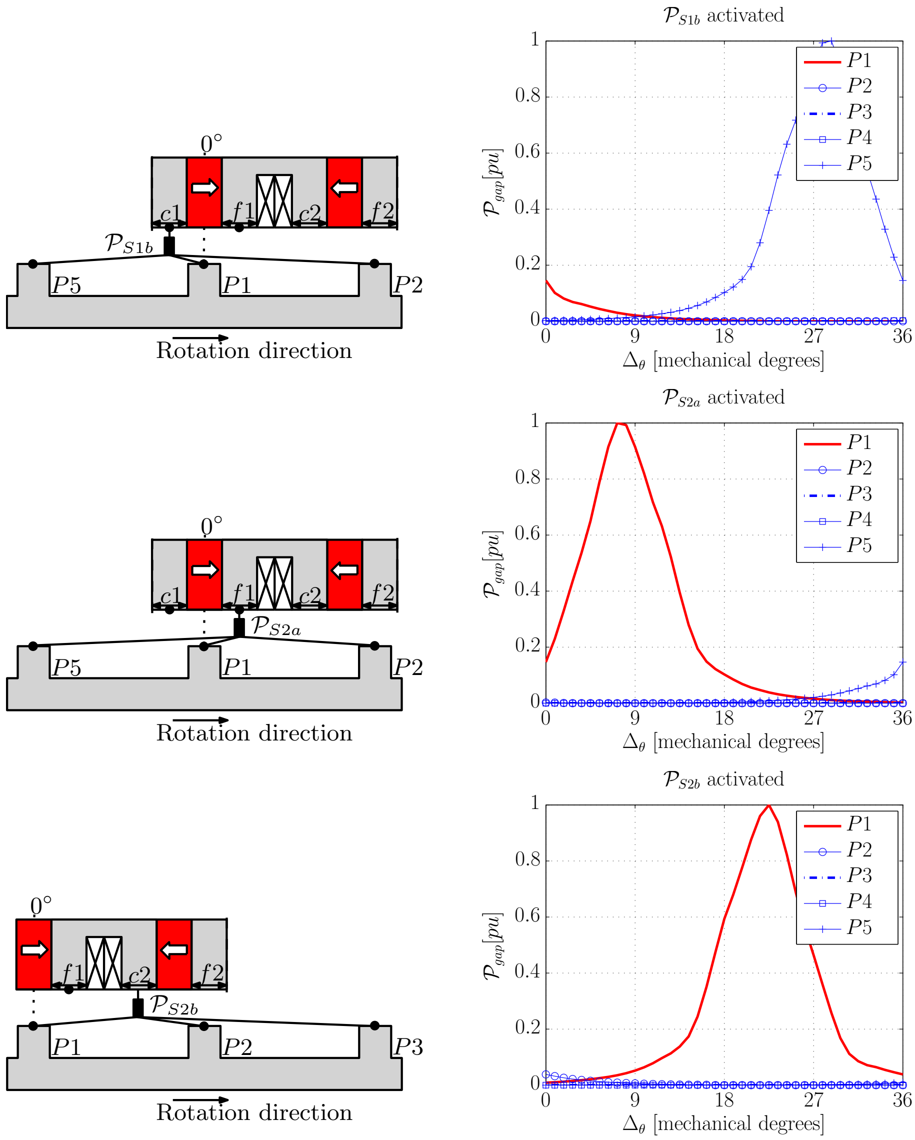

a) b)

Figure 3.13: a) Airgap permeances between rotor teeth $P1$-$P5$ and stator tooth $c1$,$f1$, and $c2$, b) $\mathcal{P}_{gap}(\Delta_\theta)$ calculated by the tooth contour method.

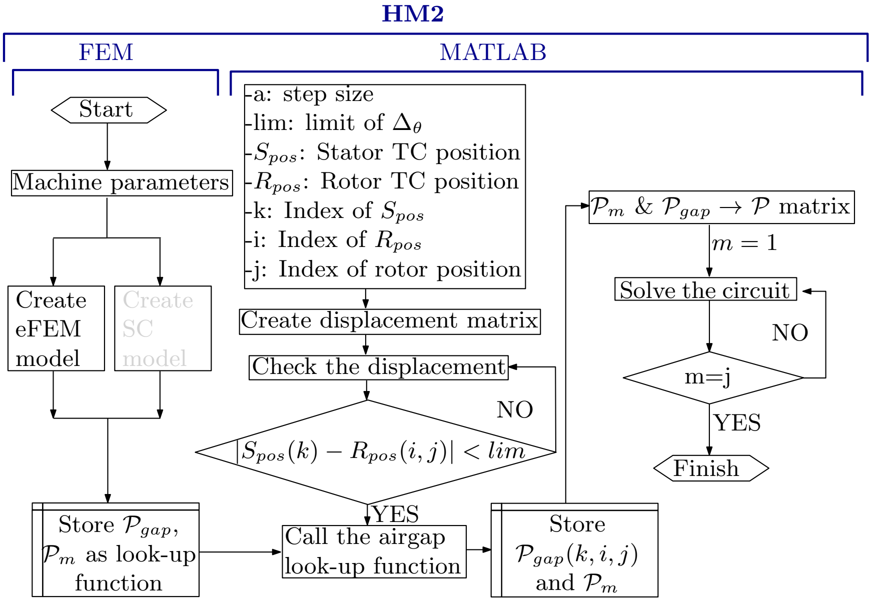

Figure 3.14: Flowchart of HM2 for the flux switching permanent magnet machine.

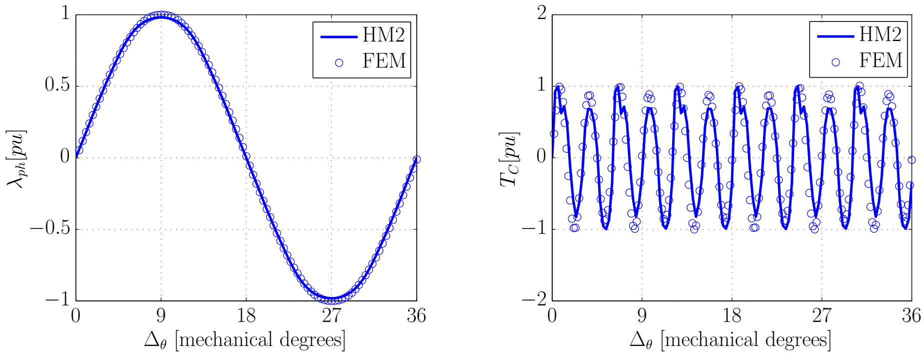

a) b)

Figure 3.15: Comparison of a) phase flux linkage λ_{ph}, and b) cogging torque calculated by HM2 and finite element method.

3.5 Summary and conclusions

In this chapter, a hybrid model, denoted HM2, has been introduced, which integrates a reluctance network model, tooth contour method (TCM), in a cascaded form with a numerical method, electrostatic finite element method (eFEM), in the modeling of structures with a double salient airgap. As such, the case study previously introduced in Chapter 2 has been used for both models. Subsequently, HM2 has been applied to a 3-phase 12/10 flux switching permanent magnet machine.

To increase the model accuracy near the boundaries, the magnetic equivalent circuit included in HM1 has been replaced by a tooth contour method leading to a finer permeance discretization. Unlike the magnetic equivalent circuit, based on simplified flux distribution, the tooth contour method has a more detailed estimation of leakage and fringing fluxes near the boundaries. Consequently, it is possible to include a larger number of permeances between the double salient structure boundaries. To model these permeances, located between the piecewise boundaries around the salient airgap (tooth contours), equivalent magnetic scalar potentials have been defined. In principle, any accurate technique, such as Fourier analysis or finite element method, could adequately simulate the potential difference necessary to calculate these permeances. Due to the accuracy problems of the Fourier analysis near boundaries, as discussed in the previous chapter, the potentials have been defined using an electrostatic finite element method. Electrostatic solver has been opted for since in 2D finite element method software, scalar potentials can be defined directly on the boundaries. In the presence of extreme saliency, results have shown that HM2, i.e. the tooth contour and electrostatic finite element methods, achieved an improvement, with a discrepancy of 1.4% compared to 8.5% in HM1, due to the increased spatial discretization of the tooth contour method compared to the magnetic equivalent circuit.

The integration of TCM-eFEM has been performed through direct calculation of airgap permeances without the need for an extra optimization routine as was required when using HM1. The tooth contour method is a convenient choice for hybrid modeling, as it allows easy integration of any other modeling technique, such as electrostatic finite element method. Despite its advantage in accuracy, the electrostatic finite element method relies on additional software, resulting additional time longer than the actual solving process with only a partial model of the airgap. Although this is a drawback to be considered when choosing methods for a hybrid model, HM2 required approximately 25% of the pre-modeling time and was still 13% faster than a full finite element model, which includes material characteristics and a larger mesh size. Therefore, despite its drawbacks, using the electrostatic finite element method in a hybrid model is still a preferable choice compared to the finite element method.

The performance results achieved with HM2 indicate a higher accuracy compared to HM1 in magnetic calculations for structures with increased saliency, at the cost of an increased simulation time. The presence of the secondary software due to the electrostatic finite element method and a post-processing of its results limit the general applicability of HM2. One solution to this problem could be the coupling of MATLAB and finite element software (if applicable); however, allowing remote access could as well have increased the simulation time significantly. Another solution to these drawbacks is proposed in the next chapter by means of replacing electrostatic finite element method by conformal mapping methods.

Chapter 4

HM3: Tooth contour method and Schwarz-Christoffel mapping

"Theoretically, it is possible..." – Data

* * *

This chapter introduces the last hybrid model, HM3, which pairs the tooth contour method (TCM) and Schwarz-Christoffel mapping (SC). Both HM1 and HM2 comprise methods, FA and eFEM respectively, that require the definition of boundary conditions resulting in reduced accuracy near the boundaries. An alternative approach, applied in HM3, is to unite the boundaries of the original structure to a mapped equivalent region, without sacrificing accuracy. The airgap permeances, in the construction of HM3, are calculated in the mapped region by applying orthogonal field theory. Therefore, HM3 pairs TCM-SC, in a structure comparable to that of HM2, directly over the calculation of these airgap permeances without the need for an extra optimization routine, as was the case in HM1. Similar to HM1 and HM2, HM3 is illustrated first on the case study with a double salient airgap, and subsequently implemented to explore its appropriateness to analyze flux switching permanent magnet machines. Finally, the calculations performed using HM3 are verified with finite element analyses.

* * *

The contributions of this chapter are published in the following articles:

- Ilhan, E., Paulides, J. J. H. and Lomonova, E. A. [2014]. Hybrid modeling techniques for complex magnetic flux paths in airgap. *Proceedings of Intermag Conference*, Dresden, Germany.
- Ilhan, E., Kremers, M. F. J., Motoasca, T. E., Paulides, J. J. H. and Lomonova, E. A. [2012]. Spatial discretization methods for air gap permeance calculations in double salient traction motors. *Industry Applications, IEEE Transactions on*, 48(6):2165-2172.
- Ilhan, E., Motoasca, T. E., Paulides, J. J. H. and Lomonova, E. A. [2012]. Conformal mapping: Schwarz-Christoffel method for flux switching PM machines. *Journal of Mathematical Sciences*, 6.
- Ilhan, E., Motoasca, T. E., Paulides, J. J. H. and Lomonova, E. A.[2011]. Conformal mapping: Schwarz-Christoffel method for flux switching PM machines. *Proceedings of Computational Magnetics, COMPUMAG*, Sydney, Australia.

Both hybrid model 1 (HM1) and hybrid model 2 (HM2), introduced in the previous two chapters, are based on stand-alone techniques, Fourier analysis (FA) and electrostatic finite element method (eFEM) respectively, that required definition of boundary conditions resulting in an accuracy reduction near the boundaries. Furthermore, dependency on multiple software platforms can bring an extra burden to the integration technique in hybrid modeling. In case of HM2, TCM-eFEM integration depends on MATLAB and a commercial finite element software. To overcome these problems, an alternative approach is to unite the boundaries of the analyzed structure to an equivalent new domain. Therefore, a replacement of eFEM is proposed in this chapter, without sacrificing accuracy, by means of another stand-alone technique, i.e. conformal mapping.

In mathematics, conformal mapping is a complex valued function used to transform a domain into a simpler structure to decrease complexity of the boundary value problem. Due to its angle-preserving feature, this mapping is widely used in engineering such as in electromagnetism, biomedical engineering, and thermodynamics [99–101]. Similarly, the airgap permeance of a salient structure can be calculated alternatively (compared to eFEM in HM2) in a mapped region. Thus, the resulting hybrid model 3 (HM3), discussed in this chapter, pairs TCM with a stand-alone technique based on Schwarz-Christoffel mapping in a comparable structure to HM2.

4.1 Schwarz-Christoffel mapping

In the composition of HM3, the first stand-alone technique is TCM, which has been introduced in Chapter 3. The second stand-alone technique in HM3 is Schwarz-Christoffel (SC) mapping based on a conformal transformation, which is used in several electromagnetic problems to simplify the salient airgap of an electrical machine [102–104]. In literature, this technique is not used to calculate airgap permeances, but rather to analytically solve the Maxwell equations, summarized in Appendix A, in the equivalent (mapped) airgap with charge modeling or FA [102, 103]. In this thesis, the salient airgap flux is first transformed by SC mapping as visualized in Fig. 4.1, then it is used to calculate the airgap permeance to be integrated in TCM.

Mathematically, SC maps a complex w-domain to another complex z-domain as shown in Fig. 4.2. The mapping function $f(w) = z$ is given in closed form as:

$$f(w) = A + C \int^{w} \sum_{k=1}^{n-1} (w - w_k)^{\alpha_k - 1} dw, \tag{4.1}$$

where A and C are complex constants, α_k are the interior angles of the w points and $z_k = f(w_k)$ for $k = 1, ..., n-1$ [105]. For example Fig. 4.2, an L-shaped polygon is mapped from the complex w-domain to another complex z-domain with SC integral in (4.1). The corners of the modeled structure are called *vertices*, denoted

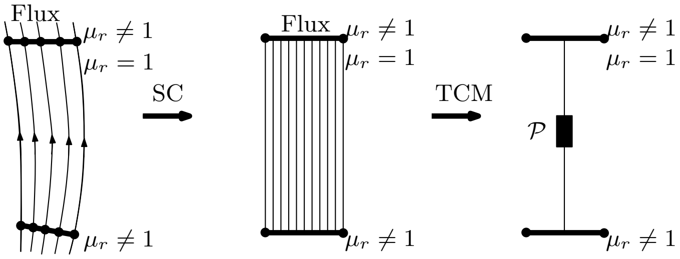

Figure 4.1: Visualization of Schwarz-Christoffel mapping and its integration to tooth contour method.

as numbers in Fig. 4.2. Around certain vertices, e.g. 1, 2, 4, 5, $f(w)$ can be defined, whose complexity is proportional to the number of these vertices. For polygons with maximum three vertices, the mapping function can be calculated explicitly. For more complicated polygons, determining $f(w)$ becomes a parameter problem, which can only be solved numerically [105]. To determine $f(w)$ numerically, the freely available MATLAB toolbox is exploited in this thesis [106]. In this toolbox, several mapping methods are available for different polygons in the z-domain e.g. disk, half plane, strip, rectangle, and Riemann surfaces [105]. Regardless of its shape, there are two general requirements to describe a polygon in the w-domain:

- The polygon has to be in a quadrilateral shape, i.e. curved lines have to be converted to straight lines.
- The vertices of the polygon have to be defined in a complex plane and the order in counterclockwise direction.

The first requirement states that the path between all vertices is straight, since an interior angle α has to be defined around each vertice k. The second requirement is to include all boundary points in the mapped region. It should be noted that all vertices both in original w-and mapped z-domains in Fig. 4.2 are in counter-clock wise direction. The relative position of the vertices is not affected by $f(w)$.

Since $f(w)$ is numerically approximated, some salient geometries can cause convergence problems referred to as *crowding*. Being a common phenomenon in computational conformal mapping, it is a result of large ratios between the polygon sides [105]. For salient electrical machines, this situation may occur in case of a large slot depth-to-airgap diameter ratio in radial direction, e.g. y-direction for the case study in Fig. 4.3. One solution to overcome this problem is to reach a suitable ratio of polygon sides by extending the boundaries in the tangential direction, e.g. x-direction for the case study, without significantly diminishing the solution accuracy. For some geometries, this solution could change the boundary value problem; however, this does not rise a significant problem within HM3 since mainly localized flux paths are of concern to calculate airgap permeances, $\mathcal{P}_{gap}$.

The calculation of $\mathcal{P}_{gap}$ is realized in SC mapping with orthogonal field diagrams

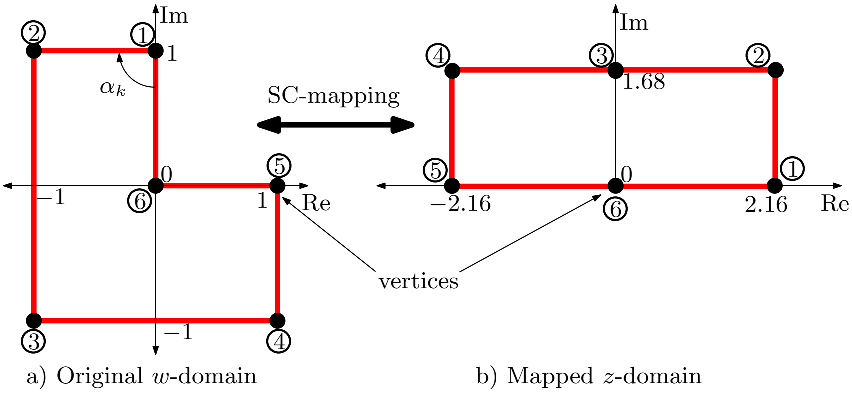

Figure 4.2: An example of Schwarz-Christoffel mapping implemented on an L-shaped polygon.

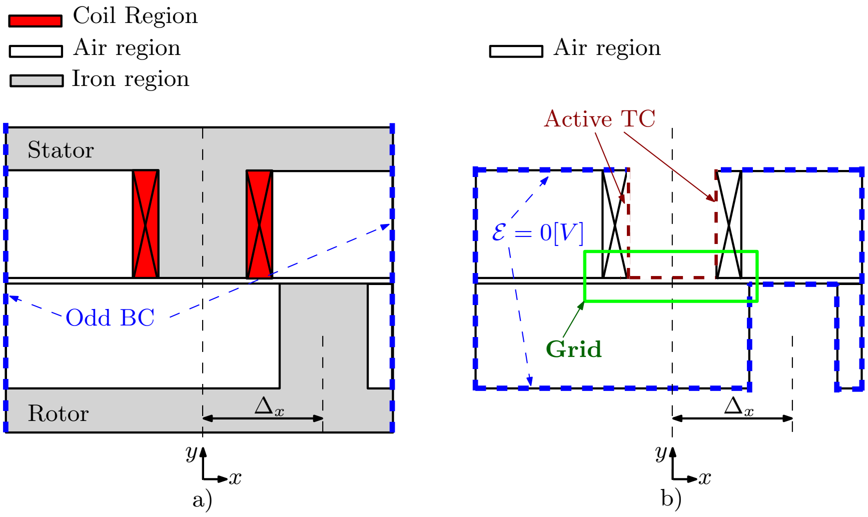

Figure 4.3: a) Case study with salient airgap structure from Fig. 3.2 with the boundary conditions (BC), and b) mapped region in Schwarz-Christoffel mapping for HM3 including the tooth contours (TC).

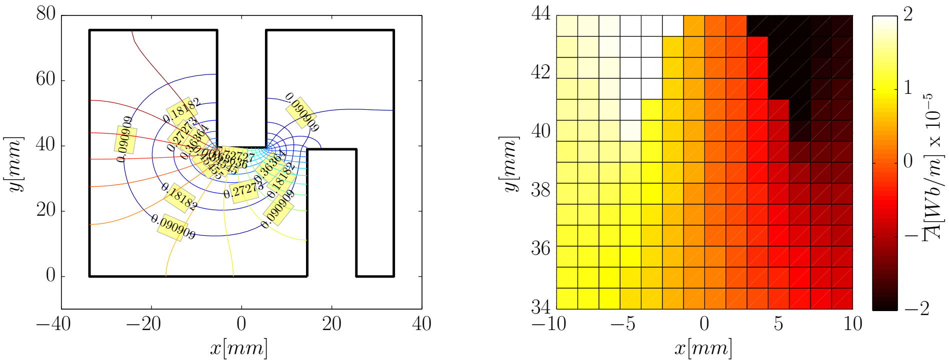

a) b)

Figure 4.4: Case study at $\Delta_x = 20[mm]$: a) Orthogonal field diagrams (OFD), and b) magnetic potential distribution in the given grid.

(OFD). If a harmonic function is mapped with SC to another complex plane, the mapping function is harmonic as well. This follows from the mapping function, which satisfies the Cauchy-Riemann equations resulting in invariance of the potential values with respect to the mapped points [107]. This feature allows the magnetic and electrical potential functions to be uniquely defined in both domains. If a magnetic potential function is considered, the potential and flux lines can be illustrated as OFDs in Fig. 2.5 [15]. Similarly, OFDs can be illustrated in SC mapping by uniquely defined electrical potential functions using the angle preservation feature of conformal maps. Based on these points, SC mapping is first implemented on the case study similar to HM1 and HM2.

4.1.1 Application to the case study

Prior to the modeling of the PM-biased salient machine, SC mapping is first implemented on the reduced-order case study in Fig. 4.3. Using the SC toolbox, the OFD of the case study with salient airgap is plotted in Fig. 4.4a. For a closer analysis, a geometric grid is created just below the stator tooth (Fig. 4.3b). For two different rotor positions $\Delta_x = 20[mm]$ (unaligned) and $\Delta_x = 0[mm]$ (aligned), the magnetic potential distribution in xy coordinates of the grid is plotted in Fig. 4.4b and 4.5d. Zooming in, i.e. Fig. 4.5b, indicates that OFD can only be calculated in the crossover region due to the numerical complexity. Based on this analysis, the coil flux linkage, λ, is calculated as a function of Δ_x by the difference between two potential points located at the stator tooth contour (TC), i.e. active TC (introduced in Chapter 3.1.1) in Fig. 4.3b. Although there is, in general, a good agreement in Fig. 4.6b, SC values have a discrepancy where the OFD lines are not in parallel, i.e. when the rotor and stator teeth are unaligned. In OFD, magnetic potential changes linearly on the activated tooth border, having

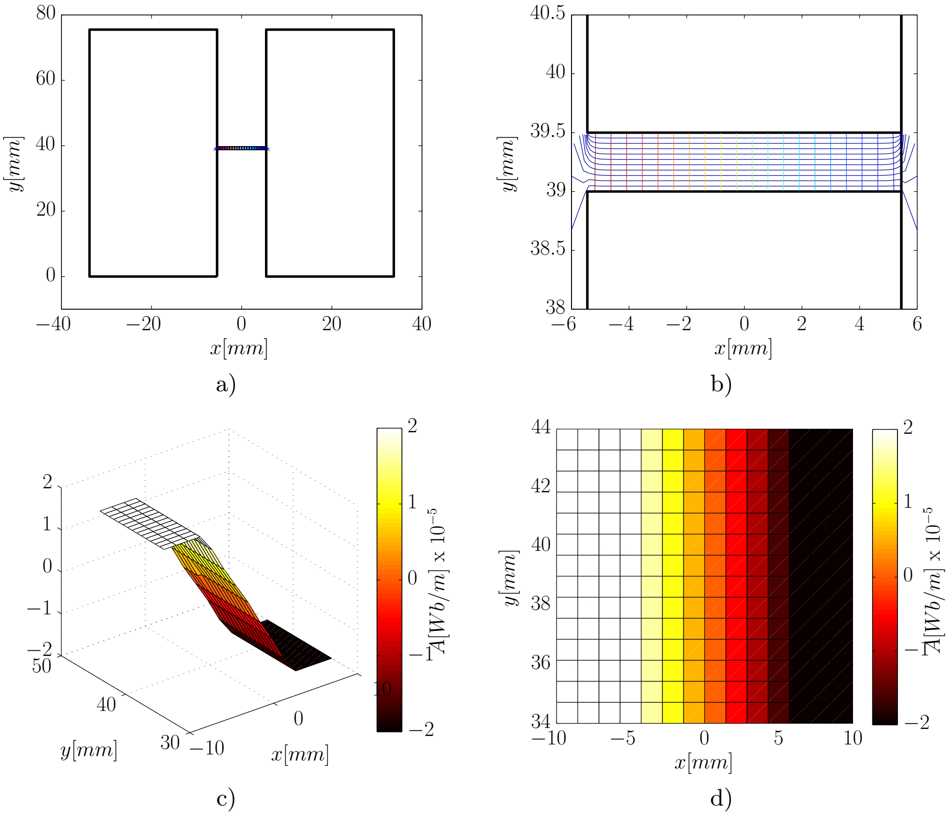

a) b)

c) d)

Figure 4.5: Case study at $\Delta_x = 0[mm]$: a-b) Orthogonal field diagrams (OFD), c) magnetic potential calculation in the given grid, and d) xy-axes view of c).

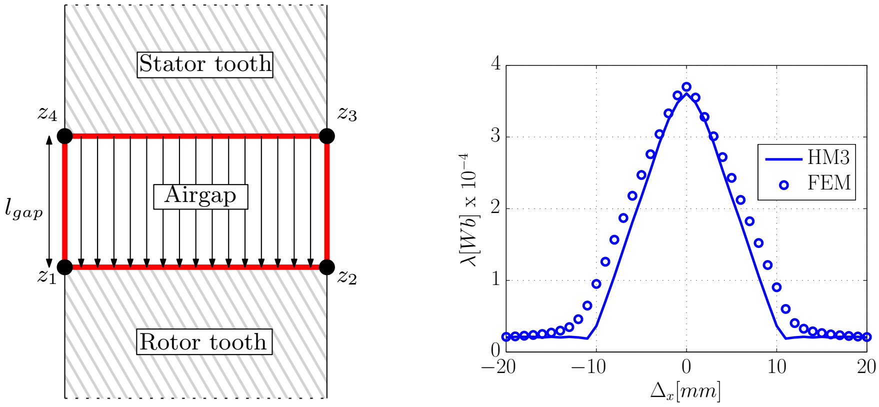

a) b)

Figure 4.6: a) Rectangular flux tube between stator and rotor teeth in z-domain and b) calculation of coil flux linkage, λ, with HM3 and finite element method.

its maximum value at the nearest point to the airgap, where the electromagnetic energy conversion takes place. However in FEM, magnetic potential is assumed to be constant along the source-tooth border (TC) line. This difference and the changing boundary conditions are the dominating reasons for the discrepancy observed in Fig. 4.6b.

4.2 Integration of tooth contour method and Schwarz-Christoffel mapping

The integration of the Schwarz-Christoffel mapping to the tooth contour method is realized fully in the MATLAB environment. With a comparable construction to HM2, discussed in Chapter 3.3, the integration commences over $\mathcal{P}_{gap}$, which is calculated in the mapped region defined by a numerically determined SC mapping function. In TCM, the permeances between relevant TCs need to be calculated as a function of rotor position. The permeance paths (flux paths) in the original domain are not straightforward to approximate. Since a rectangle is the basic 2D shape of a flux path as illustrated in Fig. 4.6a, *crrectmap* mapping function is used to obtain the rectangle polygon in z-domain. This function gives the freedom to choose any four vertices, which are corner points of the rectangle in z-domain. In this general representation, the airgap flux is assumed to flow from the surface $z_1 - z_2$ to the surface $z_3 - z_4$. To calculate the permeance of this flux tube, the geometrical choice of the vertices has to satisfy that $z_1 - z_2$ has a Dirichlet and $z_3 - z_4$ a homogeneous Neumann boundary condition [105]. The

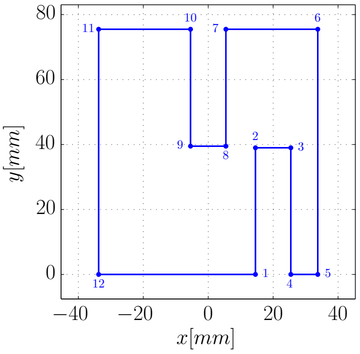

Figure 4.7: Vertices of the case study for the Schwarz-Christoffel mapping.

resulting permeance is calculated by:

$$\mathcal{P}_{gap} = \int\limits_{l_{gap}} \frac{\mu_0 S_{gap}(l_{gap})}{dl_{gap}} = \frac{\mu_0(|z_1 - z_2|)L_a}{|z_1 - z_4|}, \tag{4.2}$$

where S_{gap} is the cross section of the considered flux tube, and l_{gap} the length of the tube. The complex coordinates $z_1 - z_4$ of the rectangle are used to calculate S_{gap} and l_{gap} in (4.2). This process is next applied to the case study.

A total of twelve vertices are identified for the case study as shown in Fig. 4.7. The four vertices, i.e. z_1-z_4, required for the mapping illustrate the begin- and end-points of the two TCs, which are considered for the permeance calculation in TCM. In this structure, the first TC is chosen as the whole stator tooth between vertices 7 and 10, and the second TC can be any one of the three rotor TCs, i.e. vertices 1 to 2, 2 to 3 or 3 to 4. For example, if the stator TC and the upper rotor TC (TC_2 in Chapter 3) facing the airgap horizontally are chosen, then vertices 2, 3, 7, and 10 have to be inserted into *crrectmap* in a counterclockwise direction. These three parallel airgap permeances between one stator tooth surface and three rotor tooth surfaces are calculated with (4.2), and subsequently are united in a single permeance.

Verification

To verify the constructed HM3 in terms of extreme saliency, the sensitivity study conducted for HM1 and HM2 is repeated for HM3. Previous results in Fig. 3.7 show that HM2 achieves an improvement with a discrepancy of 1.4% compared to HM1 with 8.5%. The simulation time, however, increases in HM2 due to the involvement of eFEM. Under the same conditions, results in Fig. 4.8 show that HM3, i.e. TCM-SC, achieves the same accuracy as HM2 due to the similar structure of both hybrid models. The simulation time, however, with 29[s] is improved compared to HM2 by 9.3% and to FEM by 19.4% due to the replacement of eFEM by SC.

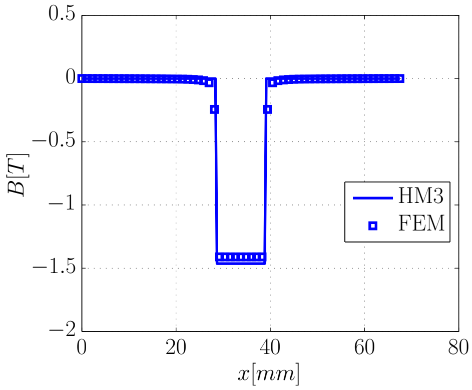

Figure 4.8: Flux density in airgap calculated by HM3 and finite element method for the parameter variations in case study at $\Delta_x = 0[mm]$.

4.3 Application of HM3 to the flux switching permanent magnet machine

Similar to the first two introduced hybrid models, HM1 and HM2, this section explores the appropriateness of HM3 to analyze PM-biased salient machines on an example 3-phase 12/10 flux switching permanent magnet (FSPM) machine as previously discussed in Chapters 2.5-3.4.

4.3.1 Schwarz-Christoffel mapping for the machine

In the composition of HM3, the stand-alone technique SC is used to estimate $\mathcal{P}_{gap}$ in the flux switching permanent magnet machine. Similar to the case study, the periodical part of the airgap is surrounded by one stator period together with one rotor tooth, as illustrated in Fig. 4.9a. Since SC mapping only applies to quadrilateral polygons, all curved boundaries need to be transformed into linear ones. The curved airgap boundary can be linearly discretized and implemented in the mapping function (4.1); however, it will considerably increase computational time. Therefore, to obtain the w-domain coordinates of each relevant (x, y) point of the airgap boundary, following pre-mapping function is used:

$$w = \ln(s) = \ln(|s|) + i \cdot \arg(s) = \ln(\sqrt{(x^2 + y^2)}) + i \cdot \arctan(\frac{y}{x}), \qquad (4.3)$$

with $s = x + iy$. Using (4.3), the airgap in s-domain is transformed into a polygon in w-domain as seen in Fig. 4.9b and with the vertices indicated in Fig. 4.9c.

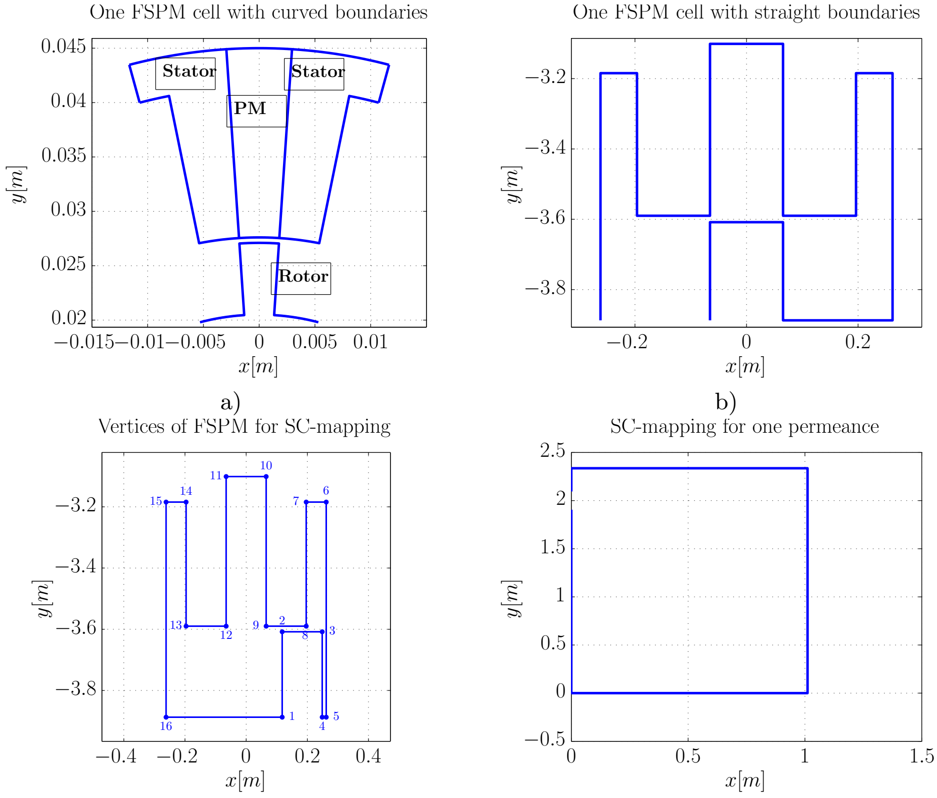

a) b)

c) d)

Figure 4.9: Sequential steps in the Schwarz-Christoffel mapping of the flux switching permanent magnet machine: a) Elementary cell in s-domain, b) airgap region in w-domain, c) vertices of b), and d) airgap region in z-domain

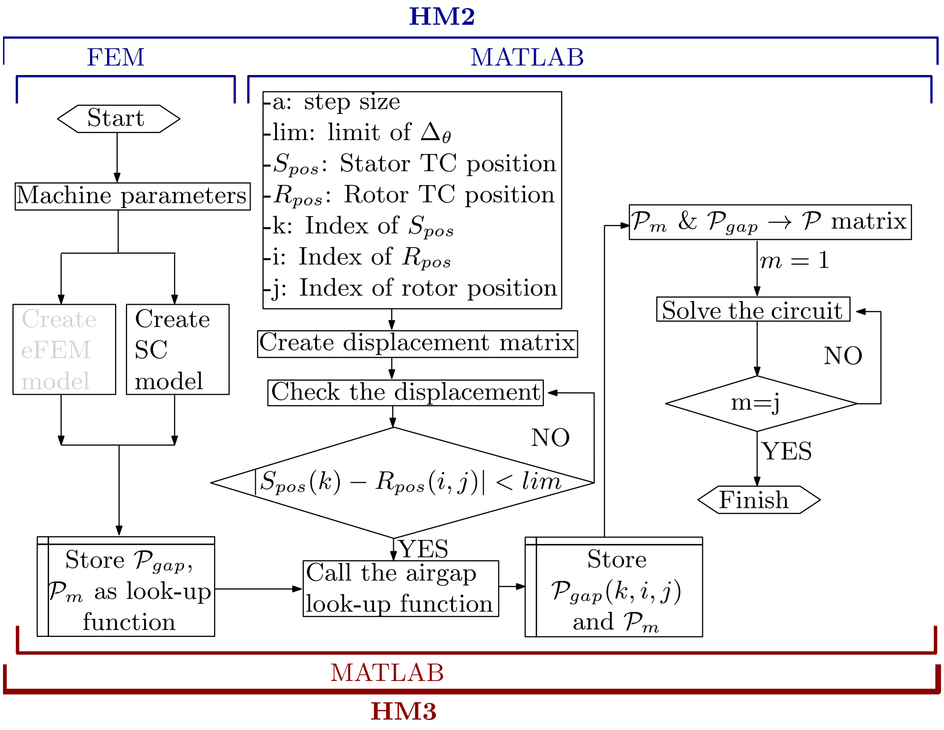

Figure 4.10: Flowchart of HM3 for the flux switching permanent magnet machine in comparison (indicated as light gray) with HM2 in Fig. 3.14.

Similar to the case study, mapping function *crrectmap* is applied to the corresponding stator vertices 11-14 as $z_1 - z_2$ and rotor vertices 1-2, 2-3 and 3-4 as $z_3 - z_4$. Hence, airgap flux paths in w-domain are projected into rectangular flux tubes in z-domain, as seen in Fig. 4.9d. Consequently, $\mathcal{P}_{gap}$ is calculated for that rotor position is calculated using (4.2).

To obtain $\mathcal{P}_{gap}\Delta_\theta$, the rotor needs to be moved for one electrical cycle. However, using the symmetry present in one elemantary cell (Fig. 4.9a), where the stator teeth are located on both sides of PM, the simulation time can be reduced by 50%. This situation corresponds mathematically to even symmetry ($f(x) = f(-x)$). Subsequently, only one stator tooth side, i.e. half electrical cycle, is required for simulations.

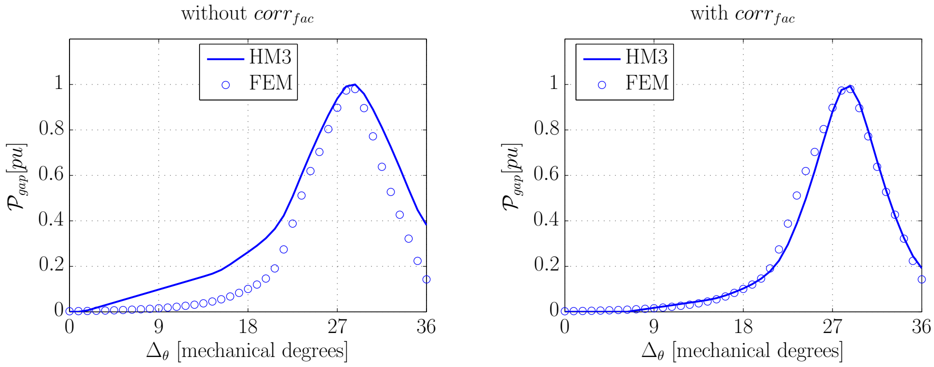

a)

b)

Figure 4.11: Calculation of airgap permeance, $\mathcal{P}_{gap}$, with HM3 and finite element method a) without and b) with correction factor $corr_{fac}$.

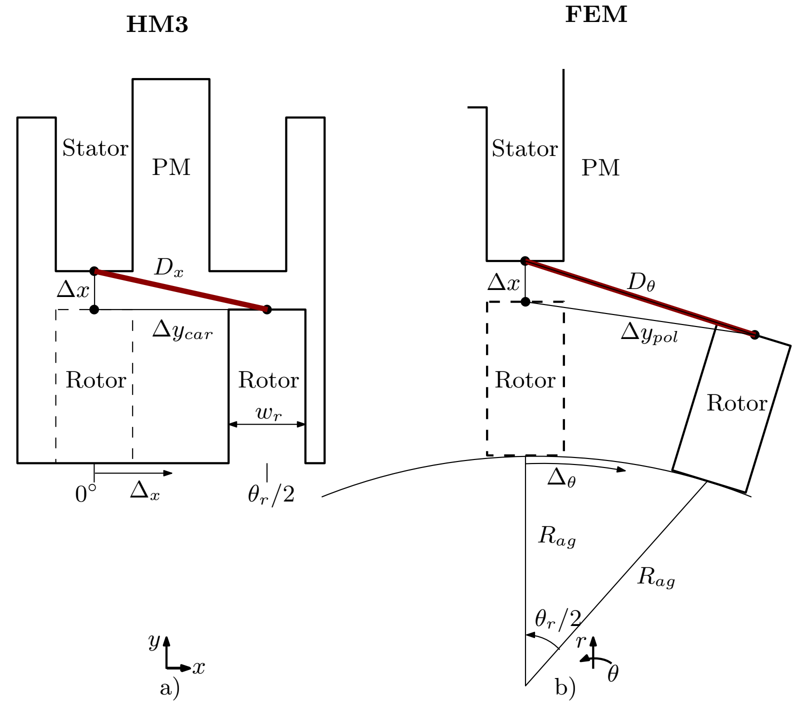

a)

b)

Figure 4.12: Flux switching permanent magnet machine geometries used in a) HM3, and b) finite element method.

4.3.2 Integration of HM3 for the machine

The integration technique of HM3, which pairs TCM-SC has a comparable structure to HM2, by replacing eFEM with SC, as illustrated in Fig. 4.10. Due to the implementation of SC, the need for an extra software platform, i.e. FEM, is eliminated for the calculation of $\mathcal{P}_{gap}$. Related results in Fig. 4.11a show a deviation between HM3 and FEM due to the difference in the relative distance between relevant stator and rotor tooth in translation and rotation, as illustrated in Fig. 4.12. Therefore, a predetermined correction factor, $corr_{fac}$, is introduced depending on rotor position as:

$$corr_{fac} = \frac{D_x}{D_\theta}, \tag{4.4}$$

where D_x indicates the distance in the SC frame and D_θ in FEM as shown in Fig. 4.12. In the SC frame, the rotor tooth width is $\theta_r = 7.5°$, thus $w_r = 0.1309[mm]$, which has no physical importance but only used to calculate the ratios. Since $corr_{fac}$ varies with the rotor position, it depends on the y-axis position in SC and on the θ-axis position in FEM. For consistency in the equations, the distance calculations for both D_x and D_θ are given in the same, i.e. Cartesian, coordinate system:

$$\begin{aligned} D_{x,\theta} &= \sqrt{(\Delta x)^2 + (\Delta y)^2}, \\ \Delta x &= g, \\ \Delta y_{car} &= \frac{w_r}{\theta_r} \cdot ([0 : \frac{\pi}{N_r}]) = \frac{|z_3 - z_4|}{\frac{2\pi}{4N_s}} \cdot ([0 : \frac{\pi}{N_r}]), \\ \Delta y_{pol} &= \frac{R_{ag}}{2} sin([0 : \frac{\pi}{2N_r}]). \end{aligned} \tag{4.5}$$

All angular displacements in (4.5) are presented in electrical degrees. Both D_x and D_θ are distances calculated for the half electrical period, which corresponds to $[0 : \frac{\pi}{N_r}] = [0° : 18°]$ in mechanical degrees. Using $corr_{fac}$, the results from SC and FEM show a very good agreement in Fig. 4.11b with a discrepancy of only 0.8%, compared to the previous results in Fig. 4.11a.

Verification

To verify the constructed HM3 of FSPM, phase flux linkage, λ_{ph}, and torque, T_C, calculations are performed based on (2.19). The discrepancies observed in Fig. 4.13 between the rms-values of respective comparisons are 1.51% for λ_{ph} and 2.9% for T_C calculations. The maximum discrepancies in the overall values is 7.3% for λ_{ph} and 5.2% for T_C. These results deviate from FEM slightly more than HM2 for FSPM modeling. The overall simulation time for HM3 is $720[s]$ compared to the $900[s]$ by FEM leading to 9% decrease in simulation time compared to HM2 and 20% decrease compared to FEM.

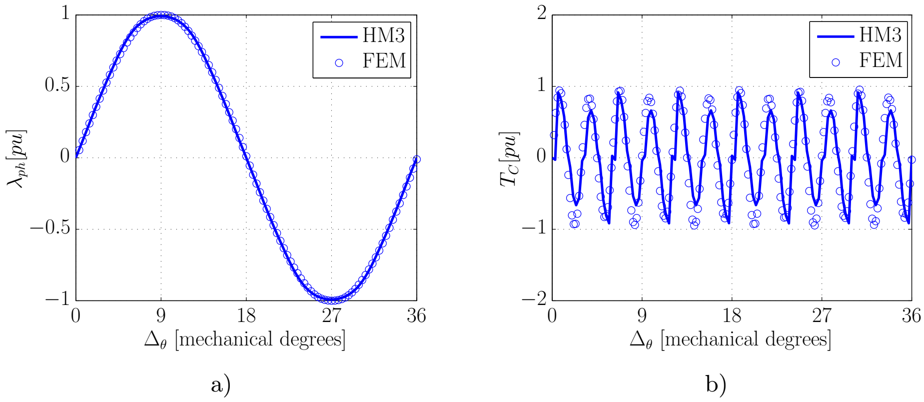

Figure 4.13: Comparison of a) phase flux linkage, and b) cogging torque calculated by HM3 and finite element method.

4.4 Summary and conclusions

In this chapter, a hybrid model, denoted HM3, has been introduced, which integrates the reluctance network model, tooth contour method (TCM), in a cascaded form with a conformal mapping method, Schwarz-Christoffel mapping, in the modeling of structures with a double salient airgap. As such, the case study previously introduced in Chapter 2 has been used for both models. Subsequently, HM3 has been applied to a 3-phase 12/10 flux switching permanent magnet machine.

HM3 offers an alternative to the use of Fourier analysis and electrostatic finite element method and their accompanying decrease in accuracy on boundaries. This method maintains accuracy by uniting the boundaries around materials with a relative permeability close to one, i.e. air, magnet, coil. Furthermore, this approach is based on mapping the original structure to an equivalent rectangular region, i.e. with only four boundaries. As such, this transformation has been realized by a conformal mapping technique SC with orthogonal field theory, replacing the electrostatic finite element method in HM2. In the presence of extreme saliency, HM2 and HM3 have provided comparable accuracy. Although results for the case study have shown that HM3, i.e. tooth contour method and Schwarz-Christoffel mapping, achieved an improvement with a discrepancy of 1.4% compared to 8.5% in HM1 due to the increased spatial discretization obtained through the tooth contour method.

The integration of TCM-SC has been performed by directly calculating the airgap permeances without the need for extra optimization, as was the case with HM1. These calculations have been realized in the mapped region, which has been acquired via a numerically approximated (MATLAB toolbox) mapping function, requiring boundaries as polygons. Therefore, a geometric correction factor has been formulated for machines with rotational displacement, i.e. flux switching permanent magnet machine. This factor can conveniently be generalized for other electrical machines with a comparable structure. For less complex airgap structures, i.e. those with negligible saliency, calculation of the mapping function could have been done analytically for an improved simulation time; however, this option is not valid for the structures studied in this thesis. The total calculation time of the solving process has been proven 20% shorter with HM3 compared to finite element method and 9% compared to HM2.

The performance results of HM3 indicate higher accuracy than HM1 in magnetic calculations for structures with increased saliency, at the cost of an increased simulation time. The achieved high level of accuracy is comparable to that of HM2, however, without the necessity for secondary software and post-processing, leading to an improved simulation time.

Chapter 5

Performance evaluation of the hybrid models

"You see but you do not observe. The distinction is clear." – Sherlock Holmes (A Scandal in Bohemia)

* * *

This chapter reviews the three hybrid modeling methods introduced through Chapters 2-4. Their performance is evaluated in terms of accuracy, simulation time, inclusion of a nonlinear BH-characteristic, end effects and design flexibility.

* * *

The contributions of this chapter are published in the following articles:

- Ilhan, E., Paulides, J. J. H. and Lomonova, E. A. [2014]. Hybrid modeling techniques for complex magnetic flux paths in airgap. *Proceedings of Intermag Conference*, Dresden, Germany.

Hybrid modeling techniques, introduced in Chapters 2-4, combine mathematical approaches with different levels of abstraction, i.e. stand-alone techniques, to solve either the first-order partial differential Maxwell equations or the second-order partial differential Poisson and Laplace equations. A global cross-comparison could help in the understanding of the individual advantages and disadvantages of each hybrid model. Therefore, the analysis presented in this chapter is aimed to construct a global picture of the proposed hybrid models and to stipulate which method is applicable or more suitable for the design and analysis of a PM-biased salient machine. The findings here are based on the combined analysis obtained both from the case study in Fig. 2.1 and on the 3-phase 12/10 flux switching permanent magnet machine (FSPM) in Fig. 1.5. The comparison of the hybrid models, HM1-3, is evaluated in terms of model accuracy, simulation time, inclusion of nonlinear BH-characteristic, end effects, and design flexibility.

5.1 Model accuracy

Accuracy is a broadly used scientific term, which indicates the proximity between two values. Part I of this thesis has been dedicated to the development of theoretical models, hence the comparison has been realized to the finite element method (FEM), due to its high level of accuracy. The model accuracy is evaluated in two parts for extreme and moderate saliency.

For extreme saliency

The sensitivity to parameters is evaluated on the case study specifically for variations leading to a high ratio of slot depth-to-airgap length, i.e. saliency. As the saliency increases, the accuracy of Fourier analysis (FA) decreases rapidly as observed in Fig. 5.1. The initial parameters given in Table 2.1 provided a moderate saliency with a discrepancy below 5% region. To investigate the effect of extreme saliency, i.e. $l_{st}/g = 360$, the initial parameters are varied to $J_{eff} = 2[A/mm^2]$ and $g = 0.1[mm]$. Using only the stand-alone technique FA for this case, the field distribution in airgap has deviated 16% from FEM. Integration of the magnetic equivalent circuit (MEC) to FA, leading to HM1, has resulted an improved accuracy by 8.5% and has damped the oscillations. With advancing MEC by the tooth contour method (TCM), HM2-HM3 have achieved a further improvement of 1.4%.

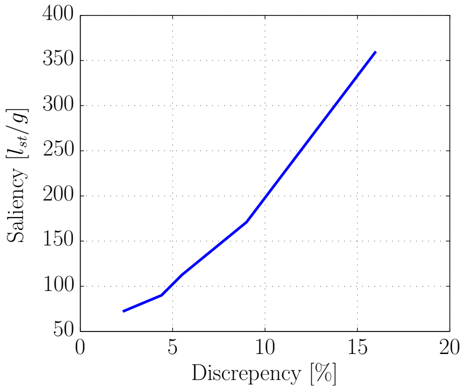

Figure 5.1: Discrepancy percentages of the Fourier analysis with increasing saliency.

For moderate saliency

Material tolerances or the magnetic design can limit the extent of saliency in a PM-biased salient machine. As such, in case of the case study with dimensions in Table 2.1, FA, thus HM1 has performed well, with a maximum of 2.3% discrepancy compared to FEM values. The discrepancy here, with a moderate slot depth-to-airgap length ratio of 72, is considerably lower compared to the case study with an extreme saliency ratio of 360, while maintaining a similar magnetic loading.

In the case with extreme saliency, the studies indicated HM1 as the least accurate model. For a PM-biased salient machine with moderate saliency, e.g. the analyzed FSPM, results have shown the opposite, i.e. HM1 with 0.62% has the lowest discrepancy followed by HM2 with 1.12%, and HM3 with 2.9%. These results are based on cogging, T_C, calculations since they show the highest sensitivity to a correct modeling of salient airgap.

The fundamental differences between the abstraction levels in HM3 affect the accuracy performance as well. In the Schwarz-Christoffel mapping (SC), thus HM3, potential changes linearly on the activated tooth border, having its maximum value at the nearest point to the airgap where the electromagnetic energy conversion took place. However in FEM, magnetic potential is assumed to be constant along the source-tooth border. The difference observed in flux linkage calculations between HM2-HM3, also for FSPM, has been a result of different TCM circuits. In both modeling techniques, the rotor tooth consisted of three TCs; however, the stator tooth has been considered as a single TC for HM3, whereas in HM2, the stator has been divided into multiple TCs. For FSPM, this situation has been observed in vertices of 11-14 as shown in Fig. 4.9c.

5.2 Simulation time

Global comparison of simulation time can be deceptive since software, hardware variations and user's knowledge of the modeling technique could increase the preparation time of the model. Thus, this particular time has been discarded in the comparative analysis of simulation time. In all analyzed methods for the case study, FEM has required the longest simulation time of 36$[s]$, due to the remeshing of the geometry with each step. HM1 has shown the shortest simulation time with 8$[s]$. HM2 has shown a shorter simulation time with 32$[s]$ compared to FEM, because its calculations only partially relied on FEM. HM3 has taken 29$[s]$ running solely in MATLAB compared to HM2, which required additional software for electrostatic finite element method (eFEM) calculations and post-processing of results as highlighted in Fig. 4.10. Similar results have been also achieved in FSPM analysis, where FEM has required the longest computational time of 900$[s]$. HM1 has shown the best performance with 198$[s]$, followed by HM3 with 720$[s]$ and HM2 with 782$[s]$. To summarize, although FEM is time optimized, both HM2 and HM3 have shown an improvement in simulation time by 13% and 20% respectively, and even HM1 up to four times.

5.3 Inclusion of a nonlinear BH-characteristic

In this thesis, all hybrid models have been implemented as linear magnetic models. If desired, each model can be extended to include the nonlinear BH-characteristic of soft magnetic material due to the incorporated reluctance network models, i.e. MEC and TCM. Similar to the approach of Carter, introduced in Chapter 1.3.1, one approach is presented in Appendix B, which focuses on finding an equivalent airgap structure in HM1 to represent the nonlinear magnetic behavior. The presented method includes only the first quadrant of BH-characteristic as illustrated in Fig. B.1. Since there is no global function to represent the airgap section, it is based on a point wise comparison of magnetic flux density. In the case of HM2 and HM3, finding of the equivalent airgap would have been accomplished by adapting the airgap permeance function. As an advantage, inclusion of nonlinearity in HM3 by widening the airgap could diminish the crowding effect discussed in Chapter 4.1. Consequently, a reduction in simulation time could be achieved up to three to four times.

5.4 End effects

The proposed hybrid modeling techniques have evaluated only 2D electromagnetic problems. All models except for HM3 could be extended to incorporate end effects by a 3D approach, which is not discussed here but increasingly researched in literature [108]. HM3 is an exception due to the difficulty to determine the mapping function of SC. In the FSPM design, discussed in Part II of the thesis, end effects are included by means of a factor in flux calculations.

5.5 Design flexibility

The analysis for sensitivity to parameter variations has shown that HM2-HM3 are capable to include a larger parameter space compared to HM1. The limitation of HM1 is due to the discrete behavior of MEC. Furthermore, the integration technique of HM3 provides a full reconciliation of the sub-models in the same platform, resulting in a higher flexibility compared to HM2 for the design phase. In HM1, the sub-models are running *independently*, therefore this model poses more limitations and a higher number assumptions to be satisfied.

5.6 Summary

In this chapter, a comparative analysis has been presented for the three hybrid modeling techniques in terms of accuracy, simulation time, inclusion of a nonlinear BH-characteristic, end effects and design flexibility. The results presented here can be generalized for the modeling of devices with a comparable structure and physical qualities as PM-biased salient machines. Design aspects of these machines are discussed in Part II of the thesis.

Part II

Flux switching permanent magnet machines

Chapter 6

Design considerations

For everything, there is a first time. – Spock (the Wrath of Khan)

* * *

To research the underlying fundamental principles and for the practical corroboration of the models presented in Part I, Part II of this thesis focuses on researching a design routine for a specific PM-biased machine structure, i.e. flux switching PM machine (FSPM) meant for high-acceleration applications.

This first chapter of Part II concerns a design analogy to compare the acceleration performance of FSPMs. Therefore, parallels are drawn between the FSPM prototype that is designed and a state-of-the-art industrial machine, i.e. a brushless PM (PMAC) motor (benchmark) with good acceleration capability. To allow for a comparative analysis, the FSPM is designed to mostly utilize the same components as the benchmark motor. Based on the sizes of these components, electromagnetic design equations for FSPM are derived and complemented with the most relevant mechanical and thermal considerations. As such, a generalized mechanical (mass-based) inertia formulation is presented for FSPM along with a discussion of the *virtual* (loss-based) inertia component. This virtual inertia component is mainly related to the magnetic resistance of rotor. Finally, a thermal model is created based on thermal equivalent circuits (TEC) to allow estimation of the operational limits of an FSPM specifically designed for high-acceleration applications.

* * *

The contributions of this chapter are published in the following articles:

- Ilhan, E., Paulides, J. J. H. and Lomonova, E. A. [2014]. Hybrid modeling techniques for complex magnetic flux paths in airgap. *Proceedings of Intermag Conference*, Dresden, Germany.
- Ilhan, E., Kremers, M. F. J., Motoasca, T. E., Paulides, J. J. H. and Lomonova, E. A. [2013]. Transient thermal analysis of flux switching PM machines. *Ecological Vehicles and Renewable Energies, International Conference and Exhibition on*, Monaco.

6.1 Flux switching permanent magnet machines

Flux switching machines have a relatively young research history since their first introduction in 1955 by Rauch and Johnson [47–49]. Electrical machines with both magnets and coils included in the stator and a SRM like rotor, i.e. flux switching permanent magnet (FSPM) machine, regained attention since the 1990's. This particular machine brings together the merits of switched reluctance machines (SRM) and brushless ac permanent magnet (PMAC) machines, as discussed in Chapter 1.4. The salient rotor without PMs, illustrated in Fig. 6.1a, not only provides a low noise and robust structure, however also has the potential for low inertia. This potential for low inertia combined with the PM-biased stator that can produce a high torque provides that potentially a high acceleration can be reached with FSPMs. Until this thesis, torque maximization of FSPMs has been the main research concern in literature [41, 109, 110]. However, its dynamic capabilities, i.e. suitability for high-acceleration applications, has not yet been treated or published in design perspective to the author's knowledge. This applicability of FSPM for high acceleration is assessed based on a performance comparison to a state-of-the-art industrial machine. This paralleled performance evaluation results in a dedicated design analogy as discussed in this chapter.

6.2 Design analogy

A comparison between the different machine topologies is a cumbersome task since many variables have to be considered and it is difficult to decide which variables should be kept as constants and which may vary [111, 112]. The constraints and assumptions made when comparing possibilities can indeed be biased by the machine designer [113]. Most generally, the basis for comparison is founded on constant electromagnetic airgap shear stress, being the product of electric loading and magnetic loading, and indeed the constancy of both of those factors [13]. The metric used for these comparisons is usually that of the masses of the active materials, i.e. steel, copper, and magnet material. However, in order to establish a reliable comparison, a sufficient amount of different machine designs has to be considered. In this thesis, a comparison of FSPM's performance is made on its high-acceleration capability. Since the dynamic characteristics can be best observed as a response during the application, a spindle cutter motion profile is presented. Furthermore, industrial benchmark machine used in performance comparison is introduced which exhibits good acceleration capability. Consequently, the design requirements and constraints are laid down.

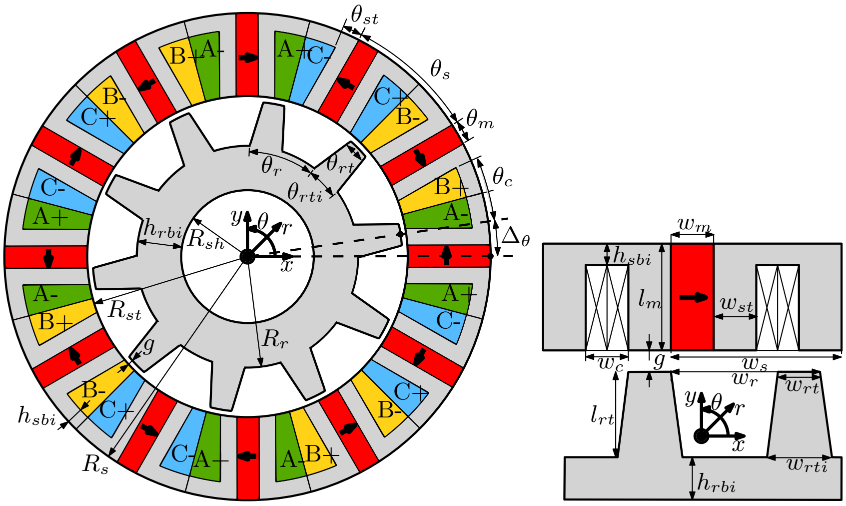

a) b)

Figure 6.1: Parameters of a 3-phase 12/10 flux switching permanent magnet machine in the a) original geometry, and b) rectangular approximation.

6.2.1 High-acceleration motors

Typically, speed and position controlled motors are used in machine tooling, spindle-drives and process control. In such systems, a dynamic operation comes forward as a requirement depending mainly on the acceleration capability of the motor. Within this thesis, the theoretical acceleration is defined as the ratio of stall torque, T_0, to motor inertia, J_M [114]. Since a design analogy is drawn between the FSPM prototype and an industrial benchmark motor, the stall torque definition is based on the continuous torque characteristic of the benchmark as shown in Fig. 6.2b [115]. In practice, however, acceleration of the motor is limited by a number of factors such as:

- Thermal effects on motor's torque capability,
- Power and current limitations of the drive,
- Controllers behavior (e.g. PI, PID constants),
- Sub-transient reactance of the motor related to fault currents,
- Incremental inductance of the motor,
- Mechanical rotor with mass-based inertia, and
- Virtual rotor with loss-based inertia.

Considering the acceleration, the current and torque limiting factors in this list can be neglected in the motor design stage, except for the last two items related to the inertia. Inertia is a broad terminology commonly used in engineering, which can be generalized as the resistance to any state changing behavior. The total J_M mainly, if not only, depends on the physical dimensions of the rotating parts, i.e. mechanical (mass-based) inertia. Additionally, an excess inertia is created due the magnetic resistance of the soft magnetic material in rotor, air friction (windage) in airgap or mechanical friction between elements, i.e. *virtual* (loss-based) inertia. In power distribution networks, this terminology relates to a way (including a suitable controller) for the stabilization of the grid frequency during sudden peaks of load request or in case of a high loss [116–118]. Similarly in this thesis, it refers to the overall loss-based inertia components, which is important for FSPM since the rotor solely consist of iron.

High-acceleration motors are specially designed to have a high torque output and low inertia. As the torque requirement grows, the acceleration capability of PMAC motors tends to drop as shown in Fig. 6.2a. A similar behavior can be observed also in dc machines as discussed in [119]. To evaluate this dynamic capability, a speed profile is introduced related to a spindle cutter requiring a high acceleration.

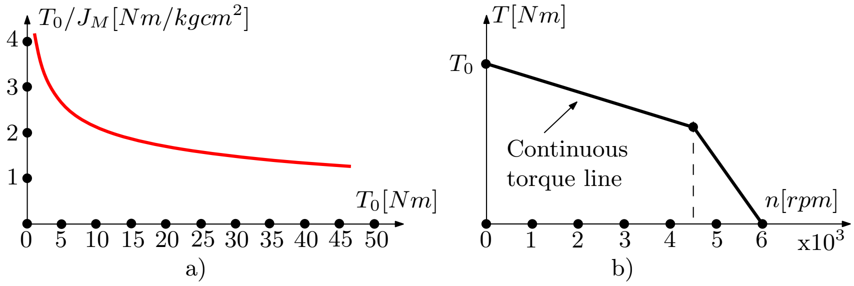

Figure 6.2: a) Torque-to-inertia (T_0/J_M) comparison of brushless ac PM (PMAC) motors [115] with respect to T_0. b) Typical torque-speed characteristic of a high-acceleration motor.

6.2.2 Spindle cutters

Today, computer numerical controlled (CNC) systems provide a high level of tracking accuracy and a fast response in various process control systems. Among such machines, better part quality and improved cycle times can be achieved by spindle-drives. Specific spindles used for milling can reach very high speeds ($>40000[rpm]$) at lower torque values with an example presented in Fig. 6.3a [120]. In this example, the cutting tool can be integrated directly to the hollow shaft of spindle motor, i.e. direct-drive solution. In another common practice, the motor is put aside of the tool and energy is transferred mechanically over a belt, pulley or gear with an example shown in Fig. 6.3b [121], i.e. indirect-drive solution. In both cases, the load inertia is *reflected* or *matched* to the motor side proportional to the gear ratio during the system design. This is important in terms of system stability; for example, for a high resonance frequency of the system, motor and load inertia are desired to be low as possible. For applications, where the drive requires a higher torque, the spindle speed is reduced for the same power range, because at the same speed with a higher torque, the bearing size has to be increased. This option is undesired due to the increased amount of losses. A widely implemented spindle application is material cutting, where torque requirement increases proportionally with the hardness of the material. For lighter materials, such as wood and aluminium, less torque is required, thus high speed spindles are more suitable for them, whereas harder materials such as stainless steal require a lower speed. Additionally, the depth of the cut in the material determines the power range of the required spindle. For this thesis, a periodical trapezoid motion profile in Fig. 6.4 is chosen to be implemented for power applications of $2-3[kW]$. In this spindle rotation profile, the machine has to reach a minimum speed of $2100[rpm]$ before cutting starts [122]. According to the requirements of the spindle cutter, a benchmark motor is selected for the paralleled performance evaluation with FSPM.

6.2.3 Benchmark motor

A state-of-the-art industrial benchmark machine with good acceleration capability is selected for the comparative performance evaluation of FSPM. In the considered power and speed range of spindle cutters, available commercial low-voltage brushless PMAC motors of $400[V]$ vary in the range of $2000-6000[rpm]$ with torques up to $10[Nm]$ [114,115,123]. Based on the motion profile in Fig. 6.4, the benchmark motor is selected, i.e. the CMP71L series with a maximum speed of $4500[rpm]$ manufactured by the SEW motor company [115]. The characteristics of this motor are identifying design requirements and constraints of FSPM.

6.2.4 Design requirements and constraints

The typical torque-speed characteristic of high-acceleration motors, e.g. benchmark, in Fig. 6.2b shows that at lower speeds, the motor naturally can provide higher torques due to the less losses. As such, at the stall torque, T_0, range copper losses, P_{Cu}, are the dominant losses, whereas iron losses, P_{Fe}, and eddy current induced PM losses, $P_{e,PM}$, are the primary reason for the derating in torque production. Such characteristics are based on the continuous motor operation limited by the thermal considerations. Although they alone cannot be sufficient to assess the dynamic motor performance, depending on them, preliminary design requirements can be drawn as the maximization of its acceleration, T_0/J_M, stall torque, T_0, overloading capability, T_{max}/T_0, and a smooth torque profile with a maximum

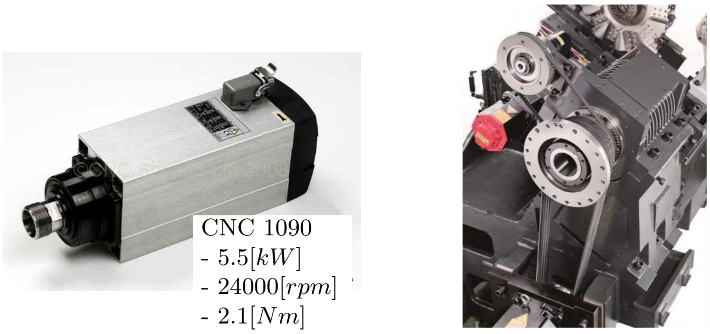

a) b)

Figure 6.3: Industrial motor for a) direct-drive spindle [120], and b) indirect-drive with belt transmission [121].

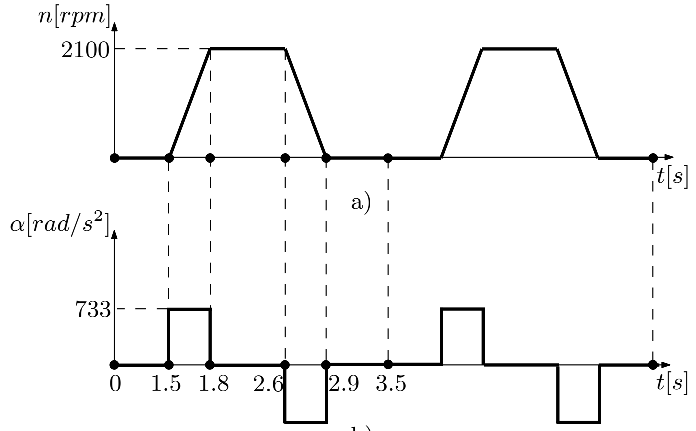

b)

Figure 6.4: A spindle-drive a) speed, and b) acceleration profiles.

ripple of $1 - 1.5\%$ [123]. In this context, the stall torque is treated as the average electromagnetic torque $T_{em} = T_0$ at lower speeds up to $200[rpm]$ [114].

The paralleled performance evaluation restricts the design space of FSPM to similar design constraints as the benchmark. Most high-acceleration applications require a balance of restrictions in volumetric space, stall torque and mechanical speed. Additionally, existing motor solutions have already installed control hardware, where any modification is usually undesirable. Consequently, design constraints, based on the benchmark, are grouped as:

- Volumetric: R_s, L_a, R_{sh},
- Electrical: m, $V_{ph,max}$,
- Mechanical: n_{max}, bearings, shaft, and
- Thermal: P_{loss}, frame.

where R_s is the stator outer radius (Fig. 6.1a), L_a the stack length, R_{sh} shaft radius, m number of phases, $V_{ph,max}$ the maximum phase voltage, n_{max} the maximum mechanical speed and P_{loss} power dissipation at natural convection. Mechanical and thermal parts, i.e. bearings, shaft and frame, used in the FSPM design are identical to the benchmark. The remaining machine parameters are determined based on the equations given in the next sections grouped as electromagnetic, mechanical and thermal. Since the hybrid modeling techniques, presented in Part I of the thesis, have been implemented both on the original FSPM geometry shown in Fig. 6.1a and on an equivalent motor geometry shown in Fig. 6.1b, the design considerations cover both structures.

6.3 Electromagnetic design considerations

In this section, basic electromagnetic design considerations reported in literature are summarized in relation to the specified design specifications and constraints.

6.3.1 Stator and rotor pole number

The first design question is to determine the stator, N_s and rotor, N_r pole numbers. Unlike the brushless PMAC machines, where N_r is determined by the number of magnets on the rotor, for FSPMs, N_s is determined by the magnet number, as discussed in Chapter 1.4.1. Due to the switching flux, rotor teeth act like rotor magnets, which determines N_r, and thus the pole pair $p = N_r$. Furthermore, [47] identifies the most important design consideration as $N_s \neq N_r$. The opposite relation ($N_s = N_r$) results in a constant flux path with less flux variation, thus a lower back-emf generation and a smaller energy conversion. The N_r teeth create saliency in the rotor required for torque production, otherwise flux linkage between stator and rotor follows a low inductance path. Another relationship between the N_s and N_r is given in [49] based on the following relations:

$$N_r = \frac{2\pi}{\theta_r}, \tag{6.1}$$

$$N_s = \frac{2\pi}{\theta_s}, \tag{6.2}$$

$$\theta_r = \frac{\theta_s}{1 \pm \frac{n}{2m}}, \tag{6.3}$$

$$\frac{N_r}{N_s} = 1 \pm \frac{n}{2m}, \tag{6.4}$$

where n is an integer number with the remaining parameters illustrated in Fig. 6.1a. In these equations, an even number N_s and N_r are required to have a resultant zero radial stress on the rotor. A simpler relationship compared to (6.4) is proposed by [124] based on the following equations:

$$N_s = mk_1, \tag{6.5}$$

$$N_r = N_s \pm k_2, \tag{6.6}$$

with k_1 and k_2 being integer numbers. Considering zero radial stress condition, the relationship in (6.6) can be brought one step further. Since N_s is an even number, either the number of phases m or k_1 has to be even, similarly for an even N_r, k_2 has to be even as well. Based on these equations, possible N_s/N_r combinations are presented in Table 6.1 for the constrained $m = 3$.

Table 6.1: Stator and rotor pole (N_s/N_r) combinations for 3-phase FSPM with balanced radial forces

3-phase						
N_s	6	12	18	24	30	36
N_r	2	2	6	4	10	6
	4	4	12	8	20	12
	8	6	24	12	40	18
	10	8	30	16	50	24
	-	10	-	20	-	30
	-	14	-	28	-	42
	-	16	-	32	-	48
	-	18	-	36	-	54
	-	20	-	40	-	60
	-	22	-	44	-	66

6.3.2 Stator and rotor diameter

The stator bore radius, R_{st}, can be defined via the split ratio, $s_r = \frac{R_{st}}{R_s}$. For the constrained R_s, it is impossible to construct the motor in a fixed volume for values with $s_r > 0.8$, whereas $s_r < 0.4$ results in nonrealistic machine geometries. To estimate the airgap length g, the following relations in [13] can be used:

$$\text{If } L_a/(2R_r) \cong 1 \text{ then } g = 0.5\%(2R_r). \tag{6.7}$$

$$\text{If } L_a/(2R_r) > 1 \text{ then } g = 1\%(2R_r). \tag{6.8}$$

6.3.3 Permanent magnets

The magnets present in FSPM are magnetized over their width, w_m, whether they are block shaped or arc shaped as considered in Fig. 2.2a. In the motor geometry, each consecutive PM has an alternating magnetization direction causing a polarity switch in the phase flux linkage as the salient rotor moves. Furthermore, the location of PMs, i.e. sandwiched on both sides by soft magnetic material, enables a flux focusing effect [125] compared to PMAC with surface mounted magnets. As with any machine with magnets, choice of PMs highly depends on the operating temperature and required torque of FSPM. It must be noted that magnetic properties of magnets are more sensitive to temperature rise than magnetic properties of laminated steel.

6.3.4 Laminations

For the considered power range, $0.35[mm]$ or $0.50[mm]$ lamination thickness is generally suitable. Depending on the level of expected losses and coercivity (BH-characteristic), the grade of the lamination should be chosen.

6.3.5 Stator and rotor tooth width

If stator tooth width, w_{st} (or θ_{st}), is varied, magnet width, w_m (or θ_m), and coil width, w_c (or θ_c), have to be adjusted simultaneously to maintain the magnetic symmetry in FSPM. As such, a smaller w_{st} creates a larger magnet and slot area, which eventually leads to an increased magnetic and electrical loading, which could bring the machine quickly into saturation [126]. The rotor tooth width, w_{rt}, can be taken equal to w_{st} or varied to minimize the torque ripple [127].

6.3.6 Stator and rotor yoke height

For the back-iron (yoke) height, it is usually recommended not to go below the tooth width [13]. Since R_s is constrained, decreasing the stator yoke height, h_{sbi}, results in an increased electrical loading. For a straight stator tooth, a deeper slot causes in average a wider slot with an increased flux leakage [126]. On the rotor side, minimization of soft magnetic material is crucial for a low mass-based motor inertia. In this process, nonsaturation of the material should be ensured depending on the flux path present in the machine hence the rotor yoke height needs to satisfy $h_{rbi} > h_{sbi}$ [127].

6.3.7 Stator and rotor tooth shape

In many FSPM designs, w_{st} is kept equal to each other at the airgap and yoke sides of the stator tooth to provide a larger coil space [40, 51, 53, 128]. As for the rotor tooth, most commonly a tapered tooth is implemented with $w_{rti} > w_{rt}$ ($\theta_{rti} > \theta_{rt}$) as shown in Fig. 6.1. To investigate the tapered shape, the rotor tooth inner ratio $k_{rti} = w_{rti}/w_{rt}$ is introduced. This ratio is typically $[1 - 2.5]$ for $w_{st} = w_{rt}$ to ensure that the rotor tooth does not saturate at the bottom part.

6.3.8 Stator winding

The concentrated stator (armature) windings in FSPM are distributed in the machine geometry occupying two phase coils per slot, i.e. double layered. For the 3-phase 12/10 FSPM, four coils are connected in series for each phase. In this section, winding distribution, winding factor, slot fill factor and end windings are evaluated mainly based on the synchronous machine approach. In fact, the working principle of FSPM has elements both from SRM and PMAC; therefore both torque production mechanisms discussed in Chapters 1.2.1-1.4.1 play a role in this machine. Therefore, the equations presented here can be subject to change depending on the operation principle and physical construction of the PM-biased salient machine.

Winding distribution

The number of slots for the 12/10 FSPM is $N_s = 12$, where the pole pair number p equals to the rotor teeth number $N_r = p = 10$, hence slots per pole per phase is:

$$q = \frac{N_s}{2mp} = \frac{12}{60} = 0.2. \tag{6.9}$$

Since q is not an integer, 12/10 FSPM is a fractional slot machine. According to [15], for brushless PMAC motors with $q < 0.5$, poly-phase concentrated stator

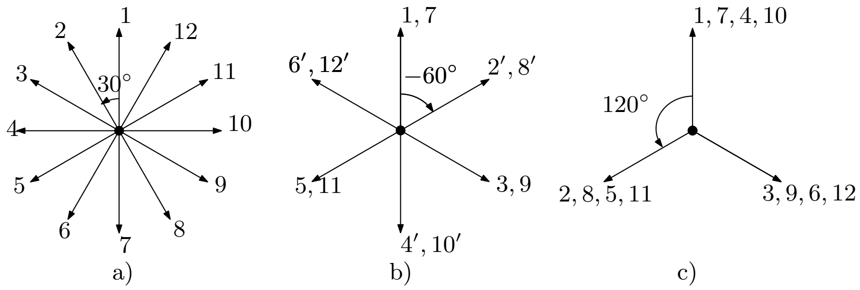

Figure 6.5: Star-of-slot of the back-emf vectors for the 12/10 flux switching permanent magnet machine in a) mechanical, and b-c) in electrical degrees.

windings are appropriate, thus, they are double layered and concentrated. Mechanical displacement between stator slots is $\theta_{ms} = \frac{360}{N_s} = 30°$, leading to the stator slot angle (electrical displacement between stator slots) $\theta_{es} = p\theta_{ms} = 300°$. Since between two phases $\theta_e = 120°$ is required and $300° = -60°$, two slots (slots 1-3) are present between consecutive phases. It should be noted that not the coils but slots are counted. Accordingly, the winding distribution is shown as in Fig. 6.5.

Winding factor

Various factors such as spatial distribution of windings, presence of slots (saliency), skewing of stator/rotor, or end effects limit the emf production in the windings. Their effect can be accounted for by coefficients, e.g. the Carter coefficient introduced in Chapter 1.3.1. Another such a coefficient is the winding factor, k_w, which depends on the distribution factor, k_d, pitch factor, k_p, and skew factor, k_s, as:

$$k_w = k_d k_p k_s. \tag{6.10}$$

For the 12/10 FSPM, the back-emf phasors are shown as in Fig. 6.5. The four coils connected in series can be shown for phase A as $1, 7, 4', 10'$. Due to the magnetization direction of PMs, $4', 10'$ have a reverse polarity, which eventually leads to superimposed coils for one phase back-emf. In (6.10), k_d counts for the effect of different coil back-emf phasors. Because the coil emf's in 12/10 FSPM are superimposed, there is no visible distribution effect, i.e. $k_d = 1$. Independent of the star of slots, the second factor in (6.10) counts for the effect that the stator slot pitch (30° mechanical) is different than the pole pitch (18° mechanical). In (6.10), k_p can be calculated by [85]:

$$k_p = sin(0.5(\xi - \pi)) = 0.86, \tag{6.11}$$

where ξ is the slot pitch angle, i.e. $\xi = 30p = 300°$ electrical. Since there is no skew considered initially, the winding factor for the 12/10 FSPM is calculated as

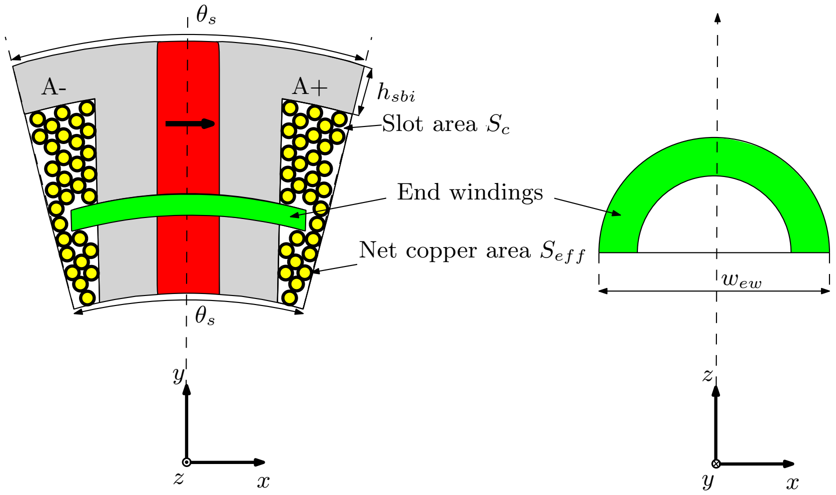

Figure 6.6: Slot area and end windings.

$k_w = 0.86$.

Slot fill factor

The slot fill factor describes the usability of the slot. In low-voltage machines, materials such as slot liner, slot key, slot separator between phases, wire insulation or potting material occupy the slot space together with copper [15]. Machines with a higher fill factor can show better thermal characteristics. In this thesis, the slot fill factor is defined as [13]:

$$k_f = \frac{\sum \text{Net copper area}}{\text{Slot area (winding space)}} = \frac{S_{eff}}{S_c}, \tag{6.12}$$

for which $k_f = 0.5$ is a typical value for brushless PMAC machines [13].

End windings

End windings of FSPM are concentrated around one PM sandwiched by stator teeth as illustrated in Fig. 6.6. Its length, L_{end}, are approximated as semi-circles in z-direction on both sides with a diameter:

$$L_{end} = w_{ew} = 2\pi(R_s - h_{sbi})/N_s. \tag{6.13}$$

6.3.9 Number of turns

Due to the interdependence of machine parameters, number of turns per phase, N_{ph}, can be determined by a design program, by an iterative process or even by trial-and-error [13]. In this thesis, N_{ph} is calculated, though not optimized, in an iterative approach depending on the constrained $V_{ph} = 230[V]$ and $n_{max} = 4500[rpm]$. The phase voltage in time domain, $v_{ph}(t)$, has the following expression:

$$v_{ph}(t) = i_{ph}(t)R_{ph} + \frac{\lambda_{ph}(t)}{dt} + L_{ph}\frac{di_{ph}(t)}{dt}, \tag{6.14}$$

where $i_{ph}(t)$ is the phase current in time domain, R_{ph} the phase resistance, λ_{ph} the phase flux linkage, and L_{ph} the phase inductance. If L_{ph} is neglected, (6.14) can be rewritten with the effective phase current, I_{ph}, as:

$$V_{ph} = I_{ph}R_{ph} + E_{ph}, \tag{6.15}$$

where E_{ph} is the phase back-emf. In this equation, R_{ph} can be estimated as:

$$R_{ph} = R_{coil}L_{coil} = R_{coil}(N_{ph}(2L_a + \pi w_{ew}) + 2\pi R_s), \tag{6.16}$$

where R_{coil} is the specific dc resistance of the coil and L_{coil} the estimated length of phase coil. Similar to other ac machines, in some FSPMs, such as designed for high speed in traction applications, the switching high airgap field and the high current density can cause significant losses due to the skin and proximity effects [129–131]. Although these phenomena are not included in the design process, that is discussed in Chapter 7, it can become significant as a major drawback of the open slots due to the spatial and time harmonics present in permanent magnet flux, which impinges on the coil [132]. A useful means of determining the likely influence of induced eddy currents in a given conductor is to compare its radius with the classical skin depth, δ, derived for the particular case on an isolated single conductor carrying a sinusoidal current [132]. For the mechanical constraint on the maximum speed, a skin depth of $\delta = 2.4[mm]$ is calculated using the formula in [13]. To estimate the length of the resistance, the following equation is employed:

$$L_{coil} = N_{ph}(2L_a + \pi w_{ew}) + 2\pi R_s), \tag{6.17}$$

where the first term in the equation corresponds the actively used coil part, the second term the end windings and the last term the connection between the four coil sides of 90° mechanical apart. The second term in (6.15) is the back-emf:

$$E_{ph} = \frac{1}{\sqrt{2}}(\Phi_{max}k_{3D})k_w w_e N_{ph} = \frac{1}{\sqrt{2}}(\Phi_{max}k_{3D})k_w(\frac{2\pi}{60}n_{max}p)N_{ph}, \tag{6.18}$$

where Φ_{max} is the amplitude of the fundamental flux harmonic linked by the phase winding for the 2D open-circuit operation. End effects may be included in the modeling phase as in [77]; however, in this thesis, they are represented by a 3D correction factor, k_{3D}, that is $0 < k_{3D} < 1$. After the arrangements, (6.15) can be simplified as $V_{ph} \approx f(n_{max}, N_{ph})$. Accordingly, conductor size can be determined based on S_{eff} as:

$$N_{ph} = \frac{S_{eff}}{\pi(0.5D_{cond})^2}, \tag{6.19}$$

where D_{cond} is the diameter for bare copper. The extra thickness, such as the insulation, backlack material or slotliner are already taken into account with k_f in S_{eff}. In general, the smaller D_{cond} lead to increased copper losses, whereas the larger D_{cond} can cause winding problems due to the increased tension in the wire. The conductor size can be also changed by parallel conductors. Following the electromagnetic design aspects, next section focuses on mechanical design considerations for FSPM.

6.4 Mechanical design considerations

According to the design requirements given in Chapter 6.2.4, lowering J_M is a mechanical design requirement. For the mechanical parts as shaft and bearing, only mass-based inertia can be defined, whereas rotor has both mass-based and loss-based inertias. Since the rotor of FSPM is not a simple cylinder, mass-based inertia equations based on geometric approximations are derived and verified with a 3D mechanical computer aided design (CAD) software.

6.4.1 Mechanical (mass-biased) inertia

To calculate the rotor inertia, first smaller sub-elements with simple geometric shapes are created, which are later on summed to determine the equivalent inertia of the total system. It consists of a hollow cylinder inertia, J_C, and N_r iron teeth inertia as illustrated in Fig. 6.7. The axis of rotation of hollow cylinder is around the z-axis (around 0), along the axial length of the machine. The general equation for J_C is:

$$J_C = \frac{1}{2} m_C (r_1^2 + r_2^2), \tag{6.20}$$

where m_C is the mass of the hollow cylinder, r_1 and r_2 are the inner and outer radius as shown in Fig. 6.8.

The inertia of one rotor tooth consists of a rectangle inertia, J_R, and two right-angled triangle inertias, J_T, as shown in Fig. 6.8. The moment of inertias for the

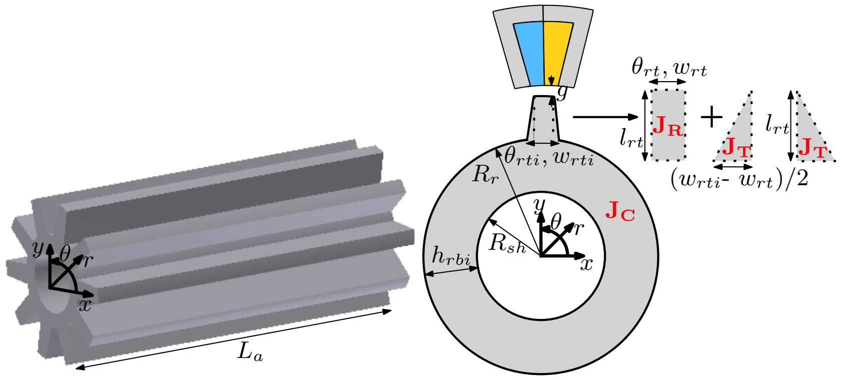

a) b)

Figure 6.7: a) Real, and b) approximated rotor.

rectangle, J'_R, and for one triangle, J'_T, around one edge (around $0'$) are:

$$J'_R = m_R \frac{(w^2+h^2)^2}{24}, \tag{6.21}$$

$$J'_T = m_T (\frac{(w^2+h^2)}{18})^2, \tag{6.22}$$

which are based on the second moment of inertia (polar moment of inertia) equations around the indicated axes in Fig. 6.8 [126].

Individual inertias can be added together only if a common rotation axis is provided. Since the axis of rotation of J'_R and J'_T is located around $0'$, it is translated from $0'$ to 0 by using parallel axis theorem:

$$J = J' + mr^2, \tag{6.23}$$

where the distance between two axis of rotations r equals to R_r as illustrated in Fig. 6.8. Taking into account the translation, the final equations for the rectangle inertia, J_R, and triangle, J_T, become:

$$J_R = J'_R + m_R r^2 = m(\frac{(w^2+h^2)^2}{24} + (\frac{h}{2} + R_r)^2), \tag{6.24}$$

$$J_T = J'_T + m_T r^2 = m(\frac{(w^2+h^2)}{18})^2 + (\frac{h}{3} + R_r)^2). \tag{6.25}$$

Based on the general equations for J_C, J_R and J_T, first the volume, V, then the mass, m and finally the inertia of each part are calculated. The inertia of the hollow cylinder, J_C, is calculated by:

$$V_C = \pi(R_r^2 - R_{sh}^2)L_a, \tag{6.26}$$

$$m_C = V_C \rho_{Fe}, \tag{6.27}$$

$$J_C = \frac{1}{2} m_C (R_{sh}^2 + R_r^2), \tag{6.28}$$

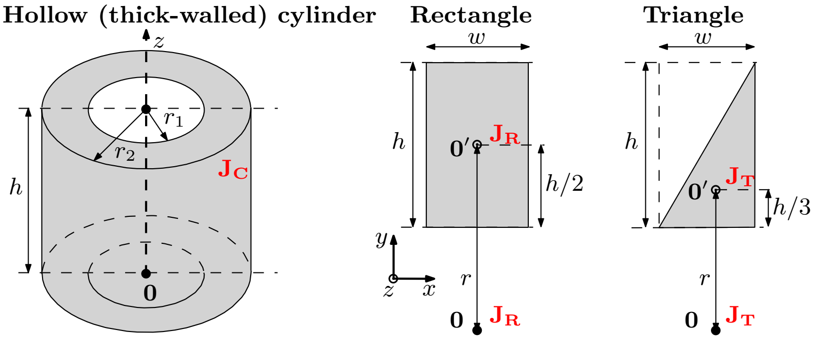

Figure 6.8: Moment of inertias of basic geometries used in rotor.

where ρ_{Fe} is the mass density of steel material. The inertia of the rectangle, J_R, is calculated by:

$$V_R = l_{rt} w_{rt} L_a = l_{rt}(\theta_{rt} R_{ag}) L_a, \tag{6.29}$$

$$m_R = V_R \rho_{Fe}, \tag{6.30}$$

$$J_R = m_R(\frac{(w_{rt}^2 + l_{rt}^2)^2}{24} + (\frac{l_{rt}}{2} + R_r)^2). \tag{6.31}$$

The inertia of the triangle, J_T, is calculated by:

$$V_T = l_{rt}(\frac{w_{rti} - w_{rt}}{2}) L_a = l_{rt}(\frac{w_{rt}}{2}(k_{rti} - 1)) L_a, \tag{6.32}$$

$$m_T = V_t \rho_{Fe}, \tag{6.33}$$

$$J_T = m_T((\frac{(\frac{w_{rti} - w_{rt}}{2})^2 + l_{rt}^2}{18})^2 + (\frac{l_{rt}}{3} + R_r)^2). \tag{6.34}$$

The shaft inertia, J_{sh}, consists of multiple solid cylinders, as shown in Fig. 6.9a. The connection between two adjacent cylinders is shown in Fig. 6.9b. Two cylinders can be added as:

$$V_{Sh_1} = \pi(R_{sh}^2) L_a, V_{Sh_2} = \pi(R_{sh_o}^2) L_{sh}, \tag{6.35}$$

$$m_{Sh_1} = V_{Sh_1} \rho_{st}, m_{Sh_2} = V_{Sh_2} \rho_{st}, \tag{6.36}$$

$$J_{Sh_{1-2}} = \frac{1}{2} m_{sh_1}(R_{sh}^2) + \frac{1}{2} m_{sh_2}(R_{sh_o}^2), \tag{6.37}$$

where ρ_{st} is the mass density of stainless steel and R_{sh_o} is the outer shaft radius elongated from the frame with a length of L_{sh}. The total shaft inertia is estimated by the summation of all cylinders.

The bearing inertia, J_B, consists of the rotating parts of two deep groove ball bearings as shown in Fig. 6.10. These are suitable for highly dynamic loads and overloading situations commonly observed in dynamic systems.

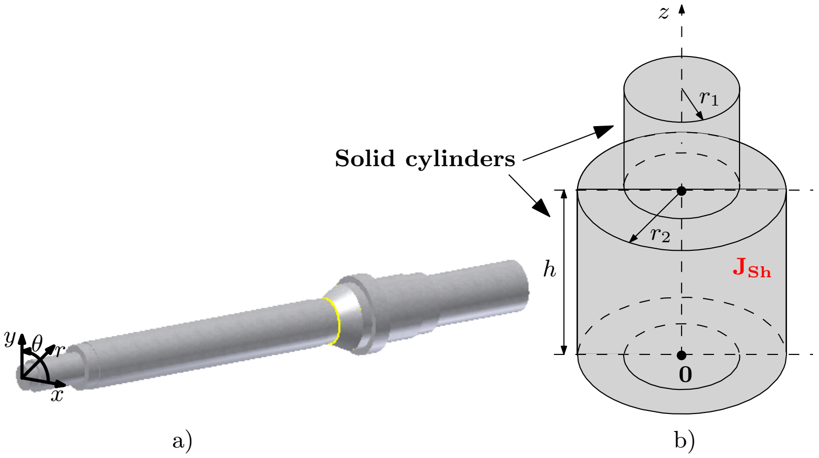

Figure 6.9: a) Real, and b) approximated shaft.

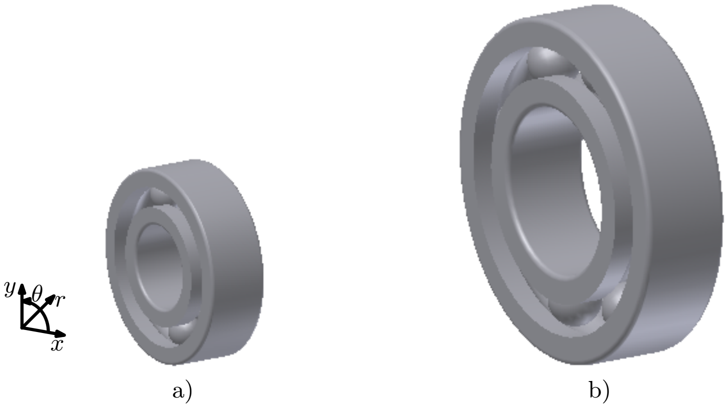

Figure 6.10: a) SKF 6202 single row deep groove ball bearing, and b) NSK 6206Z deep groove ball bearing.

6.4.2 Virtual (loss-based) inertia

As introduced earlier in Chapter 6.2.1, virtual inertia is affected by the dynamic behavior of the motor. The effect of loss-based inertia components are referred to the virtual inertia. These losses comprise iron losses due to the magnetic resistance of rotor, mechanical losses due to the air friction (windage) in airgap and due to friction between elements. These all contribute as an excess inertia term, J_{Fe}, thus should be added to the general inertia equation.

6.4.3 Motor inertia

Summation of all inertia components lead to the total motor inertia:

$$J_M = J_C + N_r(J_R + 2J_T) + J_{Sh} + J_B + J_{Fe}. \tag{6.38}$$

Since the shaft and bearings are fixed mechanical components, they are not treated in next chapter as design parameters. Furthermore, the effect of J_{Fe} is omitted since the system dynamics are not accounted for in this stage, but later in Chapter 8. Following the electromagnetic and mechanical design choices, next section focuses on the thermal design considerations for FSPM.

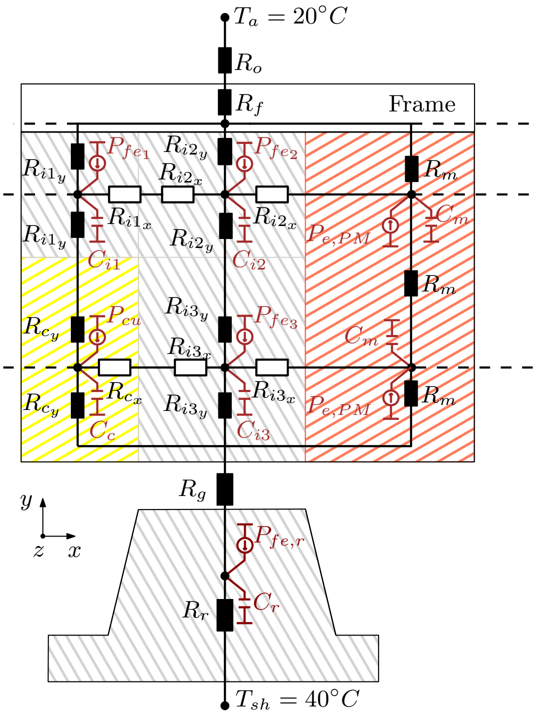

Figure 6.11: Thermal equivalent circuit of the flux switching machine.

Table 6.2: Parameters of the thermal equivalent circuit

Region Name	**Parameter**	**Heat Transfer**	**Losses**
Stator back-iron	R_{i1_x}, R_{i1_y} R_{i2_x}, R_{i2_y}	Conduction	P_{Fe_1} P_{Fe_2}
Stator tooth	R_{i3_x}, R_{i3_y}	Conduction	P_{Fe_3}
PM	R_m	Conduction	$P_{e,PM}$
Coil	R_{c_x}, R_{c_y}	Conduction	P_{Cu}
Frame	R_f	Conduction	–
Outer convection	R_o	Convection	–
Rotor	R_r	Conduction	$P_{Fe,r}$
Airgap	R_g	Convection	–

6.5 Thermal model

Thermal modeling plays an important role in the design process of an electrical machine to set the operational limits and the choice of insulation class [133, 134]. Analytical and numerical methods can be used to model the steady state and transient heat flow in the machine. Although advanced numerical models make use of equations in fluid dynamics and thermodynamics, for electrical machine analysis, a more practical method is, i.e. thermal equivalent circuits (TEC) [135–138]. Based on the analogy between thermal and electrical circuits, TEC of FSPM is given in Fig. 6.11 with the parameters in Table 6.2 and the following assumptions [15, 132, 139]:

- The heat flow in the axial direction is omitted and only radial direction is considered in the cross section of the motor (xy-plane) due to the low heat conductivity in the axial direction (lamination),
- The rotary machine geometry is analyzed mainly in rectangular shapes,
- All materials are assumed to be isotropic; therefore, the heat distribution is assumed to be homogeneous in the cross section,
- No contact resistances are used in TEC model, because the contact surfaces are assumed to be perfectly smooth,
- Only the heat convection and conduction are considered, radiation is omitted due to its negligible effect.

In steady state analysis, TEC model is solved for the average power losses:

$$\mathbf{T} = \mathbf{G}^{-1}\mathbf{P}, \tag{6.39}$$

where **T** represents the nodal temperature matrix, **G** the inverse of conductive and convective thermal resistances and **P** the power losses in the machine consisting of P_{Cu}, P_{Fe} and $P_{e,PM}$. The solving procedure of TEC and loss calculations are explained in Appendix D. To represent the temperature variation in FSPM, thermal capacitances, **C**, are added at each node with a heat source (power loss) as shown in Fig. 6.11:

$$\mathbf{P} = \mathbf{C}\frac{d\mathbf{T}}{dt} + \mathbf{GT}, \tag{6.40}$$

$$\frac{d\mathbf{T}}{dt} = \mathbf{C^{-1}P} - \mathbf{C^{-1}GT}. \tag{6.41}$$

Due to the negligible heat storage capability of air, this region does not need to be represented in TEC, i.e. no capacitance is added in the airgap region. In (6.41), first order differential equations have are solved to get the time domain responses. This can be numerically done by matrix iterations. In such case, the time step, dt, for each iteration has to be chosen carefully for the results to converge a constant value. To avoid this problem, using Laplace transformation, all circuit elements are transformed to frequency domain **s**, i.e. the differential equations are represented by polynomial functions:

$$\mathbf{T}(\mathbf{s}) = \mathbf{G}(\mathbf{s})^{\mathbf{-1}}\mathbf{P}(\mathbf{s}). \tag{6.42}$$

The thermal capacitances are added to the matrix $\mathbf{G}(\mathbf{s})$. After the circuit calculations, the nodal temperatures of $\mathbf{T}(\mathbf{s})$ are transformed back to the time domain as $\mathbf{T}(\mathbf{t})$ with inverse Laplace transformation. The process is summarized in Appendix D, whereas the resistive elements of TEC are given in the next parts.

6.5.1 Conductive resistances

The rotary FSPM under study consists of curved core (both stator and rotor iron), curved coil slot, rectangular PMs and a rectangular frame. The curved iron geometry can be analyzed in rectangular shapes making use of geometric modifications, similar to the ones introduced in Chapter 2.5.1. This way, the losses can be considered the same in both geometries. The resulting TEC model of FSPM consists of T-shaped smaller circuit parts mainly consisting of resistive elements. To obtain the T-equivalent circuits, each material is first divided into rectangles as illustrated in Fig. 6.11. The smaller regions are divided into two equal thermal resistances. To include the losses, a current source is added in the middle node. Since a homogeneous heat distribution is assumed in the material, the middle node gives the average temperature in the material. For each part of TEC, the equations for conductive resistances are derived next.

The stator iron is divided into three regions as shown in Fig. 6.11 with thermal conductivity constants in Table 6.3. The thermal conduction resistances for iron in xy-directions are calculated as:

$$R_{i1_x} = \frac{(w_c/2)}{\lambda_{Fe} h_{sbi} L_a}, R_{i1_y} = \frac{0.5 h_{sbi}}{\lambda_{Fe}(w_c/2) L_a}, \tag{6.43}$$

$$R_{i2_x} = \frac{0.5 l_{st_x}}{\lambda_{Fe} h_{sbi} L_a}, R_{i2_y} = \frac{0.5 h_{sbi}}{\lambda_{Fe} l_{st_x} L_a}, \tag{6.44}$$

$$R_{i3_x} = \frac{0.5 w_{st}}{\lambda_{Fe}(l_m - h_{sbi}) L_a}, R_{i3_y} = \frac{0.5(l_m - h_{sbi})}{\lambda_{Fe} w_{st} L_a}. \tag{6.45}$$

In FSPM, each PM is sandwiched by stator iron teeth in y-direction. Since the thermal conductivity of iron is on average three times higher than PM, the main heat flow is in the y-direction. To see the temperature distribution inside PM, it is divided into two regions, one located near the airgap (lower PM) and one located near the frame (upper PM). The thermal conduction resistance for PM in y-direction is calculated as:

$$R_m = \frac{l_m}{3\lambda_{PM} w_m L_a}. \tag{6.46}$$

For the aluminium frame with the thickness l_f, the conduction resistance is defined as:

$$R_f = \frac{l_f}{\lambda_{Al}(2((w_c/2) + w_{st}) + w_m) L_a}. \tag{6.47}$$

The winding slot does not consist of a homogeneous material, but of copper and insulation. To represent the whole slot region with one thermal resistance, a simplification is done by using an equivalent thermal conductivity. The simplified thermal resistances for the slot region are calculated as:

$$R_{cx} = \frac{(w_c/2)}{\lambda_{Cu,eq}(l_m - h_{sbi}) L_a}, R_{cy} = \frac{0.5(l_m - h_{sbi})}{\lambda_{Cu,eq}(w_c/2) L_a}, \tag{6.48}$$

where $\lambda_{Cu,eq}$ is the equivalent thermal conductivity of the slot region. The modeling of the slot region and estimation of $\lambda_{Cu,eq}$ are explained in Appendix D, which is valid for the speed range of the benchmark motor, i.e. up to $4500[rpm]$. Its value in Table 6.3 is determined based on an assumed fill factor of $k_f = 0.5$ and a potting material with a thermal conductivity of $\lambda_r = 0.2[Wm^{-1}\ {}^\circ C^{-1}]$, which are adapted to the final prototype accordingly in Chapter 8.

The salient rotor is transformed to a (nonsalient) hollow cylinder based on [140]. The thermal conductivity and specific heat capacities stay constant, the mass density is changed accordingly by keeping the mass equal to the original value. The thermal resistance for the rotor is defined as:

$$R_r = \frac{N_s}{4\pi\lambda_{Fe} L_a}\left(2ln\left(\frac{R_{ag}}{R_{sh}}\right)\right), \tag{6.49}$$

where N_s is the stator pole number, R_{ag} the radius in mid-airgap and R_{sh} the shaft radius. For the thermal model, only $1/N_s$ of the total machine is considered.

Table 6.3: Thermal constants

Region Name	**Symbol**	**Thermal Conductivity** $[Wm^{-1}\,{}^{\circ}C^{-1}]$
Permanent Magnet (PM)	λ_{PM}	9
M270-35A (radial direction)	λ_{Fe}	28
Slot (Copper and insulation)	$\lambda_{Cu,eq}$	0.68*
Frame (Al.)	λ_{Al}	235
		Thermal Convection Coef. $[Wm^{-2}\,{}^{\circ}C^{-1}]$
Motor outer surface	h_o	5

*This value is updated for the final prototype.

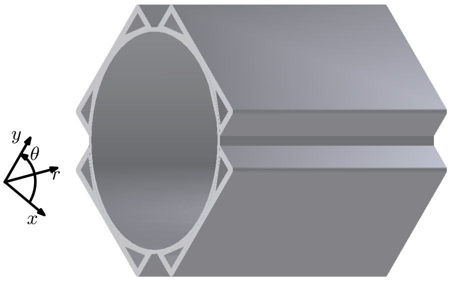

Figure 6.12: Benchmark motor frame.

6.5.2 Convective resistances

The heat transfer between the motor outer surface (frame) and the environment is done by natural convection, which is modeled by a thermal resistance. If the frame is cylindrical, the convection resistance is calculated by:

$$R_o = \frac{N_s}{h_o 2\pi (R_s + l_f) L_a}, \tag{6.50}$$

where h_o is the outer convection coefficient, R_s the stator outer radius and N_s the stator pole number. The value of h_o is empirically obtained in laboratory conditions for natural convection. For most high-acceleration motors in low-voltage range, i.e. the benchmark, the frame is rectangular, which can employ air ducts as seen in Fig. 6.12. If no forced air cooling is used via the air ducts, (6.50) becomes:

$$R_o = \frac{N_s}{h_o C L_a}, \tag{6.51}$$

where C is the circumference of the rectangular frame, which is used for the FSPM prototype. The calculation of airgap convective resistance R_g is explained in detail in Appendix D.

6.6 Summary and conclusions

The applicability assessment of machine classes by any means is a cumbersome and subjective task. Within this thesis, a comparison based on acceleration performance has been chosen. Therefore, a flux switching permanent magnet machine is contrasted with a state-of-the-art industrial machine, i.e. a brushless ac PM motor with good acceleration capability. This parallel performance evaluation has restricted the design space to similar volumetric (stator volume), electrical (maximum phase voltage, phase number), mechanical (maximum speed, bearings, shaft), and thermal (frame, power dissipation) design constraints. Based on these constraints, electromagnetic design considerations for flux switching permanent magnet machines have been derived and extended to include the most relevant mechanical and thermal aspects. Furthermore, the design requirements of a high-acceleration motor have been identified as minimizing mechanical (mass-based) inertia, maximizing stall torque, maximizing the overloading capability, and obtaining a smooth torque profile with a maximum torque ripple of $1 - 1.5\%$. For this analysis, a general mechanical inertia formulation has been presented for flux switching permanent magnet machines along with a thermal model based on thermal equivalent circuits to estimate operational limits.

The constraints identified in this chapter are based on an existing low-voltage motor solution, i.e. the benchmark. The generalized equations have been provided in such way that they can be adapted to different flux switching permanent magnet machine configurations. The discussion of the inertia indicates that the mechanical (mass-based) inertia, formulated in this section, is not the only component affecting the acceleration capability. Another important parameter has been introduced as the *virtual* (loss-based) inertia caused by the magnetic resistance of rotor due to iron losses, air friction (windage) in airgap and mechanical friction between moving, e.g. rolling, elements. Their practical implementation are shown in the following two chapters on the prototype design (Chapter 7) and its experimental verification for the performance comparison to the benchmark (Chapter 8).

Chapter 7

Prototype design

"It is a capital mistake to theorize before one has data. Insensibly one begins to twist facts to suit theories, instead of theories to suit facts." – *Sherlock Holmes (A Scandal in Bohemia)*

* * *

This chapter introduces the design aspects of an FSPM for high-acceleration applications within an established framework. The complexity of the design process is reduced by introducing certain parameter ratios representing the interdependence of several machine parameters. Due to the high number of investigated parameters, the hybrid model with the lowest simulation time, i.e. HM1 in Chapter 2, has been chosen to research the effect of machine parameters. The various resulting different motor structures are investigated in relation to multiple design requirements with the goal of achieving high acceleration, high torque output and high overloading capability. Lastly, a final candidate enabling a smooth torque profile is selected for the rotor design.

* * *

The contributions of this chapter are published in the following articles:

- Ilhan, E., Balyovski, T. L., Paulides, J. J. H., and Lomonova, E. A. [2014]. Servo flux switching PM machines. *Proceedings of the International Conference on Electric Machines*, Berlin, Germany.

7.1 Design framework

The design of any machine is an elaborated procedure. Generally, rules of thumb can estimate the motor parameters, which make it often a suggestive procedure. However, for new classes of machines, such as a flux switching permanent magnet machine (FSPM). Even this kind of suggestive procedures are not yet readily available in literature. Furthermore, most research concerns adaptations or optimization on existing FSPM structures, and only a few concentrate on design procedures [53, 128, 141, 142]. In this thesis, the design aim of FSPM prototype is to assess its relevancy in high-acceleration applications based on a performance comparison. Hence, a generalized framework for FSPM design is illustrated in Fig. 7.1. Sizing of this prototype is performed according to the design requirements and constraints as were given in Chapter 6. Due to these design constraints and material tolerances, HM1 is opted for the analysis of the initial as well as final designs. Compared to hybrid models HM2 and HM3, this method shows the best performance in terms of simulation time. Next, a magnetic parametric search is performed to determine design candidates that comprise high acceleration and high torque. Following the investigation of numerous motor structures, three design candidates are evaluated first electrically then thermally for their overloading capability. Subsequently, one candidate is optimized for a smooth torque profile. To account for the end effects, the 3D factor, k_{3D}, is included in the final prototype.

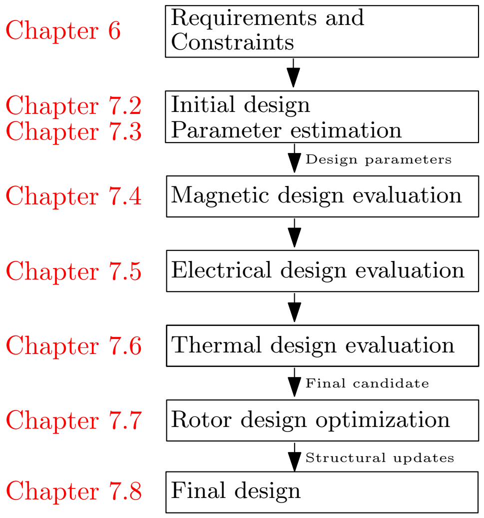

Figure 7.1: Generalized design framework of the flux switching permanent magnet machine.

Motors meant for high-acceleration applications are usually denoted by their stall torque, T_0, and maximum mechanical speed, n_{max} [114, 115, 123]. Rated torque

Table 7.1: Initial flux switching machine size and parameters

Symbol	**Description**	**Value**	**Unit**
R_s	Stator outer radius	53.35	$[mm]$
s_r	Split ratio	0.6	-
R_{st}	Stator inner radius	$R_s s_r = 32.01$	$[mm]$
g	Airgap length	0.6 ($\%1D_r$)	$[mm]$
R_r	Rotor radius	$R_{st} - g = 31.41$	$[mm]$
R_{sh}	Shaft radius	11	$[mm]$
R_{ag}	Center of airgap radius	$R_r + g/2 = 31.71$	$[mm]$
L_a	Axial length	128	$[mm]$
h_{sbi}	Stator back-iron thickness	$w_{st} = \frac{2\pi R_{ag}}{4N_s} = 4.15$	$[mm]$
θ_s	Angular stator width	$360°/N_s$	°
θ_m	Angular magnet width	$\theta_s/4$	°
θ_c	Angular coil width	$\theta_s/4$	°
θ_{st}	Angular stator tooth width	$\theta_s/4$	°
θ_r	Angular rotor width	$360°/N_r$	°
θ_{rt}	Angular rotor tooth width	θ_{st}	°
k_{rti}	Rotor tooth inner ratio	2.3	-
θ_{rti}	Angular rotor tooth inner width	$k_{rti}{}^* \ \theta_{rt}$	°
B_r	Remanent flux density of PM	1.2	$[T]$
μ_{pm}	Relative permeability of PM	1.05	-
J_{eff}	Effective current density	2.7	$[A/mm^2]$
n_{max}	Maximum speed	4500	$[rpm]$
N_{ph}	Number of turns per phase	40	-

values are commonly avoided in the motor description, since this depends on current density, J_{eff}, i.e. thermal conditions. In theory, any torque-speed value below the (thermal) continuous operation line (Fig. 6.2b) can be characterized as a rated value. Thus, for comparison in the chapter, the terminology T_{em} is referred not as rated but as continuous electromagnetic torque, and all torque values are normalized. Furthermore, during the design stage, the motor is considered to operate within a lower speed range ($< 200[rpm]$) resulting a negligible amount of speed depended losses. Consequently, the design requirements related to T_0 are represented here by the electromagnetic torque, T_{em}.

7.2 Initial design

Based on the design constraints (benchmark motor) and design equations as were given in Chapter 6, the initial FSPM dimensions in Fig. 6.1 are determined as:

- From the design constraints, axial length, L_a, is a known parameter. According to (6.8), if ($L_a/R_r > 2$), airgap length, g is 0.5% of rotor radius, R_r. Since $g << 2R_r$, R_r can be approximated by stator inner radius, R_{st}.

- For PMs, a sintered Neodymium-Iron-Boron N40SH is used with a minimum remanence of $B_r = 1.2[T]$ and a relative permeability of $\mu_r = 1.05$. The adhesive material used in the construction of the prototype to glue these magnets goes rapidly down in its strength for temperatures above $135[°C]$, i.e. setting the maximum allowable temperature in the motor.

- For stator and rotor lamination, M270-35A is chosen, which starts to saturate at approximately $B_{t_{max}} = 1.6[T]$, i.e. indicated as the maximum allowable flux density in either stator and rotor teeth.

- Stator tooth width, w_{st}, is kept equal to the slot width, w_c, magnet width w_m, rotor tooth width, w_{rt}, and stator back-iron, h_{sbi}, as shown in Fig. 6.1. Based on the constraint R_{sh}, the rotor back-iron is determined as $h_{rbi} = 3h_{sbi}$.

- Rotor tooth inner ratio, $k_{rti} = \frac{\theta_{rti}}{\theta_{rt}}(= \frac{w_{rti}}{w_{rt}})$, and split ratio, $s_r = \frac{R_{st}}{R_s}$, are important design parameters. For $k_{rti} > 2.3$, s_r can be varied only in a limited interval, therefore $k_{rti} = 2.3$ is chosen for the initial design. According to [53], $s_r = 0.6$ is an optimum with the highest torque output, based on this value R_{st} is determined.

- For concentrated windings in Fig. 6.1a, the number of turns per phase is calculated as $N_{ph} = 40$ for the given voltage and speed constraints. The slot fill factor is estimated as $k_f = 0.5$ [126].

The determined values for the initial prototype design are clearly summarized in Table 7.1. Using these machine dimensions, the initial FSPM is analyzed with HM1, which was introduced in Chapter 2 for linear magnetic analysis and extended in Appendix B for nonlinear analysis. The flux density in the airgap is calculated by HM1 is verified using FEM in Fig. 7.2a, whereas the resulting electromagnetic torque is verified in Fig. 7.2b. The results are in good agreement to estimate the design parameters in the forthcoming analysis. Hereby are the torque and inertia values normalized based on the initial design.

7.3 Design parameter estimation

In this section, key design parameters are investigated in accordance with the design requirements given in Chapter 6, i.e. related to acceleration, torque and overloading capability. The requirement related to a smooth torque profile is discussed on the final design in Chapter 7.7.

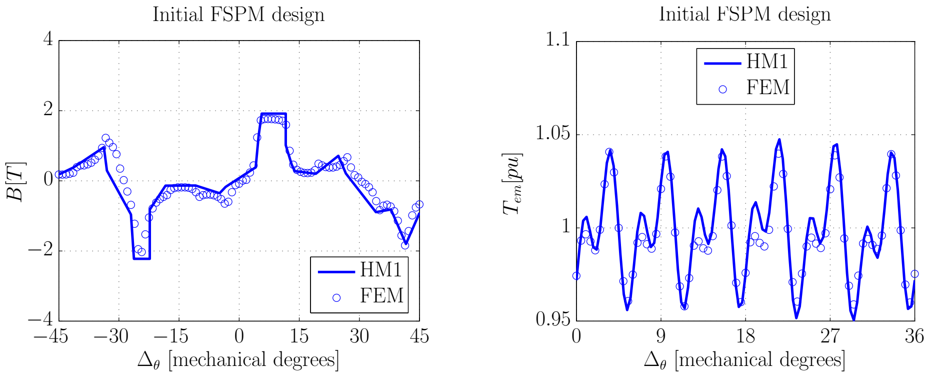

a) b)

Figure 7.2: Initial machine design with HM1 verified using finite element method for a) the flux density in the airgap in open-circuit, and b) the electromagnetic torque, T_{em}.

7.3.1 Parameters affecting acceleration capability

The first design requirement is a high acceleration, which depends by definition (Chapters 6.2.1-7.1) on continuous torque, T_{em}, and motor inertia, J_M. Since FSPM is a salient machine, its acceleration depends not only on rotor diameter, D_r, as in the case of nonsalient machines. To determine the design parameters for acceleration, motor inertia equations from Chapter 6 are applicable. Neglecting shaft, bearings and effect of virtual inertia, the acceleration of FSPM has the following expression based on (6.38):

$$\frac{T_{em}}{J_M} = \frac{0.5D_r^2 QBL_a}{J_C + N_r(J_R + 2J_T)}, \tag{7.1}$$

where B is the magnetic loading, and Q the electrical loading. In this case, the general equation for FSPM's inertia with the mass density, ρ_{Fe}, is:

$$J_M = \rho_{Fe}L_a\Big(\frac{1}{2}\big[R_{sh}^4 - R_r^4\big] + N_r\big[l_{rt}w_{rt}\big(\frac{[w_{rt}^2 + l_{rt}^2]^2}{24} + [\frac{l_{rt}}{2} + R_r]^2\big)$$

$$+2l_{rt}\big(\frac{w_{rti} - w_{rt}}{2}\big)\big([\frac{(\frac{w_{rti}-w_{rt}}{2})^2 + l_{rt}^2}{18}]^2 + [\frac{l_{rt}}{3} + R_r]^2\big)\big]\Big), \tag{7.2}$$

which shows dependency on the rotor tooth parameters, i.e. rotor pole (teeth) number, N_r, rotor tooth length, l_{rt}, rotor tooth width, w_{rt}, and rotor tooth inner width, w_{rti}, in addition to D_r. In this context, l_{rt} is a design parameter since N_r is constant. The parameters w_{rt} and w_{rti} depend on the rotor tooth inner ratio, k_{rti}. It should be noted that inertia calculations are based here on mechanical (mass-based) inertia equations.

7.3.2 Parameters affecting torque capability

Another design requirement is a high torque output. In literature, many FSPM optimization or *design* techniques are based on torque maximization and/or torque ripple minimization by independently varying split ratio, s_r, and rotor tooth width ratio, $tw_r = \theta_{st}/\theta_{rt}$ [127, 143, 144]. Such a parameter variation is performed in Fig. 7.3 for the initial design. The torque variation with s_r is shown in Fig. 7.3a, and with tw_r in Fig. 7.3c. The inertias of the respected parameter variations are shown in Figs. 7.3b-d. Result in Fig. 7.3a indicates, although rotor diameter increases at lower s_r, the torque output does not show a proportional increase.

Related to the first design requirement, i.e. acceleration, a high torque output is beneficial. For torque maximization in (7.1), the parameters have to be chosen to optimize D_r, B and Q. The design parameter s_r affects rotor diameter directly, since the stator outer dimensions are constrained by R_s and L_a. The design parameter tw_r has an effect on rotor in terms of inertia. In addition to D_r, s_r affects also PM and coil slot sizes. While s_r is increasing, D_r increases, whereas B and Q decrease, in which case the effect of s_r on torque cannot be reasoned, and should be evaluated by means of a model. An investigation done by [127] makes this evaluation by keeping the copper losses constant, which is implemented in the results of Figs. 7.3a-c. This is realized by adapting current density and the winding resistance, as the effective coil area is changing. However, as s_r is varied, the slot pitch is changing as well due to the varying airgap circumference. Hence, keeping the copper losses constant fixes Q only as long as s_r is not varied. Furthermore, this analysis shows that the parameter s_r has a more dominant effect on inertia than the effect of tw_r, because all rotor parameters, except for the shaft diameter, are scaled depending on s_r. Due to the dependency on torque and on inertia according to (7.2), one cannot conclude at this point whether lowering s_r optimizes the motor design for a high acceleration.

7.3.3 Parameters affecting overloading capability

The third design requirement is a high overloading capability, i.e. ability to reach higher torque values. Torque optimization procedures discussed in Chapter 7.3.2 indicate a 25% difference between the linear and nonlinear results in Figs. 7.3a-c. This highlights the disadvantage of an FSPM in terms of overloading capability for the structure with $\theta_{st} = \theta_s/4$ while varying only the design parameter s_r. In this analysis, for smaller s_r, where the airgap circumference gets smaller, the magnet width, θ_m (or w_m), is decreased while the magnet height, l_m, is increased leading to a coupled change both in B and Q. Choosing a lower grade magnet, i.e. with a lower magnet remanence, B_r, could diminish the difference between Figs. 7.3a-c by only affecting B; however it may result a lower torque output. Instead, the implementation of the design parameter s_r has to be adapted in a more fundamental approach to decouple its effect on B and Q. To accomplish the decoupling, a new parameter is introduced for simultaneous parametrization

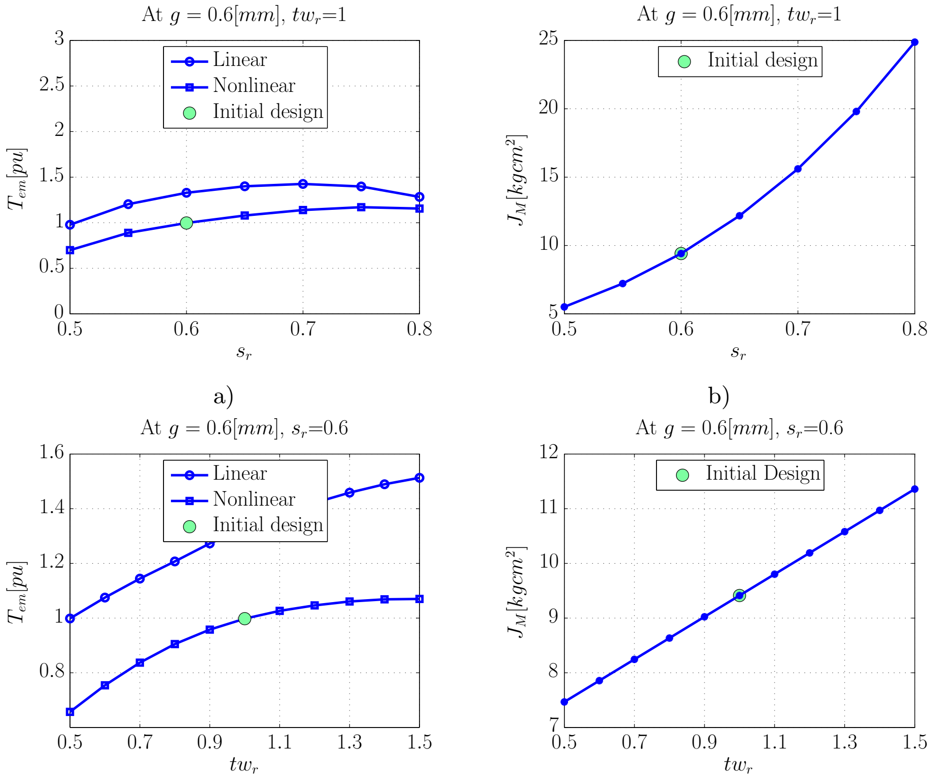

a) b)

c) d)

Figure 7.3: Torque, T_{em}, and motor inertia, J_M, calculations of the initial flux switching permanent magnet machine design for a-b) s_r and c-d) tw_r variations.

together with s_r. The additional design parameter is stator tooth width ration, $x\theta_{st}$, with x times of its original value $\theta_s/4$. Similar to s_r, $x\theta_{st}$ affects B and Q simultaneously. For initial sizing in Chapter 7.2, w_c is kept equal to w_m and w_{st}. By changing $x\theta_{st}$, this relationship does not hold anymore. While w_{st} is widened, w_m and w_c are reduced at the same rate to keep the magnetic symmetry in the stator, whereas $w_{rt} = w_{st}$. Since an excessive amount of B is observed with the initial dimensions, only increasing w_{st} is regarded ($> 1.0\theta_{st}$) in the magnetic design. Conclusively, to satisfy the three design requirements, the following design parameters discussed in this section:

- Magnet remanence, B_r,
- Split ratio, $s_r = R_{st}/R_s$,
- Stator tooth width ratio, $x\theta_{st}(= xw_{st})$,
- Rotor tooth length, l_{rt},
- Rotor tooth inner ratio, $k_{rti} = \theta_{rti}/\theta_{rt}(= w_{rti}/w_{rt})$,
- Magnet length, l_m, and
- Rotor tooth width ratio, $tw_r = \theta_{st}/\theta_{rt}(= w_{st}/w_{rt})$,

are evaluated in the following sections.

7.4 Magnetic design evaluation

In this section, the effect of design parameters on the flux density within the soft magnetic material is evaluated. Within this evaluation, the design is constrained to the linear region of the first quadrant of BH-characteristic. This allows the applicability of the well-known dq transformation for this FSPM, similar to a brushless ac PM (PMAC) motor [68, 145]. This validity of dq transformation is partly lost in the nonlinear region due to the oscillations as present in dq flux linkage [51]. Additionally, a nonsaturated machine design naturally has a higher overloading capability. Therefore, the magnetic design at d-axis with maximum phase flux linkage, λ_{ph}, is limited to $B_{t_{max}} = 1.6[T]$ for the selected lamination M270-35A introduced in Chapter 7.2.

7.4.1 Effect of magnet strength

Initial machine design introduced in Chapter 7.2 has shown a saturating characteristic. Since the magnetic design of FSPM is constrained to a linear operation, optimization of hard magnetic material is required. This can be accomplished in its volume or by the choice of its properties, i.e. the PM strength or magnet remanence, B_r, as investigated in this section. To lower the magnetic loading in the initial FSPM, a lower grade magnet can be chosen, as shown in Fig. 7.4. According to the result, a less strong magnet should be used with a typical remanence of $B_r = 0.8[T]$. This solution, however, is not implemented due to the lower energy content of magnets with this B_r; therefore, next part focuses on the volumetric optimization of the PM.

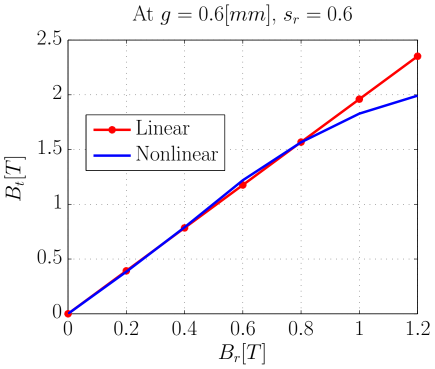

Figure 7.4: Effect of magnet strength (remanence), B_r, on magnetic loading in open-circuit.

7.4.2 Combined effect of split and stator tooth width ratios for $s_r > 0.7$

In another approach, i.e. to optimize the magnet volume, the combined effect of two design parameters, split ratio, s_r, and stator tooth width ratio, $x\theta_{st}$, is investigated by keeping stator back-iron, h_{sbi} and rotor back-iron, h_{rbi} constant at their initial values. In this analysis, g, k_{rti}, and R_{sh} are fixed to their initial values in Table 7.1. The aim of this parametric search is to obtain suitable (s_r, $x\theta_{st}$) pairs, which stay within the limit of magnetic loading. The analysis for linear (Fig. 7.5a) and nonlinear (Fig. 7.5b) soft magnetic material yields different (s_r, $x\theta_{st}$) pairs as seen in Fig. 7.5c. Only results with $s_r = [0.7 : 0.8]$ are calculated for a variation of $x\theta_{st} = [1.0 : 1.26]\theta_{st}$, since configurations with $s_r < 0.7$ yield higher magnetic loading for the initial dimensions. The established nine motor configurations are denoted *Designs A-I* as shown in Fig. 7.6. Despite different configurations, the resulting acceleration values, T_{em}/J_M, in Fig. 7.5e differ slightly for the linear and

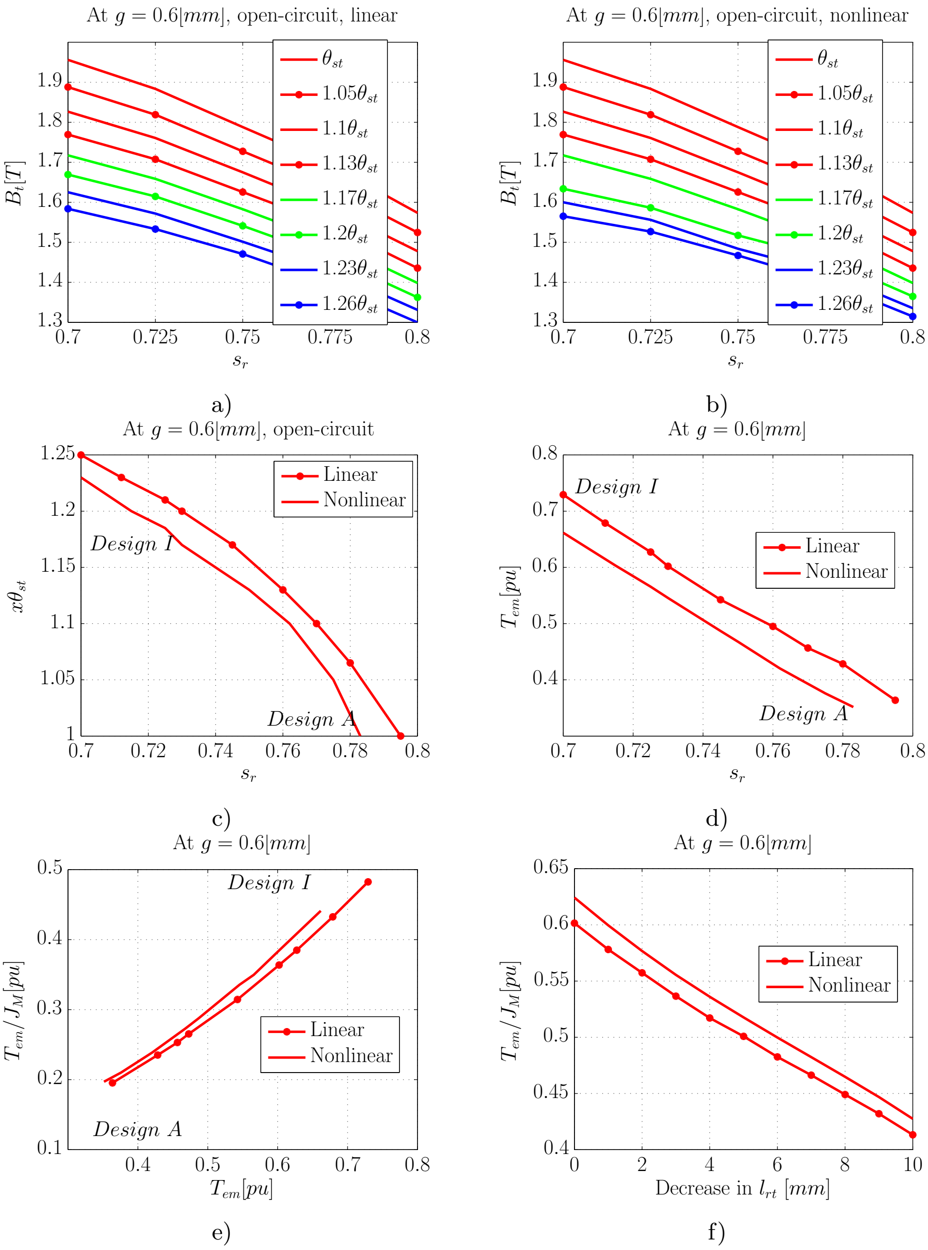

a)

b)

c)

d)

e)

f)

Figure 7.5: The split ratio, s_r, and stator tooth width ratio, $x\theta st$, varied for a) linear and b) nonlinear calculation of flux density in stator tooth, B_t. The target magnetic loading reached with c) (s_r, $x\theta st$) pairs for $B_t = 1.6[T]$ leading to d) T_{em} and e) T_{em}/J_M results. f) Effect of rotor tooth length on *Design I* with $k_{rti} = 1$.

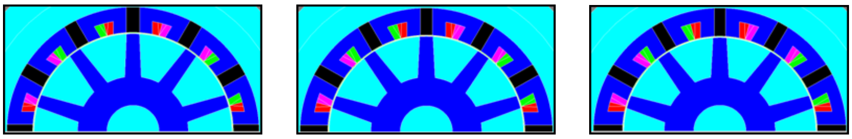

a) Des. A (0.795, 1.0θ_{st}) b) Des. B (0.78, 1.05θ_{st}) c) Des. C (0.77, 1.1θ_{st})

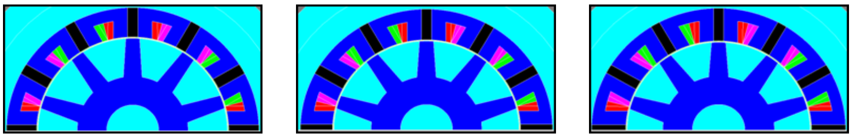

d) Des. D (0.76, 1.13θ_{st}) e) Des. E (0.745, 1.17θ_{st}) i) Des. F (0.73, 1.2θ_{st})

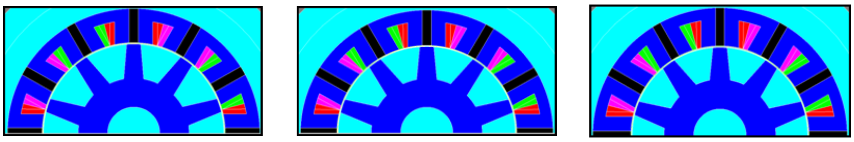

g) Des. G (0.725, 1.21θ_{st}) h) Des. H (0.712, 1.23θ_{st}) i) Des. I (0.7, 1.25θ_{st})

Figure 7.6: a-i) Motor *Designs A-I* with different split and stator tooth width ratios (s_r, $x\theta_{st}$) satisfying the magnetic loading limit.

nonlinear magnetic analysis. Among these, the motor configuration with highest T_{em}/J_M, i.e. *Design I*, is selected for further analysis.

7.4.3 Effect of rotor tooth length

Based on motor *Design I*, the effect of the rotor dimensions is investigated further. Increasing the rotor back-iron height, h_{rbi}, increases inertia without any effect on the torque, leaving two other design parameters: rotor tooth length, l_{rt}, and rotor tooth inner ratio, k_{rti}. First, the parameter l_{rt} is varied for a straight tooth, i.e. $k_{rti} = 1$. To lower the inertia at a constant rotor back-iron, the area between shaft and rotor back-iron is filled with a light nonmagnetic material, e.g. aluminium, as illustrated in Fig. 7.7a. Decreasing l_{rt}, as shown in Fig. 7.7b-c, does not affect torque. Due to the increase in motor inertia, J_M, acceleration, T_{em}/J_M, decreases as shown in Fig. 7.5f. If $l_{rt} > w_{rt}$, the saliency of the machine is sufficient to create the optimal torque. Another result obtained concerns the effect of rotor tooth shape. *Design I* with $k_{rti} = 2.3$ in Fig. 7.5e has a higher torque output compared to the one with $k_{rti} = 1$ in Fig. 7.7b; however, the latter provides a higher acceleration. Since the torque decrease is not that significant, a rotor tooth with $k_{rti} = 1$ is more beneficial for a high-acceleration motor design. Among the compared motor designs in Fig. 7.6, *Design I* with $k_{rti} = 1$ shows best performance in terms of T_{em} and T_{em}/J_M maximization, resulting in the first design candidate. The results in Fig. 7.5 indicate that if magnetic loading is kept lower than 1.6[T], the linear and nonlinear results coincide, thus, only linear analysis is performed henceforth.

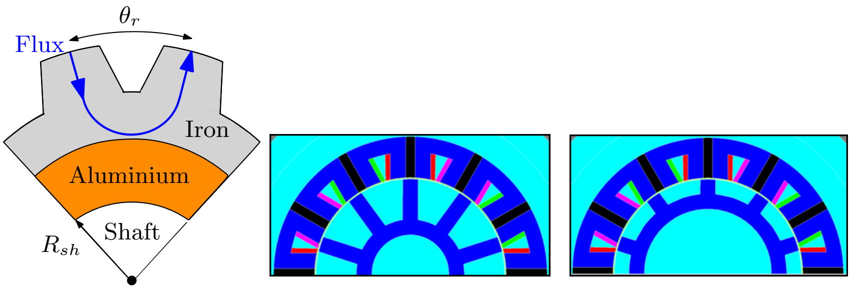

a) b) c)

Figure 7.7: a) Replacing the back-iron by lighter material, e.g. aluminium, and b-c) variation of rotor tooth length, l_{rt}, in *Design I* with rotor tooth inner ratio, $k_{rti} = 1$.

7.4.4 Effect of magnet length

Another pre-determined design parameter is magnet length, l_m, which can be used to optimize the magnet volume, as discussed in this part. Parametric search performed in Fig. 7.5 indicates that a lower split ratio, s_r gives in a higher acceleration, T_{em}/J_M.

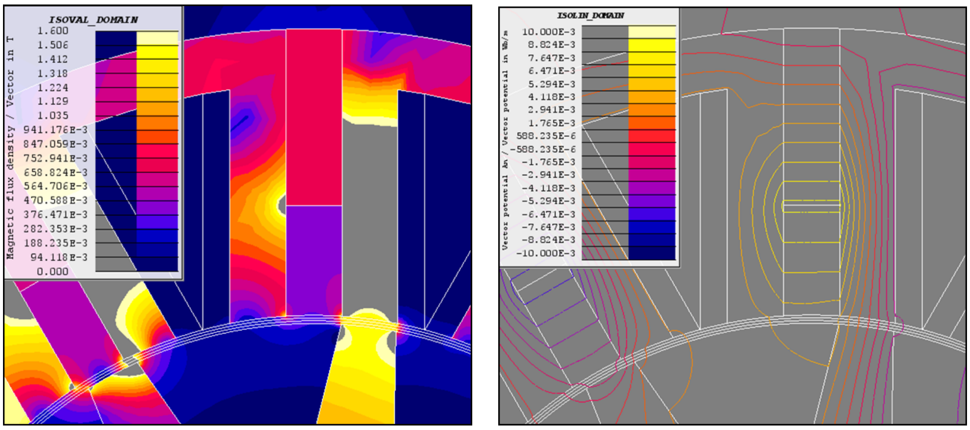

a) b)

Figure 7.8: a) Flux density distribution, and b) magnetic vector potential distribution for decreasing magnet length, l_m, at the airgap side for stator tooth width ratio $1.0\theta_{st}$ in open-circuit.

Due to high magnetic loading, it was not possible in Chapter 7.4.2 to investigate $s_r < 0.7$. To overcome this problem, the magnet length, l_{rt}, is decreased for the initial conditions, i.e. with stator tooth width ratio, $1.0\theta_{st}$, and rotor tooth width ratio, $k_{rti} = 2.3$. First, the magnet length is decreased at the airgap side, causing saturation in the neighboring tooth as illustrated in Fig. 7.8a. This is an unexpected behavior since the highest flux density is usually observed in the tooth tip. Although the relative permeability of magnet and air are similar, the air region below the magnet has no mmf source. Smaller magnet provides a new reluctance path below the magnet. This reluctance is smaller compared to the airgap reluctance between the stator and rotor teeth, in which case the flux lines follow the shorter path below the magnet as seen in Fig. 7.8b.

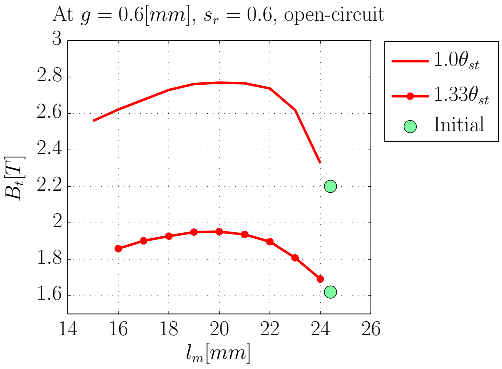

Figure 7.9: Flux density in the upper tooth, $B_t(T)$, next to lower magnet limit, with decreasing magnet length, l_m.

Next, the flux density in the upper part of the tooth, B_t, is observed as the magnet is decreased along its radial length. The result in Fig. 7.9 shows that B_t first increases as a result of the decreasing reluctance of the air region, located just below the magnet region, due to the increasing cross section (along l_m). However, the resulting increase in the flux density is not continuous. As the magnet decreases further, it also becomes weaker as an mmf source. After a certain limit, the flux density in the upper tooth starts decreasing. One solution to decrease the saturation occurring in the tooth is, increasing the stator tooth width ratio further than the investigated values in Chapter 7.4.2, i.e. to $1.33\theta_{st}$. Consequently, an improved flux density distribution is achieved in Fig. 7.10a. Although the area above $1.6[T]$ is smaller than the one in Fig. 7.8a, the tooth tip is still less saturated than the upper tooth. In a final investigation, the magnet is decreased from the frame side. A new reluctance path occurs this time above the magnet, and the flux lines tend to follow more their intended path, as shown in Figs. 7.10a-d. Despite this improvement, decreasing l_m leads in both cases, shown in Figs. 7.10a-b, to a significant drop both in torque and acceleration. Consequently, l_m optimization deemed not to be effective in line with the design requirements, instead, the distinctive properties of the new magnet arrangement, as a result of increasing $x\theta_{st}$, are researched further.

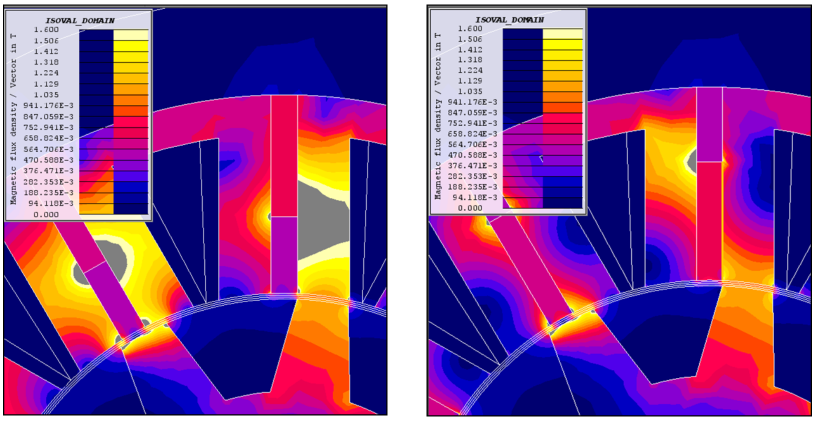

a) l_m decreased at the airgap side b) l_m decreased at the frame side

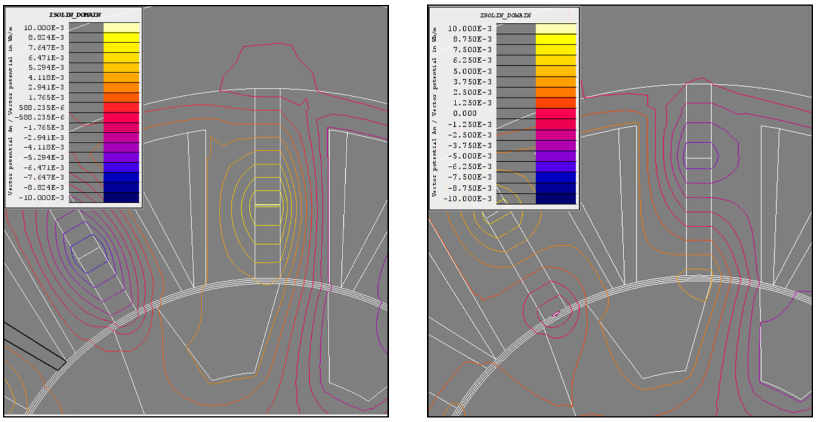

c) l_m decreased at the airgap side d) l_m decreased at the frame side

Figure 7.10: a-b) Flux density distribution, and c-d) magnetic vector potential distribution for decreasing magnet length, l_m, at the airgap side for $1.33\theta_{st}$ in open-circuit operation.

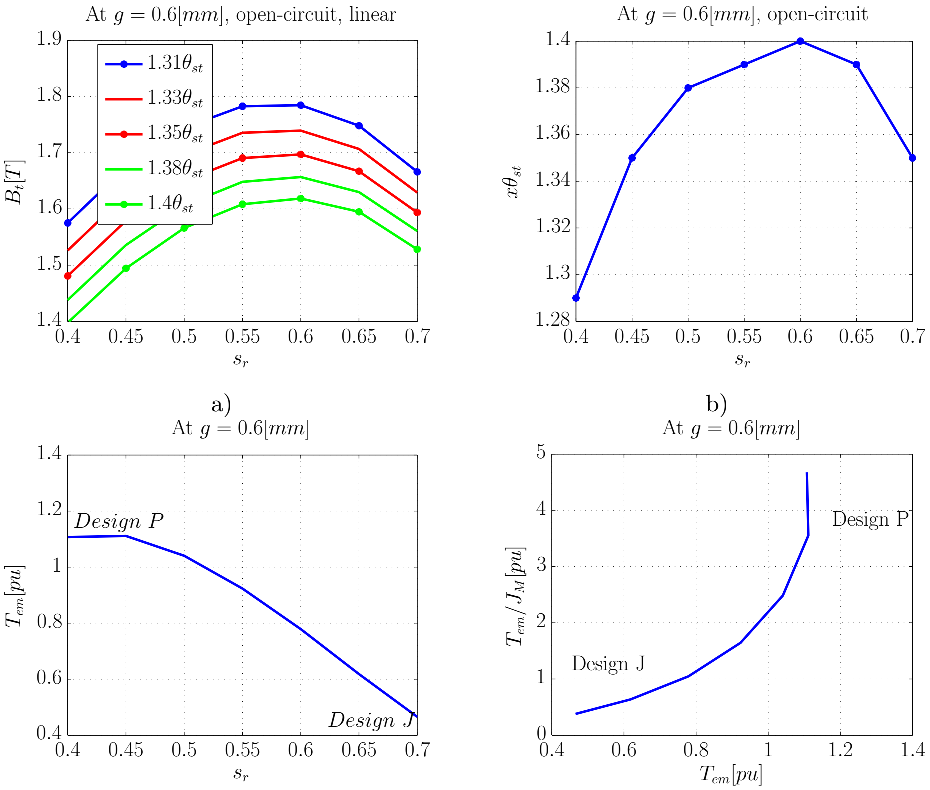

a) b)

c) d)

Figure 7.11: The split ratio, s_r, and stator tooth width ratio, $x\theta st$, varied for a) target magnetic loading. b) Determined (s_r, $x\theta st$) pairs at $B_t = 1.6[T]$ leading to c) T_{em}, d) T_{em}/J_M results.

7.4.5 Combined effect of split and stator tooth width ratios for $s_r < 0.7$

In Chapter 7.4.2, machine configurations with a split ratio of $s_r < 0.7$ could not be achieved with the chosen interval of the stator tooth width ratio, $x\theta_{st}$. Since decreasing magnet length, l_m, is not an efficient way to decrease the magnetic loading, as shown in Chapter 7.4.4, the interval of stator tooth width ratio is increased further to $x\theta_{st} = [1.31 : 1.4]\theta_{st}$, and the split ratio is decreased to an interval of $s_r = [0.4 : 0.7]$. For this analysis, the results from Chapter 7.4.3 are also used with $k_{rti} = 1$ and $h_{rbi} = h_{sbi} = w_{rt} = w_{st}$. This magnetic arrangement results in an improved acceleration for *Design I* compared to tapered rotor tooth with $k_{rti} = 2.3$. Result in Fig. 7.11a shows that by increasing w_{st}, the magnetic loading is indeed brought down to acceptable values. Hence, due to the decrease in rotor diameter, D_r, (for lower s_r values), B_t tends to decrease for $s_r < 0.6$.

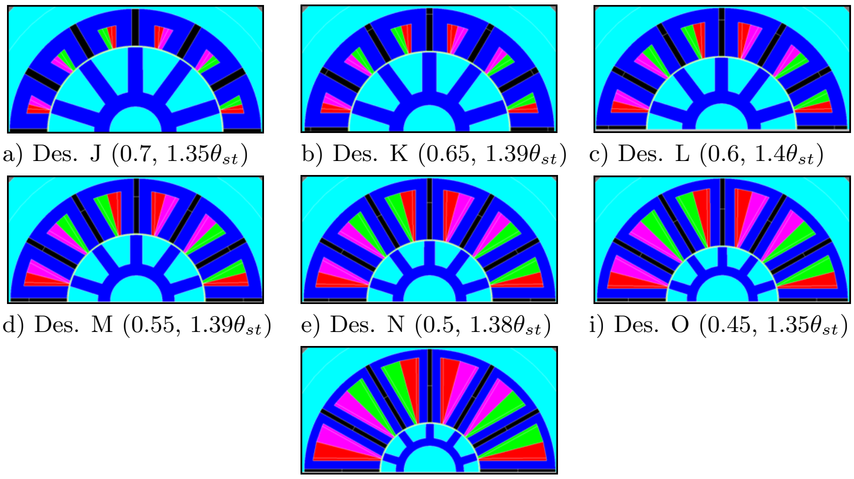

a) Des. J (0.7, 1.35θ_{st}) b) Des. K (0.65, 1.39θ_{st}) c) Des. L (0.6, 1.4θ_{st})

d) Des. M (0.55, 1.39θ_{st}) e) Des. N (0.5, 1.38θ_{st}) i) Des. O (0.45, 1.35θ_{st})

g) Des. P (0.4, 1.29θ_{st})

Figure 7.12: a-i) Motor *Designs J-P* with different split and stator tooth width ratios (s_r, $x\theta_{st}$) satisfying the magnetic loading limit.

Similar to the analysis performed in Chapter 7.4.2, seven $(s_r, x\theta_{st})$ pairs are established, as plotted in Fig. 7.11b, corresponding to motor *Designs J-P* shown in Fig. 7.12. The resulting torque, T_{em}, and acceleration, T_{em}/J_M, are plotted in Figs. 7.11c-d respectively. Due to larger coil area, torque increases with decreasing s_r and the highest torque is achieved at $s_r = 0.45$, by increasing slot leakage proportional to the slot depth. As s_r decreases, the rotor becomes smaller, thus, contributing to acceleration. Consequently, two motor configurations, i.e. *Designs M-N*, are selected for further analysis considering maximization of acceleration and torque.

7.4.6 Effect of rotor tooth shape

In the last analysis, the effect of the design parameter, rotor tooth inner ratio, k_{rti}, is investigated on the chosen *Designs M-N*. This parameter defines the rotor tooth shape to be more straight or more tapered. The analysis is conducted in an interval of $k_{rti} = [1 : 1.9]$, since for values of $k_{rti} > 1.9$, the geometry is constrained by the remaining motor dimensions for both *Designs M-N*. The results are shown in Figs. 7.13a-b for torque and acceleration respectively. As rotor tooth gets more tapered with increasing k_{rti}, a small increase is observed in the output torque in Fig. 7.13a. However, due to the increased J_M, the acceleration drops as seen in Fig. 7.13b. Both *Designs M-N* with $k_{rti} = 1.3$ show the best performance in terms of T_{em}/J_M and T_{em}; therefore, these configurations are chosen as the second and third design candidates.

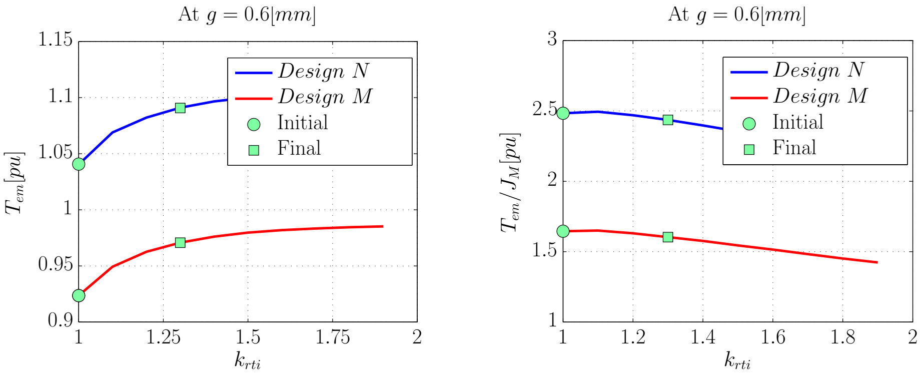

a) b)

Figure 7.13: Influence of rotor tooth inner ratio, k_{rti}, on motor *Designs M-N* for a) T_{em}, and b) T_{em}/J_M results.

Table 7.2: Design candidates from magnetic design

Design	s_r	$x\theta_{st}$	k_{rti}	$T_{em}[pu]$	$T_{em}/J_M[pu]$
I(I)	0.7	1.3	1	0.57	0.38
II(M)	0.55	1.39	1.3	0.96	1.6
III(N)	0.5	1.38	1.3	1.08	2.4

7.4.7 Design candidates

In the magnetic design evaluation, numerous motor configurations are investigated. Three of them, i.e. motor *Designs I-M-N* given in Table 7.2, are selected as the design candidates for further analysis. Among the candidates, *Design I* exhibits the lowest torque and acceleration, as well as the lowest magnetic loading (theoretically advantageous in terms of overloading capability). The other two candidates, *Designs M-N*, come forward in terms of high-acceleration capability and high torque output. Henceforth, the motor *Designs I-M-N* are referred as *Designs I-III*. To verify the hybrid model, one design candidate, e.g. *Design II* is compared to FEM. Results in Figs. 7.14a-b show that both HM1 and FEM are in very good agreement similar to the initial design in Figs. 7.2a-b with comparable T_{em}. Next, the parameter variation similar to Fig. 7.3, is applied to *Design II*. The results in Fig. 7.15 indicate a difference of maximum 2.7%, compared to the *saturated* initial design with a 25% difference between the linear and nonlinear results. Here, a smaller variation interval for s_r and tw_r is present in Fig. 7.15 compared to Fig. 7.3 due to different k_{rti} values between initial and final motor configurations. The comparison indicates a more efficient use of magnetic material without sacrificing torque capability and acceleration. In the following sections, the selected design candidates undergo electrical and thermal design evaluations.

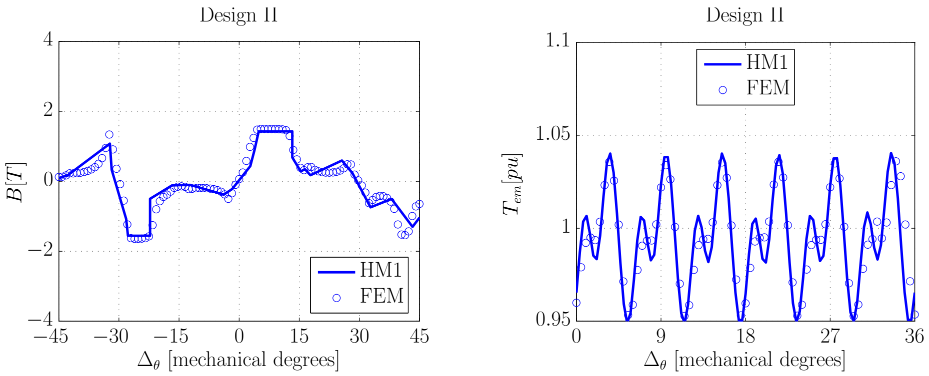

a) b)

Figure 7.14: *Design II* with HM1 verified using finite element method for a) the flux density in the airgap in open-circuit, and b) the electromagnetic torque, T_{em}.

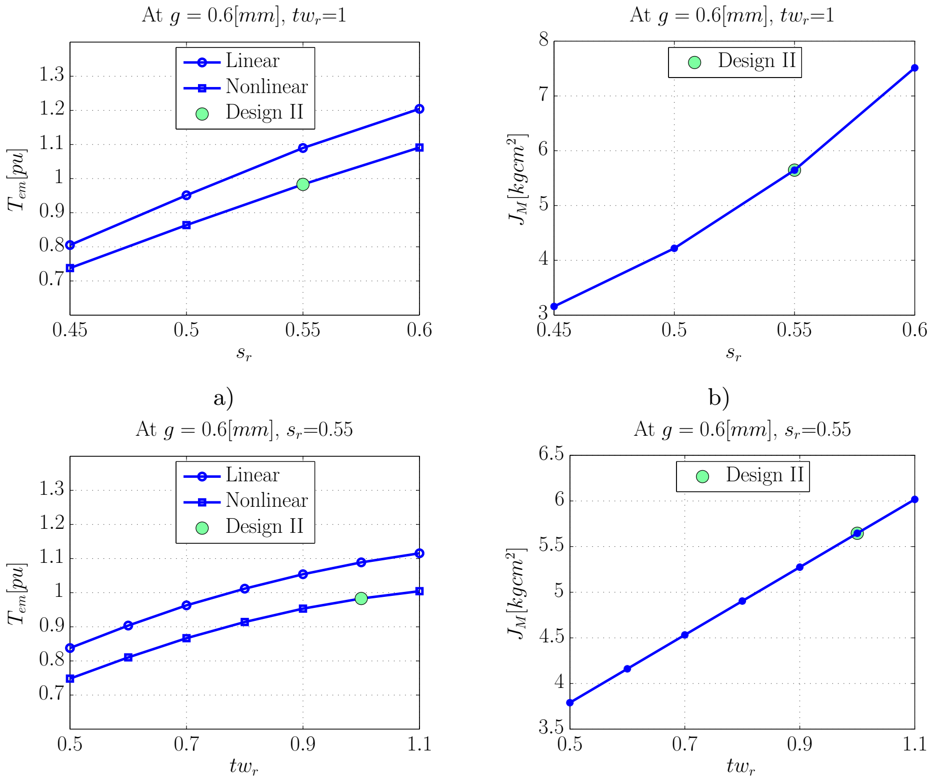

c) d)

Figure 7.15: Torque, T_{em}, and motor inertia, J_M, calculations of *Design II* for a-b) s_r and c-d) tw_r variations.

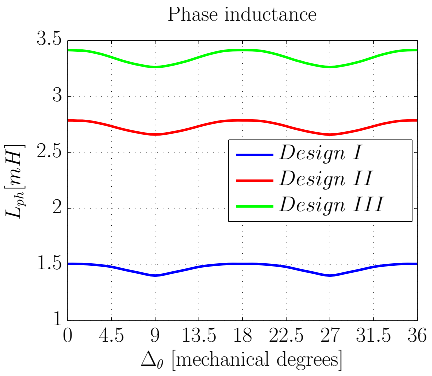

Figure 7.16: Phase inductances of *Designs I-III*.

7.5 Electrical design evaluation

In this section, electrical parameters of the three design candidates (*Designs I-III*) are investigated with respect to number of turns, resistance and inductance values. These values are calculated to evaluate their relationship with the electrical limits and equations given in Chapter 6.3.

7.5.1 Number of turns and conductor size

The first electrical quantities determined for the design candidates are number of turns, N_{ph}, and conductor size, D_{Cu}, based on (6.15). The maximum speed and voltage constrain these as $N_{ph} < 53.2$ for *Design I*, $N_{ph} < 67.25$ for *Design II*, and $N_{ph} < 74.07$ for *Design III*. Since there are four coils connected in series for the 3-phase 12/10 FSPM, N_{ph} should be a multiple of four. Combined requirements lead to $N_{ph} = 52$ for *Design I*, $N_{ph} = 64$ for *Design II*, and $N_{ph} = 72$ for *Design III*. Followingly, the maximum conductor size is determined as $D_{Cu} < 1.25[mm]$ for *Design I*, $D_{Cu} < 1.63[mm]$ for *Design II*, and $D_{Cu} < 1.74[mm]$ for *Design III*. The indicated conductor diameters are of bare copper without insulation for a fill factor of $k_f = 0.5$, and all values are well below the skin depth indicated in Chapter 6.3.9.

7.5.2 Phase resistance and inductance

Determining the conductor size, the phase resistance, R_{ph}, is calculated next for *Designs I-III* with the relationships in (6.16)-(6.17). The resulting resistance for *Design I* is $R_{ph} = 0.247[\Omega]$, for *Design II* $R_{ph} = 0.176[\Omega]$ and for *Design III* $R_{ph} = 0.175[\Omega]$. Based on position dependent current and flux linkage values, the phase inductances can be calculated as in Fig. 7.16. The results indicate only a small position dependency in all three designs; therefore, the reluctance torque component is negligible in this machine configuration as discussed in Chapter 1.2.1.

7.6 Thermal design evaluation

In this section, a thermal evaluation of the three design candidates, i.e. *Designs I-III*, is investigated with respect to their overloading capability and thermal behavior. The thermal characteristic of any system is of highly nonlinear nature affected by various dynamics. Thus, the evaluation here is merely intended to get a first order approximation to estimate the candidates behavior in terms of overloading capability and thermal behavior.

7.6.1 Overloading capability

The design requirement on the overloading capability is defined in this thesis as the ratio of the motor's maximum torque capability, T_{max}, to its stall torque, T_0. In line with the design analogy, the acceleration requirement is defined based on the stall torque, as discussed in Chapter 6.2.1, therefore the linkage between acceleration and the maximum torque is not researched. For the overloading capability, two main limiting factors are investigated here separately, related to the magnetic and thermal behavior of motor *Designs I-III.* The magnetic limit is determined by the linear relationship between current and torque in continuous duty cycle, i.e. the machine saturation limit. This relationship is shown in Fig. 7.17 for each motor's respective design values. Results indicate that *Design I* has a linear relationship, i.e. highest overloading capability, whereas *Design II* can be magnetically overloaded three-four times and *Design III* two-three times.

The second and more crucial factor determining the overloading capability is the thermal limit, which is bounded by the cooling properties of the motor and material tolerances. In the thermal design constraints, discussed in Chapter 6.2.4, natural convection and identical frame usage as the benchmark motor are present. Therefore the maximum heat dissipation of the motor, i.e. power loss at maximum torque, determines the thermal limit. Since identical frames are used, the maximum torque of the benchmark motor could be taken to determine the power

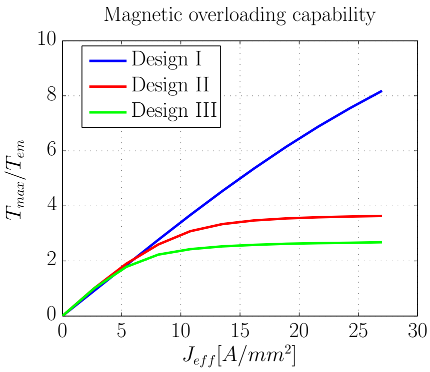

Figure 7.17: Magnetic overloading capabilities of *Designs I-III* depending on current density, J_{eff}.

loss at maximum torque. At the lower speed range for which the design analysis is made, copper losses, P_{Cu}, are dominant. For the corresponding current densities, the thermal overloading calculations result in $T_{max}/T_{em} = 12.7$ for *Design I*, 3.6 *Design II* and 2.65 for *Design III.* All these values are higher than their magnetic limits except for *Design I*, which has a nearly linear $T(J_{eff})$ relationship. Yet, considering both magnetic and thermal overloading capability, *Design I* has the best performance.

7.6.2 Thermal behavior

To investigate the thermal behavior of FSPM, an overview of its electromagnetic losses is given in Appendix D. As an example, these losses, i.e. the iron losses, P_{Fe}, and eddy current PM losses, $P_{e,PM}$, are plotted as a function of speed in Fig. 7.18 for *Design II.* In FSPM, the dominant losses are P_{Fe} with approximately 60% present in stator. The overall distribution of losses, with the majority present in the stator, results in a convenient natural cooling mechanism. Including also copper losses, P_{Cu}, the thermal behavior of *Designs I-III* is estimated with TEC from Chapter 6.5. The analysis is performed for the designed J_{eff} at a constant speed of $200[rpm]$, and an ambient temperature of $T_a = 20[°C]$. In the worst case, the maximum steady state temperature in the coil reaches $75[°C]$, which is well below the limit $135[°C]$ set by magnet glue, discussed in Chapter 7.2. With this section, the early design stage is completed in terms of magnetic, electrical and thermal design evaluations. Next section introduces the selection of the final design candidate and rotor optimization to satisfy the last design requirement, i.e. a smooth torque profile.

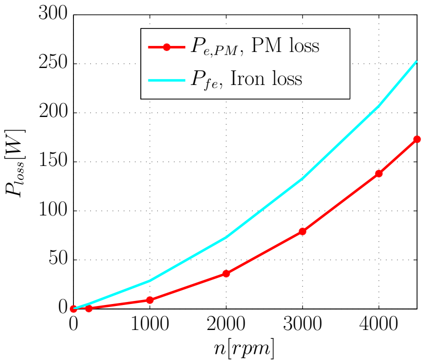

Figure 7.18: Electromagnetic losses (2D) of *Design II*

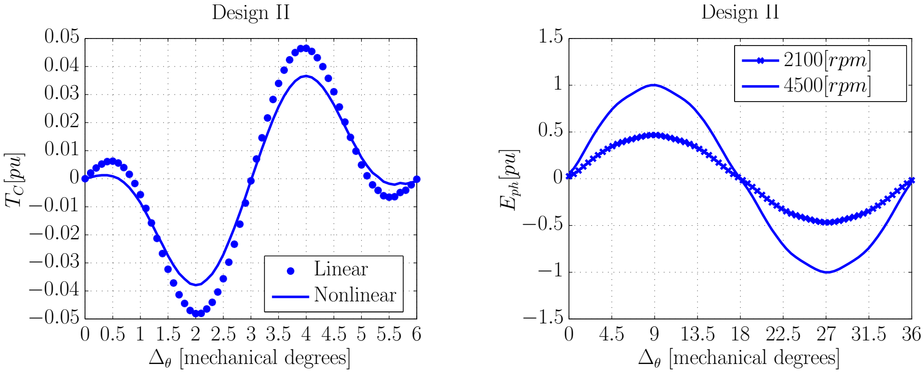

a) b)

Figure 7.19: Analysis of *Design II* for a) cogging torque, and b) phase back-emf at different speeds.

7.7 Rotor design optimization

Among the investigated design candidates, *Designs II-III* come forward in terms of highest acceleration and stall torque, whereas *Designs I-II* show the best overloading capability. To satisfy the three design requirements, *Design II* is chosen as the final candidate. In this section, rotor optimization is performed on *Design II* to achieve a smooth torque profile, i.e. $T_C/T_{em} < 1 - 1.5\%$ as discussed in Chapter 6.2.4, and to minimize mass-based inertia structurally.

7.7.1 Smoothing torque profile

Due to its salient airgap embracing PMs, FSPM exhibits cogging torque undesired in dynamic and high-acceleration applications. In this part, first, this torque component is analyzed followed by the back-emf. Furthermore, solutions are researched to diminish the adverse effect of saliency.

Cogging torque analysis

For the cogging, T_C, analysis, *Design II* is investigated for a linear magnetic and nonlinear analysis as presented in Fig. 7.19a, where they do not differ significantly. A harmonic analysis for the linear T_C is performed in Fig. 7.20a, which indicates the factors of 6^{th} harmonic are significant in one electrical cycle. For one period of the cogging torque, 6^{th}-12^{th}-18^{th} correspond actually to 1^{st}-2^{nd}-3^{rd} harmonics. The smallest common multiple of 12 stator and 20 rotor poles ($p = N_r = 10$) is $60°$ electrical degrees, making the 6^{th} harmonics the most significant.

Back-emf analysis

For the back-emf, E_{ph}, analysis *Design II* is investigated for its shape related to cogging at various speeds as presented in Fig. 7.19. Due to the magnetic circuit of the 12/10 FSPM and alternating magnetization of PMs, E_{ph} is expected to have a sinusoidal shape, as shown in Fig. 7.19b for the spindle speed (Chapter 6.2.2) $2100[rpm]$ and maximum speed $4500[rpm]$ (Chapter 6.2.3). Including the effect of losses, i.e. $P_{e,PM}$, the harmonic analysis of E_{ph} is performed in Fig. 7.20b, which verifies that it is sinusoidal with the largest nonfundamental harmonic, i.e. 7^{th} harmonic, $< 1\%$. Although the effect of cogging is not observed in the back-emf profile, it is still undesired for high-acceleration applications, therefore the next discussions concentrate on the methods to minimize this effect.

Effect of rotor tooth shape

In literature, one common method applied to reduce cogging effect, T_C/T_{em}, is widening the iron teeth at the airgap side at the expense of lowering torque, T_{em}. This method is investigated in Fig. 7.21 by varying rotor tooth width ratio, tw_r. The ratio T_C/T_{em} in Fig. 7.21a shows two optima at $tw_r = 1.4$ and $tw_r = 1.9$. This is commonly witnessed in the cogging minimization of PMAC motors. While minimizing T_C, the acceleration decreases rapidly as seen in Fig. 7.21b due to the decreasing T_{em} and increasing inertia, J_M. For the value of $tw_r = 1.4$, $T_C/T_{em} = 4.55\%$ drops to 1.9%, whereas for $tw_r = 1.9$ $T_C/T_{em} = 4.55\%$ drops to 1.85%. Although T_C is minimized significantly at both optima, this solution is not implemented due to adverse effect on acceleration.

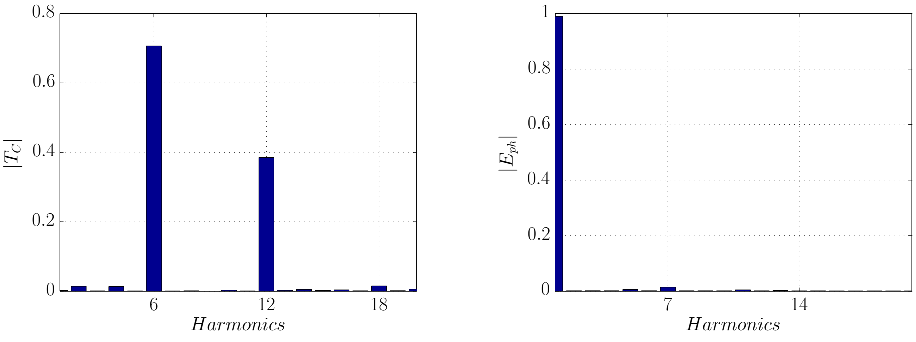

a) b)

Figure 7.20: Harmonic analysis of *Design II* given in percentage for a) cogging torque, T_C, and b) phase back-emf, E_{ph}.

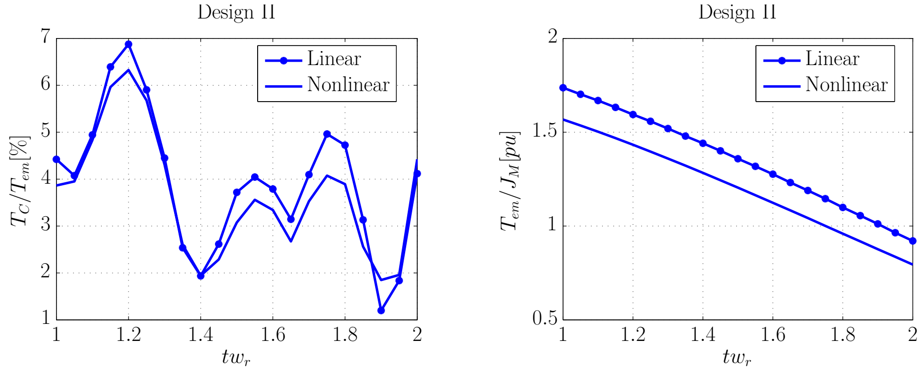

a) b)

Figure 7.21: Effect of widening rotor tooth w_{rt} with tw_r on a) torque ripple, T_C/T_{em}, and b) acceleration, T_{em}/J_M.

Rotor skewing

Another way to minimize cogging is skewing of either stator or rotor, so that cogging torque, T_C, mitigates over the axial length. Due to the complicated stator structure, it is decided to investigate the effect of rotor skewing. Similar to PMAC machines, where rotor PMs are skewed, skewing can be implemented in two ways: step-skewing or continuous skewing.

The first technique is applying step skewing as seen in Fig. 7.22a. Along each n^{th} step, the rotor is continuous in the axial length. The angle between each step, θ_{ss}, is the total skew angle, θ_{sk}, divided by the number of applied steps, N_{sk}, as:

$$\theta_{ss} = \frac{\theta_{sk}}{N_{sk}}. \tag{7.3}$$

To find the required number of N_{sk}, the cogging torque from each segment is shifted and superimposed, the cogging torque can be written as [146]:

$$T_C(\theta) = \sum_{n=1}^{N_{sk}} \sum_{k=1}^{\infty} T_{C_k} sin(k(\theta - (n-1)\theta_{sk})), \tag{7.4}$$

where T_{C_k} is the amplitude of k^{th} harmonic. The results for the step skewing in Fig. 7.23 show that $N_{sk} = 3$ gives sufficient T_C minimization. For a 3-step skewing, T_C/T_{em} in Fig. 7.23a drops from 4.55% to 0.54%. Disadvantages of the skewing is observed in Fig. 7.23b, where peak back-emf drops by 5.24%, causing a similar drop in the total torque production; however, the drop in the acceleration is acceptable with a decrease of 4.1%.

The second technique is to apply the skew through the axial length of the rotor as seen in Fig. 7.22b. If θ_{sk} equals to $6°$, T_C period, in theory, the result is $T_C = 0$. However, in practice there could be still minor fluctuations observed in the torque profile. This technique is applied to the final prototype design, resulting a drop of 5% in back-emf, which does not account for the end effects and interactions in the axial length.

7.7.2 Inertia minimization

A common method in practice to lower the mass-based motor inertia is to provide holes in the rotor such as shown in Fig. 7.24a for a PMAC motor. These holes should be located at a place with minimal influence on the magnetic flux paths, i.e. not to cause a significant loss in torque production. An additional constraint is the mechanical stiffness of the structure, which could be jeopardized by the high speed and temperature. Based on the magnetic structure of FSPM, triangular-shaped holes are proposed as shown in Fig. 7.22b. For a final analysis of the prototype, a 3D FEM is created to investigate end effects.

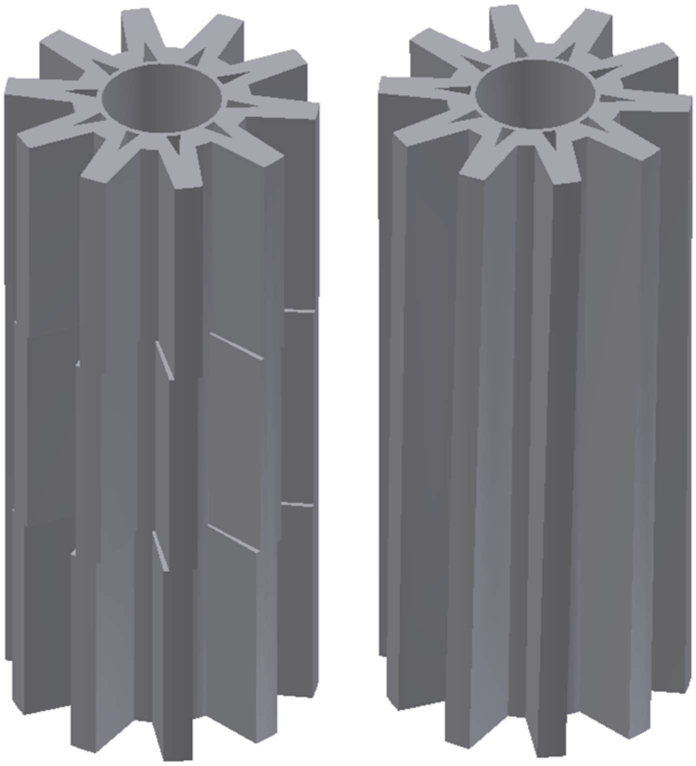

a) b)

Figure 7.22: a) 3-step, and b) continuous skewed rotor.

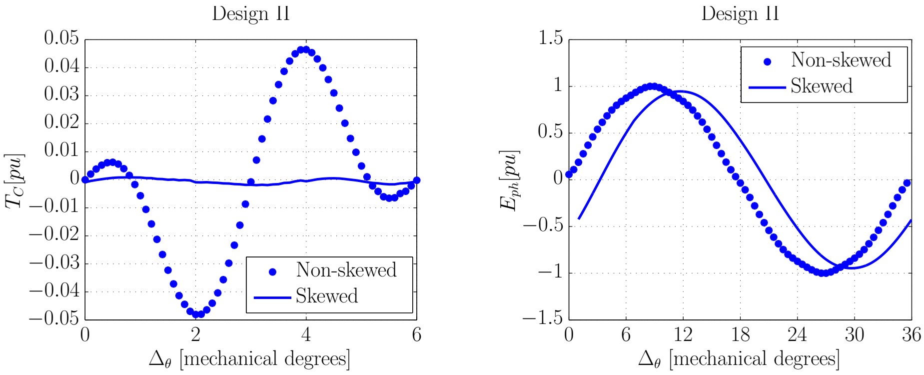

a) b)

Figure 7.23: a) Cogging torque, and b) back-emf at maximum speed for skewed and non-skewed rotors of *Design II*.

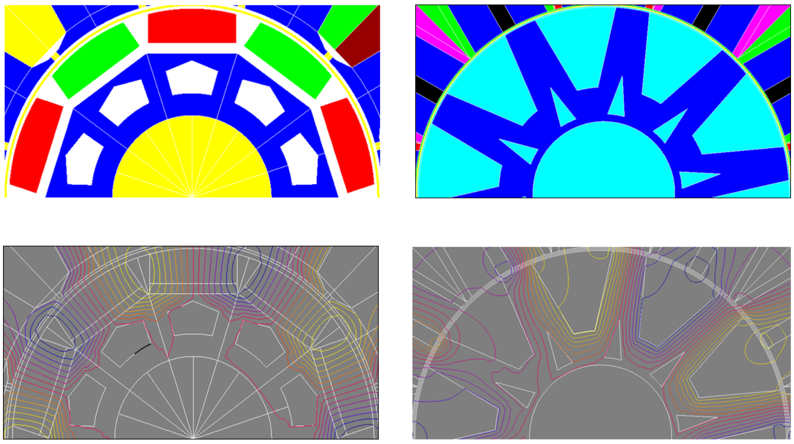

a) b)

Figure 7.24: Inertia minimization with triangular-shaped rotor holes in the a) benchmark motor, and b) *Design II*.

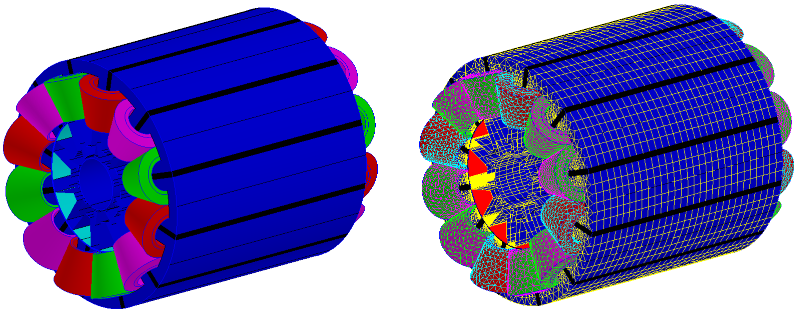

a) b)

Figure 7.25: a) 3D finite element model of the prototype, and b) mesh elements.

7.8 End effects and final design

The magnetic, electrical and thermal design evaluations have been based on 2D modeling approaches. In FSPM, PM volume is utilized by the flux focusing, whereas significant leakage flux exists at the ends and outer surfaces of the stator [77]. Thus, end effects are investigated with 3D FEM model given in Fig. 7.25. Based on the simulation results, the 3D factor introduced in (6.18) is estimated as $k_{3D} = 0.77$. Further investigations show that end effects do not change significantly within the overloading torque range of the prototype, thus k_{3D} can be used as a constant parameter. With this final analysis, parameters of the FSPM prototype are summarized in Table 7.3.

Table 7.3: Final prototype size and parameters

Symbol	**Description**	**Value**	**Unit**
R_s	Stator outer radius	53.35	$[mm]$
s_r	Split ratio	0.55	-
$x\theta_{st}$	Stator tooth width ratio	1.39	-
g	Airgap length	0.6 $(\%1D_r)$	$[mm]$
R_{sh}	Shaft radius	11	$[mm]$
L_a	Axial length	128	$[mm]$
θ_s	Angular stator width	$360°/N_s$	°
θ_m	Angular magnet width	$(\theta_s/4)(2-x\theta_{st})$	°
θ_c	Angular coil width	$(\theta_s/4)(2-x\theta_{st})$	°
θ_{st}	Angular stator tooth width	$(\theta_s/4)x\theta_{st}$	°
h_{sbi}	Stator back-iron thickness	$w_{st} = \frac{2\pi R_{ag}}{4N_s} = 5.31$	$[mm]$
θ_r	Angular rotor width	$360°/N_r$	°
θ_{rt}	Angular rotor tooth width	θ_{st}	°
k_{rti}	Rotor tooth inner ratio	1.3	-
θ_{rti}	Angular rotor tooth inner width	$k_{rti}{}^* \ \theta_{rt}$	°
h_{rbi}	Rotor back-iron thickness	h_{sbi}	$[mm]$
B_r	Remanent flux density of PM	1.2	$[T]$
μ_{pm}	Relative permeability of PM	1.05	-
n	Speed	4500	$[rpm]$
N_{ph}	Number of turns per phase	64	-

7.9 Summary and conclusions

In this chapter, a cross-analysis between design parameters of the flux switching permanent magnet machine (FSPM) has been presented in a general framework for high-acceleration applications, leading to a final prototype design.

The design of an electrical machine requires a multidimensional approach due to the interdependence of its parameters and the various design requirements. Accordingly, the complexity of the optimization process is reduced in this chapter by introducing certain parameter ratios. Such ratios have been proposed and implemented in literature for torque optimization processes, but not for acceleration. A parametric search based on such proposed ratios has revealed that optimization parameters from literature do not always result in optimum designs for high-acceleration applications. For the newly-designed flux switching permanent magnet machine in this thesis, i.e. the prototype, the split ratio, stator tooth width ratio, and rotor tooth inner ratio have been determined to be key design parameters in terms of maximization of acceleration and stall torque. It is noteworthy that the stator tooth width ratio has enabled variation of flux switching permanent magnet machine structures to improve torque production within the chosen design constraints.

During the evaluation of the design parameters, results have also proven the torque production mechanisms discussed in Chapter 1. The (phase) inductance of the flux switching permanent magnet machine has illustrated very little position dependency, although the rotor is salient in nature. Thus, the electromagnetic design considerations introduced in Chapter 6 have shown vast similarities to brushless ac PM (PMAC) machines, although the winding area is compromised by the magnets, which are offsetted by flux focusing to elevate the airgap flux density. These equations have been implemented in this chapter for the design process of the prototype together with the parametric search, which has resulted in various motor configurations. Among the investigated motor structures, one configuration that satisfies the design considerations in acceleration, torque and overloading capability, has been selected as the final candidate. Its rotor has been designed to achieve a smooth torque profile. A continuous rotor skewing for torque ripple minimization and triangular-shaped holes for 'mass-based' inertia minimization have been proven most optimal. However, mass-based inertia is not the only component affecting acceleration capability, as discussed in the previous chapter. The next chapter quantifies this effect in the scope of the dynamic performance comparison along with the construction and experimental verification of the prototype design.

Chapter 8

Construction and experimental verification

"Instruments register only those things they're designed to register. Space still contains infinite unknowns." – Spock (The Naked Time)

* * *

This chapter introduces the applicability of PM-biased salient machines for high acceleration by quantifying their performance in a comparison to a state-of-the-art solution, i.e. the benchmark motor introduced in Chapter 6. Hence, a skewed FSPM prototype is constructed based on the design presented in the previous chapter. The distinctive properties of the realization are discussed related to the winding structure and stator assembly. Furthermore, modeled average torque, cogging, and back-emf calculations are experimentally verified, along with the thermal model. Finally, in the thermal and dynamic performance assessments, torque and inertia measurements are conducted on both machines, prototype and benchmark, for a speed profile of a reduced-order spindle-drive.

* * *

The contributions of this chapter are published in the following articles:

- Ilhan, E., Balyovski, T. L., Paulides, J. J. H., and Lomonova, E. A. [2014]. Servo flux switching PM machines. *Proceedings of the International Conference on Electric Machines*, Berlin, Germany.
- Balyovski, T. L., Ilhan, E., Tang, Y., Wijnands, C. G. E., Paulides, J. J. H. and Lomonova, E. A. [2014]. Control of dc-excited flux switching machines for traction applications. *Ecological Vehicles and Renewable Energies, International Conference and Exhibition on*, Monaco.

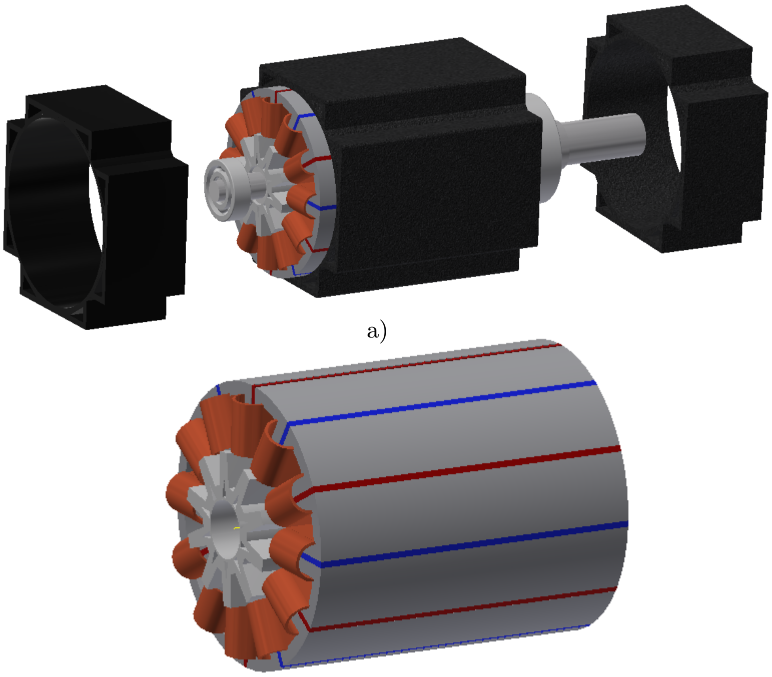

a)

b)

Figure 8.1: Illustration of the prototype with a) frame, bearings and shaft, and b) motor only.

8.1 Realization of the prototype

To assess the performance of PM-biased salient machines for high acceleration, a prototype is constructed based on the design presented Chapter 7. Due to the comparative assessment, certain parts of the prototype, i.e. shaft, bearings and frame, have been constrained to the benchmark motor introduced in Chapter 6.2.3. This section discusses the construction of the FSPM prototype, illustrated in Fig. 8.1, with interest to winding structure and stator assembly. Compared to stator part, the construction of rotor is simpler, since it only consist of stacked (glued) M270-35A lamination of $0.35[mm]$ thickness with a continuous skew of $\theta_{sk} = 6°$. The challenge in the realization of the prototype lies in the stator construction to maximize the slot fill factor, k_f, which was assumed 0.5 during the design in Chapter 7.2.

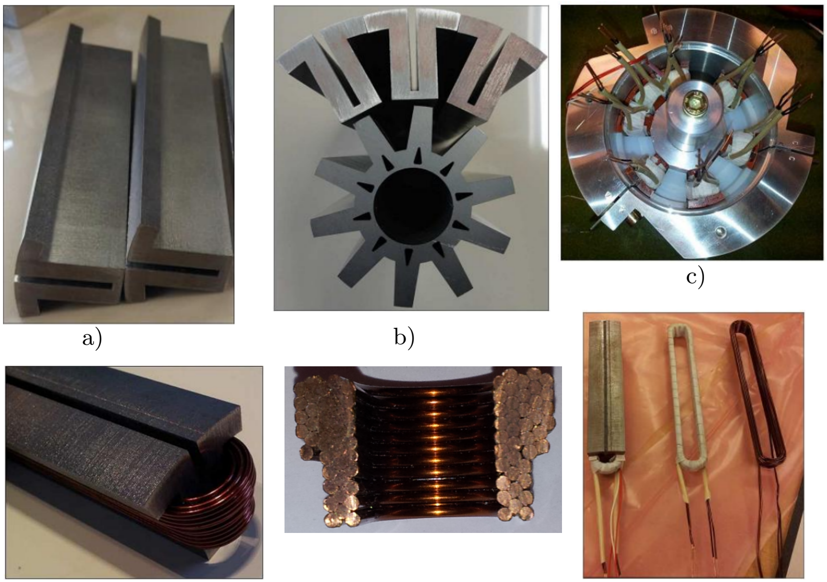

a) b) c) d) e) f)

Figure 8.2: a) Bare stator iron elements, b) bare stator and rotor iron elements, c) assembly tool, d) 2x1.06$[mm]$ backlack of grade 2, e) coil cross section, and f) finished stator elements.

8.1.1 Winding structure

Narrow coil slots create a challenge to achieve a high k_f in the construction of FSPM. The prototype consists of concentrated windings, four connected in series, wound around each PM. Due to the irregular slot shape, the coil distribution is expanded over the whole slot area by using wedge shaped *pre-wound* coils. Considering the narrow slot width, w_c, pre-wound coils could not be slided through this opening; therefore stator is produced in separate elements as shown in Fig. 8.2a. In Chapter 7.5, maximum conductor size of prototype was determined as $D_{Cu} < 1.63[mm]$, which is very thick to firmly form for the prototype's slot dimensions. Thus, instead of one wire with 16 turns per coil, two sets parallel windings of 1.06$[mm]$ thickness are used as shown in Figs. 8.2d-f, achieving $k_f = 0.42$. After winding twelve stator segments, each with a PM as shown in Fig. 8.2d, the stator assembly is discussed next.

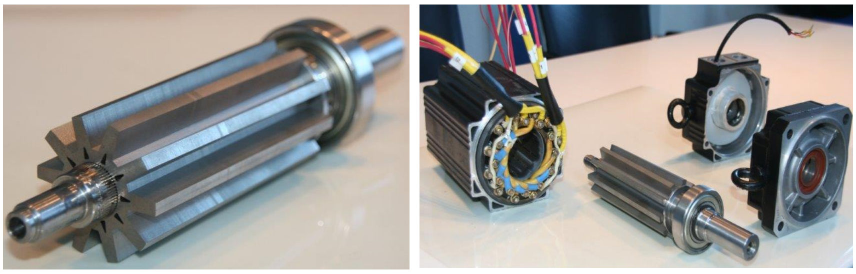

a) b)

Figure 8.3: a) Finalized rotor in close-up, and b) completed prototype with housing.

8.1.2 Stator assembly

Location of PMs causes a modular stator structure, therefore this part is produced consisting of twelve separate pieces as shown in Figs. 8.2a-c. Each piece is prepared first by gluing the PM and then wounding the coil around it. Extra iron pieces are provided just below PMs, as shown in Fig. 8.2a-c, for increased mechanical integrity during the assembly process [147]. Additionally, segmented block magnets (each comprising ten pieces) are used along the axial length, L_a, to reduce losses induced by eddy currents in PM. After finalization of individual stator elements as in Fig. 8.2d, they are pressed together in an assembly tool for potting [147]. In the final stage, extra iron pieces on the bottom part of PMs are removed by milling. The realized prototype is shown in Figs. 8.3a-b. The skewed rotor with triangular-shaped holes to reduce mass-based inertia is shown close-up in Fig. 8.3a, and the completed prototype with frame in Fig. 8.3b. To verify the realized prototype, a test setup is built as discussed in the next section.

8.2 Test setup

For the experimental verification of the prototype, and performance evaluations of the prototype and benchmark, a test setup, illustrated in Fig. 8.4, is built. A load motor, denoted as M2, is attached mechanically to the shaft of the test motor, denoted as M1. The mechanical coupling of M1 and M2 (Bosch B4.170.050) is realized via a torque sensor (Kistler 4503A-series) and two rigid couplings (BK3.60). The mass-based inertia of the coupling is $J_C = 3.9[kgcm^2]$, whereas the inertia of M2 is $J_L = 40.8[kgcm^2]$, of torque sensor for measuring end $J_{T_M} = 0.54[kgcm^2]$ and for drive end $J_{T_L} = 1.16[kgcm^2]$. The designed prototype has a mass-based inertia of $5.59[kgcm^2]$, i.e. 9.83% less than the benchmark. Position information is processed via the resolver of M1, where analog sine and cosine signals are converted by a programmable A/D converter. For thermal measurements, 3-wire PT100 sensors are attached to coil slot and housing of M1. Both machines are regulated via dSpace (CP1104) and MATLAB platforms, where speed, current

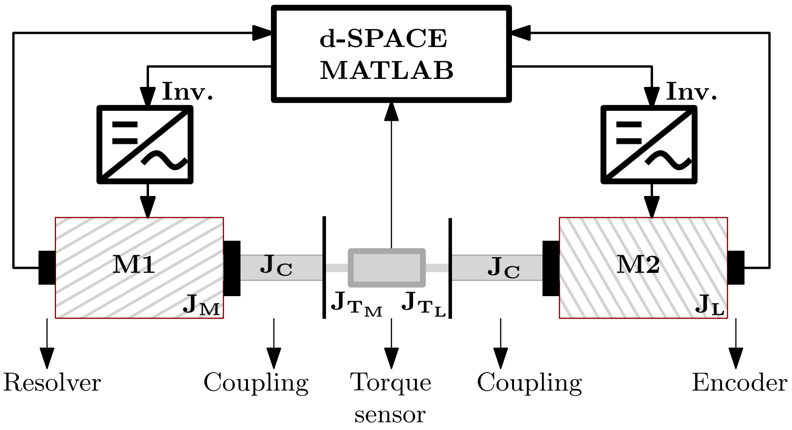

Figure 8.4: Layout of the test setup used for the measurements on the prototype and benchmark motors.

and thermal regulation is performed by discrete PI controllers based on [51]. The following sections contain the measurement data obtained from this setup for the experimental verification of the prototype and performance comparison between prototype and benchmark.

8.3 Experimental verification of the prototype

Hybrid modeling techniques presented in Part I of the thesis, and the prototype design in Part II have been only verified using FEM. This section concerns experimental verification of these models for back-emf and electromagnetic torque of the prototype, which is also verified for the thermal operation limits estimated by TEC.

8.3.1 Verification of back-emf

In the design phase of the prototype, hybrid model (HM1), introduced in Chapter 2, has been opted for due to the moderate saliency of FSPM. To verify the realized prototype, first phase back-emf, E_{ph}, is measured by moving the rotor externally with the load motor M2 at a constant speed of $1000[rpm]$. Results in Fig. 8.5 show that measured E_{ph} is in a very good agreement with the modeled results from HM1 and FEM. The discrepancy between the rms-values of modeled and measured E_{ph} is only 0.38%. The resulting voltage constant per 1000 $[rpm]$ has a peak value of $81.26[V]$. Next, electromagnetic torque is analyzed in for rated torque and cogging, respectively.

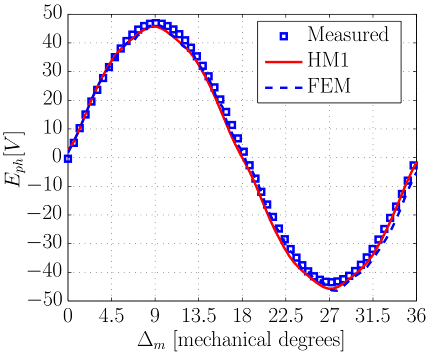

Figure 8.5: Modeled and measured prototype phase back-emf at $1000[rpm]$.

8.3.2 Verification of electromagnetic torque

Electromagnetic torque, T_{em}, of the prototype is measured by loading it with M2 at a constant speed of $1[rpm]$, for the designed current density in Chapter 7. For the skewing effect, cogging torque calculated by HM1 is subjected to (7.4). The comparison between modeled and measured T_{em} values is shown in Fig. 8.6a. The average value of the measured torque, i.e. rated, is in a very good agreement with the modeled ones with only 0.39% discrepancy. However, the torque ripple shows a larger deviation from the modeled due to the dominating inertia of M2, which exhibits a much larger torque ripple than M1. For cogging torque, T_C, estimation, M1 and M2 are mechanically decoupled and a known mass is connected to the shaft of M1 via a force meter (ATI SI-40-2). The mass is subjected to free fall, whereas the force is continuously logged in dSpace. The steady state measurements are used in the determination of the cogging torque as given in Fig. 8.6b, where the maximum T_C is $< 0.02[Nm]$, i.e. $T_C/T_{em} < 0.2\%$. In the verification of E_{ph} and T_{em}, prototype is operated at start-up conditions before the derating commences due to thermal effects, which are evaluated in Chapter 8.4. Prior this analysis, thermal model, introduced in Chapter 6 and implemented for prototype design in Chapter 7, is experimentally evaluated in the next part.

8.3.3 Verification of thermal model

To estimate the operational limits of the prototype during the design phase, a thermal model has been created based on TEC introduced in Chapter 6.5. In this part, the created TEC is verified at a constant power dissipation. The measurement is performed over a time interval of approximately three hours, where the rotor of the (current controlled) prototype is moved externally with the load motor M2 at a constant speed of $200[rpm]$. During the experiment, the ambient temperature has fluctuated around $2-3[°C]$. As discussed in Chapter 6.5.1, ther-

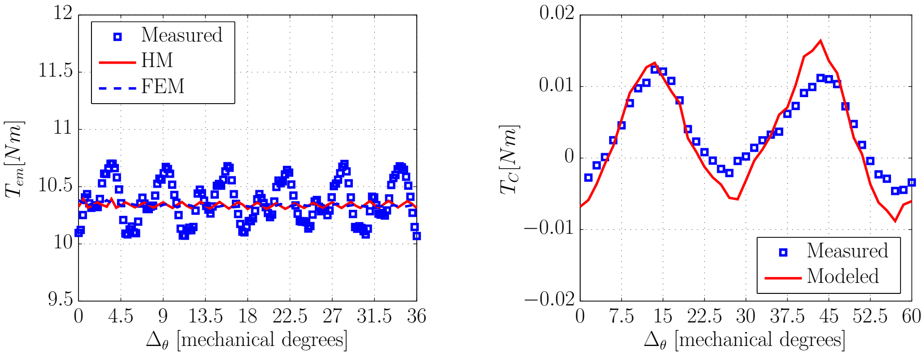

a) b)

Figure 8.6: Modeled and measured prototype for a) electromagnetic torque, T_{em}, at $1[rpm]$, and b) cogging torque, T_C.

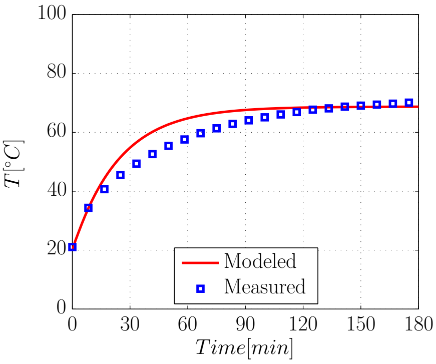

Figure 8.7: Modeled and measured prototype at $200[rpm]$ with an ambient temperature of $T_a = 20[°C]$.

mal conductivity of the insulation material in the coil region is updated for the final prototype as $\lambda_r = 0.7[Wm^{-1}\ °C^{-1}]$, as well as the fill factor to $k_f = 0.42$. Furthermore, the outer (natural) convection coefficient is empirically determined as $h_o = 5[Wm^{-2}\ °C^{-1}]$ under laboratory conditions and the thermal conductivity of air, λ_{air}, is updated according to the new airgap length, g, using (D.16). The results in Fig 8.7 show that an adequate approximation is achieved in steady state with a discrepancy of $< 2[°C]$, whereas prototype's transient thermal behavior is captured. The difference results from the assumptions summarized in Chapter 6.5. Among these, the main cause is likely to be the neglect of the contact resistance between the stator core and the frame. This interface tends to have a reasonable thermal conductivity if a shrink-fit into the aluminium casing is employed [132]. Following sections focus on the performance comparison between prototype and benchmark for high acceleration.

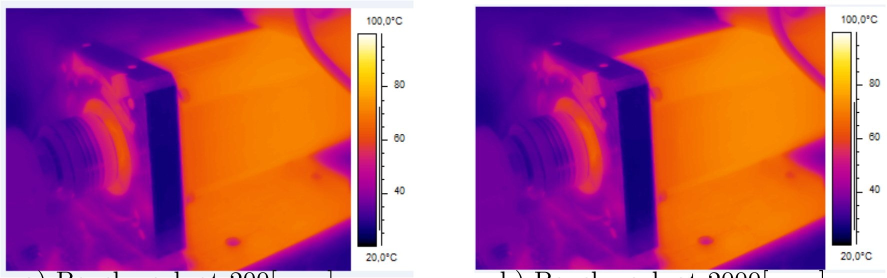

a) Benchmark at 200[rpm] b) Benchmark at 2000[rpm]

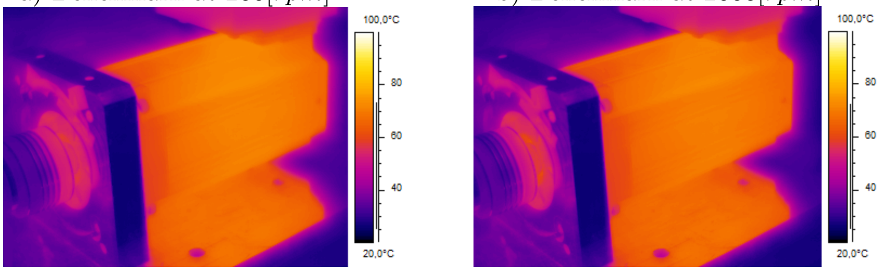

c) Prototype at 200[rpm] d) Prototype at 2000[rpm]

Figure 8.8: Benchmark and prototype motors during thermal tests at a constant housing temperature of $T_h = 60[^\circ C]$.

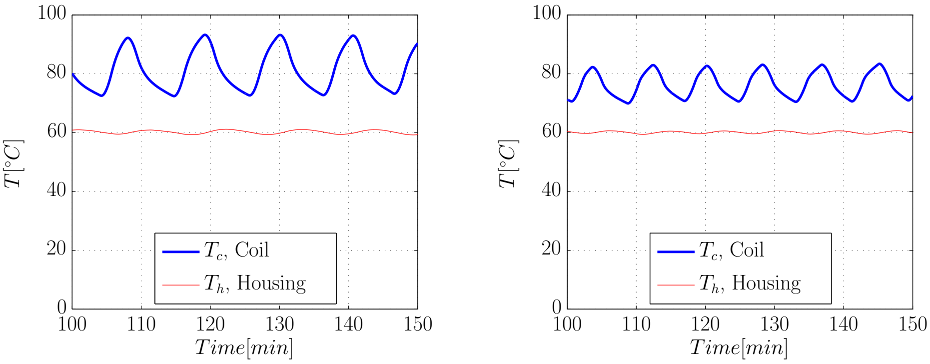

a) b)

Figure 8.9: Regulated housing temperature for $T_h = 60[^\circ C]$ and coil temperature, T_c, in steady state for a) benchmark, and b) prototype motors.

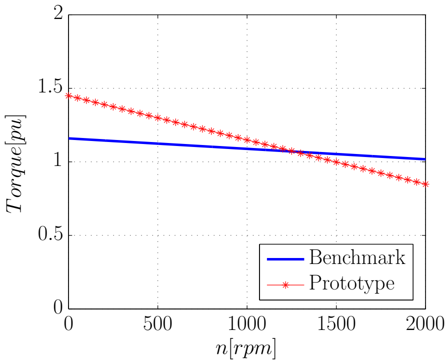

Figure 8.10: Normalized derating torque-speed characteristic of benchmark and prototype motors during thermal tests at constant housing temperature of $T_h = 60[°C]$.

8.4 Thermal performance evaluation

The applicability of PM-biased salient machines for high acceleration can be quantified by their performance in comparison to the benchmark. For this evaluation, prototype has been constrained in Chapter 6.2.4 to identical power dissipation, i.e. equal housing (frame) temperature. Thus, performance assessment of prototype is discussed in this section based on torque-speed measurements performed and compared with the benchmark motor. Due to copper (P_{Cu}), iron (P_{Fe}) and eddy current induced PM ($P_{e,PM}$) losses, heat is generated in the motor, from which P_{Fe} and $P_{e,PM}$ grow exponentially causing a derating in torque production. This effect is evaluated over constant power dissipation of frame. To obtain this analysis, housing temperature, T_h, has been regulated to keep a constant average value over the speed range. Steady state housing and coil, T_c, temperatures are shown in Fig. 8.9, where T_c shows a higher oscillation compared to T_h. The thermal control is performed via the regulation of torque request, therefore response time of T_c is much faster compared to T_h. Both motor's thermal conditions are also pictured thermally in Figs. 8.8a-d for $T_h = 60[°C]$, indicating only slight fluctuations due to the thermal flux formed around motor during measurements. Based on these conditions, torque measurements are conducted both for prototype and benchmark at various speeds.

The typical torque-speed characteristics of a high-acceleration motor has a derating characteristic due to the losses increasing with speed, i.e. P_{Fe} and $P_{e,PM}$. This characteristic is in fact an exponentially decreasing function, where the exponent depends on the motor type and operating temperature, that is normally supplied as a linearized function by most manufacturers (Fig. 6.2b). A similar approach is performed in the thermal comparison of the motors performance at $T_h = 60[°C]$ and the results are normalized around the design torque value pre-

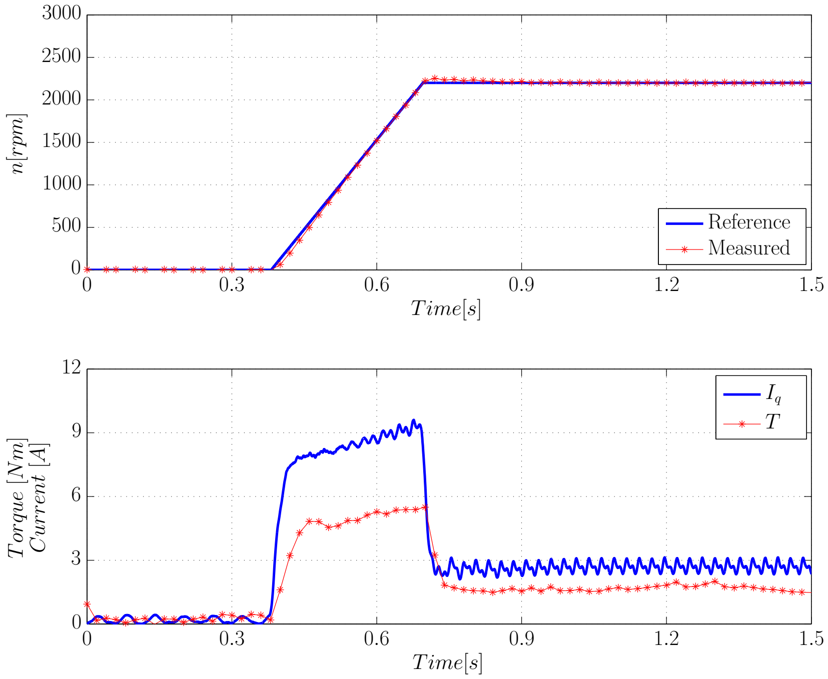

Figure 8.11: Speed profile and torque(T)-current(I_q) response of prototype at $I_d = 0$.

sented in Chapter 7. Results Fig. 8.10 indicate a higher stall torque, T_0, for the prototype motor compared to the benchmark motor. As the speed increases at constant power dissipation, this advantage diminishes due to the double frequency of prototype, i.e. faster increasing losses compared to benchmark. Conclusively, the acceleration (based on mass-based inertia) of the prototype is 30% higher for T_0 values compared to the benchmark. Following the thermal performance evaluation, next section focuses on their dynamic performances for a given motion profile to evaluate their acceleration capability.

8.5 Dynamic performance evaluation

A smooth and fast tracking of a given motion profile defines the dynamic performance evaluation between prototype and benchmark. In this context, both the smoothness of torque response and dynamic inertia measurement are evaluated in this section. Therefore, the speed profile of a reduced-order spindle-drive given in Chapter 6.2.2 and the tracking response of prototype are shown in Fig. 8.11

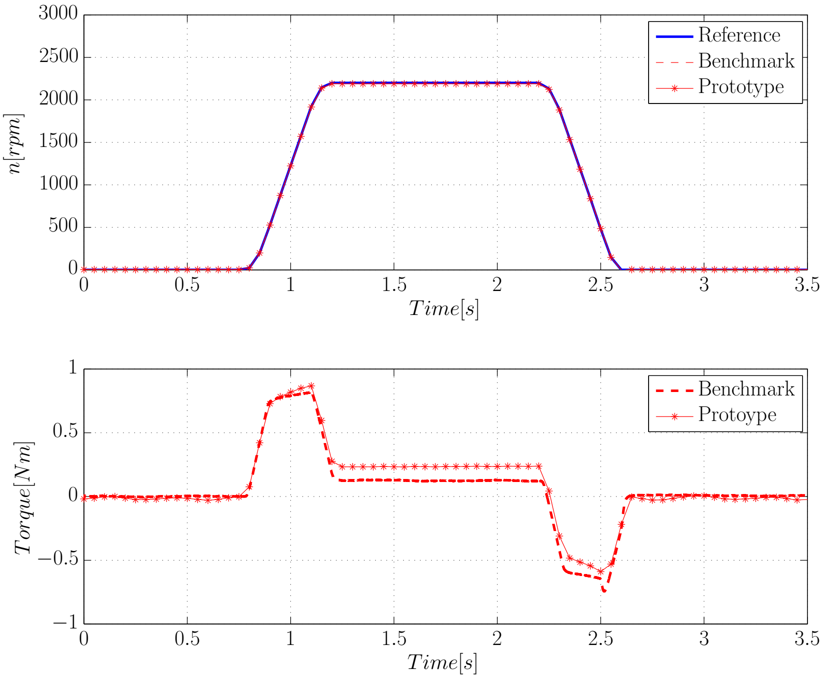

Figure 8.12: Speed profile implemented by load machine and torque response of benchmark and prototype motors to investigate the effect of virtual (loss-based) inertia.

along with current and torque responses. Despite the salient airgap of FSPM, the prototype exhibits a highly dynamic speed and smooth torque profile due to the design methodology discussed in Chapter 7.1. Next, dynamic inertia measurements are performed by implementing the speed profile on the load machine M2. From the resulting torque and acceleration, the inertia of M1 is calculated both for benchmark and prototype motors. Following the measurements in Fig. 8.12, a 15% increase in inertia of benchmark is observed compared to its mechanical (mass-based) inertia. In the case of the prototype, the effect of virtual (loss-based) rotor inertia is higher with 34% increase compared to its mass-based inertia estimated by (7.2). Despite the increase in the prototype, the overall acceleration of the prototype is still 23% higher than the benchmark.

8.6 Summary and conclusions

In this chapter, the construction and experimental verification of the flux switching permanent magnet machine prototype have been presented to assess its performance in high-acceleration applications. The assessment of the prototype has been based on a comparative analysis with an industrial benchmark motor solution.

The suitability of an electrical machine for a certain application is best demonstrated by quantifying its performance in a comparison to a state-of-the-art solution, i.e. a benchmark motor. Hence, a skewed prototype, designed in the previous chapter, has been constructed to assess the performance of PM-biased salient machines for high acceleration versus the benchmark motor. Modeled and measured average torque and back-emf calculations have illustrated a small, $< 1\%$ respectively, discrepancy. With continuous rotor skewing, cogging and torque ripple have almost been eliminated, as illustrated by the 0.2% deviation between measured and modeled values. Furthermore, it has been determined that an empirically-tuned thermal equivalent circuit model, for constant power dissipation (at constant speed) and in steady state, provided temperatures within a deviation of $2[°C]$ between measured and modeled values. An improved result can be achieved if the interface between stator and frame is represented by a contact resistance in the thermal equivalent circuit. Measurements have illustrated that the prototype has achieved a 30% increase in acceleration (based on the mechanical (mass-based) inertia) compared to the benchmark motor, under identical thermal conditions (power dissipation). Dynamic inertia measurements (including the effect of virtual (loss-based) inertia) have been conducted on both machines using a reduced-order spindle-drive speed profile, illustrated by an increase of 23% in acceleration.

The results presented in this chapter have proven the applicability of hybrid models, the design formulations and flux switching permanent magnet machines' dynamic capability. The combined results of a higher stall torque and a lower inertia indicate a higher dynamic acceleration capability of the prototype compared to the benchmark motor.

Part III

Closing

Chapter 9

Conclusions and recommendations

"All good things must come to an end." – Q (All Good Things...)

* * *

Accurate and fast electromagnetic field prediction is essential to design permanent-magnet-biased (PM-biased) salient machines that are ready to face the future. Within this thesis, various modeling methods have been discussed with a specific focus on the employment of pairing electromagnetic modeling techniques, i.e. hybrid modeling, as has been portrayed in Part I. Consequently, Part II has been dedicated to the design aspects of a particular PM-biased machine, namely, a fast-accelerating skewed 3-phase 12/10 flux switching PM motor, for practical corroboration of these hybrid models. In this closing chapter, the main conclusions have been extracted with relation to the defined research objectives. Finally, the scientific contributions of the thesis have been addressed and recommendations are provided for future research.

* * *

9.1 Conclusions of Part I

In Part I, three differently configured hybrid modeling techniques have been proposed for the analysis of PM-biased salient machines. These hybrid models (HM) have first been introduced on a reduced-order case study, i.e. a double salient structure with a complex airgap. Thereafter, each HM has been successfully applied to a 3-phase 12/10 flux switching permanent magnet (FSPM) motor. An overview on the performance of the models, presented at the end of Part I, has resulted in the selection of one particular HM for the design of the FSPM.

Combining methods to model double salient structures

An alternative approach to solving either the first-order partial differential Maxwell equations or the second-order partial differential Poisson and Laplace equations has been introduced in Chapter 1. This has been attained by pairing mathematical approaches with different levels of abstraction into *hybrid* models. The approach has focused on the modeling of structures with an unbound and salient airgap, which comprises elements with a relative permeability close to that of air, i.e. mechanical airgap, PM and coil for PM-biased salient machines. Each hybrid model has been evaluated based on its overall accuracy in Chapters 2-4.

Hybrid model 1 (HM1):
Fourier analysis and magnetic equivalent circuit

Models based on the (semi-)analytical harmonic modeling technique, i.e. Fourier analysis (FA), have been praised for their accuracy and short simulation time. However, if model saliency is extreme, e.g. in terms of slot depth-to-airgap length ratio, its accuracy is compromised in close proximity to boundaries. Further, in salient structures with a very small airgap length, results in the airgap have been compromised. Consequently, a reluctance network model, i.e. magnetic equivalent circuit (MEC), has been paired in the hybrid model to reduce these inaccuracies in double salient structures, as discussed in Chapter 2. The resulting hybrid model, i.e. FA paired with MEC, has been denoted as HM1.

Hybrid model 2 (HM2):
Tooth contour and electrostatic finite element methods

To allow more accurate modeling near the boundaries, HM1 has been replaced by a hybrid model comprising of the tooth contour method (TCM) paired with an electrostatic finite element method (eFEM). TCM advances MEC to a finer airgap permeance discretization, and therefore provides a more detailed estimation of leakage and fringing fluxes. This allows the inclusion of a larger number of permeances between the double salient airgap boundaries, forming a complex airgap. To model these permeances located between the boundaries (tooth contours), scalar potentials have been defined using an electrostatic FEM (eFEM), as discussed in Chapter 3. The resulting hybrid model, i.e. TCM paired with eFEM, has been denoted as HM2.

Hybrid model 3 (HM3):
Tooth contour method and Schwarz-Christoffel mapping

Both HM1 and HM2 include methods, FA and eFEM respectively, that require definition of boundary conditions resulting in reduced accuracy near the boundaries. An alternative approach, discussed in Chapter 4, is to unite the boundaries of the original structure to a mapped equivalent rectangular region, i.e. only four boundaries have to be used, and thus no accuracy is lost. This transformation has been realized by a conformal mapping technique, Schwarz-Christoffel (SC), replacing eFEM in the HM2 construction. Consequently, airgap permeances have been calculated by applying the orthogonal field theory. The resulting hybrid model, i.e. SC paired with TCM, has been denoted as HM3.

Performance evaluation of hybrid models

Hybrid modeling techniques, introduced in Chapters 2-4, exhibit various advantages and disadvantages when applied to the studied structures, the case study and the FSPM. The following evaluations result from a comparison of their performance, summarized in Chapter 5, in terms of accuracy, simulation time, inclusion of a nonlinear BH-characteristic, end effects and design flexibility:

In terms of accuracy: The model accuracy has been evaluated for extreme saliency, i.e. a high ratio of slot depth-to-airgap length, introduced in Chapter 2.2.2, and for moderate saliency introduced in Chapter 2.5. In the extreme case, FA results have deviated from FEM by $< 16\%$. With the integration of MEC, HM1 has decreased the difference to $< 8.5\%$. By advancing MEC by TCM, the accuracy of results obtained by HM2 and HM3 have been further improved to a discrepancy of $< 1.4\%$. If the structure does not exhibit an extreme saliency, all HMs have performed well within a discrepancy of $\sim 5\%$ compared to FEM.

In terms of simulation time: The simulation time for both structures, i.e. the case study and FSPM, has yielded similar results. For the modeling of the FSPM discussed in Chapters 2.5-3.4-4.3, all HMs have resulted in a shorter simulation time than FEM. In HM3, the sub-models have been paired within one software environment, leading to an improved simulation time compared to HM2, without diminished accuracy. As such, HM1 has shown an improvement of up to four times shorter simulation time than FEM, whereas HM2 has shown an improvement of 13% and HM3 an improvement of 20%, respectively.

In terms of including a nonlinear BH-characteristic: For the studied structures in Chapters 2-4, all HMs have been implemented as linear magnetic models. The specific structure of an FSPM can stipulate a switching high flux density pattern in the airgap, hence necessitating a nonlinear model if not constraint in the design by maximum flux density levels. In such cases, HMs could be extended to allow for nonlinear effects. An example has been shown in Appendix B, where a nonlinear BH-characteristic of the soft magnetic material is included in HM1.

In terms of end effects: End effects are an important part of machine design. This effect has been included in Chapter 6.3.9 by means of a correction factor. Analytically, all models except for SC (HM3) could be implemented in the 3D analysis of PM-biased salient machines, however this falls outside the scope of this thesis.

In terms of design flexibility: The analyses for extreme saliency in Chapters 3.3-4.2 have revealed that HM2 and HM3 are suitable methods to represent new salient or nonsalient structures. This option is limited in HM1 due to the discrete behavior of MEC.

In conclusion, in terms of accuracy for extreme saliency and design flexibility, HM2 and HM3 stand out for the modeling of devices with a comparable structure and physical qualities as PM-biased salient machines. In terms of short simulation time, HM1 performs the best. For modeling of a PM-biased salient machine, discussed in Part II, HM1 has been opted because of its speed. Considering the volumetric design constraints and material tolerances, the accuracy problem of HM1 has been deemed not to be a drawback.

9.2 Conclusions of Part II

Designing new classes of electrical machines is an elaborate process, since insight into the physical phenomena is required. This need has led to the introduction of the HM techniques in Part I. To research the underlying principles and for practical corroboration of these techniques, Part II of this thesis has focused on researching a design routine for a specific PM-biased machine structure, i.e. an FSPM dedicated to high-acceleration applications.

Design considerations of PM-biased salient machines for high acceleration

To determine whether a machine is suitable for a certain application is by any means a cumbersome and subjective task. Within this thesis, the applicability of a PM-biased salient machine in high acceleration is evaluated based on a comparative acceleration performance. Therefore, in Chapter 6, a newly-designed PM-biased salient machine, i.e. FSPM, is paralleled with a state-of-the-art industrial *servo* machine, i.e. a brushless PM (PMAC) motor with good acceleration capability. This paralleled performance evaluation has restricted the design space to similar volumetric (stator volume), electrical (maximum phase voltage, phase number), mechanical (maximum speed, bearings, shaft), and thermal (frame, power dissipation) design constraints. Based on these constraints, electromagnetic design equations for the FSPM have been derived and extended to include the most relevant mechanical and thermal considerations. Although the rotor is salient in nature, the (phase) inductance has illustrated very little position dependency. Thus, the presented electromagnetic design considerations have shown vast similarities to PMAC machines, albeit the winding area is compromised by PMs which are offsetted by flux focusing to elevate the airgap flux density. Furthermore, the design requirements of a high-acceleration motor have been identified as minimizing mechanical (mass-based) inertia, maximizing stall torque, maximizing the overloading capability, and offering a smooth torque profile with a maximum torque ripple of $1 - 1.5\%$. For this analysis, a general mechanical inertia formulation has been presented for the FSPM along with a thermal model, based on thermal equivalent circuits (TEC), to estimate operational limits.

Design parameters of PM-biased salient machines for high acceleration

The design of an electrical machine requires a multidimensional approach due to the interdependence of its parameters and the various design requirements. The complexity of the optimization process is reduced in Chapter 7 by introducing certain parameter ratios. For the newly-designed FSPM, i.e. the prototype, the split ratio, the stator tooth width ratio, and the rotor tooth inner ratio have been determined to be key design parameters in terms of maximization of acceleration and stall torque. To note, the stator tooth width ratio has enabled variation of FSPM structures to improve torque production within the chosen design constraints. Among the investigated motor structures, one final candidate has been selected for the rotor design to achieve a smooth torque profile. A continuous rotor skewing for torque ripple minimization and triangular-shaped holes for *mass-based* inertia minimization have been proven optimal. However, mass-based inertia is not the only component affecting the acceleration capability. Another important design parameter is the *virtual* (loss-based) inertia related to the magnetic resistance of the rotor due to iron losses, air friction (windage) in airgap and mechanical friction between moving (rolling) elements.

Demonstration of the applicability of a PM-biased salient machine for high acceleration

Electrical machines for a certain application can be best demonstrated by quantifying their performance in comparison to a state-of-the-art solution, i.e. a benchmark motor. Hence, a skewed FSPM prototype has been constructed to assess the performance of 'PM-biased salient machines for high acceleration' versus the benchmark PMAC motor, as discussed in Chapter 8. Modeled and measured average torque, and back-emf calculations have illustrated a small, 1% respectively, discrepancy. With continuous rotor skewing, cogging and torque ripple have almost been eliminated, i.e. there remains only a 0.2% deviation between the measured and modeled values. Furthermore, an empirically-tuned TEC model has provided temperatures varying within $2[^\circ C]$ from the measured value, for a constant power dissipation (at constant speed) and in steady state. Additional measurements have illustrated that the FSPM prototype has achieved a 30% increase in acceleration (for mechanical (mass-based) inertia) compared to the benchmark motor under identical thermal conditions (power dissipation). Dynamic inertia measurements (including the effect of virtual (loss-based) inertia) have been conducted on both machines using a reduced-order spindle-drive speed profile, illustrated an increase of 23% in acceleration.

9.3 Thesis contributions

The models presented in Part I - MEC, FA, TCM, SC and FEM - are not new nor are the implementations of MEC, FA and FEM for double salient FSPM or the concept of hybrid modeling. No contributions have been made with respect to the theory and mathematics of the discussed modeling techniques. The combination of these models, however, is unique for FSPMs. The following scientific contributions follow:

- *Development of hybrid models for more accurate electromagnetic modeling for a small airgap in double salient structures.* The proposed methods increase the functionality of the design tool by utilizing each algorithm's respective strength to reduce design uncertainties such as discontinuity, lowered accuracy near boundaries, material properties or manufacturing tolerances.
- *Application of hybrid models to a PM-biased salient machine.* The models are applied to a PM-biased salient machine topology, and take account of the effects of flux switching, flux focusing, slotting and cogging.

The parameter variations and optimization procedures of an FSPM presented in Part II are not new for single optimization problems, such as torque maximization. However, the applicability of an FSPM in high acceleration has not, to the author's knowledge, yet been presented in the context of dual optimization problems, i.e. maximization of torque output and minimization of inertia. Although improvements have been achieved, the design strategy has not been primarily intended to find the optimal machine configuration, but rather to evaluate each parameter's contribution to the demands of the application. During the practical verification stage, no contributions were made in terms of hardware and control algorithms, but a detailed assessment of an FSPM has been undertaken to determine its advantages and limitations compared to a state-of-the-art industrial motor solution. The following scientific contributions have been derived from these comparisons:

- *Evaluation of design rules for PM-biased salient machines for high acceleration.* Electromagnetic, mechanical and thermal design considerations are evaluated according to the requirements of high acceleration. General inertia equations are formulated for an FSPM. The key design parameters are identified in terms of acceleration, torque profile and thermal overloading capability. Structural solutions, such as rotor skewing and triangular-shaped holes, are provided for this class of machines to achieve a high acceleration under the effects of slotting and cogging.
- *Demonstration of the relevancy of PM-biased salient machines in applications requiring a high acceleration.* A prototype has demonstrated the suitability of a PM-biased salient machine in high acceleration. Thermal and dynamic characteristics have showed superior performance compared to an industrial solution. The assessment has included a study on the effect of the virtual (loss-based) inertia.

9.4 Recommendations for future work

Historically, electromagnetic modeling and machine design have been some of the most fundamental, yet still challenging, topics in the field of electrical engineering. For new machine classes such as PM-biased salient machines, disparity remains between their theoretical and experimental analysis. This thesis has been dedicated to making *a research effort* to close this gap. The following recommendations are provided for future research related to Part I and Part II of the thesis, respectively.

Recommendations of Part I

- *Incorporation of magnetic nonlinearity:* Local magnetic saturation is a phenomenon observed in FSPMs, thus a high magnetic loading could limit the selection of applicable modeling techniques. One approach has been presented incorporating the nonlinear first quadrant BH-characteristic to HM1 using an iteration loop based on MEC. For HM2 and HM3, TCM consists of an identical network as MEC, except for the airgap. Therefore, the nonlinear iteration loop used for HM1 could be adapted to HM2 and HM3 as well. To improve simulation time, the same effect could also be realized by adapting the airgap permeance function. For an adequate comparison, all hybrid methods should be upgraded to incorporate magnetic nonlinearity and compared to each other to determine which method best supports the nonlinearity. The solution provided in this thesis could be generalized, such as by incorporating the effect of different magnetization directions, or by investigating the minor BH-loops occurring locally in stator and rotor. Such solutions could also further enlighten the energy conversion mechanisms in FSPMs.
- *Analysis of end effects:* End effects, both in the radial and axial direction, are an important part of machine design, and have been included in this thesis in the form of a correction factor related to flux linkage. Its calculation has been performed using a very time consuming FEM, therefore it is recommended that an analytical approach be incorporated into the hybrid modeling technique in the future.

Recommendations of Part II

- *Study of the torque production mechanism in FSPM:* In this thesis, an attempt has been made to describe the working principle of flux switching machines; however, no direct mathematical relationships have been provided between the physical motor parameters and the electromagnetic torque. Such a study on the torque production mechanism would certainly improve the understanding of the underlying physical interactions in the machine and the design process for various applications.
- *Machine design with energy conversion loops:* A brief introduction to the topic of energy conversion loops has been made in this thesis. Until now, these loops have been defined for known machine types, which are either represented by global loops for the whole machine, or local loops focusing on certain parts of the machine. By investigating the contribution of each local loop to the overall energy change, the torque production can be estimated, thus a more effective machine design approach could be achieved.
- *Mathematical definition of virtual (loss-based) inertia:* The effect of virtual (loss-based) inertia has been determined to influence the acceleration of

FSPMs. A mathematical definition of this effect could enhance the design rules for high-acceleration applications. Including this effect under identical thermal operation conditions, as in this thesis, would certainly create an improved basis for the performance evaluations in dynamic applications.

- *Control, motion profile and efficiency issues:* The control aspects in this thesis have been kept at a general level to provide an identical basis of comparison for the investigated machines. Certainly, with dedicated control algorithms an improved motor performance could have been achieved; for example, by implementing certain current harmonics, the torque ripple could be eliminated as an alternative to the rotor skewing proposed in this thesis. Furthermore, increasing the complexity of the considered motion profile (spindle cutter) would also create a greater dynamic challenge for the performance assessment. Additionally, an overall efficiency analysis of the motor and controller could be helpful in this assessment. In this efficiency analysis, it can be useful to consider the particular problems of frequency dependent contributions to copper loss in terms of nonuniform sharing of current between parallel paths, nonuniform current distribution within an individual conductor due to eddy currents, and induced eddy currents within the conductor bundle as a result of incident-time varying fields.

Appendix A

Postulate

A high percentage of today's electrical machines operate within low frequencies represented by static and/or quasi-static fields. Significant works in the classic electromagnetic field theory, electrodynamics, were conducted by Ampère, Faraday and Gauss, who presented their findings in four integral equations [3].

Original equations

Ampère's law states:

$$\int_C \mathbf{H} \cdot d\mathbf{l} = \int_S \mathbf{J} \cdot d\mathbf{S} = \mathcal{F}, \tag{A.1}$$

where **H** is the magnetic field strength along a closed path, C, due to a current carrying conductor with a current density, **J**, through the surface, S. In the original equation of (A.1), there is an addition to **J**, $\frac{\partial \mathbf{D}}{\partial t}$, resulting from time varying of electrical flux density, **D**. For the field frequencies in electrical machines, this term becomes obsolete. Using $\mathcal{F}$, (2.5) can be related to (A.1), where in fact electrical energy is transformed to magnetic energy.

Regarding the nature of magnetic fields, the magnetic Gauss' law states:

$$\oint_S \mathbf{B} \cdot d\mathbf{S} = 0, \tag{A.2}$$

where flux paths form closed surfaces, S, with different flux densities, **B**.

From energy transformation point, the counter part of (A.1) is Faraday's law [4,5]:

$$\int_C \mathbf{E} \cdot d\mathbf{l} = -\frac{d}{dt} \int_S \mathbf{B} \cdot d\mathbf{S} = -\frac{d\Phi}{dt}, \tag{A.3}$$

where **E** is the electrical field strength. The difference between the static and quasi-static fields is apparent in (A.3). The right side of the equation becomes zero for static field due to the absence of eddy (Foucault) currents, which are caused by time varying **B**.

The law is regarding the nature of electrical fields, where Gauss stated:

$$\oint_S \mathbf{D} \cdot d\mathbf{S} = \int_V \rho d\mathbf{V}, \tag{A.4}$$

where ρ is free electrical volume charge density of the volume, V.

Maxwell's equations

Maxwell redefined and unified (A.1-A.4) later in closed form partial differential equations as [9]:

$$\nabla \times \mathbf{H} = \mathbf{J}, \tag{A.5}$$

$$\nabla \cdot \mathbf{B} = 0, \tag{A.6}$$

$$\nabla \cdot \mathbf{E} = \frac{\partial \mathbf{B}}{\partial t}, \tag{A.7}$$

$$\nabla \times \mathbf{D} = \rho. \tag{A.8}$$

To solve these equations, additionally geometric simplifications (symmetries, periodicities), boundary conditions and constitutive relationships are necessary. For example, by introducing the magnetic vector potential, **A**, **B** can be written as:

$$\mathbf{B} = \nabla \times \mathbf{A}. \tag{A.9}$$

Using the constitutive relation:

$$\mathbf{B} = \mu_0 \mu_r \mathbf{H} + \mu_0 \mathbf{M}, \tag{A.10}$$

where μ_0 is the air permeability, μ_r is the relative permeability of the concerned medium and **M** is the magnetization vector, (A.5-A.6) can be written together as the Poisson equation:

$$\nabla^2 \mathbf{A} = -\mu_0 (\nabla \times \mathbf{M} + \mathbf{J}). \tag{A.11}$$

Appendix B

Nonlinear modeling

One approach to include the nonlinear BH-characteristic in hybrid modeling is using a reluctance network model. For the nonlinear magnetic equivalent circuit (MEC), the soft magnetic material with $\mu = \frac{dB}{dH}$ behavior in $B = \mu H$ is linearized in intervals, and magnetic flux is assumed to enter iron perpendicular in each linearized interval. The second assumption might contradict the nonperpendicular flux lines in nonlinear magnetic structures; however, in the nonlinear system representation this assumption is applied not locally but globally. An exemplary BH-curve of the soft magnetic material is shown in Fig. B.1a.

Nonlinear system representation

To solve the nonlinear system of equations, the BH-curve is discretized into small intervals. In each interval, a linearization is performed with a line function in form of (B.1). Following the discretization, $B = \mu H$ takes the form of (B.1) and the BH relationship becomes linear in the intervals indicated as red dotted tangent lines in the Fig. B.1a. In these intervals, flux entering the soft magnetic material is assumed to be perpendicular, therefore only the normal component of B is taken into account in MEC with the following relationships:

$$B_{Fe} = B_0 + \mu_0 \mu_{Fe} H_{Fe}, \tag{B.1}$$

$$\mathcal{F}_0 = \frac{B_0 l_{Fe}}{\mu_0 \mu_{Fe}}, \tag{B.2}$$

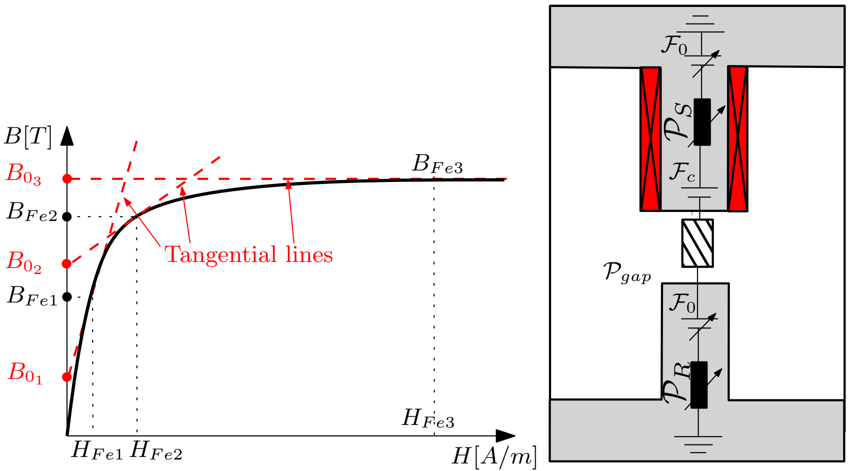

a) b)

Figure B.1: a) Typical nonlinear BH-curve of a soft magnetic material. b) Magnetic equivalent circuit of the case study, double salient airgap structure, at $\Delta_x = 0[mm]$ with nonlinear soft magnetic material.

$$\mathcal{P}_{Fe} = \int\limits_{l_{Fe}} \frac{\mu_0 \mu_{Fe} S_{Fe}(l_{Fe})}{dl_{Fe}}, \tag{B.3}$$

where μ_{Fe} is the iron relative permeability, and l_{Fe} the length of the flux tube in iron with the cross section, S_{Fe}. The BH-curve values of the soft magnetic material are represented by (B_{Fe}, H_{Fe}) as shown in Fig. B.1a. In the linearization, (B.1) is used similar to the $B(H)$ relationship of hard magnetic materials, i.e. of PMs. In the presence of external magnetic fields, localized hard magnetic domains in microscopic level occur inside the soft magnetic material. The nonlinear soft magnetic material has a remanent permeance, B_0, due to this external field, which acts as an *internal mmf* source, $\mathcal{F}_0$. This source is shown in Fig. B.1b in series with the iron permeance, $\mathcal{P}_{Fe}$, i.e. $\mathcal{P}_S$ and $\mathcal{P}_R$. For the nonlinear analysis in Fig. B.1b, the resulting flux density in the same region is $B_{mec} = 0.995[T]$, whereas $0.952[T]$ is obtained by nonlinear FEM with M270-35A, leading to a 4.6% difference.

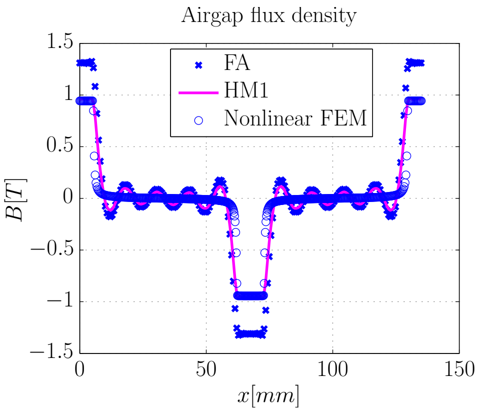

Figure B.2: Normal component of airgap flux density calculated by the Fourier model, HM1 and finite element method for the nonlinear structure in Fig. B.1b.

Modeling of case study

Nonlinear HM1 is verified by comparing the airgap field calculations with FEM, as shown in Fig. B.2. As a reference, FA calculation is also included in the linear analysis resulting obviously higher flux densities with the initial airgap size, $g_{ini} = 0.5[mm]$. For HM1 with adapted airgap length, the results have similar characteristic as FA except for the region over stator-rotor tooth alignment. The 4.6% discrepancy at this peak is due to the difference between nonlinear MEC and FEM.

Modeling of FSPM

The nonlinear MEC is limited to one rotor position in the open-circuit analysis as explained in Chapter B. As such, field calculations using MEC, $B_{mec}(\theta)$, in Fig. B.4a-b capture the linear and nonlinear behavior as verified with FEM. In both cases, the highest discrepancy is smaller than $0.2[T]$ observed at field values $B_{mec}(\theta) > 1$.

MEC is constructed based on the normal component of airgap flux density, hence according to (2.2) $B_{fa}(\theta) = B_p(q)$ is considered for the FA calculation, which is verified in Fig. B.5 with FEM in the center of the airgap. Due to the higher accuracy of FA, FA-FEM agreement is visibly improved compared to the linear MEC-FEM agreement in Fig. B.4a. However, in Fig. B.5b, this agreement is lost because FA cannot yet take into account saturation of the soft magnetic material. Consequently, the discrepancy between the rms-values of FA and FEM rises extremely from 0.67% to 29.16%. The positions, where FA and FEM results differ,

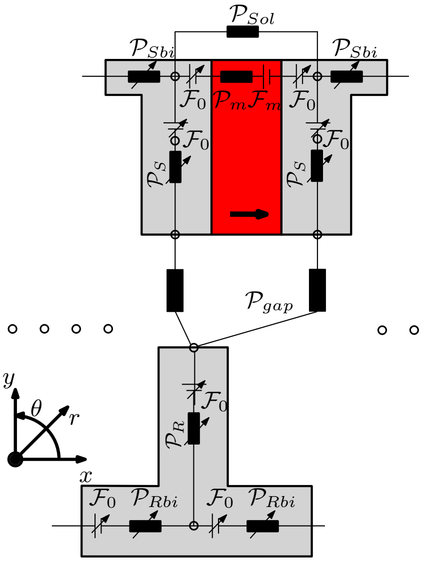

Figure B.3: Simplified nonlinear magnetic equivalent circuit for one elementary cell.

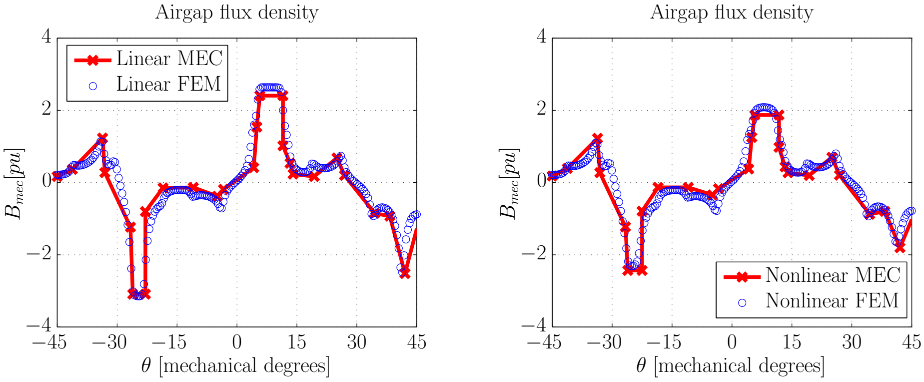

a) b)

Figure B.4: Open-circuit airgap B_{mec} comparison between magnetic equivalent circuit and finite element method for rotor at $\Delta_\theta = 9°$ in the a) linear, and b) nonlinear magnetic analysis.

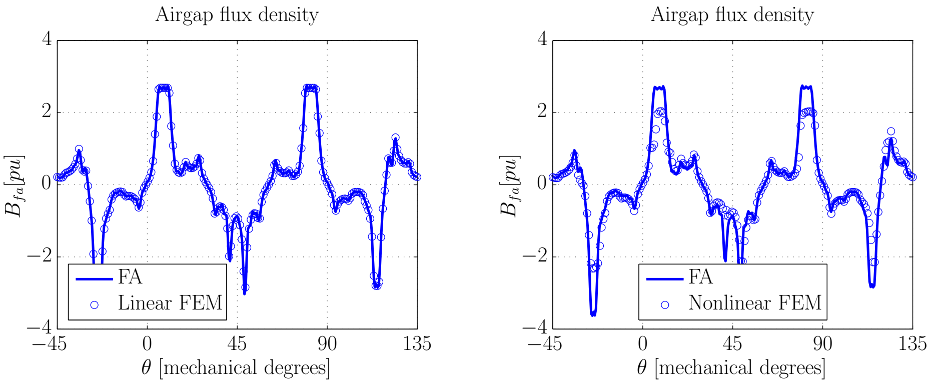

a) b)

Figure B.5: Normal component of B_{fa} comparison in the center of airgap including the armature reaction for rotor position $\Delta_\theta = 9°$ in a) linear Fourier analysis and b) nonlinear Fourier analysis in the modified geometry verified with finite element method in the original geometry.

correspond to the stator-rotor tooth alignment with the highest saturation levels.

Nonlinear solving process

The nonlinear iteration loop is shown in Fig. B.6. The elementary cell of the FSPM, shown in Fig. B.3, is extended in MATLAB code to three cells to achieve the required symmetry. Differential permeability, $\mu_{dif} = \frac{\Delta B}{\Delta H}$ (with $\mu_{dif} = \mu_{Fe}\mu_0$), and the extrapolated value, B_0, of each interval are determined in each iteration step. Before the iterative calculations, the initial values for μ_{dif} of each iron permeance is set to the initial permeability where B and H are zero. In the initial conditions, B_0 values are set to zero, corresponding to the linear operating point at no current ($H = 0$). In the next step, with the new values of μ_{Fe} and B_0, the iron permeances, $\mathcal{P}_{Fe}$, and *internal mmf* source, $\mathcal{F}_0$, are recalculated. Iteration stops once the differential permeabilities in each iron part converge a value after approximately 10-15 iterations for the treated model.

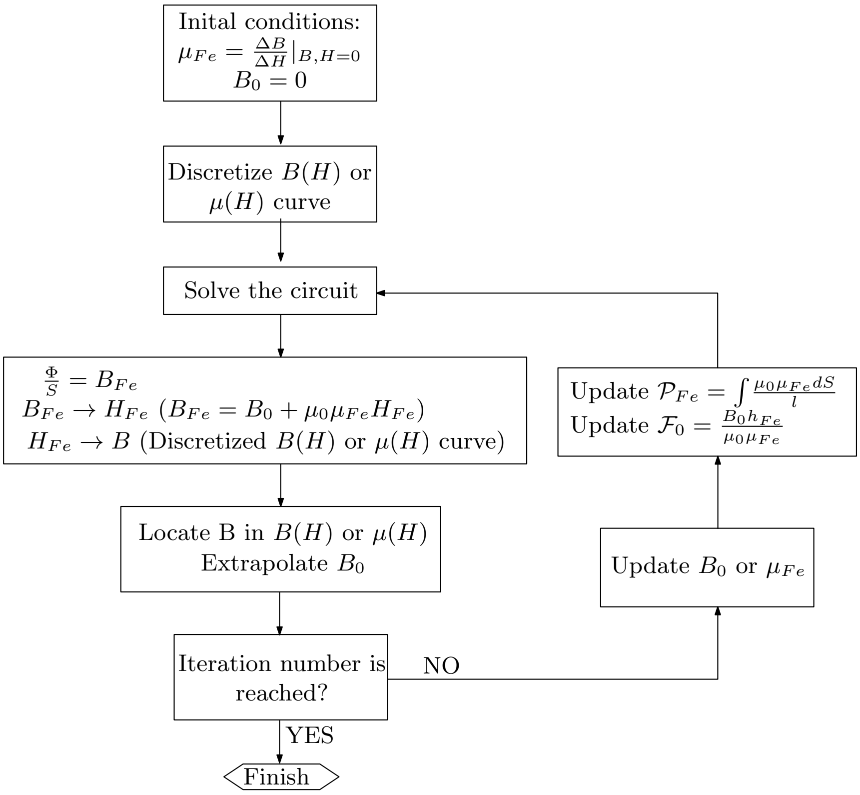

Figure B.6: Flowchart of the nonlinear solving process.

Appendix C

Solving of magnetic equivalent circuit

MEC solving process

MATLAB code used to solve magnetic equivalent circuit (MEC) is explained here on an example. The procedure is based on the node-voltage method. The mesh-current method is also possible to solve such circuits, but the node-voltage method compared to the mesh-current method is more suitable since it not only works in planar but also in nonplanar (i.e. no crossing of the circuit branches) circuits.

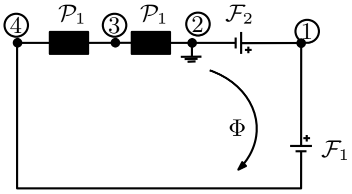

Figure C.1: Example of the magnetic equivalent circuit problem.

In general, for any magnetic circuit $[\Phi] = [\mathcal{P}][\mathcal{F}]$ is valid. The loop in Fig. C.1 can be solved straightforward; however, a MEC of an electric machine consists of many loops and branches. All MEC result in an equation of the form **Ax**=**z**, a linear equation system, since no depending sources exist. The square **A** matrix contains the known quantities, such as permeances, the **x** matrix contains the desired quantities and **z** some constants, i.e. the sources. Furthermore, the size of **A** matrix is $(m + n) \times (m + n)$, where n is the number of nodes and m the number of independent voltage sources. **A** matrix is constructed in four parts as $A = \begin{bmatrix} A_1 & B_1 \\ C_1 & D_1 \end{bmatrix}$, from which only the A_1 and B_1 matrices need to be constructed since C_1 matrix is the transpose of B_1, and D_1 is a square zero matrix (no depending sources). The $(n \times n)$ A_1 matrix is a square permeance matrix only with the passive elements and is based on the following:

- The matrix is symmetric, i.e. $A_1^T = A_1$, thus constructing only the upper or lower diagonal of the matrix is sufficient, and the rest is added as the transpose,
- The permeances on the diagonal of the matrix, A_{1ii} (self permeances), are the sum of all permeances connected to the node i, and
- The off-diagonal elements A_{1ij} (mutual permeances) are the negative of the permeance values between i-j nodes.

The $(n \times m)$ B_1 matrix has only 0, 1 and -1 elements. Each location in the matrix corresponds to a particular node (first dimension) or a voltage source (second dimension). If the positive terminal of the i^{th} voltage source is connected to node k, then the element (i,k) in the B_1 matrix equals to 1. If the negative terminal of the i^{th} voltage source is connected to node k, then the element (i,k) in the B_1 equals -1. Otherwise, those elements of B_1 are zero. For the source matrix, $\mathbf{z}$, the voltage sources have to be sorted either by row-to-row scanning, or column-to-column.

MATLAB code for MEC solving process

In the first step, the known quantities of the circuit are defined, i.e. the mmf sources and permeance values.

```
%% Define sources
F1=2;
F2=2;

%% Define permeances
P1=3;
P2=3;
```

Next, the total number of nodes and the node with the earth connection are defined:

```
nodes=4; % TOTAL NODE NUMBER
earth=2; % NODE WITH EARTH CONNECTION
```

Number of equations necessary per voltage variable is (*nodes*-1). One equation is eliminated due to the presence of the earth node, where the *mmf* voltage is set to zero value. For consistency in the matrix indexes and node numbers, the elimination of this equation is left to the end of the solving process. For the source matrix, first an empty square matrix is created by the size of the node number. As previously mentioned, the square source matrix with the variable F is not $\mathbf{z}$ and it is modified later in the code. The sources are assigned to the indexes with the corresponding node number. The first index is always assigned to the lower node number, this way only the upper half diagonal of the source matrix is filled. This rule is actually based on the filling of the permeance matrix, because this matrix is symmetric. The number of sources is stored in the variable *numsources*.

```
F=zeros(nodes); %SOURCE MATRIX of MMF_s
F(1,2)=F1;
F(1,4)=F2;
numsources=numel(find(F));
```

Next, the permeance matrix is built starting from the upper half diagonal.

```
% Permance matrix
NODE_A=zeros(nodes);
%¬¬¬
NODE_A(2,3)   = P1;
NODE_A(3,4)   = P2;
```

The rest of the permeance matrix is filled based on the symmetry of the matrix, thus $NODE_A$ matrix and its transpose are summed up. After putting the diagonal elements and negating the positive off-diagonal elements, we finally construct the A_1 matrix.

```
NODE_A = NODE_A+NODE_A';%use the symmetry of the permeance matrix
A1 = diag(sum(NODE_A))−NODE_A;%to fill the diagonal elements sum the columns
%and put these to the diagonal elements of the permeance matrix
```

Next, empty B_1 and $\mathbf{z}$ matrices are created:

```
z = zeros(nodes+numsources,1);
B1= zeros(nodes,numsources);
```

For both of these matrices, the information about the location of the source is necessary. They are put in a double for-loop to scan all the elements of the bigger source F loop and locate the nonzero elements of F.

```
k=0;
for row = 1:nodes
    for col = 1:nodes
        if F(row,col)≠0;
            k=k+1; %%counts the sources
            B1(row,k) =  1;
```

```
            B1(col,k) = −1;
            z(nodes+k)      = F(row,col);
        end
    end
end
```

Next, C_1 and D_1 matrices are generated:

```
C1=B1';
D1=zeros(numsources);
```

The larger A matrix comprises these four matrices as:

```
A= [A1 B1; C1 D1];
```

Due to excess equations on the node with earth connection, the corresponding row and columns are deleted from all the matrices.

```
A(earth,:) =[];%delete the  row on the reference node
A(:,earth) =[];%delete the  column on the reference node
z(earth)=[];%delete the  entry on the reference node
```

With a matrix manipulation, the linear system is solved.

```
x=A\z;
```

The unknown matrix, $\mathbf{x}$, contains the nodal voltages of the circuit and the two current values.

```
Nodal_voltages=x(1:nodes−1)
Source_currents=x(nodes:end)
```

The results are:

```
Nodal_voltages =

     2
     0
     0


Source_currents =

     0
     0
```

MATLAB code for Golden Section Method (GSM)

Sample MATLAB code used in the optimization routine of HM1:

```
%% EXAMPLE CODE TO MINIMIZE THE 3rd PREDEFINED ERROR FUNCTION
%(Hybrid Criterion C)
g=0.5e−3; %set to initial value

t=0.38197; %from Golden Ratio
g_low=g; %set to the initial value because it has to get bigger to simulate
%saturation
g_up=2.5*g;
∆_g=1e−5; %aimed error
epsilon=∆_g/(g_up−g_low); %tolerance
n=round(−2.078*log(epsilon)); %number of iterations


g1=(1−t)*g_low+t*g_up;
reg=Fourier_open_circuit(g1,∆_z,Rout_stat,Rin_stat,La,h_mag,...
h_rot_tooth,ts_y,Nr,Ns,rpm,mu_mr,Br,N,I,Position); %initial calculation...
%for the lower boundary value
Bfor1=reg(6).Bp;

g2=(1−t)*g_up+t*g_low;
reg=Fourier_open_circuit(g2,∆_z,Rout_stat,Rin_stat,La,h_mag,...
h_rot_tooth,ts_y,Nr,Ns,rpm,mu_mr,Br,N,I,Position); %initial calculation...
%for the higher boundary value
Bfor2=reg(6).Bp;

for j=1:n

  if  abs(trapz(abs(Position),abs(Bfor1))−trapz(abs(Position),abs(B_m)))...
       > abs(trapz(abs(Position),abs(Bfor2))−trapz(abs(Position),abs(B_m)))

        g_low=g1;
        g1=g2;
        Bfor1=Bfor2;
        g2=(1−t)*g_up+t*g_low;
        reg=Fourier_open_circuit(g2,∆_z,Rout_stat,Rin_stat,La,h_mag,...
        h_rot_tooth,ts_y,Nr,Ns,rpm,mu_mr,Br,N,I,Position); %new boundary c.
        Bfor2=reg(6).Bp;

    else
        g_up=g2;
        g2=g1;
        Bfor2=Bfor1;
        g1=(1−t)*g_low+t*g_up;
        reg=Fourier_open_circuit(g1,∆_z,Rout_stat,Rin_stat,La,h_mag,...
        h_rot_tooth,ts_y,Nr,Ns,rpm,mu_mr,Br,N,I,Position); %new boundary c.
        Bfor1=reg(6).Bp;

    end
    Bfor=(Bfor1+Bfor2)/2; %update the field  in airgap for each g(i)
    error(j)= abs(trapz(abs(Position),abs(Bfor))−trapz(abs(Position),...
abs(B_m)))/trapz(abs(Position),abs(B_m)); %for each iteration one perc. err.
    g_matrix(j)=(g1+g2)/2; %for each iteration one g is determined
```

```
end
```

Please note the code with the rows $Bfor1 = Bfor2$ (and vice versa): For a smaller simulation time $err(g1) = err(g2)$ is not taken as the $B_{fa}(g1) - B_{mec} = B_{fa}(g2) - B_{mec}$, but as $B_{fa}(g1) = B_{fa}(g2)$ because the results from MEC are simplified already on both sides of the equation.

Appendix D

Solving of thermal equivalent circuit

Construction of matrices

The solving process of the thermal equivalent circuit (TEC) is explained here on an example given in Fig. D.1. The losses in the machine are represented by an independent current source labeled P. The known temperature is represented by an independent voltage source labeled T. Known and unknown parameters are sorted in a general matrix equation as:

$$\mathbf{x} = \mathbf{A^{-1}z}, \tag{D.1}$$

where $\mathbf{x}$ is the matrix with unknown quantities, $\mathbf{A}$ holds the passive elements such as resistances and elements of the value 1, -1 and 0 according to the location of the known independent voltage sources. The matrix $\mathbf{z}$ has the values of independent voltage and current sources.

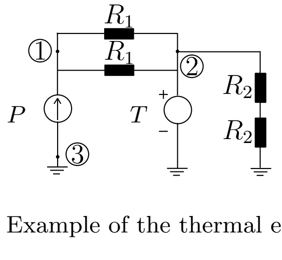

Figure D.1: Example of the thermal equivalent circuit.

A matrix is the largest matrix of (D.1) with the following structure:

$$\mathbf{A} = \begin{bmatrix} \mathbf{A1}_{(n\times n)} & \mathbf{B1}_{(n\times m)} \\ \mathbf{C1}_{(m\times n)} & \mathbf{D1}_{(m\times m)} \end{bmatrix}_{(m+n)\times(m+n)}$$

with (n+1) nodes and (m) independent voltage sources the following sub-matrices. Note that the matrices are of size (n) not ($n+1$), due to the elimination of one row and one column with the earth connection.

A1 has the thermal conductances of the circuit. The upper diagonal elements are written as negative. For the circuit in Fig. D.1, there is only one such element with the matrix index (1x2). Due to the symmetry the elements with indexes (1x2) and (2x1) are identical. The final **A1** matrix has the following form:

$$\mathbf{A1} = \begin{bmatrix} R_1^{-1} + R_1^{-1} & -(R_1^{-1} + R_1^{-1}) \\ -(R_1^{-1} + R_1^{-1}) & (R_1^{-1} + R_1^{-1}) + (R_2 + R_2)^{-1} \end{bmatrix}$$

The elements of **B1** (and **C1**) matrix show whether any voltage source is present in the circuit. The element 0 indicates that no source is connected, 1 indicates that the positive terminal of the source is at the node side and −1 indicates that the negative terminal is at the node side. Since there is no dependent source in the circuit, **D1** is a zero matrix. All three matrices are written as:

$$\mathbf{B1} = \begin{bmatrix} 0 \\ 1 \end{bmatrix}$$

$$\mathbf{C1} = \mathbf{B1}^T = \begin{bmatrix} 0 & 1 \end{bmatrix}$$

$$\mathbf{D1} = \begin{bmatrix} 0 \end{bmatrix}$$

Consequently, **A** has in the following form:

$$\mathbf{A} = \begin{bmatrix} R_1^{-1} + R_1^{-1} & -(R_1^{-1} + R_1^{-1}) & 0 \\ -(R_1^{-1} + R_1^{-1}) & (R_1^{-1} + R_1^{-1}) + (R_2 + R_2)^{-1} & 1 \\ 0 & 1 & 0 \end{bmatrix}$$

The matrix **z** has the known quantities, i.e. independent voltage and current source values. **P** shows the independent current sources connected to all the nodes of the circuit (except for the earth node), and **T** shows all the independent voltage sources. For the independent current sources (power loss), the sign is taken positive as the thermal flux flow is in the direction to the node. In case, there are more than one current source connected to the same node, they are written as a summation:

$$\mathbf{z} = \begin{bmatrix} \mathbf{P}_{(n\times 1)} \\ \mathbf{T}_{(m\times 1)} \end{bmatrix}_{(m+n)\times 1} \quad with$$

$$\mathbf{P}_{(n\times 1)} = \begin{bmatrix} 1 \\ 0 \end{bmatrix}, and$$

$$\mathbf{T}_{(m\times 1)} = \begin{bmatrix} 5 \end{bmatrix}.$$

After constructing **A** and **z** matrices, **x** matrix is solved in the following form:

$$\mathbf{x} = \begin{bmatrix} \mathbf{T}_{\mathbf{n}(n\times 1)} \\ \mathbf{P}_{\mathbf{n}(m\times 1)} \end{bmatrix}_{((m+n)\times 1)},$$

where T_n shows the nodal temperatures at each node, n, and P_n shows the heat flow via the known temperatures (via the voltage source).

General losses

For FSPM, the considered losses are copper losses, eddy current losses in magnets and iron losses in the stator and rotor. Their general equations are presented accordingly.

Copper (Joule) losses (P_{Cu})

Copper losses, P_{Cu}, inside the machine can be predicted by:

$$P_{Cu} = mI_{ph}^2 R_{ph} = mJ_{eff}^2 \rho_{Cu} V_{Cu}, \tag{D.2}$$

where m is the phase number, I_{ph} the effective phase current with a corresponding current density, J_{eff}, R_{ph} phase resistance, ρ_{Cu} the electrical resistivity of copper and V_{Cu} volume of copper winding.

Iron (core) losses (P_{Fe})

Iron losses, P_{Fe}, depend on the shape and variation of the flux density. The shape of the flux density in the soft magnetic material can be divided as sinusoidal and nonsinusoidal. The latter flux density can cause additional minor BH-loops due to the higher number of harmonics. Widely accepted models for iron loss calculations have been proposed by Bertotti, Fiorillo, Novikov and Preisach. These losses can be divided into three categories as hysteresis, classical eddy current and excess losses. The first two types are generally used in the literature for traditional iron loss calculations, while the third one is usually determined by the difference of the model and measurements. In this section, the equations are based on loss density in $[W/kg]$.

Hysteresis losses

Hysteresis losses are a result of the steel resistance to the changes in its magnetic state [13, 148]. The resulting power loss for one electrical cycle is proportional to the area enclosed by the BH-curve (hysteresis curve) of that material. The lost energy is required to move the magnetic domain walls in the core. Most common model to calculate the hysteresis loses is based on Steinmetz equation as:

$$P_{hys} = k_h B_{max}^n f, \tag{D.3}$$

where k_h and n are material dependent coefficients, f is the frequency and B_{max} is peak flux density (assuming a sinusoidal B). Typically, $n = 1.6-2.2$ depending on the values of B_{max} and f. For nonsinusoidal flux density waveform, a correction factor C_h is added to (D.3) as:

$$P_{hys} = C_h k_h B_{max}^n f. \tag{D.4}$$

Correction factor C_f can be estimated by:

$$C_f = 1 + \frac{k}{B_{max}} \sum_{i=1}^{n} \Delta B_i, \tag{D.5}$$

where $k = 0.6-0.7$, n is the number of minor loops and ΔB_i change of flux density around a minor loop, i.e. the flux density magnitude of each minor loop [149].

Eddy (Foucault) current losses

The second component of the classical iron losses is eddy current losses, which are caused by the changing magnetic field. The variation in the magnetic flux causes circulating currents in the iron core due to its electric resistivity. These losses can be calculated by:

$$P_e = C_e B_{max}^2 f^2, \tag{D.6}$$

where C_e is the eddy loss coefficient. This coefficient is calculated with:

$$C_e = \frac{\pi^2 \sigma d^2}{6}, \tag{D.7}$$

where σ is the electrical conductivity of the iron core and d is the core thickness. To calculate P_e, (D.6) can be used only if magnetic flux penetrates in the core compeletly, i.e. if the lamination thickness is smaller than skin depth. For nonsinusoidal flux density distribution, (D.6) can be extended to cover the harmonic flux densities, B_k, for k^{th} harmonic as:

$$P_e = C_e f^2 \sum_{k=1}^{\infty} k^2 B_k^2. \tag{D.8}$$

Independent on the shape of the flux density, among the classical definition of iron losses, the hysteresis losses are proportional to the product, (fB_{max}), whereas eddy current losses are proportional to $(fB_{max})^2$.

Excess (anomalous) losses

In practice, the sum of the classical iron losses (hysteresis and eddy current) vary from the measurements. The difference is referred to as excess loss. It is mainly caused by the circulating parasitic micro-currents with a high frequency. They can be estimated by:

$$P_{ex} = k_{ex} B_{max}^{1.5} f^{1.5} = \sqrt{\sigma G S V_0} B_{max}^{1.5} f^{1.5}, \tag{D.9}$$

where G is a dimensionless constant depending on the material, V_0 on the magnetization properties and S is the cross section area of the lamination. According to the theory of Bertotti, V_0 is a constant field depending on the difference of coercitive magnetic field strength between two magnetic objects. Similar to the classical iron losses, excess loss calculated by (D.9) can be extended for nonsinusoidal flux density as:

$$P_{ex} = \frac{k_{ex}}{T} \int_0^T \left| \frac{dB}{dt} \right|^{1.5} dt, \tag{D.10}$$

where T corresponds to one electrical cycle period in time, t.

The total iron loss P_{Fe} can be calculated by adding the three components as:

$$P_{Fe} = P_{hys} + P_e + P_{ex}. \tag{D.11}$$

Eddy current magnet losses ($P_{e,PM}$)

Similar to eddy current iron losses, magnet losses, $P_{e,PM}$, occur in PM machines due to these circulating currents. The time-space-varying magnetic field induces a voltage, which causes eddy currents in PMs due to their electrical resistivity.

FEM calculation of losses

In FEM software, P_{Cu} and $P_{e,PM}$ are calculated taking into account the electrical resistivity of the material in addition to their magnetic properties. For magnets an electrical resistivity of $1.5\cdot10^{-6}[\Omega m]$ is used and for copper coils $16.78\cdot10^{-9}[\Omega m]$. Since these losses depend on the time-varying magnetic field, a transient magnetic model is created. The $P_{e,PM}$ are calculated based on:

$$P_{e,PM} = L_a \int_S \mathbf{E}\cdot\mathbf{J}dS, \tag{D.12}$$

where $\mathbf{E}$ is electric field is multiplied with current density, $\mathbf{J}$, over the surface area, S. For the eddy current losses in the magnets, S corresponds to the total surface area in the radial cross-section of the machine. Iron loss calculations are based on the Bertotti model and Steinmetz equations. The loss density $[W/kg]$ is calculated as:

$$P_{Fe} = P_{hys} + P_e + P_{ex} = k_h B_{max}^2 f + C_e B_{max}^2 f^2 + 8.67 k_e B_{max}^{1.5} f^{1.5} \tag{D.13}$$

As seen in (D.13), the model used in FEM is a combination of (D.3), (D.6) and (D.9), assuming of a sinusoidal flux density distribution. For one electrical period, (D.13) takes the form:

$$\frac{1}{T}\int_0^T dP_{Fe}(t)dt = k_{Fe}\left(k_h B_{max}^2 f + \frac{1}{T}\int_0^T \frac{C_e}{2}\left(\frac{dB(t)}{dt}\right)^2 dt\right) +$$

$$k_{Fe}\left(\frac{k_{ex}}{T}\int_0^T \left|\frac{dB(t)}{dt}\right|^{1.5} dt\right) \tag{D.14}$$

In (D.14), it can be seen that for the periodic state, the equation is a combination of (D.3),(D.6) and (D.10). In the last two terms of (D.14), the frequency component, f, disappears due to the time integral over one electrical cycle. In FEM, (D.14) is solved at each node of the concerned area (on the stator and rotor faces), where B_{max} corresponds to the maximum flux density at that node and k_{Fe} being the fill factor of the iron material. Using (D.14), the iron losses in stator and rotor can be calculated for one electrical period, from which average iron loss can be calculated at constant speed. The coefficients, k_h and k_e, are determined from the material properties and given in Table D.1.

Table D.1: Material properties as used in loss calculations

Symbol	Description	Value	Unit
d	Lamination thickness	0.35	$[mm]$
k_e	Coefficient of eddy current losses	143.327	$[Ws(Tm^3)^{-1}]$
k_h	Coefficient of hysteresis losses	$2.38 \cdot 10^6$	$[(\Omega m)^{-1}]$
P_{Fe}	Loss density @ $1.6[T]$ and $400[Hz]$	70.24	$[Wkg^{-1}]$

Modeling of airgap region

The airgap is generally modeled as a conductive material in thermal FEM simulations, whereas convection is usually used for TEC as the heat transfer mode. The Taylor and Nusselt numbers are widely used in literature to determine the nature of the heat flow, e.g. laminar, vortex or turbulent [150–152]. The Taylor number depends on the machine geometry, operational speed and the cooling fluid. Since no forced cooling is used for FSPM, the Taylor number, T_A, is proportional to $g^{1.5}/r_r^{0.5}$, where g is the airgap length and r_r is the rotor radius. For FSPM, this ratio is very small, i.e. a laminar heat flow is considered. In this case, Nusselt number is taken as $Nu = 2$ for the speed range of the benchmark motor [135]. The Nu and T_A numbers do not count for the effect of motor saliency. To account for saliency, motor airgap can be modeled as a thin region just above the rotor teeth in half-airgap [140]. For the rated speed and machine parameters, half-airgap is modeled as a conductive material with Nusselt number ($Nu = 2$) with the following convection resistance:

$$R_g = \frac{1}{h_{eq}S}, \tag{D.15}$$

where the equivalent airgap convection coefficient, h_{eq}, with thermal conductivity of the air, λ_{air}, is:

$$h_{eq} = \frac{Nu\lambda_{air}}{2(g/2)} \tag{D.16}$$

and $1/N_s$ of the airgap surface is:

$$S = \frac{2\pi R_{ag}L_a}{N_s}. \tag{D.17}$$

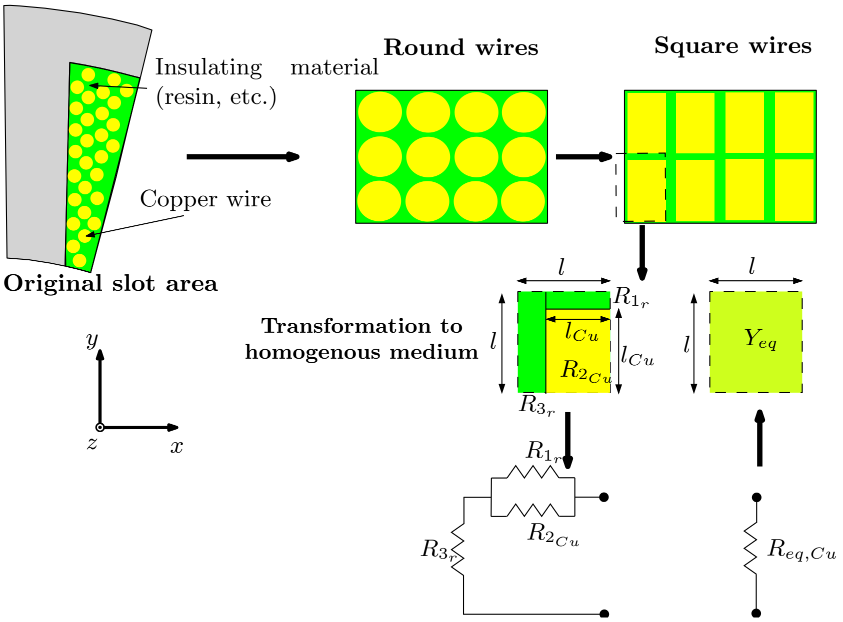

Figure D.2: Modeling of coil slot region.

Modeling of slot region

Different materials and the shape of slots and windings, make TEC implementation difficult. Modeling of these regions can be in form of detailed geometric representations or simplified to an equivalent homogeneous medium with an average thermal conductivity. The most common techniques are [150]:

- Representation by average (composite) thermal conductivity,
- Geometric equations based on the conductor geometry, and
- T-equivalent circuits to estimate thermal resistance.

Although the exact representation of the slot with the conductors gives a better visualisation about the temperature distribution in the slot, TEC is not improved significantly. Therefore, the average (composite) thermal conductivity, $\lambda_{Cu,eq}$, method is chosen to represent the stator slot as illustrated in Fig. D.2 [150]. The three thermal resistances, R_{1_r}, $R_{2_{Cu}}$ and R_{3_r}, represent the resin and copper, which are calculated as:

$$R_{1_r} = \frac{l_{Cu}}{(l - l_{Cu})L_{Cu}\lambda_r}, R_{2_{Cu}} = \frac{1}{L_{Cu}\lambda_{Cu}}, \text{ and } R_{3_r} = \frac{(l - l_{Cu})}{l_{Cu}L_{Cu}\lambda_r.} \qquad \text{(D.18)}$$

where L_{Cu} is the length of the winding, λ_r and λ_{Cu} are the thermal conductivities of insulation material and copper, respectively. The equivalent resistance is:

$$R_{eq,Cu} = \frac{R_{1_r} R_{2_{Cu}}}{R_{1_r} + R_{2_{Cu}}} + R_{3_r}. \tag{D.19}$$

Another way to define the equivalent slot resistance is:

$$R_{eq,Cu} = L_{Cu} \lambda_{Cu,eq}, \tag{D.20}$$

where $\lambda_{Cu,eq}$ is used to calculate coil thermal resistances R_{cx} and R_{cy} in section II. By equating (D.19) and (D.20), the following relation holds:

$$\lambda_{eq,Cu} = \lambda_r \frac{(1 - \sqrt{k_f})\lambda_k + \sqrt{k_f}\lambda_{Cu}}{\lambda_r + (1 - \sqrt{k_f})\sqrt{k_f}\lambda_{Cu}}, \tag{D.21}$$

where the slot fill factor k_f is defined as:

$$k_f = \frac{S_{Cu}}{S_{slot}} = \left(\frac{l_{Cu}}{l}\right)^2. \tag{D.22}$$

Since $\lambda_{Cu} >> \lambda_r$, (D.20) can be rewritten as:

$$\lambda_{eq,Cu} = \frac{\lambda_r}{1 - \sqrt{k_f}}. \tag{D.23}$$

MATLAB code for TEC solving process

A similar MATLAB script, introduced in Appendix C, is implemented to solve the TEC in the Laplace domain. The inverse Laplace transfer function is used to obtain the time dependent solution of one node. The process is summarized in Fig. D.4. The marked blocks show the s-domain calculations, which eventually enter the inverse Laplace transformation for the time domain results. For this inverse Laplace transformation, the MATLAB function *ilaplace* is used, which becomes unstable with the increasing number of nonlinear elements in the circuit, i.e. number of thermal capacitances. The function *ilaplace* was unable to find a symbolic explicit answer, therefore the transformation had still expressions of s with imaginary constants, where in fact only expressions of t should be present. To solve this problem, another function *vpa* is used, that forces this semi-explicit function of t and s to a be a function only of t. This function approximates the complex constants to real numbers taking based on the whole symbolic expression. The precision of the approximation can also be specified by the number of digits for the real constants. In this case, a number of 15 digits was sufficient.

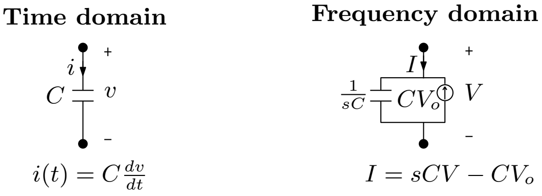

Figure D.3: s-domain parallel equivalent circuit for the capacitance.

Representation in Laplace domain

Each material in the machine has a different specific heat capacity, c_p. Thermal capacitance value, C_{th}, can be calculated by:

$$C_{th} = c_p m = c_p V \rho, \tag{D.24}$$

where m is the mass, V the volume and ρ the mass density of the respective material. In s-domain, resistance and capacitance are described as the following:

$$Z_R(s) = R, \text{ and } Z_C(s) = \frac{1}{sC} = -\frac{j}{wC}. \tag{D.25}$$

During the transient analysis, the temperature of all materials start at ambient temperature represented by the initial condition in the circuit analysis. Initial condition in the Laplace transformation is represented by additional current or voltage sources. The choice whether to add a current or voltage source depends on what kind of an equivalent circuit is constructed. For series equivalent circuits, current source and for parallel equivalent circuits, voltage source is adequate. Since it is more suitable to add parallel components to the existing TEC, the equivalent circuit transformation in Fig. D.3 is used to include the capacitances. The included independent current sources are not represented in Fig. 6.11 only for illustrative purposes. The specific heat capacities and mass densities of the materials used in FSPM are summarized in Table D.2. Similar to the thermal resistance and capacitance, known constant nodal temperatures are also transformed into s-domain by multiplying with $1/s$.

Table D.2: Heat capacities and mass densities of relevant regions

Symbol	**Region**	**Specific heat capacity** $[J(kg^{\circ}C)^{-1}]$
c_{PM}	PM	450
c_{Fe}	M270-35A (radial direction)	460
c_{Cu}	Slot	487
		Mass density $[kgm^{-3}]$
ρ_{PM}	PM	5990
ρ_{Fe}	M270-35A (radial direction)	7700
ρ_{Cu}	Slot	6380

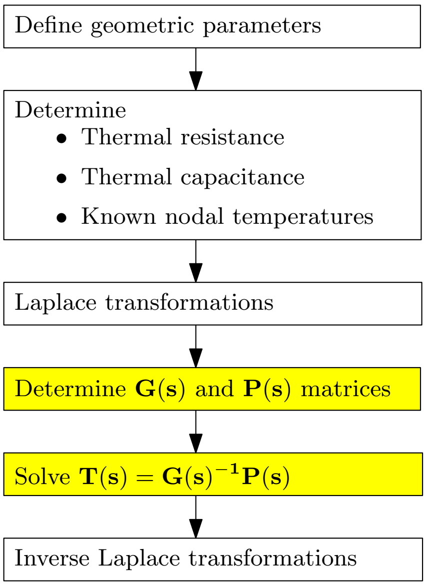

Figure D.4: Flowchart of the solving process for the thermal equivalent circuit.

Nomenclature

Symbol	**Description**	**Unit**	**Chapter**
A	Magnetic vector potential, complex integration constant	$[\star]$	1-4
B	Magnetic flux density, magnetic loading	$[T]$	1-4
B_r	Remanent flux density, normal component of magnetic flux density	$[T]$	2,3,7
C	Complex integration constant, circumference	$[\star]$	4,6
$\mathbf{C}$	Thermal capacitance matrix	$[J\ ^{\circ}C^{-1}]$	6
D	Electrical flux density, distance in translating or rotating motion, diameter	$[\star]$	1,3-4,6,8
D_r	Rotor diameter, normal component of electrical flux density	$[\star]$	1,3
E	Voltage	$[V]$	1,6,8
F	Force	$[N]$	2-5
$\mathbf{G}$	Thermal conductance matrix	$[W\ ^{\circ}C^{-1}]$	6
H	Magnetic field strength	$[Am^{-1}]$	1-2
I	Current	$[A]$	
J	Current density, moment of inertia (mechanical, virtual)	$[\star]$	1-4,6-8
L	Inductance	$[H]$	1
L_a	Axial (stack) length	$[m]$	1-4,6-8
L_{coil}	Length of coil	$[m]$	6
L_{end}	Length of end winding	$[m]$	6
M	Volume magnetization	$[Am^{-1}]$	1
N	Number of turns	-	1,6,7
N_r	Rotor pole number	-	1-4,6,7
N_s	Stator pole number	-	1-4,6,7
N_{sk}	Number of step skew	-	7
$\mathbf{P}$	Loss matrix	$[W]$	6
P_{Cu}	Copper (Joule) loss	$[W]$	6-8

Symbol	Description	Unit	Chapter
$P_{e,PM}$	Eddy current loss in PMs	$[W]$	6-8
P_{Fe}	Iron loss	$[W]$	6-8
$P*$	Rotor tooth number	[-]	3
Q	Electrical loading	$[Am^{-1}]$	1,7
R	Electrical, thermal resistance	$[\star]$	1,6
R_{ag}	Mid-airgap radius	$[m]$	1-2,4,7
R_{pos}	Rotor tooth contour position	[-]	3-4,6
R_r	Rotor radius	$[m]$	2,6,7
R_s	Stator outer radius	$[m]$	2,6,7
R_{sh}	Shaft radius	$[m]$	6,7
R_{st}	Stator inner radius	$[m]$	2,6,7
S	Area	$[m^2]$	1-3
S_c	Coil slot area	$[m^2]$	6
S_{pos}	Stator tooth contour position	[-]	3-4
$\mathbf{T}$	Temperature matrix	$[^\circ C]$	6
T_c	Temperature of coil	[°C]	8
T_C	Cogging torque	$[Nm]$	3-5,7,8
T_{em}	Rated torque	$[Nm]$	2,7,8
T_h	Temperature of housing	$[^\circ C]$	8
T_0	Stall torque	$[Nm]$	1,6,7
V	Volume, voltage	$[\star]$	1,6
W	Energy or work	$[J]$	1
W_{ele}	Electrical energy	$[J]$	1
W_m	Magnetic energy	$[J]$	1
W'_m	Magnetic coenergy	$[J]$	1
W_{mech}	Mechanical energy	$[J]$	1
a	Step size	$[m]$	3-4
$corr_{fac}$	Correction factor	$[m]$	4
d	Direct axis, harmonic number	[-]	7
$\mathbf{e}$	Unit vector	[-]	2
g	Airgap length	$[m]$	1-4,6,7
h_o	Thermal convection coefficient	$[Wm^{-2}\ ^\circ C^{-1}]$	6
h_{rbi}	Rotor back-iron height	$[m]$	2,6,7

Symbol	**Description**	**Unit**	**Chapter**
h_{sbi}	Stator back-iron height	$[m]$	2,6,7
i	Current (time domain)	$[A]$	6
k_d	Winding distribution factor	[-]	6
k_f	Fill factor	[-]	6-8
k_p	Winding pitch factor	[-]	6
k_{rti}	Rotor tooth inner ratio	[-]	6,7
k_s	Winding skew factor	[-]	6
k_w	Winding factor	[-]	6
k_{3D}	3D Correction factor	[-]	6-8
k_*	Integer number	[-]	6
l	Path length	$[m]$	1-2,4
l_m	Magnet length	$[m]$	2,6,7
l_{rt}	Rotor tooth length	$[m]$	2,6,7
l_{st}	Stator tooth length	$[m]$	2,6,7
m	Number of phases, number of mechanical output terminals	[-]	1,6,7
n	Number of electrical input terminals, speed	[-]	1,6,7
p	Number of poles	[-]	6,7
q	Number of slots per pole per phase, quadrature axis	[-]	6,7
r	Radius, cylindrical or polar coordinate (normal direction)	$[m]$	1-4
s	Laplace domain indicator	[-]	6
s_r	Split ratio	[-]	6,7
t	Time	$[s]$	1,6
tw_r	Rotor tooth width ratio	[-]	7
v	Velocity, voltage (time domain)	$[\star]$	1,6
w	Spatial frequency, original complex domain	$[\star]$	2,4
w_c	Coil slot width	$[m]$	2,6,7
w_e	Electrical speed	$[rad\ s^{-1}]$	6
w_m	Magnet width	$[m]$	2,6,7
w_r	Rotor periodical width	$[m]$	2,6,7

Symbol	**Description**	**Unit**	**Chapter**
w_{rt}	Rotor tooth width	$[m]$	2,6,7
w_{st}	Stator tooth width	$[m]$	2,6,7
x	Cartesian coordinate	$[m]$	1-4
$x\theta_{st}$	Stator tooth width ratio	[-]	7
y	Cartesian coordinate	$[m]$	1-4
z	Cartesian or cylindrical coordinate (longitudinal direction) , mapped complex domain	$[\star]$	1-4
Δ	Relative difference	$[\star]$	1-5
$\mathcal{E}$	Electrical scalar potential	$[V]$	3-4
$\mathcal{F}$	Magnetomotive force	$[A]$	1-3
$\mathcal{F}_c$	Magnetomotive force of coil	$[A]$	2
$\mathcal{F}_m$	Magnetomotive force of magnet	$[A]$	2
$\mathcal{P}$	Permeance	$[H]$	1-2
$\mathcal{P}_c$	Coil slot leakage permeance	$[H]$	3
$\mathcal{P}_{gap}$	Airgap permeance	$[H]$	1-5
$\mathcal{P}_m$	Magnet permeance	$[H]$	2
$\mathcal{P}_{ml}$	Magnet leakage permeance	$[H]$	2-3
$\mathcal{P}_R$	Rotor permeance	$[H]$	2-3
$\mathcal{P}_{Rbi}$	Rotor back-iron permeance	$[H]$	2-3
$\mathcal{P}_S$	Stator permeance	$[H]$	2-3
$\mathcal{P}_{Sbi}$	Stator back-iron permeance	$[H]$	2-3
$\mathcal{P}_{Sol}$	Stator outer leakage permeance	$[H]$	2-3
$\mathcal{P}_{S**}$	Stator tooth permeance of stator cell '*' and stator tooth '*'	$[H]$	2-3
$\mathcal{P}_{R*}$	Rotor tooth permeance of tooth '*'	$[H]$	2-3
$\mathcal{P}_{S*R*}$	Airgap permeance between stator tooth '*' and rotor tooth '*'	$[H]$	2-3
Φ	Magnetic flux	$[Wb]$	1-2,6
$\mathcal{R}$	Reluctance	$[H^{-1}]$	1-2
α_k	Interior angle	$[\star]$	4

Symbol	**Description**	**Unit**	**Chapter**
δ	Standard deviation	[-]	3
ε_0	Permittivity of vacuum (8.854×10^{-12})	$[Fm^{-1}]$	3
θ	Angle, cylindrical coordinate (tangential direction)	$[\star]$	1
θ_c	Angular coil width	$[\star]$	2,6,7
θ_k	Rotational mechanical displacement	$[\star]$	1,6
θ_m	Angular magnet width	$[\star]$	2,6,7
θ_r	Angular rotor width (1 period)	$[\star]$	2,6,7
θ_{rt}	Angular rotor tooth width	$[\star]$	2,6,7
θ_{rti}	Angular rotor tooth inner width	$[\star]$	2,6,7
θ_s	Angular stator width (1 period)	$[\star]$	2,6,7
θ_{sk}	Total skew angle	$[\star]$	7,8
θ_{ss}	Step skew angle	$[\star]$	7
θ_{st}	Angular stator tooth width	$[\star]$	2,6,7
λ	Magnetic flux linkage, thermal conductivity	$[\star]$	1-6
μ	Magnetic permeability	$[Hm^{-1}]$	2,3,7
μ_0	Permeability of vacuum ($4\pi10^{-7}$)	$[Hm^{-1}]$	1-2
μ_r	Relative permeability	[-]	1-2
μ_{Fe}	Relative permeability of iron	[-]	2
ξ	Slot pitch angle	$[\star]$	-
ρ	Electrical volume charge density	$[Cm^{-3}]$	1
ρ	Mass density	$[kgm^{-3}]$	6
φ	Magnetic scalar potential	$[A]$	4

[⋆] Unit depends on the context

Abbreviation	Description
BEM	Boundary element method
FA	Fourier analysis
FDM	Finite difference method
FEM	Finite element method
FSPM	Flux switching permanent magnet (machine)
HM	Hybrid model
MEC	Magnetic equivalent circuit
M1	Test motor
M2	Load motor
OFD	Orthogonal field theory
PM	Permanent magnet
PMAC	Permanent magnet alternating current (machine)
SC	Schwarz-Christoffel
TC	Tooth contour
TCM	Tooth contour method
TEC	Thermal equivalent circuit
ac	Alternating current
Al	Aluminium
arg	Argument
cond	Conductor
Cu	Copper
dc	Direct current
eff	Effective
eFEM	Electrostatic finite element method
em	Electromagnetic
emf	Electromotive force
err	Error
Fe	Iron
gap	Airgap
ini	Initial
mean	Mean value
max	Maximum
mmf	Magnetomotive force
ph	Phase
rms	Root mean square
th	Thermal
2D	Two-dimensional
3D	Three-dimensional

Bibliography

[1] H. K. Brugsch [1881]. *A history of Egypt under the Pharaohs, derived entirely from the monuments.* Harvard University.

[2] T. A. Lipo [2007]. *Introduction to ac machine design.* Wisconsin Power Electronics Research Center, University of Wisconsin.

[3] E. J. Rothwell and M. J. Cloud [2001]. *Electromagnetics.* CRC Press.

[4] M. Faraday [1843-1850]. On magnetic actions; and on the magnetic condition of all matter. *Abstracts of the papers communicated by the Royal Society of London.*

[5] M. Faraday [1844]. On static electrical inductive action. *Philosophical Journal*, 22(144):200–204.

[6] J. Henry [1886]. *Scientific writings of Joseph Henry*, volume 30. The Smithsonian Institution.

[7] W. W. R. Ball [1960]. *A short account of the history of mathematics.* Dover Publications Inc., New York.

[8] H. A. Lorentz [1892]. *La theorie electromagnetique de Maxwell et son application aux corps mouvants.* E. J. Brill, Harvard University collection.

[9] J. C. Maxwell [1873]. *A treatise on electricity and magnetism.* Clarendon Press, Oxford.

[10] J. M. D. Coey [1996]. *Rare-earth iron permanent magnets, (Monographs on the Physics and Chemistry of Materials).* Oxford Science Publications.

[11] S. Kudarauskas [2004]. *Introduction to oscillating electrical machines.* Klaipeda, Lithuania.

[12] F. J. M. Thoolen [1993]. *Development of an advanced high speed flywheel energy storage system.* PhD thesis, Eindhoven University of Technology.

[13] J. R. Hendershot Jr. and T. J. E. Miller [2010]. *Design of brushless permanent-magnet machines.* Motor Design Books LLC.

[14] D. A. Staton, R. P. Deodhar, W. L. Soong, and T. J. E. Miller [1996]. Torque prediction using the flux-mmf diagram in ac, dc, and reluctance motors. *Industry Applications, IEEE Transactions on*, 32(1):180–188.

[15] J. Pyrhonen, T. Jokinen, and V. Hrabovcova [2009]. *Design of rotating electrical machines*. John Wiley and Sons.

[16] E. P. Furlani [2001]. *Permanent magnet and electromechanical devices*. Academic Press.

[17] L. Encica [2008]. *Space-mapping optimization applied to the design of a novel electromagnetic actuator for active suspension*. PhD thesis, Eindhoven University of Technology.

[18] J. Hopkinson [1893]. *Original papers on dynamo machinery and allied subjects*. The W. J. Johnston Company, Limited and Whittaker in New York.

[19] D. A. Staton, T. J. E. Miller, and S. E. Wood [1993]. Maximising the saliency ratio of the synchronous reluctance motor. In *Electric Power Applications, IEE Proceedings*, volume 140, pages 249–259.

[20] Y. Gong, K. T. Chau, J. Z. Jiang, Y. Chuang, and L. Wenlong [2009]. Design of doubly salient permanent magnet motors with minimum torque ripple. *Magnetics, IEEE Transactions on*, 45(10):4704–4707.

[21] A. Kronberg [2012]. Salient pole motor inverter design. Master's thesis, University of Uppsala.

[22] G. J. Li, X. Ojeda, E. Hoang, M. Gabsi, and C. Balpe [2010]. Design of double salient interior permanent magnet machine based on mutually coupled reluctance machine for increasing the torque density and flux-weakening capability. *Industrial Electronics, ISIE, IEEE International Symposium on*, pages 1253–1258.

[23] F. W. Carter [1900]. Note on airgap and interpolar induction. *IEE*, 29:925–933.

[24] F. W. Carter [1926]. The magnetic field of the dynamo electric machine. *IEE*, 64:1115–1138.

[25] E. Levi [1984]. *Polyphase motors - A direct approach to their design*. John Wiley & Sons.

[26] R. H. Park [1929]. Two-reaction theory of synchronous machines generalized methods of analysis, part i. *AIEE*, 48:716–730.

[27] E. R. Lwithwaite [1967]. Magnetic equivalent circuits for electrical machines. *Electrical Engineers, Proceedings of the Institution of*, 114:1805–1809.

[28] T. C. O'Connell, P. T. Krein, M. Yilmaz, and A. Friedl [2008]. On the feasibility of using large-scale numerical electric machine field analysis software in complex electric drive system design tools. In *Control and Modeling for Power Electronics, Workshop on*, pages 1–8.

[29] H. Bai, S. D. Pekarek, J. Tichenor, W. Eversman, D. J. Buening, G. R. Holbrook, M. L. Hull, R. J. Krefta, and S. J. Shields [2002]. Analytical derivation of a coupled-circuit model of a claw-pole alternator with concentrated stator windings. *Energy Conversion, IEEE Transactions on*, 17(1):32–38.

[30] L. Pichon and A. Razek [1990]. Force calculation in axisymmetric induction devices using a hybrid fem-bem technique. *Magnetics, IEEE Transactions on*, 26(2):1050–1053.

[31] A. Nysveen and R. Nilssen [1997]. Time domain simulation of magnetic systems with a general moving geometry. *Magnetics, IEEE Transactions on*, 33(2):1394–1397.

[32] T. C. O'Connell and P. T. Krein [2010]. A time-harmonic three-dimensional vector boundary element model for electromechanical devices. *Energy Conversion, IEEE Transactions on*, 25(3):606–618.

[33] M. V. K. Chari and S. J. Salon [2000]. *Numerical methods in electromagnetism.* Academic press, Harcout, California.

[34] J. J. B. Biemond, N. van de Wouw, and H. Nijmeijer [2010]. Nonsmooth bifurcations of equilibria in planar continuous systems. *Nonlinear Analysis: Hybrid Systems*, 4(3):451–474.

[35] M. F. Heertjes and H. Nijmeijer [2008]. Hybrid control for motion systems with improved disturbance rejection. In *ENOC08*, pages 1–6.

[36] Ki-Sik Lee, M. J. DeBortoli, M. J. Lee, and S. J. Salon [1991]. Coupling finite elements and analytical solution in the airgap of electric machines. *Magnetics, IEEE Transactions on*, 27(5):3955–3957.

[37] Y. Zhilichev [2000]. Analysis of permanent magnet machines using crossing macro-elements. *Magnetics, IEEE Transactions on*, 36(5):3122–3124.

[38] L. Encica, J. J. H. Paulides, and E. A. Lomonova [2009]. Space-mapping optimization in electromechanics: an overview of algorithms and applications. *COMPEL*, 28(5):1216–1226.

[39] R. L. Owen, Z. Q. Zhu, and G. W. Jewell [2010]. Hybrid-excited flux-switching permanent-magnet machines with iron flux bridges. *Magnetics, IEEE Transactions on*, 46(6):1726–1729.

[40] W. Fei, P. C. K. Luk, D. Miao, and J. Shen [2014]. Investigation of torque characteristics in a novel permanent magnet flux switching machine with an outer-rotor configuration. *Magnetics, IEEE Transactions on*, 50(4):1–10.

[41] K. S. Chai and C. Pollock [2002]. Using genetic algorithms in design optimization of the flux switching motor. In *Power Electronics, Machines and Drives, International Conference on*, pages 540–545.

[42] Y. Tang, T. E. Motoasca, J. J. H. Paulides, and E. A. Lomonova [2011]. Investigation of winding topologies for flux switching machines. In *Proceedings of International Symposium on Electromagnetic Fields in Mechatronics, Electrical and Electronic Engineering, ISEF*, pages 1–8.

[43] H. Pollock, C. Pollock, R. T. Walter, and B. V. Gorti [2003]. Low cost, high power density, flux switching machines and drives for power tools. In *Proc. IEEE Ind. Appl. Soc. Annu. Meeting*, pages 1451–1457.

[44] W. Hua, Z. Q. Zhu, M. Cheng, Y. Pang, and D. Howe [2005]. Comparison of flux-switching and doubly-salient permanent magnet brushless machines. In *Electrical Machines and Systems, ICEMS. Proceedings of the Eighth International Conference on*, pages 165–170.

[45] M. Andriollo, G. Martinelli, A. Morini, and A. Tortella [2004]. Application of the surface-current method to the analysis of saturated electromagnetic devices. *COMPEL*, 23(1):328–347.

[46] Y. Tang, J. J. H. Paulides, T. E. Motoasca, and E. A. Lomonova [2012]. Flux-switching machine with dc excitation. *Magnetics, IEEE Transactions on*, 48(11):3583–3586.

[47] S. E. Rauch and L. J. Johnson [1955]. Design principles of flux-switch alternators. power apparatus and systems, part iii. *Transactions of the American Institute of Electrical Engineers*, pages 1261–1268.

[48] S. E. Rauch [1958]. Magnetic circuit properties of the flux-switch inductor alternator. *Transactions of the American Institute of Electrical Engineers*, 77(2):307–312.

[49] E. Hoang, A. H. Ben-Ahmed, and J. Lucidarme [1997]. Switching flux permanent magnet polyphases synchronous machines. In *European Conference on Power Electronics and Applications*, volume 3, pages 903–908.

[50] A. Zulu, B. Mecrow, and M. Armstrong [2009]. A wound-field three-phase flux-switching synchronous motor with all excitation sources on the stator. In *Energy Conversion Congress and Exposition, ECCE*, pages 1502–1509.

[51] T. L. Balyovski, E. Ilhan, Y. Tang, C. G. E. Wijnands, J. J. H. Paulides, and E. A. Lomonova [2014]. Control of dc-excited flux switching machines for traction applications. In *Ecological Vehicles and Renewable Energies, EVER, International Conference and Exhibition on*, pages 1–6.

[52] L. Somesan, E. Padurariu, I. A. Viorel, and L. Szabo [2012]. Design of a permanent magnet flux-switching machine. In *ELEKTRO*, pages 256–259.

[53] Z. Q. Zhu, Y. Pang, D. Howe, S. Iwasaki, R. Deodhar, and A. Pride [2005]. Analysis of electromagnetic performance of flux-switching permanent-magnet machines by nonlinear adaptive lumped parameter magnetic circuit model. *Magnetics, IEEE Transactions on*, 41(11):4277–4287.

[54] S. D. Chishko, Y. Tang, J. J. H. Paulides, and E. A. Lomonova [2014]. Dc excited flux-switching motor: Rotor structural optimization. In *Electrical Machines and Systems, ICEMS. Proceedings of the International Conference on*, pages 1–5.

[55] X. Liu and Z. Q. Zhu [2012]. Influence of rotor pole number on electromagnetic performance of novel variable flux reluctance machine with dc-field coil in stator. In *Power Electronics and Motion Control Conference, IPEMC*, volume 2, pages 1108–1115.

[56] A. Thomas, Z. Q. Zhu, G. W. Jewell, and D. Howe [2008]. Flux-switching pm brushless machines with alternative stator and sotor pole combinations. *Journal of Asian Electric Vehicles*, 6(1):1103–1110.

[57] Y. Wang, Z. W. Huang, J. X. Shen, and C. F. Wang [2008]. Comparison and study of 6/5- and 12/10-pole permanent magnet flux-switching motors considering flux-weakening capability. In *Electrical Machines and Systems, ICEMS. Proceedings of the Eighth International Conference on*, pages 3262–3265.

[58] E. Ilhan, T. E. Motoasca, J. J. H. Paulides, and E. A. Lomonova [2011]. Energy conversion loops for flux-switching PM machine analysis. In *Proceedings of International Symposium on Electromagnetic Fields in Mechatronics, Electrical and Electronic Engineering, ISEF*, pages 1–8.

[59] Y. Amara, G. Barakat, J. J. H. Paulides, and E. A. Lomonova [2013]. Overload capability of linear flux switching permanent magnet machines. In *Proceedings of the Ninth International Symposium on Linear Drives for Industry Applications*, volume 416-417, pages 345–352.

[60] H. Giberti and S. Cinquemnani [2012]. The specific accelerating factor to compare brushless motors. In *Biennial Conference on Engineering Systems Design and Analysis, ASME*, pages 409–417.

[61] H. Giberti and S. Cinquemnani [2010]. Servo motor classification based on the acceleration factor. In *International Institution of Informatics and Systemics, IMETI Conference Proceedings*, pages 1–6.

[62] E. Ilhan, M. F. J. Kremers, T. E. Motoasca, J. J. H. Paulides, and E. A. Lomonova [2012]. Spatial discretization methods for air gap permeance calculations in double salient traction motors. *Industry Applications, IEEE Transactions on*, 48(6):2165–2172.

[63] E. Ilhan, B. L. J. Gysen, J. J. H. Paulides, and E. A. Lomonova [2010]. Analytical hybrid model for flux switching permanent magnet machines. *Magnetics, IEEE Transactions on*, 46(6):1762–1765.

[64] E. Ilhan, J. J. H. Paulides, L. Encica, and E. A. Lomonova [2010]. Tooth contour method implementation for the flux-switching PM machines. In *Electrical Machines, ICEM, International Conference on*, pages 1–6.

[65] E. Ilhan, J. J. H. Paulides, and E. A. Lomonova [2014]. Hybrid modeling techniques for complex magnetic flux paths in airgap. In *IEEE International Magnetics Conference, INTERMAG*, pages 1–2.

[66] E. Ilhan, M. F. J. Kremers, T. E. Motoasca, J. J. H. Paulides, and E. A. Lomonova [2013]. Transient thermal analysis of flux switching PM machines. In *Ecological Vehicles and Renewable Energies, EVER, International Conference and Exhibition on*, pages 1–7.

[67] E. Ilhan, M. F. J. Kremers, T. E. Motoasca, J. J. H. Paulides, and E. A. Lomonova [2013]. Nonlinear performance characteristics of flux-switching PM motors. *Journal of Engineering, Hindawi Publications*, pages 1–8.

[68] E. Ilhan, M. F. J. Kremers, T. E. Motoasca, J. J. H. Paulides, and E. A. Lomonova [2012]. Sensitivity analysis for phase inductances in flux-switching PM machines. In *Electrical Machines, ICEM, International Conference on*, pages 763–768.

[69] E. Ilhan, J. J. H. Paulides, and E. A. Lomonova [2012]. Fast torque estimation of in-wheel parallel flux switching machines for hybrid trucks. *COMPEL*, 1(31):40–53.

[70] E. Ilhan, T. L. Balyovski, J. J. H. Paulides, and E. A. Lomonova [2014]. Servo flux switching PM machines. In *Electrical Machines, ICEM, International Conference on*, pages 1–6.

[71] D. C. J. Krop, J. W. Jansen, and E. A. Lomonova [2013]. Decoupled modeling in a multifrequency domain: Integration of actuation and power transfer in one device. *Magnetics, IEEE Transactions on*, 49(6):3009–3019.

[72] B. L. J. Gysen, E. Ilhan, K. J. Meessen, J. J. H. Paulides, and E. A. Lomonova [2010]. Modeling of flux switching permanent magnet machines with fourier analysis. *Magnetics, IEEE Transactions on*, 46(6):1499–1502.

[73] Z. J. Liu and J. T. Li [2007]. Analytical solution of air-gap field in permanent-magnet motors taking into account the effect of pole transition over slots. *Magnetics, IEEE Transactions on*, 43(10):3872–3883.

[74] K. J. W. Pluk, T. A. van Beek, J. W. Jansen, and E. A. Lomonova [2014]. Modeling and measurements on a finite rectangular conducting plate in an eddy current damper. *Industrial Electronics, IEEE Transactions on*, 61(8):4061–4072.

[75] J. Wang, G. W. Jewell, and D. Howe [1999]. A general framework for the analysis and design of tubular linear permanent magnet machines. *Magnetics, IEEE Transactions on*, 35(3):1986–2000.

[76] B. L. J. Gysen [2011]. *Generalized harmonic modeling technique for 2D electromagnetic problems-Applied to the design of a direct-drive active suspension system.* PhD thesis, Eindhoven University of Technology.

[77] Z. Zhu, J. T. Chen, Y. Pang, D. Howe, S. Iwasaki, and R. Deodhar [2007]. Modeling of end-effect in flux-switching permanent magnet machines. In *Electrical Machines and Systems, International Conference on*, pages 943–948.

[78] W. E. Boyce and R. C. DiPrima [2001]. *Elementary differential equations and boundary value problems.* John Wiley & Sons.

[79] W. Thomson [1856-1857]. *Proceedings Royal Society London*, 8:546–550.

[80] M. Amrhein and P. T. Krein [2009]. 3-d magnetic equivalent circuit framework for modeling electromechanical devices. *Energy Conversion, IEEE Transactions on*, 24(2):397–405.

[81] M. Amrhein and P. T. Krein [2009]. Force calculation in 3-d magnetic equivalent circuit networks with a maxwell stress tensor. *Energy Conversion, IEEE Transactions on*, 24(3):587–593.

[82] Y. Tang, J. J. H. Paulides, and E. A. Lomonova [2013]. Analytical modeling of flux-switching in-wheel motor using variable magnetic equivalent circuits. *ISRN Automotive Engineering*, pages 1–10.

[83] V. Ostovic [1989]. *Dynamics of saturated machines.* Springer, Berlin.

[84] P. Venkataraman [2002]. *Applied optimization with MATLAB programming.* John Wiley & Sons, Inc.

[85] Y. Tang, J. J. H. Paulides, and E. A. Lomonova [2013]. Topologies of flux switching machines for in-wheel traction. In *Ecological Vehicles and Renewable Energies, EVER, International Conference and Exhibition on*, pages 1–7.

[86] W. Hua, M. Cheng, and G. Zhang [2009]. A novel hybrid excitation flux-switching motor for hybrid vehicles. *Magnetics, IEEE Transactions on*, 45(10):4728–4731.

[87] Z. Q. Zhu and J. T. Chen [2010]. Advanced flux-switching permanent magnet brushless machines. *Magnetics, IEEE Transactions on*, 46(6):1447–1453.

[88] K. Boughrara, T. Lubin, and R. Ibtiouen [2012]. General subdomain model for predicting magnetic field in internal and external rotor multiphase flux-switching machines topologies. *Magnetics, IEEE Transactions on*, 49(10):5310–5325.

[89] Y. Amara, E. Hoang, M. Gabsi, M. Lecrivain, and S. Allano [2005]. Design and comparison of different flux-switch synchronous machines for an aircraft oil breather application. *European Transactions on Electrical Power*, 41(15):497–511.

[90] H. C. Roters [1958]. *Electromagnetic devices.* John Wiley & Sons, Inc.

[91] D. C. J. Krop [2013]. *Integration of dual electromagnetic energy conversions- Linear actuation with integrated contactless energy transfer.* PhD thesis, Eindhoven University of Technology.

[92] M. L. Bash, J. M. Williams, and S. D. Pekarek [2010]. Incorporating motion in mesh-based magnetic equivalent circuits. *Energy Conversion, IEEE Transactions on*, 25(2):329–338.

[93] T. Ramonosoa, J. A. Farooq, A. Djerdir, and A. Miraoui [2009]. Reluctance network modelling of surface permanent magnet motor considering iron nonlinearities. *Energy Conversion and Management*, 50:1356–1361.

[94] V. A. Kuznetsov [1990]. *General method of calculation of magnetic fields and processes in electric machines having discrete space-distribution windings.* PhD thesis, Moscow.

[95] M. F. J. Kremers, T. E. Motoasca, J. J. H. Paulides, and E. A. Lomonova [2011]. Analysis of a fractional slot permanent magnet machine for a series hybrid truck. In *Ecological Vehicles and Renewable Energies, EVER, International Conference and Exhibition on*, pages 1–9.

[96] V. A. Vyacheslav and P. Brochet [2003]. Numerical modeling of electromagnetic process in electromechanical systems. *COMPEL*, 22(4):1142–1154.

[97] Cedrat [2012]. *User guide Flux.* Cedrat.

[98] J. Stewart [1999]. *Calculus early transcendentals.* Brooks/Cole Publishing Company.

[99] Z. Qi, Y. Guo, and B. Wang [2011]. Blind direction-of-arrival estimation algorithm for conformal array antenna with respect to polarisation diversity. *Microwaves, Antennas Propagation, IET*, 5(4):433–442.

[100] A. Elnakib, A. El-Baz, M. F. Casanova, G. Gimel'farb, and A. E. Switala [2010]. Image-based detection of corpus callosum variability for more accurate discrimination between dyslexic and normal brains. In *Biomedical Imaging: From Nano to Macro, IEEE International Symposium on*, pages 109–112.

[101] K. Boughrara, R. Ibtiouen, D. Zandarko, O. Touhami, and A. Rezzoug [2010]. Magnetic field analysis of external rotor permanent-magnet synchronous motors using conformal mapping. *Magnetics, IEEE Transactions on*, 46(9):3684–3693.

[102] D. C. J. Krop, E. A. Lomonova, and A. J. A. Vandenput [2008]. Application of Schwarz-Christoffel mapping to permanent-magnet linear motor analysis. *Magnetics, IEEE Transactions on*, 44(3):352–359.

[103] B. L. J. Gysen, E. A. Lomonova, J. J. H. Paulides, and A. J. A. Vandenput [2008]. Analytical and numerical techniques for solving Laplace and Poisson equations in a tubular permanent magnet actuator: Part II. Schwarz-Christoffel mapping. *Magnetics, IEEE Transactions on*, 44(7):1761–1767.

[104] M. Markovic, M. Jufer, and Y. Perriard [2004]. Analyzing an electromechanical actuator by Schwarz-Christoffel mapping. *Magnetics, IEEE Transactions on*, 40(4):1858–1863.

[105] T. A. Driscoll and L. N. Trefethen [2002]. *Schwarz-Christoffel mapping: Cambridge Monogrpahs on Applied and Computational Mathematics*. Cambridge.

[106] `http://www.math.udel.edu/~driscoll/software/SC/index.html`.

[107] R. L. Finney, M. D. Weir, and F. R. Giordano [2001]. *Thomas' Calculus*. Mike Roche.

[108] D. T. E. H. van Casteren, J. J. H. Paulides, and E. A. Lomonova [2014]. 3D numerical surface charge model including relative permeability: the general theory. In *IEEE International Magnetics Conference, INTERMAG*, pages 1–2.

[109] A. Chen, R. Nilssen, and A. Nysveen [2010]. Analytical design of a high-torque flux-switching permanent magnet machine by a simplified lumped parameter magnetic circuit model. In *Electrical Machines, ICEM, International Conference on*, pages 1–6.

[110] J. F. Bangura [2006]. Design of high-power density and relatively high-efficiency flux-switching motor. *Energy Conversion, IEEE Transactions on*, 21(2):416–425.

[111] A. Parviainen [2005]. *Design of axial-flux permanent-magnet low-speed machines and performance comparison between radial-flux and axial-flux machines*. PhD thesis, Lappeenranta University of Technology.

[112] R. Wrobel, D. Salt, N. Simpson, and P. H. Mellor [2014]. Comparative study of copper and aluminium conductors - future cost effective pm machines. In *Power Electronics, Machines and Drives, PEMD, IET International Conference on*, pages 1–6.

[113] S. Huang, J. Luo, F. Leonardi, and T. A. Lipo [1998]. A general approach to sizing and power density equations for comparison of electrical machines. *Industry Applications, IEEE Transactions on*, 34(1):92–97.

[114] Bosch Drives [2013]. *Bosch Servodyn, Servomotoren SE Handbuch Nr.0.2*, 3831/d3-04/90 edition.

[115] SEW-Eurodrive [2013]. *Synchronous Servomotors, CMP40-CMP100*, 17014417/en edition.

[116] G. Delille, B. Francois, and G. Malarange [2010]. Dynamic frequency control support: A virtual inertia provided by distributed energy storage to isolated power systems. In *Innovative Smart Grid Technologies Conference Europe, ISGT*, pages 1–8.

[117] L. Zeni, A. J. Rudolph, J. Mnster-Swendsen, I. Margaris, A. D. Hansen, and P. Srensen [2013]. Virtual inertia for variable speed wind turbines. *Wind Energy*, 16(8):1225–1239.

[118] G. Capriz and P. Giovine [1987]. On effects of virtual inertia during diffusion of a dispersed medium in a suspension. *Archive for Rational Mechanics and Analysis*, 98(2):115–122.

[119] G. W. Younkin [2003]. *Industrial servo control systems-fundementals and applications.* Marcel Dekker, New York.

[120] `http://www.cncsupport.co.uk`.

[121] `http://blog.cnccookbook.com/2012/03/18/`.

[122] G. Kirckof [2012]. *Servomotor sizing and application.* International Society for Automation, ISA, North Carolina, USA.

[123] Kollmorgen [2013]. *Product manual, Synchronous Servomotors.*

[124] J. T. Chen and Z. Q. Zhu [2010]. Winding configurations and optimal stator and rotor pole combination of flux-switching PM brushless ac machines. *Energy Conversion, IEEE Transactions on*, 25(2):293 –302.

[125] A. A. B. Brojeny and J. R. Clem [2004]. Four coplanar superconducting strips: flux-focusing effects and inductance. *Superconductor Science and Technology*, 17(11):1275–1282.

[126] T. J. E. Miller [2002]. Optimal design of switched reluctance motors. *Industrial Electronics, IEEE Transactions on*, 49(1):15–27.

[127] Z. Q. Zhu, Y. Pang, J. T. Chen, Z. P. Xia, and D. Howe [2008]. Influence of design parameters on output torque of flux-switching permanent magnet machines. In *Vehicle Power and Propulsion Conference, VPPC IEEE*, pages 1–6.

[128] Z. A. Husin, E. Sulaiman, and T. Kosaka [2014]. Design studies and effect of various rotor pole number of field excitation flux switching motor for hybrid electric vehicle applications. In *Power Engineering and Optimization Conference, PEOCO, IEEE International*, pages 144–149.

[129] S. Iwasaki, R. P. Deodhar, Yong L., A. Pride, Z. Q. Zhu, and J. J. Bremner [2009]. Influence of PWM on the proximity loss in permanent-magnet brushless ac machines. *Industry Applications, IEEE Transactions on*, 45(4):1359–1367.

[130] P. H. Mellor, R. Wrobel, and N. McNeill [2006]. Investigation of proximity losses in a high speed brushless permanent magnet motor. In *Industry Applications Conference, IAS Annual Meeting*, volume 3, pages 1514–1518.

[131] A. S. Thomas, Z. Q. Zhu, and G. W. Jewell [2009]. Proximity loss study in high speed flux-switching permanent magnet machine. *Magnetics, IEEE Transactions on*, 45(10):4748–4751.

[132] J. J. H. Paulides [2005]. *High performance 1.5MW 20,000rpm permanent magnet gnerator with uncontrolled rectifier for 'more-electric' ship applications.* PhD thesis, University of Sheffield.

[133] B. Funieru and A. Binder [2008]. Thermal design of a permanent magnet motor used for gearless railway traction. In *Industrial Electronics, IECON. Annual Conference of IEEE*, pages 2061–2066.

[134] J. G. Amoros, P. Andrada, and B. Blanque [2010]. An analytical approach to the thermal design of a double-sided linear switched reluctance motor. In *Electrical Machines, ICEM, International Conference on*, pages 1–4.

[135] P. H. Mellor, D. Roberts, and D. R. Turner [1991]. Lumped parameter thermal model for electrical machines of tefc design. *Electric Power Applications, IEE Proceedings*, 138(5):205–218.

[136] F. P. Incropera and D. P. DeWitt [2002]. *Fundementals of heat and mass transfer.* John Wiley and Sons.

[137] P. Magnone, C. Fiegna, G. Greco, G. Bazzano, S. Rinaudo, and E. Sangiorgi [2012]. Numerical simulation and modeling of thermal transient in silicon power devices. In *Ultimate Integration on Silicon, ULIS, International Conference on*, pages 153–156.

[138] Z. Harijaona, R. Cantin, and G. Guarracino [2009]. Numerical modeling of impact of radiation exchanges between wood and building thermal comfort. In *Advances in Computational Tools for Engineering Applications, ACTEA. International Conference on*, pages 249–254.

[139] K. Boynov [2008]. *Efficiency and time-optimal control of fuel cell-compressor-electrical drive systems.* PhD thesis, Eindhoven University of Technology.

[140] L. Guangjin, J. Ojeda, E. Hoang, M. Gabsi, and M. Lecrivain [2012]. Thermal-electromagnetic analysis for driving cycles of embedded flux-wwitching permanent-magnet motors. *Vehicular Technology, IEEE Transactions on*, 61(1):140–151.

[141] M. M. A. Mazlan, E. Sulaiman, and T. Kosaka [2014]. Design study of single phase outer-rotor hybrid excitation flux switching motor for hybrid electric vehicles. In *Power Engineering and Optimization Conference, PEOCO, IEEE International*, pages 138–143.

[142] C. H. T. Lee, K. T. Chau, L. Chunhua, and Q. Chun [2014]. Design and Analysis of a New Multitoothed Magnetless Doubly Salient Machine. *Applied Superconductivity, IEEE Transactions on*, 24(3):1–4.

[143] L. E. Somesan, K. Hameyer, E. Padurariu, I. Viorel, and C. Martis [2012]. Sizing-designing procedure of the permanent magnet flux-switching machine based on a simplified analytical model. In *Optimization of Electrical and Electronic Equipment, OPTIM, 13th International Conference on*, pages 653–658.

[144] A. Serena and M. Molinas [2012]. Design of an arch-shaped fspm generator for the seaquest concept. In *Electrical Machines, ICEM, International Conference on*, pages 627–632.

[145] W. Hua and C. Ming [2006]. Inductance characteristics of 3-phase flux-switching permanent magnet machine with doubly-salient structure. In *Power Electronics and Motion Control Conference, IPEMC*, volume 3, pages 1–5.

[146] R. Krishnan [2010]. *Permanent magnet synchronous and brushless dc motor drives*. CRC Press, Taylor and Francis Group.

[147] F. J. M. Thoolen [May 2013]. Private communication.

[148] N. H. Vrijsen, J. W. Jansen, and E. A. Lomonova [2013]. Prediction of magnetic hysteresis in the force of a pre-biased e-core reluctance actuator. In *Electric Machines Drives Conference, IEMDC*, pages 1450–1457.

[149] J. Lavers, P. Biringer, and H. Hollitscher [1978]. A simple method of estimating the minor loop hysteresis loss in thin laminations. *Magnetics, IEEE Transactions on*, 14(5):386–388.

[150] D. A. Staton, A. Boglietti, and A. Cavagnino [2003]. Solving the more difficult aspects of electric motor thermal analysis. In *Electric Machines Drives Conference, IEMDC*, volume 2, pages 747–755.

[151] J. F. Trigeol, Y. Bertin, and P. Lagonotte [2006]. Thermal modeling of an induction machine through the association of two numerical approaches. *Energy Conversion, IEEE Transactions on*, 21(2):314–323.

[152] J. Nerg, M. Rilla, and J. Pyrhonen [2008]. Thermal analysis of radial-flux electrical machines with a high power density. *Industrial Electronics, IEEE Transactions on*, 55(10):3543–3554.

Samenvatting

Hybrid modeling techniques embracing permanent-magnet-biased salient machines

Dynamische toepassingen vereisen een hoge koppeldichtheid en profiteren van een robuuste rotor met een lage inertie. Tegenwoordig worden deze toepassingen gedomineerd door borstelloze permanente magneetmotoren. Echter, vertande, door permanente magneten voorgemagnetiseerde machines met verbeterde prestaties verrijzen doordat zowel de permanente magneten als de spoelen in de stator geplaatst worden. De statorspoelen zien een door de permanente magneten opgewekte hoge fluxdichtheid in de luchtspleet wanneer de statortanden en rotorpolen in lijn staan. Door de statorspoelen te bekrachtigen wordt daarmee een kracht geleverd tussen een statortand en een rotorpool. Op deze manier kunnen koppeldichtheden vergelijkbaar met die van borstelloze permanente magneetmotoren bereikt worden ondanks een gereduceerde elektrische belasting, terwijl er een rotor met rechte tanden gebruikt wordt, welke vergelijkbaar is met een geschakelde reluctantie rotor. Deze specifieke structuur bedingt een patroon van hoge fluxdichtheden binnenin de dubbel vertande luchtspleet. Daarom worden numerieke technieken toegepast voor de analyse van deze structuren. Deze technieken zijn in het algemeen echter het minst efficint qua rekenkracht voor zulke nieuwe machineontwerpen en zijn moeilijk te hanteren in een vroeg ontwerpstadium, wanneer de invloed van een aantal variabelen moet worden onderzocht.

Dit proefschrift zoekt combinaties van (semi-)analytische, ruimtelijk gediscretiseerde en mapping technieken voor de analyse van door permanente magneten voorgemagnetiseerde machines met vertanding, meestal flux schakelende permanente magneetmachines (FSPM) genoemd. Naast de noodzaak voor nieuwe elektromagnetische modelleermethoden voor FSPM wordt er een significante hoeveelheid aandacht besteed aan de ontwerpaspecten specifiek voor toepassingen met een hoge acceleratie. Beide onderwerpen komen respectievelijk in deel I en deel II van dit proefschrift aan bod.

Een model van structuren met dubbele vertanding kan gerealiseerd worden met talloze losstaande technieken. Voor de FSPM zijn dit bijvoorbeeld eindige elementen methode (FEM), magnetisch equivalent circuit en (semi-)analytische Fourier-serie analyse. Om de individuele voordelen van deze methodes te benutten en een grotere flexibiliteit in het ontwerpproces te behalen worden alternatieve methodes onderzocht in deel I. Deze methodes lossen eerste orde partile Maxwell differentiaalvergelijkingen dan wel tweede orde partile Poisson en Laplace differentiaalvergelijkingen op door mathematische methodes met verschillende mate van abstractie in drie hybride modellen (HM) te combineren:

HM1 Fourier-serie analyse en magnetisch equivalente circuit,

HM2 Tand contour methode en elektrostatische eindige-elementenmethode, en

HM3 Tand contour methode en Schwarz-Christoffel transformatie.

Elk hybride model wordt eerst geïntroduceerd in een versimpelde analyse, gevolgd door hun implementatie op de FSPM in volgorde van oplopende nauwkeurigheid. Voor beide structuren worden de methodes voor de HM gekoppeld op basis van de berekeningen van het magnetisch veld in de dubbel vertande luchtspleet. Voor HM1 wordt dit bereikt door de geometrische parameters aan te passen, in het geval van HM2 door een fijne discretisatie van de elektrostatische velden en bij HM3 door middel van simplificatie via mapping functies. Deze hybride modellen kunnen door hun toegevoegde functionaliteit, in tegenstelling tot FEM, omgaan met problemen van verschillende aard tijdens het ontwerpproces, zoals discontinuiteiten, verminderde nauwkeurigheid in de buurt van grenzen, materiaaleigenschappen en fabricatietoleranties. Een vergelijking tussen deze modellen laat de individuele voordelen in nauwkeurigheid, simulatietijd, het meenemen van magnetische niet-lineariteit, eindeffecten en mate van flexibiliteit in het ontwerp zien onder bepaalde beperkingen in toepasbaarheid.

Ontwerpvraagstukken worden vaak opgelost door een bepaalde structuur te optimaliseren en aan de hand van relatieve beoordelingen te bepalen of het eindproduct een acceptabele oplossing is, wat niet noodzakelijk een globaal optimum is. In deel II, over het ontwerpproces van FSPM voor applicaties met hoge acceleratie, worden deze dubbelzinnigheden vermeden door de belangrijkste ontwerpparameters te onthullen in een gegeneraliseerde aanpak die magnetische, thermische en mechanische ontwerpstappen omhelst. Een thermisch model is gecreerd op basis van een equivalent circuit om de bedrijfdslimieten te voorspellen. De optimalisatie van de rotor, waaronder het minimaliseren van de inertie en het verkrijgen van een zo glad mogelijk koppelprofiel, om aan de dynamische eisen van de toepassing te voldoen valt onder het mechanisch ontwerp. Om de dynamische prestaties van de FSPM te verifiëren is een prototype ontwikkeld op basis van de algemene ontwerpaanpak met specifieke criteria van/aan hoge acceleratie, koppelprofiel en overbelasting capaciteiten. Fysische randvoorwaarden zijn bepaald aan de hand van een geavanceerdste borstelloze permanente magneetmotor met goede acceleratie als maatstaf. Onder identieke thermische limieten behaalt het nieuw ontwikkelde FSPM prototype een relatief hogere acceleratie dan de referentiemotor.

Ozet

Hybrid modeling techniques embracing permanent-magnet-biased salient machines

Bu tez aki cevirmeli ve sabit miknatis etkilesimli motorlarin hibrit modellenmesi hakkindadir. Dinamik uygulamalarda kullanilan makinalarin yuksek moment uretebilmesi bir gerekliliktir. Ayrica rotorun eylemsizlik momentinin dusuk olmasi da bu konuda bir avantaj saglar. Bu tip uygulamalarin dusuk gerilim sinifina ait olanlari icin, fircasiz sabit miknatisli (PMAC) makinalar cogunlukla tercih edilmektedir. Gunumuzde bu makinalara alternatif olarak, sabit miknatis etkilesimli ve cikik kutuplu (PM-biased salient) makinalar daha yuksek performanslariyla one cikmaktadirlar. Bu makinalarin PMAC'lere gore en buyuk fiziksel farki statorunda hem sargisini hem sabit miknatisini barindirmasidir. PM-biased salient makinalarinda rotor ve stator kutuplari (disleri) hizalandiginda, stator uzerindeki sargilar hava boslugunda miknatislar tarafindan uretilen siddetli bir aki gorur. Bu anda stator sargilari uyarilarak stator disi ve rotor kutbu arasinda kuvvet olusturularak moment uretilir. Uretilen moment PMAC makinalaridakine benzer bir yogunluga sahiptir, ve anahtarlamali reluktans motorundaki (SRM) gibi cikik kutuplu rotor araciligiyla elde edildigi icin PMAC'ye gore daha dusuk bir elektriksel yuklenme gerektirir. Hem rotor hem statorun disli yapisindan dolayi, cift tarafli cikik kutuplu (double salient) bir hava araligina sahip olan bu motorlarin, hava araligindaki yuksek aki yogunluklarinin hesaplanmasi icin sayisal yontemler tercih edilmektedir. Lakin sayisal yontemler bu tur yeni makine topolojilerinin modellenmesi icin genellikle hesaplamalarda verimli degildir. Ozellikle makine dizayn asamasinda bir cok degiskenin etkileri gozlemlendigi icin, zaman konusunda dezavantaj getirmektir.

Bu tez, aki cevirmeli ve sabit miknatisli (FSPM) motorlarin ya da PM-biased salient adiyla anilan makinalarin analizi icin (yari-)analitik, uzlamsal olarak ayrik, eslemlemeli yontemleri arastirmaktadir. FSPM makinalarinin modellenmesi icin yeni elektromanyetik yontemlerin gerekliliginin yani sira yuksek ivmeli dinamik uygulamakara ozel tasarim hususlarina da tezde detayli olarak yer verilmistir. Bahsedilen bu iki konu tezin I. ve II. kisimlarinda degerlendirilmistir.

Cift tarafli cikik kutuplu motorlar; uzlamsal ayrik, sonlu elemanlar yontemi, manyetik esdeger devre ve (yari-)analitik Fourier analizi gibi farkli ve birbirinden bagimsiz yontemlerle modellenebilir. Hem her yontemin ustun yanlarindan faydalanmak hem de tasarim esnekligini artirmak icin alternatif yaklasimlar tezin I. kisimda arastirilmistir. Bu yaklasimlar birinci dereceden kismi turevli diferansiyel Maxwell denklemlerini yahut ikinci dereceden kismi turevli diferansiyel Poisson ve Laplace Denklermlerini cozmek icin, farkli matematiksel yaklasimlari farkli soyutlama duzeylerinde eslerstirerek uc hibrit model (HM) sunulmustur:

HM1 Fourier analizi ve manyetik esdeger devre,

HM2 Dis kontur metodu ve elektrosatik sonlu elemanlar yontemi ve

HM3 Dis kontur metodu ve Schwarz-Christoffel haritalanmasi.

Her bir hibrit model, oncelikle (basitlestirilmis) bir ornek topolojide tanitildiktan sonra, modeller FSPM uzerinde uygulamali olarak gosterilmistir. Her iki yapi icin de, HM'lerin eslestirilmesinde cikik kutuplu hava araligindaki manyetik hesaplamalar temel alinmistir. Bu HM1 icin geometrik parametlerin degistirilmesiyle, HM2 icin elektrostatik alanlar icinde ince ayriklastirma ile, HM3 icinse eslemlemeli fonksiyonlar araciligiyla sadelestirme ile gerceklestirilmistir. Yuksek islevsellikleri sayesinde hibrit yontemler, sonlu elemanlar yonteminin aksine, sureksizlik, sinir yakinlarinda azalan kesinlik, malzeme ozellikleri ya da uretim toleranslari gibi belirsizliklerden kaynaklanan rastlantisal etkilerin modellenmesini yapabimektedirler. Bu modeller karsilastirilarak her birinin kesinlik, simulasyon (benzetim) suresi, manyetik karakteristiklerin (dogrusal olmayan) hesaba katilmasi ve uygulananilirlik kisitlamalari altinda sunduklari tasarim esnekligi ve uc etkisi (3 boyutlu etkiler) hususlarindaki ustunlukleri belirtilmistir.

Tasarim sorunlari genelllikle belli bir yapinin optimizasyonu ve elde edilen urunun amaca uygunlugunun degerlendirilmesiyle cozulmektedir. Lakin bu tur yerel bir optimizasyon en iyi genel sonucu vermeyebilir. Yuksek ivmeli uygulamalar icin FSPM tasarim sureciyle ilgili olan II. kisimda manyetik, isil ve mekanik tasarim asamalarindan olusan genel bir yaklasimdaki kilit tasarim parametrelerini meydana cikararak bu belirsizlikler giderilmistir. Makinanin calisma sinirlarini tahmin etmek amaciyla isil esdeger devreye dayali bir isi modeli olusturulmustur. Rotor optimizasyonu, eylemsizligini azaltmak ve duzgun bir moment profili olusturarak dinamik uygulama gereksinimlerini karsilamak amacini guden mekanik tasarimi kapsamindadir. FSPM'nin dinamik kabiliyetini dogrulamak amaciyla yuksek ivme, moment profili ve asiri yukleme kabiliyetine dayali genel yontemi temel alan bir prototip tasarlanmistir. Fiziksel sinirlamalar, basarili bir ivme kabiliyeti olan son teknoloji bir fircasiz PMAC motor kistas (benchmark) alinarak saptanmistir. Ayni isil calisma kosullarinda, yeni gelistirilmis FSPM motoru ile, kistasa nazaran daha yuksek ivme elde edilmistir.

Acknowledgements, Tesekkurler

This thesis is a result of years research into the depths of electromagnetism of machines and biochemistry of humans. It signifies the closing of one chapter in my life and the opening of a new one.

My sincere gratitude goes to Elena for offering me this project, which started during my master studies. With her support and guidance, my *baby* and me, we have come a long way in this journey resulting in this thesis. She always reminded me of the importance of listening over speaking as indicated by the Turkish proverb *Soz gumusse, sukut altindir.* Next, I wish to thank my *bigger brother* Johan for his patience and guidance. He became the *glue* and *interpreter* of this project with his positive attitude and practical experience. Besides the project, I gained also a lot of experience with giving lectures and enjoyed our various discussions. Furthermore, I would like to thank Bart, Laurentiu, and Emilia for their scientific inputs during different phases of the project.

The valuable contributions and suggestions of the committee members Prof. Mellor, Prof. Krein, Prof. Nijmeijer, dr. Thoolen and dr. Gysen enriched this work. I would like to thank each of them for their efforts in the proofreading of the thesis.

A PhD life is never complete without friends following a similar path with its ups and downs. This journey would be unbearable without the, new and old, inhabitants of Impuls 0.12 as Johan, Timo, Reyhan, Bob, Tsvetan, Tom, and Dave. Although *some* were a bit cautious in the beginning due to a female presence in the room, they all soon adapted to it (more or less). As we slowly depart from academia to industry (Timo, Johan jullie zijn bijna klaar!) the memories we shared and our passion for science and technology will sure keep us in touch. Special thanks go to Tsvetan for his help with motor controllers, the setup and his practical way of solving problems. I also would like to thank our next-door neighbors for keeping the sanity levels of our group as high as possible. The frequent chocolate supplier Yang, the language expert Sultan and my project partner Maarten, they all contributed to my evening shifts during the writing phase. In the world of electrical machines, it is precious to have female colleagues, hence I was very glad for the small talks and sportive activities we engaged with both Monica and Nancy.

As any student in the EPE group goes from theory to practice in the laboratory, Marijn, Wim and Rutger are overwhelmed by the never-ending problems and questions. From the trio, I would like to express my gratitude especially to Marijn for his practical help on the experimental setup and our nice conversations.

Besides the EPE group, Humanoid Robotics Team (later Tech United) has been my second working group in late evenings and weekends for many years. I would like to thank for the wonderful times and travels around the world for many RoboCup competitions. Our robot, TUlip, would never be able to play football without Henk, Dragan, Pieter, Jurjen, Tim, Can and many more. I will always remember the surgical operations performed in the robot, brainstorming on the mechanical or electrical problem origins, dancing exhibitions, and many more public appearances with TUlip.

Additional thanks go to CCM (Centre for Concepts in Mechatronics) and AE (Advanced Electromagnetics) for their impressive work in manufacturing the prototype. Discussions with Frans Thoolen, Peter Klijn and Laurentiu Encica gave me more insight on practical realization of a product.

Finally, I would like to thank all my friends in the Netherlands and my colleagues from the EPE group for the mutual support and great friendships. I think the biggest advantage of this group has been the connectivity in times of need, such as interpretation of Flux error messages, the public services of **The***BruceDickinson* productions with LaTeX and cover designs, hours of talks on the joys and difficulties of the personal and professional life...

Her ne kadar yaban ellerde bulunsam da birbirimizden kop(a)madığımız sevgili dostlarım Gökhan ve Sevinç'e tez stresinden beni uzak tuttukları için teşekkür ederim. Hemen her konudaki tartışmalarımızda (teknik, bilimsel, politik, komik, ...) arasıra başlarını ağrıttığım için beni mazur gördüklerine eminim.

Tezimin bu son satırlarını yazarken, geçtiğimiz yedi sene boyunca, yüksek lisans ve doktora eğitimim icin benim her kahrımı çeken aileme teşekkürün en büyüğünü bir borç bilirim. Güzel İzmirimizi ve oranın sıcak insanlarını bana tanıtan teyzemle enişteme, kardeş olmanın sadece fiziksel değil ruhen de yanyana olmak olduğunu bana öğreten Işıl'a, hayatın bir tarih sahnesi kadar katmanlı olduğunu bana hatırlatan babama teşekkür ederim.

Annecim, dünyaya açılmama önayak olup başarılarımla ne kadar gururlandığının, ama senden uzakta kaldığım için de ne kadar üzüldüğünün farkındayım. Sabrınla teze konstantre olma dozajını bana dirhem dirhem verdiğin ve de sonsuz sevgin için sana minettarım!

Thank you all / Dank u wel / Herkese çok teşekkür ederim!

Esin İlhan
Eindhoven, 2014

Curriculum Vitae

Esin Ilhan was born on June 9^{th} 1983 in Istanbul, Turkey. She received her BSc degree in Electrical Engineering from the Istanbul Technical University (ITU) in 2007. At the same year, she competed at the World-championship of Solar Boats, Solarsplash, in the USA, with the Turkish team which won the 3^{rd} place. With the full university scholarship, she obtained her MSc degree in Electrical Engineering from the Eindhoven University of Technology (TU/e) in 2009. In 2008-2013, she joined the humanoid robotics group (later TechUnited) first as student assistant, later as the head of electronics group for the annual RoboCup tournaments in the adult size league. In 2009, she started as a PhD student in the group of Electromechanics and Power Electronics at the Electrical Engineering department of TU/e. Her research topic included design, understanding and realization of parallel flux switching machines which has led to this thesis.